Durham E-Theses

Pieces of the Higgsaw

REINESS, JOEY,YANIR

Pieces of the Higgsaw

Joey Y. Reiness

A Thesis presented for the degree of
Doctor of Philosophy

Durham
University

Institute for Particle Physics Phenomenology
Department of Physics
Durham University
United Kingdom

May 2020

Pieces of the Higgsaw

Joey Y. Reiness

Submitted for the degree of Doctor of Philosophy

May 2020

Abstract: The discovery of a 125 GeV scalar boson at the Large Hadron Collider in 2012 sparked at least as many questions as it answered. The Higgs boson is unique in being the only known fundamental scalar particle, which makes it compelling in a variety of contexts. As the field of Higgs physics has developed and aged, this era-defining boson has crept into relevance throughout all areas of high-energy physics.

This thesis looks at the Higgs boson and its potential properties in three different regimes:

The first focuses on how measurements of Higgs interactions at particle colliders can be used to discern and identify signs of new physics. A novel analysis method is presented, which uses differential observables to constrain the effects of higher-energy physics within the Standard Model Effective Field Theory framework. This approach takes advantage of expected angular structures in the matrix elements to maximise sensitivity and obtain competitive bounds on the anomalous Higgs-gauge couplings.

The second takes a more theoretical approach and looks at the potential high-energy high-multiplicity behaviour of the Higgs. Multiparticle scalar production is considered in an idealised non-perturbative limit by employing a semiclassical treatment. Previous calculations of the semiclassical rate are consolidated and extended.

The third investigates the potential role of the Higgs in the dynamics of the early universe. A unified model is presented in which minimal additional field content leads to the solution of five problems in fundamental physics. The available parameter space for this model is within the reach of proposed future experiments.

These three areas of research all have the same physics at their core but are fuelled by techniques and ideas from different fields. Together they form three small distant-yet-connected pieces of the ever-growing network of Higgs-related investigations, or *Higgsaw.*

Contents

Declaration

The work in this thesis is based on research carried out in the Institute for Particle Physics Phenomenology at Durham University. No part of this thesis has been submitted elsewhere for any degree or qualification. This thesis is partly based on joint research as noted below.

- Part I is based on the articles *"Resolving the tensor structure of the Higgs coupling to Z-bosons via Higgs-strahlung"* published in Physical Review D [1] and *"Towards the ultimate differential SMEFT analysis"*, currently under review [2].

- Part II is based on the review *"Review of the semiclassical formalism for multiparticle production at high energies"* published in Physics Reports [3] as well as the article *"Precision measurements for the Higgsploding Standard Model"* published in Journal of Physics G [4].

- Part III is based on the article *"All-in-one relaxion: A unified solution to five particle-physics puzzles"* published in Physical Review D [5].

Acknowledgements

First and foremost I would like to thank my supervisor, Valya Khoze, who has been a consistent source of advice, expertise and entertaining conversation over the course of my PhD journey. I have also had the privilege of working with many other fantastic and gifted people and so I extend my thanks to my collaborators: Michael Spannowsky, Rick Gupta, Shankha Banerjee, Jakub Scholtz, Satyajit Seth and Philip Waite. None of this work would have been possible without the funding of the STFC, for which I am very grateful.

Over the past few years, the IPPP has been a wonderful place of work, learning and play; its sense of community is second to none. My PhD wouldn't have been the same without the shenanigans, from plot of the month and the IPPP musical to the soupdicate and squash ball foot golf. I'd like to thank Alex Lenz and the rest of the IPPP Outreach Team for countless adventures. I am also grateful to Giuseppe, Jack, Jonny, Lucy, Daniel, Hitham, Danny, Elliott, Gavin, Parisa and Andrew, who kindly proofread parts of this thesis.

I apologize to my officemates, who have had to experience my bizarre working habits, musical outbursts and physics frustrations. In particular, I want to thank Matthew for being the model example, Maura por mandarme a la chingada a diario, and Ryan for making me feel nutritionally incomplete.

Of all the amazing people at the IPPP, I couldn't possibly forget to mention the one and only queen of the IPPP: Trudy. Without her, nothing in the IPPP would happen. Thank you for always supporting me and being an invaluable friend. I'm also grateful to Linda, Joanne, Deborah, Adam and Paul, who have all been an important part of my Durham life.

Physics aside, I wouldn't be where I am today without the constant love and support of my family. Finally, I would like to thank May, who had the luck of meeting me as a happy-go-lucky second year yet the bad judgement to stay by my side as I developed into a weary final-year husk.

Chapter 1

Introduction

The focus of this thesis is the Higgs boson. What is it? How is it relevant to the functioning of our universe?

This chapter introduces the Higgs boson as the heart of the Standard Model – our best current model of the universe and its fundamental interactions. The Standard Model (SM) is a particle physics theory; it aims to identify the most basic of building blocks or *particles* in our universe and describe the way they interact with each other such that its predictions agree with experimental data.

The Higgs boson, discovered[2] at CERN in 2012, was the last piece of the SM puzzle. Excitement surrounding its postulation and discovery has spawned a vast variety of research areas under the umbrella term of 'Higgs physics'. The remainder of this thesis looks at three different ways the Higgs and its properties are being investigated in very different contexts. These are just three small pieces of the ever-growing Higgs jigsaw or, dare I say it, *Higgsaw*.

Note that throughout this thesis, natural units are used unless specified otherwise, such that $\hbar = c = 1$.

1.1 The Standard Model

This section summarises the Standard Model of particle physics, a theory developed and extended over the last one hundred years into its modern form presented below. For some notable works in its history, see Refs. [6–20]. For more modern textbook perspectives, see Refs. [21–25].

---

[2]More precisely, CERN discovered a new scalar particle with properties that are thus-far proving to be consistent with those expected of the Standard Model Higgs boson.

The Standard Model is a quantum field theory (QFT) with gauge symmetry $SU(3)_c \times SU(2)_L \times U(1)_Y$. QFTs combine notions from quantum mechanics with the laws of special relativity. On top of translation invariance, we require Lorentz invariance in a four-dimension Minkowski spacetime and build Lorentz invariants from objects in different unitary irreducible representations of the Poincaré group – the group of symmetries of spacetime.

In the QFT framework, particles are understood as excitations of quantum fields. In the Standard Model, these quantum fields come in different Poincaré representations based on their mass and spin. The bosonic spin-0 and spin-1 fields are embedded into Lorentz scalars and Lorentz four-vectors respectively, with gauge invariance imposed in the latter case to give the required degrees of freedom. Fermionic spin-$\frac{1}{2}$ fields take two different spinor representations, forming left- and right-handed Weyl spinors. Conventionally, pairs of these Weyl 2-spinors are combined into Dirac 4-spinors, which contain both left- and right-handed parts. These Dirac 4-spinors can be combined with the gamma matrices[1], γ^μ, to create Lorentz scalars and four-vectors.

The dynamics of a QFT are dictated by the theory's Lagrangian density, $\mathcal{L}$. Imposing the Poincaré and gauge symmetries, we can write all allowed renormalisable Lagrangian terms built from our field building blocks and spacetime derivatives. The result is the Standard Model Lagrangian[2],

$$
\begin{aligned}
\mathcal{L}_{\mathrm{SM}} = &- \frac{1}{4} F^{\mu\nu} F_{\mu\nu} \\
&+ i\bar{\Psi} \not{D} \Psi \\
&+ |D_\mu H|^2 - V(H) \\
&- y_{ij} \bar{\Psi}_i H \Psi_j + \text{h.c.}
\end{aligned}
\tag{1.1.1}
$$

where $F^{\mu\nu}$ is a gauge field strength tensor, Ψ is the Dirac spinor of a matter field and H is the Higgs doublet. The covariant derivative, D_μ, and the Higgs potential $V(H)$ are defined and discussed in Sections 1.1.2 and 1.1.3, respectively. This Lagrangian attempts to describe the behaviour of all known fundamental[3] particles and three of the four fundamental forces. The SM particle content is summarised in Table 1.1.

We now briefly look in turn at each part of the above Lagrangian, starting with the propagation and self-interactions of force-mediating gauge bosons in Section 1.1.1.

---

[1]The γ-matrices satisfy the anticommutation relation $\{\gamma^\mu, \gamma^\nu\} = 2g^{\mu\nu}$, where $g^{\mu\nu}$ is the Minkowski metric tensor.

[2]A small caveat here is a possible $F\tilde{F}$ term, which is expected to be present upon more careful inspection of the $SU(3)_c$ vacuum. The apparent lack of such a term in the SM is called the strong CP problem and is discussed further in Section 7.1.

[3]Here fundamental refers to fact that, as far as we know, these particles cannot be broken down any further; they have no substructure.

u	c	t	γ
d	s	b	g
ν_e	ν_μ	ν_τ	W, Z
e	μ	τ	h

Table 1.1: *The particle content of the Standard Model. We have three generations of quarks and leptons that make up the fermionic matter in the top-left and bottom-left respectively. The gauge bosons associated with the fundamental forces are shown in the top-right. Finally, the scalar Higgs boson is in the bottom-right corner.*

We then look at the matter fields in Section 1.1.2 and how their transformations under different gauge groups result in interactions. In Section 1.1.3 we look at the scalar sector, where the Higgs field's interactions with itself and the other SM fields results in the dynamic generation of masses via the Higgs mechanism. Finally, we comment on some shortcomings of the Standard Model, many of which are revisited in more detail in Chapter 7.

1.1.1 The gauge sector

As mentioned previous, the Standard Model has the gauge structure of $SU(3)_c \times SU(2)_L \times U(1)_Y$. Each of these three gauge groups comes with a spin-1 vector gauge field that mediates the associated force. The $SU(3)_c$ gauge group gives rise to the strong interactions, also known as Quantum Chromodynamics (QCD). The subscript c refers to *colour*, the word we use to denote charge under this interaction. The $SU(2)_L$ gauge group couples to *weak isospin*, which is only found in left-handed fermions, hence the L subscript. Finally, the $U(1)_Y$ gauge group couples to a quantity known as *hypercharge*. The three interactions associated with these groups are not the three forces we generally discuss. This is because the Higgs mechanism, described in Section 1.1.3, will cause the gauge symmetry of the SM to spontaneously break down to $SU(3)_c \times U(1)_{EM}$, where the resultant $U(1)_{EM}$ force is the familiar electromagnetism; this will also cause the gauge bosons associated with the weak force to acquire masses. Therefore, the gauge symmetry of the SM can be thought of as the strong group, $SU(3)_c$, and an electroweak sector $SU(2)_L \times U(1)_Y \to U(1)_{EM}$.

The spin-1 bosonic gauge fields are represented by four-vector potentials, like the familiar electromagnetic four-potential A^μ, that transform in the adjoint representation of the corresponding gauge group. These potentials often come packaged in a more useful structure known as the field strength tensor. For a general non-Abelian

$SU(N)$ group, this field tensor is defined as,

$$G^a_{\mu\nu} = \partial_\mu G^a_\nu - \partial_\nu G^a_\mu + g f^{abc} G^b_\mu G^c_\nu, \qquad (1.1.2)$$

where repeated indices are summed, G^a_μ represents $(N^2 - 1)$ bosonic fields for the $(N^2 - 1)$ generators of $SU(N)$, f^{abc} are the structure constants of $SU(N)$ and g is the interaction coupling strength. In QCD, $g = g_s$ and a runs from 1 to 8, giving 8 different gluons for the 8 generators of $SU(3)_c$. For $SU(2)_L$, the Gs are generally swapped for Ws and f^{abc} is simply the Levi-Civita tensor, ϵ^{abc}. The value of a runs from 1 to 3 giving three weak bosons, $\{W^1, W^2, W^3\}$. The W^1 and W^2 bosons mix to form the $W^\pm$ bosons. The W^3 boson mixes with B, the boson of $U(1)_Y$, via the Higgs mechanism to give A, the photon of electromagnetism and Z, the neutral weak boson. In the case of Abelian gauge symmetries like $U(1)_{EM}$, where $f^{abc} = 0$, the definition in Eq. 1.1.2 reduces to,

$$F_{\mu\nu} = \partial_\mu A_\nu - \partial_\nu A_\mu, \qquad (1.1.3)$$

which is the familiar expression for the electromagnetic field strength tensor. The lack of the final $f^{abc} G^b_\mu G^c_\nu$ term for $U(1)$ field tensors means that Abelian gauge bosons, such as the photon, are not classically self-interacting. These tensors are useful because the contraction $F^a_{\mu\nu} F^{a\,\mu\nu}$ is a gauge-invariant Lorentz scalar. We can now understand the first line in Eq. 1.1.1 as representing the dynamics and self-interactions of the gauge fields.

Finally, note that a mass term like $m_a^2 A^\mu A_\mu$ is not gauge invariant. As such, gauge boson are required to be massless, unless their gauge symmetry is dynamically broken, as in the case of the Higgs mechanism in Section 1.1.3.

1.1.2   The fermionic sector

The fermionic spin-$\frac{1}{2}$ matter fields are conventionally denoted by Dirac spinors, Ψ. The interactions of the gauge fields with the matter content of the Standard Model are encoded in the covariant derivative [25],

$$D_\mu = \partial_\mu - ig' B_\mu Y - ig W^a_\mu \sigma^a / 2 - ig_s G^a_\mu t^a, \qquad (1.1.4)$$

where g', g and g_s are the coupling strengths of the $U(1)_Y$, $SU(2)_L$ and $SU(3)_c$ interactions respectively. Each gauge boson is accompanied by an appropriate generator, t^a. For the $SU(2)_L$ group, these generators are proportional to the Pauli matrices, $\sigma^a / 2$. The $U(1)_Y$ generator is the identity and fields transform with different hypercharges, Y. This covariant derivative is introduced to make the term $D_\mu \Psi$ covariant, such that $\bar{\Psi} \slashed{D} \Psi \equiv \bar{\Psi} \gamma^\mu D_\mu \Psi$ is gauge invariant.

The definition of the covariant derivative changes according to the gauge group representation of the field upon which it acts. The gauge transformations of the fields in the SM can be described by three numbers: the $SU(3)_c$ representation, the $SU(2)_L$ representation and the charge Y under $U(1)_Y$.

The matter content of the SM can be arranged into five different multiplets per generation, as well as the scalar Higgs doublet, H. The representations and charges of these fields is shown in Table 1.2. Note that the matter multiplets are in either the fundamental ($\mathbf{N}$) or trivial ($\mathbf{1}$) representation of each non-Abelian group, $SU(N)$. Consider, for example, Q, which has representation $\{\mathbf{3}, \mathbf{2}, \frac{1}{6}\}$. It is a doublet ($\mathbf{2}$) of $SU(2)_L$, consisting of the left-handed parts of the up and down quark fields,

$$Q = \begin{pmatrix} u_L \\ d_L \end{pmatrix} , \tag{1.1.5}$$

where each of these two entries is also a triplet ($\mathbf{3}$) of $SU(3)_c$, for example,

$$u_L = \begin{pmatrix} u_L^r \\ u_L^b \\ u_L^g \end{pmatrix} , \tag{1.1.6}$$

where the superscripts denote the 3 different QCD *colours*: red, blue and green. Finally, Q transforms under $U(1)_Y$ with a hypercharge of $\frac{1}{6}$, and there is a similar Q multiplet for the other two generations: (c, s) and (t, b). Similarly, L is a left-handed $SU(2)_L$ doublet consisting of a neutrino[1] and a left-handed charged lepton, $L = (\nu_e\ e_L)$. We can now understand the second line in Eq. 1.1.1 as describing the dynamics and gauge interactions of the fermions.

Note that only left-handed fields transform non-trivially under $SU(2)_L$, hence the L subscript. This means that we run into complications if we want our fermions to be massive. Dirac mass terms appear in the Lagrangian as $-m\bar{\Psi}\Psi$, which when written in terms of the left- and right-handed parts becomes,

$$- m\bar{\Psi}\Psi = -m\bar{\Psi}_L\Psi_R + \text{h.c.} \tag{1.1.7}$$

It is therefore a problem if the left- and right-handed parts of a field have different gauge interactions. This is the case for all SM fermions and thus SM Dirac mass terms are not gauge invariant. Once again, we seek a dynamic generation of masses: enter the Higgs mechanism.

---

[1]Note that in the standard model, neutrinos are considered massless and left-handed; there are no right-handed neutrinos. This is in conflict with recent observations, see Section 7.2.

Field	$SU(3)_c$	$SU(2)_L$	$U(1)_Y$
Q	**3**	**2**	$\frac{1}{6}$
u_R	**3**	**1**	$\frac{2}{3}$
d_R	**3**	**1**	$-\frac{1}{3}$
L	**1**	**2**	$-\frac{1}{2}$
e_R	**1**	**1**	-1
H	**1**	**2**	$\frac{1}{2}$

LH	RH
u_L	u_R
d_L	d_R
ν_L	
e_L	e_R

Table 1.2: *The Standard Model (SM) field multiplets and their representation/charge under the three unbroken gauge groups. The first generation of the SM matter content is also shown, with its right-handed (RH) and left-handed (LH) parts grouped into these five multiplets: the Q, L doublets and the u_R, d_R, e_R singlets. Note the absence of a RH neutrino field, which does not exist in the SM. The representation and charge of the Higgs doublet is also shown, as a reference for Section 1.1.3.*

1.1.3 The Higgs mechanism

The final ingredient of the Standard Model is the Higgs field. The following description of the Higgs mechanism [13, 14, 26–28] is largely inspired by texts like Ref. [25]. The discovery of the Higgs, its production and its decays, are discussed in Chapter 2. We introduce the Higgs field as an $SU(2)_L$ doublet of two complex scalar fields, with hypercharge $Y = \frac{1}{2}$,

$$H = \begin{pmatrix} \phi^+ \\ \phi^0 \end{pmatrix} = \frac{1}{\sqrt{2}} \begin{pmatrix} \phi_1 + i\phi_2 \\ \phi_3 + i\phi_4 \end{pmatrix} , \tag{1.1.8}$$

where ϕ_i are real scalar fields. This doublet has four degrees of freedom. The dynamics of the Higgs and the Higgs mechanism are encoded in the final two lines of Eq. 1.1.1. The Higgs potential,

$$V(H) = \mu^2 H^\dagger H + \lambda (H^\dagger H)^2, \tag{1.1.9}$$

is such that for $\mu^2 < 0$ the potential has a minimum at non-zero $|H| = \sqrt{H^\dagger H}$. The Higgs doublet develops a non-zero vacuum expectation value (VEV),

$$\langle H \rangle = |H| = \frac{v}{\sqrt{2}} = \sqrt{\frac{-\mu^2}{2\lambda}} , \tag{1.1.10}$$

where the value of v has been measured to be $v \approx 246$ GeV. This non-zero vacuum state of the Higgs field is not invariant under the electroweak group, $SU(2)_L \times U(1)_Y$, which is spontaneously broken as a result.

Note that since we have 4 degrees of freedom, the requirement in Eq. 1.1.10 in

fact defines an S^3 surface of degenerate states. Gauge transformations correspond to moving between different states on this surface. Excitations along these flat directions don't cost energy and correspond to three massless Goldstone modes. On the other hand, excitations in the radial direction feel a pseudo-quadratic potential, resulting in a massive particle: the Higgs boson.

We choose ϕ_3 to be the radial direction, without loss of generality, such that $\phi_3 = v+h$, where h is the real radial perturbation corresponding to the Higgs boson. We can then use gauge transformations to go to the unitary gauge, where,

$$H = \frac{1}{\sqrt{2}} \begin{pmatrix} 0 \\ v + h \end{pmatrix}, \qquad (1.1.11)$$

and the Goldstone modes ϕ_1, ϕ_2, ϕ_4 have been entirely gauged away. Recalling the covariant derivative in Eq. 1.1.4 and keeping in mind the representation of the Higgs doublet, $\{\mathbf{1},\mathbf{2},\frac{1}{2}\}$ (as shown in Table 1.2), we see that,

$$|D_\mu H|^2 = \frac{1}{2}(\partial_\mu h)^2 + \frac{1}{4}g^2(v+h)^2 W_\mu^+ W^{-\mu} + \frac{1}{8}(v+h)^2(g^2 + g'^2)Z_\mu Z^\mu, \quad (1.1.12)$$

where the more familiar $W^\pm$ and Z bosons have been identified as linear combinations of the pre-breaking bosons,

$$W_\mu^\pm = \frac{1}{\sqrt{2}}(W_\mu^1 \mp iW_\mu^2), \qquad Z_\mu = \frac{gW_\mu^3 - g'B_\mu}{\sqrt{g^2 + g'^2}} = c_W W_\mu^3 - s_W B_\mu, \qquad (1.1.13)$$

where $c_W = \cos\theta_W$, $s_W = \sin\theta_W$ and θ_W is the angle of rotation of Z_μ with respect to the two original bosons, W^3 and B. We can now see that the $|D_\mu H|^2$ term gives interactions between the Higgs boson, h, and the weak bosons. Furthermore, the v^2 part of $(v+h)^2$ gives the weak bosons mass terms[1],

$$M_W^2 = \frac{g^2 v^2}{4}, \qquad M_Z^2 = \frac{M_W^2}{c_W^2}. \qquad (1.1.14)$$

The complimentary orthogonal boson to Z,

$$A_\mu = s_W W_\mu^3 + c_W B_\mu, \qquad (1.1.15)$$

has no coupling to the Higgs, does not acquire mass, and is identified as the photon. As a consequence, the electromagnetic coupling strength is related to the weak coupling strength via the same electroweak rotation angle $e = gs_W = g'c_W$. Similarly, one finds that the electric charge of a field is connected to its hypercharge and third

---

[1]Note that this ratio of weak boson masses is a prediction specific to the model where the Higgs field is a doublet of $SU(2)_L$. The ratio changes for other representations, see for example Ref. [29].

weak isospin component, I_3, via the relation,

$$Q_{\text{EM}} = I_3 + Y, \tag{1.1.16}$$

where the two entries of a weak doublet have $I_3 = (\frac{1}{2}, -\frac{1}{2})$. This retrospectively explains the superscripts on the Higgs doublet entries, $H = (\phi^+, \phi^0)$.

In summary, the Higgs potential prefers a non-zero VEV, which spontaneously breaks electroweak gauge symmetry. Three of the four electroweak generators are broken, with the corresponding Higgs degrees of freedom acting as the longitudinal modes of the associated gauge bosons and giving them masses. The remaining unbroken direction is a linear combination of the W^3 and B, which we identify as the generator of electromagnetism, so that the remaining unbroken subgroup is $U(1)_{EM}$ and the photon remains massless. The one remaining Higgs degree of freedom is the real Higgs boson. Using the unitary gauge expression in Eq. 1.1.11 and the potential in Eq. 1.1.9 we can identify the resultant mass of the Higgs boson,

$$m_h^2 = 2\lambda v^2 = -2\mu^2. \tag{1.1.17}$$

We now consider the final line in the SM Lagrangian in Eq. 1.1.1, which describes the Yukawa interactions of the Higgs field with two fermion fields. To maintain gauge invariance, we require that one of the fermion fields is a $SU(2)_L$ doublet and that the other is an $SU(2)_L$ singlet. Consider for example, the term,

$$- y_d \bar{d}_R H^\dagger Q + \text{h.c.} = -m_d \bar{d}d - \frac{y_d}{\sqrt{2}} h \bar{d}d, \tag{1.1.18}$$

which upon substituting the Higgs doublet in the unitary gauge gives us a down quark mass and hdd interactions. We can identify the down mass as $m_d = y_d v/\sqrt{2}$, where y_d is the Yukawa coupling. The masses of the other lower-doublet-entry fields follow suit. For up-type fields we require the conjugate Higgs doublet $\tilde{H} \equiv i\sigma^2 H^*$ and corresponding terms like $-y_u \bar{u}_R \tilde{H} Q$.

We have now seen that the Higgs mechanism successfully provides the required masses in the Standard Model. Note that while the gauge boson masses are theoretically fixed by the procedure, the fermion masses are dictated by the free Yukawa parameters, which span a large range of values. That there is no apparent theoretical motivation for the observed set of values makes many uncomfortable and is known as the flavour problem.

As one final remark, we note that since there are 3 generations of quarks, the quark Yukawa couplings form two 3×3 complex matrices, one for the up sector and one for the down sector, y_{ij}^u, y_{ij}^d. These matrices need not be diagonal. In other words, the weak interaction flavour basis can be rotated with respect to the mass basis. Suppose

that the unitary matrices U_L and D_L rotate the mass eigenstates into the flavour eigenstates. For the neutral current Z interactions these rotations arise in cancelling pairs, such as $U_L^\dagger U_L = 1$. On the other hand, charged current $W^\pm$ interactions mix the up and down sectors and thus give generation-changing interactions parametrised by the unitary Cabibbo-Kobayashi-Maskawa (CKM) matrix, $V \equiv U_L^\dagger D_L$. The CKM matrix can be specified by three angles and a phase. The phase, δ_{CKM}, is important in discussions of CP violation in Chapter 8.

1.1.4 Problems with the Standard Model

The Standard Model Lagrangian in Eq. 1.1.1 (almost) successfully describes the dynamics of all known fundamental particles and their interactions via three of the four fundamental forces: the strong force, the weak force and electromagnetism. The SM famously fails to give a particle description of gravitational interactions, which remain best-described by Einstein's more macroscopic theory of general relativity. Various attempts to combine the two theories exist, the most notable of which is string theory. Other problems with the Standard Model exist, including:

- **Hierarchy problem**: the large separation in scales between the Higgs mass $m_h \approx 125$ GeV and the Planck scale $M_P \sim 10^{18}$ GeV, see Section 1.2.2.

- **Strong CP problem**: the lack of observable CP violation in the strong sector despite CP-violating terms being allowed by the SM symmetries, see Section 7.1.

- **Neutrino masses**: recent observations in neutrino oscillations point to massive neutrinos in contrast to the massless neutrinos in the SM, see Section 7.2.

- **Baryon asymmetry**: naively, SM interactions require that matter and anti-matter be produced in equal measure, yet the universe appears to be dominated by matter, see Section 7.3.

- **Dark matter**: observations in cosmology are inconsistent with the known matter content of the universe and point to the existence of a new matter content, see Section 7.4.

- **Dark energy**: as well as dark matter, observation of accelerated cosmological expansion and closure of the universe requires a new unknown form of energy with properties distinctly different to matter [30]. Dark energy is not considered in this thesis.

- **Flavour problem**: the masses of the fermions in the standard model enter in an ad hoc way via Yukawa couplings to the Higgs. The range of fermion masses is immense, from the sub-MeV electron to the 173 GeV top quark. There seems little theoretical motivation for this hierarchy of scales. A popular solution is presented in Section 7.2.1. For more information on the flavour problem, see for example Ref. [31].

The hierarchy problem is explained in Section 1.2 as part of our discussion on the properties of the Higgs. Some of the other problems are discussed further in Chapter 7.

1.2   More on the Higgs

We have seen that the Higgs field is introduced to spontaneously break electroweak gauge symmetry and generate particle masses. Before we move on to the bulk of the thesis, it will be helpful to take a look at two more consequences of introducing the Higgs, namely the Goldstone equivalence principle and the Higgs hierarchy problem.

1.2.1   The Goldstone equivalence principle

In Section 1.1.3, we saw how the three massless Goldstone bosons could be gauged away and reinterpreted as the longitudinal modes of the weak bosons. The purely transverse massless gauge bosons 'eat' the Goldstone bosons to gain mass and a third polarisation. Hence, the longitudinal modes of $W^\pm$ and Z account for 3 of the 4 Higgs degrees of freedom, with the fourth manifesting itself as the real Higgs boson.

At high energies, the longitudinal polarisations of the massive gauge bosons exhibit behaviour resembling their Goldstone origins. In fact, it can be shown that absorption/emission amplitudes for longitudinal vectors and Goldstone scalars are identical up to a factor,

$$\mathcal{M}(X \to Y + V_L) = \mathcal{M}(X \to Y + \phi_{\mathrm{GB}}) \times (1 + \mathcal{O}(M_W/E)) , \qquad (1.2.1)$$

which approaches unity in the high-energy limit [21]. The idea that the longitudinal modes can be treated as simpler Goldstone scalars in high-energy processes is known as the Goldstone equivalence principle [32, 33]. This can help simplify calculations of high-energy amplitudes.

It is worth noting that so far we have assumed that the Higgs and Goldstone bosons are packaged into an $SU(2)_L$ Higgs doublet. This leads to inherent correlations
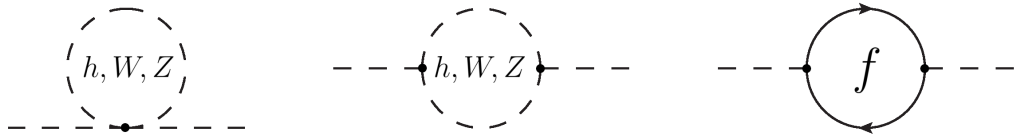
Figure 1.1: *Quadratically-diverging diagrams contributing to Higgs mass corrections in Eq. 1.2.2. There are two topologies for scalar Higgs loops via self-interaction. These topologies also exist for weak vector boson loops. Finally, any fermion, f, that couples to the Higgs contributes via a fermion loop. Given that a fermion's Higgs couplings is proportional to its mass, the top quark gives the leading fermionic contribution.*

between weak boson and Higgs interactions. Such correlations are used to assess bounds on new physics effects in Chapter 3. However, one can also consider a model in which the discovered scalar boson degree of freedom is entirely unassociated with the three Goldstone modes, such that many of these correlations vanish. This is often associated with whether or not electroweak symmetry is linearly-realised[1]. As such, the strength of bounds calculated in Chapter 3 will depend on whether or not this assumption is made. This distinction will be mentioned in the text where necessary.

1.2.2 The hierarchy problem

Here we specifically discuss the Higgs hierarchy problem. Hierarchy problems occur in quantum field theories when there are scales of vastly different magnitudes. Parameters of the theory receive corrections to their bare values via renormalization. These corrections can be large unless a symmetry is present to restrict their behaviour. The mass of the Higgs is a parameter with no such symmetric restrictions and experiences very large corrections in the absence of new physics[2]. Requiring a large bare mass to cancel the large corrections and give the smaller observed physical mass is known as fine tuning.

Consider the one-loop corrections to the Higgs mass, δm_h^2, which come from self-interactions, gauge loops and fermion loops, with the relevant Feynman diagrams shown in Fig. 1.1. These diagrams are quadratically divergent, yielding a one-loop correction,

$$\delta m_h^2 = m_h^2 - m_{h0}^2 \approx \frac{3\Lambda^2}{8\pi^2 v^2} \left[m_h^2 + 2M_W^2 + M_Z^2 - 4m_t^2 \right] , \qquad (1.2.2)$$

---

[1]For more information on how such a scenario might function, see Ref. [34]

[2]There is a subtlety here regarding whether or not the Standard Model is treated in isolation, as will be explained below.

where only the four heaviest species where included, m_{h0} is the bare mass and Λ is the cut-off or scale of new physics. We see that the corrections to the square mass are proportional to the square masses of any coupling particle. Suppose there is no new physics up to $\Lambda = M_P$, such that $m_h^2/\Lambda^2 \sim 10^{-34}$. In order to obtain the observed Higgs mass, we would require an enormous bare mass, differing to the corrections by one part in 10^{34} [22].

We see that the physical mass is highly-sensitive to the parameters of the theory; a minute change to m_{h0}^2 would have an enormous affect on $m_h^2 = m_{h0}^2 + \delta m_h^2$. To get the desired value we must *fine-tune* our parameters. Such large and tuned parameters are generally seen as *unnatural*. This fine-tuning is necessary because $m_h \ll M_p$: this is the hierarchy problem.

There is a subtlety in this statement: if the bare Higgs mass is truly a free parameter that can only be inferred by Higgs measurements, as it strictly is in the Standard Model, then there is no hierarchy problem[1]. The problem arises when we acknowledge that the Standard Model isn't the UV complete theory of the universe. In the complete theory, one expects the Higgs bare mass to be predictable via other more fundamental UV parameters. Now the question of why the bare parameter is so finely-tuned to its corrections becomes a valid concern. As such, any new UV theory should address the size of the bare mass or have a mechanism to limit the size of its corrections.

As previously mentioned, such large corrections can be restricted by symmetries. The masses of fermions and gauge bosons get corrections proportional to their masses. This arises due to symmetries that are restored in the massless limit: chiral symmetry in the case of fermions and gauge symmetry in the case of gauge bosons. This limits corrections to a logarithmic cut-off dependence, for example, for the electron [36],

$$\delta m_e = m_e \log\left(\Lambda/m_e\right) . \tag{1.2.3}$$

Since the Higgs mass is sensitive to all coupled high scales, naturalness would require that it should be of the order of the scale of new physics. This suggests that a natural theory requires new physics at the TeV scale. This motivated many extensions to the Standard Model, such as supersymmetry (see, for instance, Ref. [37]) and extra dimensions (see for example, Ref. [38]). In supersymmetry, for example, contributions from particles are cancelled by the opposite-sign contributions of their superpartners. Lack of direct observations of new fundamental particles at the Large Hadron Collider limit the applicability of this solution [39].

An alternative philosophy, known as the anthropic principle [40], says that the

---

[1]For a good discussion on these ideas, see Ref. [35].

possible model space is scanned in different parts of the universe. Development of life required $m_h \ll M_P$ and so it is only natural that we live in a patch where this is true. Perhaps there is a landscape of vacua as postulated in string theory and we simply live in a patch where the conditions are right (see, for example, Ref. [41]).

The hierarchy problem and its potential resolutions is a recurring theme in this thesis. In Part II we look at scalar multiparticle production. It has been suggested that the scale where this behaviour begins could behave as a cut-off to the Higgs mass contributions, acting as a change in phase of the theory [4, 42, 43]. In Part III, we discuss the recently-developed relaxion mechanism [44], which dynamically selects the Higgs VEV via the cosmic evolution of a new scalar particle, the relaxion.

1.3   Remainder of the thesis

The remainder of this thesis is divided into three distinct parts, corresponding to research done in different areas of Higgs physics. Each part has its own background chapter that lays the appropriate foundations for the subsequent discussions. Similarly, each part ends with a section presenting part-specific conclusions. These conclusions are combined and summarised in the Chapter 9, the final chapter of this thesis.

Note that definitions introduced in each part are specific to said part; several letters, Greek and Latin, are repurposed in different contexts. As an example, a_i denote the nine Vh angular moments in Part I; a is a coherent state variable in Part II; and $a(x)$ is an axion field in Part III. These parts address different physics and so conflicts of notation are avoided.

Part I starts in Chapter 2 with a look at particle colliders and effective field theories (EFT). We briefly discuss the experimental aspects of colliders, summarise the various Higgs production and decay channels, and introduce the Standard Model Effective Field Theory (SMEFT). We then build on this information in Chapter 3, where we present a differential analysis technique that can be used to constrain new physics effects on Higgs interactions.

In Part II we turn to the more theoretical investigation of multiparticle production and the behaviour we might expect of the Higgs at high energies as a fundamental scalar particle. We begin in Chapter 4 by describing a regime in which few high-energy scalar bosons could decay into many softer scalars. In Chapter 5, we develop the coherent state formalism, starting in quantum mechanics before moving to quantum field theory. This formalism is key in the semiclassical method employed

in Chapter 6, which allows us to calculate the multiparticle production rates non-perturbatively.

Finally, in Part III we take a more cosmological outlook and look at the role the Higgs field may have had in the evolution of our universe. We begin in Chapter 7 by summarising some problems in fundamental physics and some potential solutions. These solutions are then combined in Chapter 8, where we present a unified solution to five beyond-the-Standard-Model (BSM) puzzles. At the core of this solution is a relaxion model, which gives a dynamic explanation for the Higgs vacuum expectation value via a coupled cosmic evolution.

As mentioned previously, we wrap up this thesis in Chapter 9 by summarising the conclusions presented in each part.

Part I

The Higgs at Colliders

Chapter 2

Probing Higher-Energy Physics

We currently find ourselves in a transition of strategy. Our most advanced tool for probing high energy physics – the Large Hadron Collider – has achieved its 'main' goal in discovering the Higgs boson [45, 46], yet there have been no further direct signs of new physics. In this chapter, we comment on how higher integrated luminosities will allow us to explore more subtle signs of new physics, such as differential observables. We briefly discuss the LHC itself, review conventional resonance searches and then move on to discussing these differential observables. We finish by explaining how new higher-energy physics effects can be parametrised using effective field theory (EFT) techniques. This chapter provides the idealogical foundations for Chapter 3, where we propose and utilise a technique for constraining such new physics effects using data from current and future colliders.

2.1 Observables at colliders

2.1.1 The Large Hadron Collider

Since the start of its first run in 2009, CERN's Large Hadron Collider (LHC) has been the most relevant tool in the search for new high-energy physics. Bunches of protons from two beams are accelerated by superconducting magnets around a 27 km ring under the French-Swiss border and collide at the highest energies ever achieved. The collisions are analysed using complex detectors placed at different points along the ring. The two detectors most relevant to our discussions are ATLAS (A Toroidal LHC ApparatuS) and CMS (Compact Muon Solenoid). A schematic description of these detectors is presented below and shown in Fig. 2.2. Run 1 of the LHC, which ended in 2014, was conducted with a centre of mass energy (CME) of 7-8 TeV and

was, via results from ATLAS and CMS, responsible for the discovery of the Higgs boson [45, 46].

Previous colliders included the Tevatron at FermiLab (USA) and LEP (Large Electron-Positron collider) at CERN. The Tevatron was a proton-antiproton collider while LEP was an electron-positron collider. Hadron colliders such as the LHC and Tevatron have their advantages and disadvantages over lepton colliders like LEP:

- **Composite vs fundamental**: There are several advantages to using fundamental particles, such as leptons. Firstly, it means we know our initial conditions with much greater certainty: the energy of the collision is just the CME of the two initial particles, whose identity we know. Protons, on the other hand, are composite particles with complex partonic distributions. We are forced to infer the partons and energy in a collision from the detected decay products. We have a collision of two composite particles resulting in a collision of two possibly-different partons with different energy. Furthermore, in the case of composite particles, the partons will only carry a fraction of the initial CME. In lepton colliders, only a relatively small amount of energy is lost as initial state radiation. On the other hand, hadron colliders need not scan over energy ranges as the composite nature if the initial states leads to collisions with naturally varying energies.

  An advantage of composite particles over fundamental particles is that there is a large variety of possible initial states, unlike lepton colliders, which have a fixed initial state and quantum numbers. Protons can lead to interactions with any parton, be it quark, antiquark or gluon. This opens up the the possibility for resonant production of different spin and charge states. Hence, hadron colliders give accessibility to a larger variety of final states. This can also be a disadvantage, as the polarisation of the initial states is no longer controllable.

- **QCD**: Hadrons are bound by strong interactions and thus every constituent parton is charged under the QCD $SU(3)_C$ gauge group. This leads to a plethora of possible strong interactions and emissions. Leptons do not experience strong interactions, at least at tree-level, and thus give much cleaner collisions, with less hadronic production and thus lower backgrounds. Initial state radiation is also reduced.

- **Synchrotron radiation**: Charged particles undergoing acceleration, such as particles in a circular collider, experience loss of energy through synchrotron radiation. For a given beam energy, the loss per cycle is $\Delta E \propto R^{-1} m^{-4}$ for collider radius R and particle mass m. This explains the desire for such large

colliders. Protons are of order 2000 times more massive than electrons and thus allow us to reach much higher energies for a given radius. For example, the LHC repurposed the LEP tunnel at CERN and achieved far higher beam energies: 13 TeV vs. 209 GeV. As such, most new resonances have been discovered first at hadron colliders.

Precision electroweak measurements at LEP and the Tevatron constrained the Higgs mass to be in the range 115-140 GeV [47, 48]. With the Higgs boson predicted to be right around the corner, the LHC was the most efficient way to increase beam energies. The higher-mass hadronic initial states allow for lower energy loss by synchrotron radiation per cycle for the same collider radius. This allowed us to find the Higgs boson but comes at a cost of less clean events and lesser knowledge of initial conditions.

An important property of a collider is its estimated integrated luminosity. This is essentially a measure of how much data the collider will collect. One can obtain the real number of expected events, N, for a process of cross section σ and integrated luminosity $\mathcal{L}$,

$$N = \mathcal{L}\sigma(\hat{s}), \qquad (2.1.1)$$

where the cross section often varies with partonic centre-of-mass energy, $\sqrt{\hat{s}}$. Run 1 of the LHC accumulated approximately 20 fb^{-1}, where 1 fb $= 10^{-43}$ m^2. Run 2, which operated at 13 TeV CME and concluded in December 2018, accumulated around 150 fb^{-1}. Run 3 aims to collect 300 fb^{-1}. The future high luminosity (HL-LHC) run is estimated to achieve an integrated luminosity of 3000 fb^{-1} = 3 ab^{-1} [49]. The various bounds discussed in Chapter 3 are calculated using the HL-LHC's expected luminosity of = 3 ab^{-1}.

As mentioned above, the composite nature of hadrons and strong interactions result in very complex collision pictures at the LHC. It is of paramount importance to find ways to separate the physics of interest, the signal, from the background. A schematic diagram of a proton-proton collision is given in Fig. 2.1. Various constituent partons from the initial hadrons may interact, carrying different fractions of the hadronic momentum. Initial state partons experience initial state radiation, for example by emission of gluons. Events of interest will generally feature a hard interaction and subsequent decay products, which will experience final state radiation. All partons eventually reach lower energies and undergo hadronisation. The hadrons produced can themselves decay further. Such collimated sprays of hadronic activity are known as jets. The key to analysing such complex events is finding ways to distinguish between the final states produced by the signal process and the final states produced by other processes.
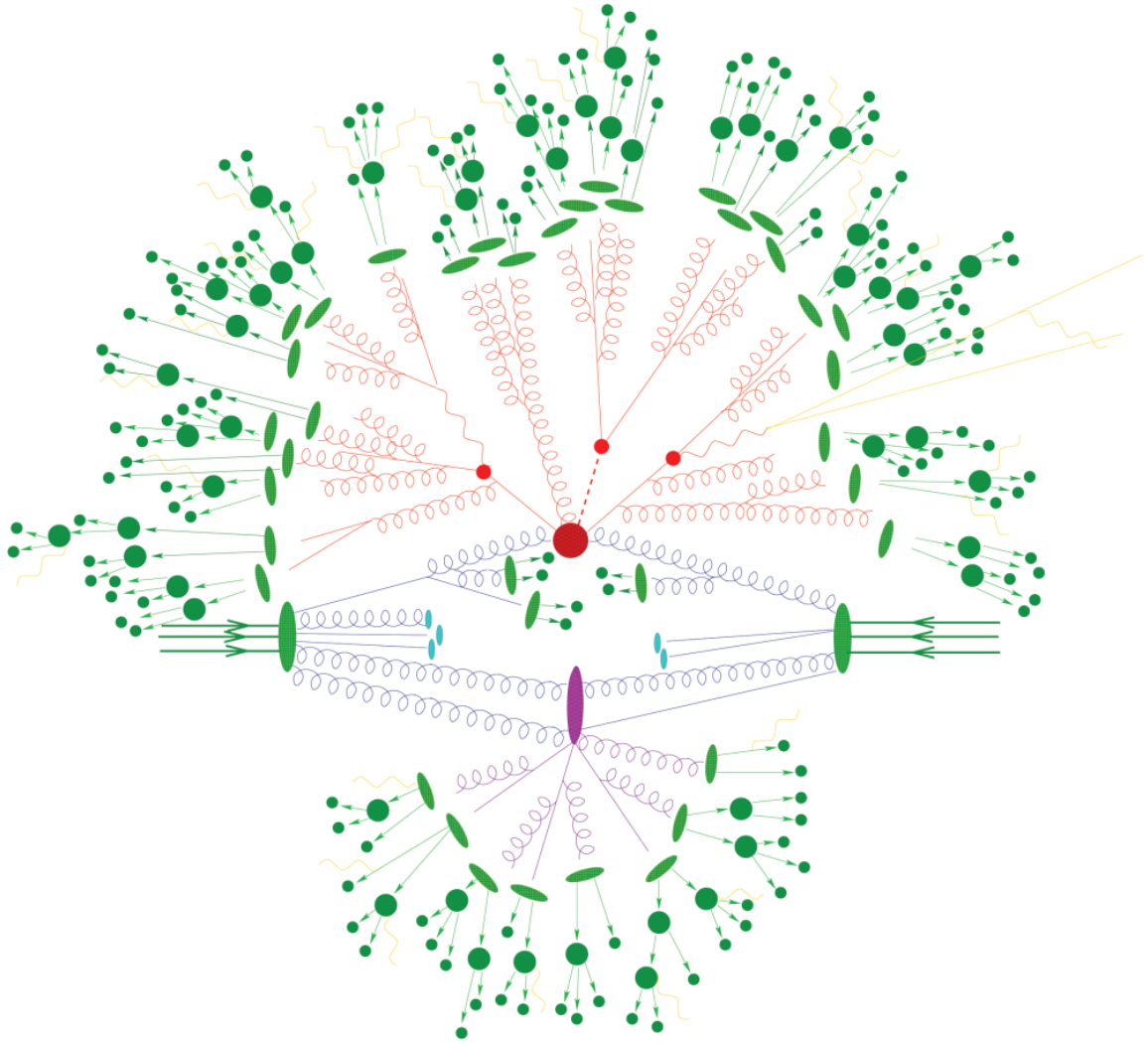
Figure 2.1: *A schematic diagram of a hard proton-proton collision at the LHC, taken with permission from Ref. [50]. The hard interaction of interest is the red blob in the centre. Particles from initial- and final-state radiation are in blue and red, respectively. These can decay and emit a variety of particles. Further activity can be expected in the form of an underlying event, in purple. All strongly-interacting particles eventually reach lower energy scales, hadronise and undergo further decay, as shown in green.*

In practice, we are only able to detect a fraction of the activity shown in Fig. 2.1. Many particles, fundamental or otherwise, are very unstable. They decay before reaching the detector and thus are never directly observed. Instead, their presence is inferred from detection of their more stable decay products. We generally translate our central hard process of interest into a set of demands for the accessible final-state content. Before moving on to potential observables, let us briefly discuss the information we can expect to obtain about a given event.

The structure of a general detector, such as ATLAS or CMS, is sketched in Fig. 2.2.
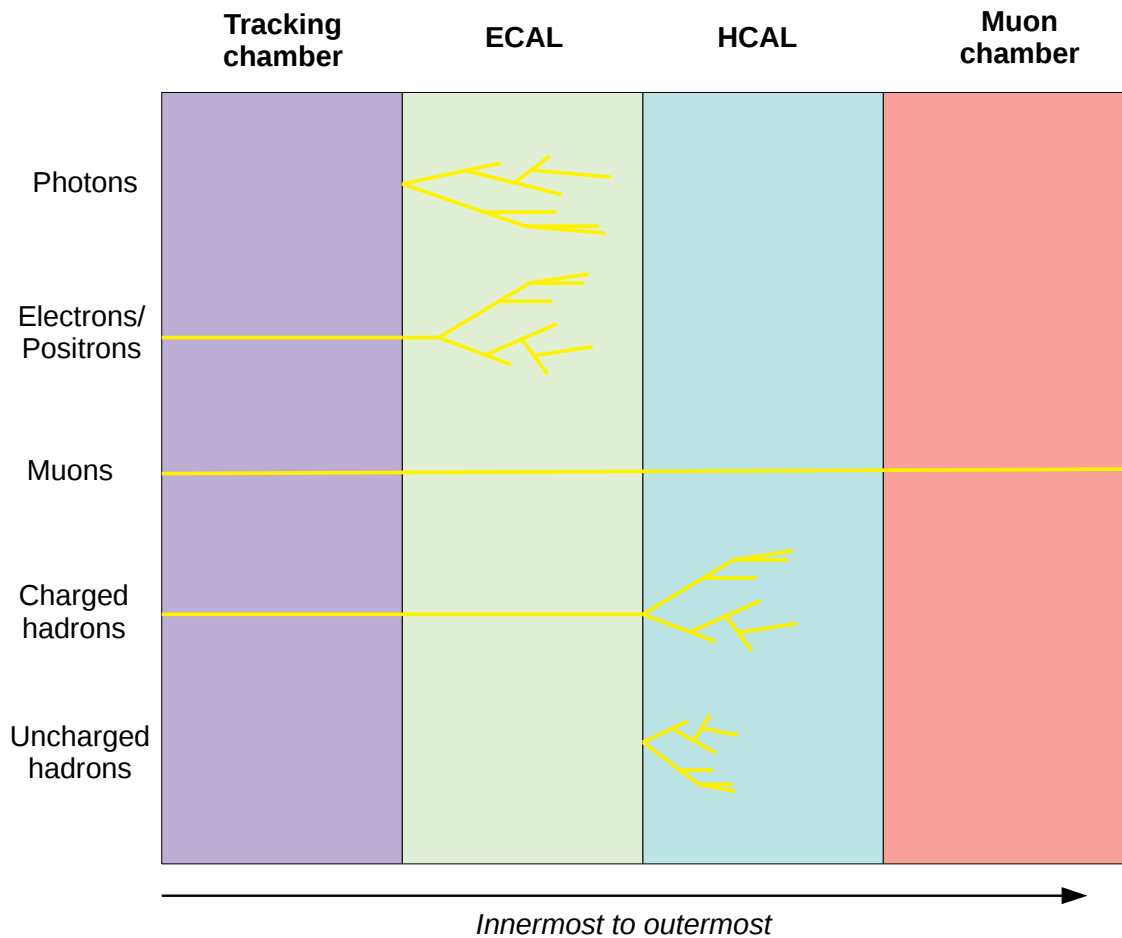
Figure 2.2: *A schematic diagram of a general hadron collider detector, such as the LHC, inspired by Ref. [51]. The tracks and behaviour of some common stable final-state particles are sketched in yellow. Note that in reality, some of these paths are curved by magnetic fields. The innermost layer is not shown above but consists of vertex detectors, which are used to assess the geometric origin of these tracks. For more information on the different layers, see the text.*

The various layers lead to characteristic signatures for different stable final-state particles, via charged tracks and energy deposits. The different layers allow measurements of certain properties of these particles, which can be used to constrain the possible mother particles:

- **Vertex detectors**: Vertex detectors in the innermost layer allow for detection of displaced secondary vertices. This is of great importance in b-tagging. Generally, the original parton responsible for a jet cannot be determined. The one exception is the b quark. A b quark is expected to decay into hadrons, one of which will have b content, in the primary vertex. The relatively long-lived B meson will then itself decay, giving a displaced vertex.

- **Tracking chamber**: This part of the detector traces out the trajectories of charged particles. Use of magnetic fields means that the momentum and charge of the charged particle can be inferred from the curvature and direction of the trajectory, respectively. Energy loss and mass can also be inferred.

- **Electromagnetic calorimeter (ECAL)**: This layer is used to measure the energies of electrons, positrons and photons. These particles cause electromagnetic showers in the ECAL via bremsstrahlung and pair production.

- **Hadronic calorimeter (HCAL)**: This layer is similar to the ECAL but measures the energies of high-energy hadrons. In analogy to the electromagnetic showers in the ECAL, high-energy hadrons entering the HCAL trigger showers of further hadrons.

- **Muon chamber**: This part of the detector is used to detect muons. Muons are not stopped by the calorimeters and have a long enough lifetime to reach this layer. As in the tracking chamber, the momentum can be inferred from the curvature induced by a magnetic field.

It should be noted that these detector layers can only detect particles in a certain range of polar angles (or *pseudo-rapidity*[1]). Rather intuitively, particles moving close to parallel with the collision axis are generally harder to detect than those moving in a more perpendicular direction.

Another important note concerns data taking. The LHC's large luminosities and cross sections result in an event rate of around 1 GHz, with each event requiring around 1 Mb of storage memory and only 1 event in 10^6 being of interest [51]. For this reason, the LHC detectors use an advanced multilevel trigger system in attempt to filter out the less important events and make data taking feasible. This also means that new signal searches may require new trigger designs. For more information, see Ref. [51].

In summary, the LHC allows us to reach higher energies than ever before. A plethora of information can be obtained from the various layers in the detectors about the stable final-state particles. This information, in turn, can be used to infer details of the original harder interaction.

---

[1]Pseudo-rapidity, η, is connected to the polar angle, θ, by the relation $\eta = \ln \cot(\theta/2)$ and varies from $[-\infty, +\infty]$. A pseudo-rapidity of zero corresponds to a trajectory perpendicular to the beam axis in the lab frame. Pseudo-rapidities are useful quantities as their differences are frame-invariant.

2.1.2 Resonance: physics at an attainable energy scale

The conventional method of new physics discovery is looking for resonances. New high-mass particles are generally unstable and will quickly decay into other particles. Hence, their production and subsequent decay appears as a resonance. The probability density for the process $X \to Y^* \to Z$ via the unstable state Y^* is given by the Breit-Wigner function,

$$f(E) = \frac{k}{(E^2 - m^2)^2 + m^2 \Gamma^2}, \qquad (2.1.2)$$

where m and Γ are the mass and decay width of the intermediate particle, and k is some constant depending on m and Γ. This function gives a peak at the particle's mass with a width proportional to Γ. From a QFT perspective, this can be understood as coming from the propagator of the unstable particle, $\sim (E^2 - m^2 + im\Gamma)^{-1}$, in the amplitude $\mathcal{M}$, which one then multiplies by its complex conjugate to obtain $|\mathcal{M}|^2$ and later the cross section $\sigma(E) \propto f(E)$.

By looking at how the number of events for certain processes vary with energy (or invariant mass) we are able to see resonances and use them to infer the unstable particle's mass and width. This is how most high-mass fundamental particles are discovered.

After LEP and Tevatron constrained the Higgs mass, m_h, to be expected in the range[1] 115-140 GeV, the LHC was built in the hope of reaching the energy required to probe the Higgs resonance. As we now know, it was successful in finding a scalar resonance in this range with properties in line with those expected of the SM Higgs boson.

In looking for the Higgs boson, all necessary production and decay channels were considered. The key to a good discovery channel is an appropriately high rate[2] and or a clean distinguishable final-state topology with low backgrounds. The dominant Feynman diagrams for the two initial discovery modes are shown in Figs. 2.3a and 2.3b. The diphoton channel gives two high-energy photons, which leave big deposits in the ECAL (see Fig. 2.2) and no track in the tracking chamber. The 4-lepton channel gives 4 isolated leptons, with one pair reconstructing the weak boson mass. These are both relatively-clean and identifiable topologies, leading to greater confidence and lower uncertainties. Compare this to the decay mode with the highest

---

[1]The more precise bound from LEP was $m_h > 114.4$ GeV at 95% CL. Tevatron excluded the ranges 100 GeV $< m_h <$ 103 GeV and 147 GeV $< m_h <$ 180 GeV at 95% CL. Precision measurements of electroweak observables at LEP and Tevatron also gave an upper bound: $m_H < 280$ GeV. Furthermore, Tevatron saw a 3σ excess in the range 115 GeV $< m_h <$ 140 GeV. See Refs. [47, 48].

[2]Note that the rate of a process is affected by both the production rate and decay branching ratio. These are shown in Tables 2.1 and 2.2.

(a) Diphoton channel

(b) 4-lepton channel
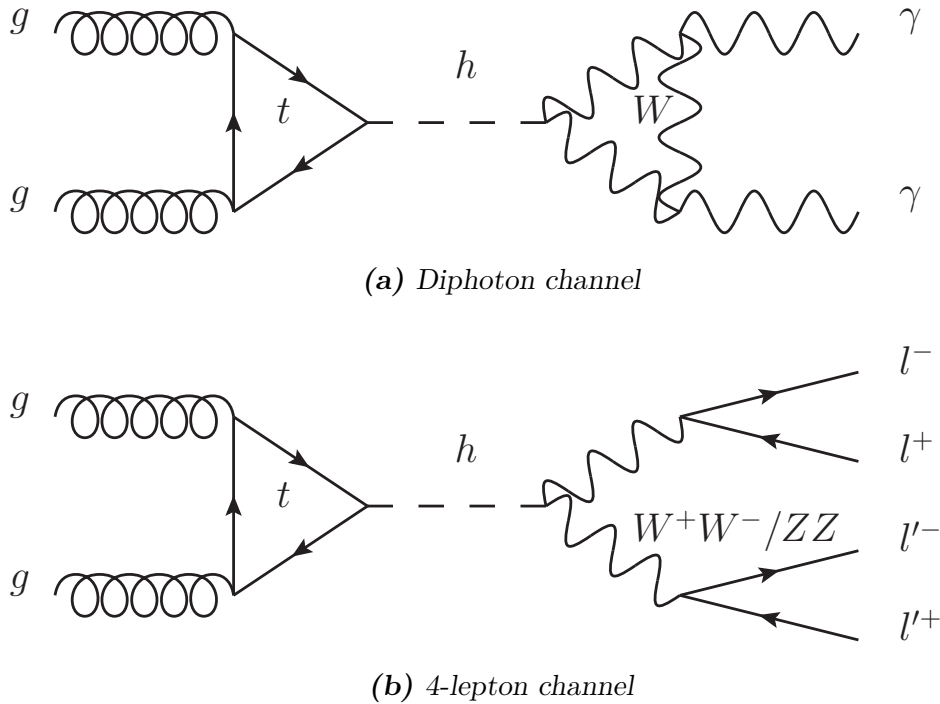
Figure 2.3: *The dominant Feynman diagrams for the two initial discovery modes of the Higgs boson. The branching ratios for these decay modes aren't the largest, but their signatures are cleaner and more distinct, making them easier to identify. In both channels, production is dominated by so-called gluon fusion. The Higgs couples most-strongly to the top quark due to its preferential coupling to massive particles, but other fermions also contribute to the loop. Other production and decay modes are listed in Tables 2.1 and 2.2, with current signal strengths shown in Fig. 2.5.*

branching ratio, $h \to b\bar{b}$, whose efficiency as an initial resonance discovery mode was hindered by its more chaotic jet signature and high backgrounds. However, this mode is becoming more relevant with improvements in jet substructure algorithms (see BDRS [52] in Appendix A.2) and b-tagging.

An example plot of the Higgs resonance at $m_h \approx 125$ GeV for the diphoton channel at ATLAS is shown in Fig. 2.4 [53]. The dominant Higgs production mode for the diphoton and 4-lepton channels is gluon fusion, as seen in Fig. 2.3a. Another production mode, known as Wh/Zh associated production or *Higgs-strahlung*, was less important for the initial resonance discovery but lepton tagging makes it the most sensitive channel for the $h \to b\bar{b}$ decay mode. Crucially, associated production provides access to the hWW and hZZ couplings. This mode is the focus of the differential analysis in Chapter 3. The dominant production and decay modes, as well as the associated inclusive cross sections and branching ratios, are shown in Tables 2.1 and 2.2 for a Higgs boson with mass $m_h = 125$ GeV. Furthermore,
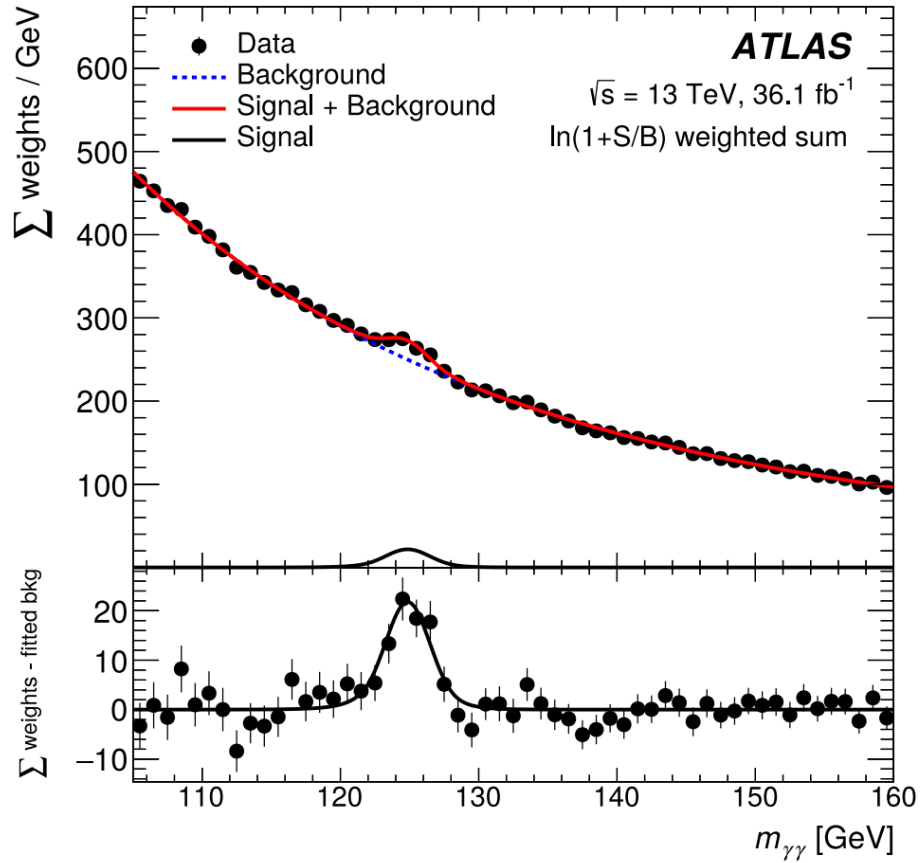
Figure 2.4: *Results published by the ATLAS collaboration [53] for the Higgs resonance in the diphoton channel (see Fig. 2.3a). We see a clear deviation from the background at the Higgs mass $m_h \approx 125$ GeV. This is the Higgs resonance. For more information on this plot, please see the original publication, Ref. [53].*

current results from ATLAS for the signal strengths of different combinations of these production and decay modes are shown in Fig. 2.5. For more information on the various modes, see Refs. [25, 54].

The key limitation to resonance searches is that one must be able to reach the necessary energies to probe the resonance. With Run 2 concluded, we have still not seen any direct signs of new physics within the energy reach of the LHC. It is possible that we will see no further resonances until we build a new higher-energy collider, such as the proposed Future Circular Colliders (FCC) [56–58]. Even then, we may see nothing; the next new physics scale could be well out of reach for the foreseeable future. In such a case we must turn to more indirect searches.

Production mode	Cross section/pb
Gluon fusion	44
Vector boson fusion	3.7
Wh associated production	1.4
Zh associated production	0.87
$t\bar{t}h$ associated production	0.51

Table 2.1: *Inclusive Higgs production cross sections for a Higgs mass $m_h = 125$ GeV and a centre of mass energy $\sqrt{s} = 13$ TeV. Values are taken from the Higgs Working Group [54] and carry an uncertainty of order 1-10%. As mentioned in the text, gluon fusion is the dominant production mechanism. For a summary of these production mechanisms see Ref. [25].*

2.1.3   Differential observables: physics at an unattainable energy scale

We are now forced to consider the scenario in which the next new physics energy scale, Λ, is much larger than the reach of the Large Hadron Collider. Although we are not able to directly see the associated resonances, we can look for more subtle clues. The presence of new physics may well affect the high-energy tails of distributions or indirectly impact the value of some observables.

At earlier stages of the LHC's runtime, the integrated luminosity was relatively low. The best way to look for the small deviations expected due to new physics at a distant scale was via total rate information [59,60]. With data scarce, looking differentially in kinematic variables would result in insufficient statistics to draw strong conclusions. But this is beginning to change. With Run 2 collecting around 150 fb^{-1} and the high luminosity HL-LHC aiming to collect 3 ab^{-1}, looking differentially is becoming a very valid approach. The era of high luminosity is upon us.

Differential searches open up a wealth of analytic opportunity. Variation in new physics (NP) effects with different kinematic parameters gives key information for constraining the possible interactions responsible. This information would be entirely missed in a total-rate analysis. Furthermore, there are some NP contributions that simply vanish if not studied differentially. Consider the schematic case of a process with square amplitude $|\mathcal{M}|^2$,

$$|\mathcal{M}|^2 \sim |\mathcal{M}|^2_{\text{SM}} + 2\text{Re}(\mathcal{M}^*_{\text{SM}}\mathcal{M}_{\text{BSM}}), \qquad |\mathcal{M}|^2_{\text{Int}} \equiv 2\text{Re}(\mathcal{M}^*_{\text{SM}}\mathcal{M}_{\text{BSM}}) \propto \cos\theta,$$

$$(2.1.3)$$

where θ is some kinematic angle. The total rate is related to the integral of this square amplitude over this angle. The NP interference effect, $|\mathcal{M}|^2_{\text{Int}}$, vanishes upon integration. Looking differentially allows us to *resurrect* [61] these effects

Decay mode	BR
$b\bar{b}$	58%
WW^*	21%
gg	8.8%
$\tau\tau$	6.3%
$c\bar{c}$	2.9%
ZZ^*	2.6%
$\gamma\gamma$	0.23%
$Z\gamma$	0.15%
$\mu\mu$	0.022%
Γ_{tot}	4.1 MeV

Table 2.2: *Branching ratios for the dominant decays modes of the Higgs boson and the total decay width, Γ_{tot}, shown for a Higgs mass $m_h = 125$ GeV. Each of these values has an uncertainty of around 3-10%. Values taken from the Higgs Working Group [54]. This table is inspired by Ref. [25], where one can find a more in depth discussion of these decay modes.*

that would otherwise be missed. Generally, one finds that different types of new physics interactions contribute to different differential structures. By carrying out a differential analysis, one can in theory obtain bounds on the contributions from the different underlying interactions. This is exactly the problem we tackle in Chapter 3.

With the view that the next NP scale is not directly accessible, one must decide how to parametrise the NP effects on the lower-energy accessible observables and interactions. Ideally, said parametrisation should be model-independent and make only minimal assumptions on the mechanics at the higher-energy new physics scale. This is where we turn to Effective Field Theory (EFT) descriptions and, in particular, the Standard Model Effective Theory (SMEFT).

2.2   Effective field theories

Different physics dominates at different scales. If one had to consider physics at all scales for any given problem, making any sort of accurate physical prediction would be a daunting (if not impossible) task indeed.

The 'decoupling' of scales – the idea that only physics at the scale of the problem is relevant – has been key in the development of our understanding of physics. The predictive power of Newton's theory of gravitation, for example, was not affected by his lack of knowledge of quantum inter-atomic interactions within the massive body;

ATLAS
$\sqrt{s}$ = 13 TeV, 24.5 − 79.8 fb^{-1}
m_H = 125.09 GeV, $|y_H|$ < 2.5
p_{SM} = 71%

Legend: ⊢•⊣ Total ▯ Stat. ▮ Syst. ▮ SM

	Channel	Total	Stat.	Syst.
ggF	$\gamma\gamma$	0.96	± 0.14	(± 0.11 , $^{+0.09}_{-0.08}$)
	ZZ^*	1.04	$^{+0.16}_{-0.15}$	(± 0.14 , ± 0.06)
	WW^*	1.08	± 0.19	(± 0.11 , ± 0.15)
	$\tau\tau$	0.96	$^{+0.59}_{-0.52}$	($^{+0.37}_{-0.36}$, $^{+0.46}_{-0.38}$)
	comb.	1.04	± 0.09	(± 0.07 , $^{+0.07}_{-0.06}$)
VBF	$\gamma\gamma$	1.39	$^{+0.40}_{-0.35}$	($^{+0.31}_{-0.30}$, $^{+0.26}_{-0.19}$)
	ZZ^*	2.68	$^{+0.98}_{-0.83}$	($^{+0.94}_{-0.81}$, $^{+0.27}_{-0.20}$)
	WW^*	0.59	$^{+0.36}_{-0.35}$	($^{+0.29}_{-0.27}$, ± 0.21)
	$\tau\tau$	1.16	$^{+0.58}_{-0.53}$	($^{+0.42}_{-0.40}$, $^{+0.40}_{-0.35}$)
	$b\bar{b}$	3.01	$^{+1.67}_{-1.61}$	($^{+1.63}_{-1.57}$, $^{+0.39}_{-0.36}$)
	comb.	1.21	$^{+0.24}_{-0.22}$	($^{+0.18}_{-0.17}$, $^{+0.16}_{-0.13}$)
VH	$\gamma\gamma$	1.09	$^{+0.58}_{-0.54}$	($^{+0.53}_{-0.49}$, $^{+0.25}_{-0.22}$)
	ZZ^*	0.68	$^{+1.20}_{-0.78}$	($^{+1.18}_{-0.77}$, $^{+0.18}_{-0.11}$)
	$b\bar{b}$	1.19	$^{+0.27}_{-0.25}$	($^{+0.18}_{-0.17}$, $^{+0.20}_{-0.18}$)
	comb.	1.15	$^{+0.24}_{-0.22}$	(± 0.16 , $^{+0.17}_{-0.16}$)
$t\bar{t}H+tH$	$\gamma\gamma$	1.10	$^{+0.41}_{-0.35}$	($^{+0.36}_{-0.33}$, $^{+0.19}_{-0.14}$)
	VV^*	1.50	$^{+0.59}_{-0.57}$	($^{+0.43}_{-0.42}$, $^{+0.41}_{-0.38}$)
	$\tau\tau$	1.38	$^{+1.13}_{-0.96}$	($^{+0.84}_{-0.76}$, $^{+0.75}_{-0.59}$)
	$b\bar{b}$	0.79	$^{+0.60}_{-0.59}$	(± 0.29 , ± 0.52)
	comb.	1.21	$^{+0.26}_{-0.24}$	(± 0.17 , $^{+0.20}_{-0.18}$)

x-axis: −2, 0, 2, 4, 6, 8

$\sigma \times$ BR normalized to SM

Figure 2.5: *Results published by the ATLAS collaboration [55] for the cross section $\times$ branching ratio (normalised to SM) of different combinations of production and decay modes of the Higgs boson. We see that different production mechanisms better probe different decay modes. Associated VH production, for example, provides much smaller uncertainties on the $b\bar{b}$ channel than vector boson fusion (VBF). For more information, see the original publication, Ref. [55].*

nor were predictions of large-scale planetary motion affected by the planet-surface topography.

In the context of high energy physics this is both a blessing and a curse. The decoupling means we can build a highly predictive quantum field theory (QFT) without knowing the full particle content of the universe. Heavier particles that cannot be produced on-shell at the scale of interest have a negligible effect on the result of calculations, generally giving contributions proportional to powers of the ratio of the two scales. However, it also makes it harder to discover new physics and

particles, as we do not see their effects until we approach their energy scale.

Conventionally, this is the wisdom employed in the construction of particle colliders: higher-energy collisions equates to probing shorter length scales. The search for resonances generally motivates us to construct a less-precise higher-energy machine rather than concentrate on improving the precision of lower-energy experiments, hence the existence of the Large Hadron Collider (LHC). Of course, it will be rather a long time before we get a significant upgrade in energy from the LHC, such as the proposed Future Circular Collider (FCC) [56–58]. As such, much of this chapter focuses on information we can get from improved luminosity and thus statistics at the LHC and high-luminosity LHC (HL-LHC).

Effective theories take advantage of the separation of scales[1] [62]. If we are studying physics at the scale m, we can ignore physics at $E \gg m$ and $E \ll m$, by sending masses to infinity and zero respectively. In the context of QFTs, we can absorb the small affects of higher-energy physics into a tower of new higher-dimension non-renormalisable operators. Consider the Lagrangian of a model with heavy particle content ψ_H and light particle content ψ_L,

$$\mathcal{L}_{\text{full}}(\psi_H, \psi_L) = \mathcal{L}_H(\psi_H, \psi_L) + \mathcal{L}_L(\psi_L), \tag{2.2.1}$$

with light-particle mass scale m and heavy-particle mass scale Λ. We can now integrate out the heavy field content by the path integral,

$$\int \mathcal{D}\psi_H \exp\left[i \int \mathcal{L}_{\text{full}}(\psi_H, \psi_L)\right] = \exp\left[i \int \mathcal{L}_{\text{eff}}(\psi_L)\right], \tag{2.2.2}$$

where the new effective Lagrangian is now,

$$\mathcal{L}_{\text{eff}}(\psi_L) = \mathcal{L}_L(\psi_L) + \delta\mathcal{L}(\psi_L). \tag{2.2.3}$$

As it stands, $\mathcal{L}_{\text{eff}}(\psi_L)$ is non-local. A key subtlety in the route to the effective field theory (EFT), is the expansion of the new piece, $\delta\mathcal{L}(\psi_L)$, into an infinite tower of operators of increasing dimension,

$$\mathcal{L}_{\text{EFT}}(\psi_L) = \mathcal{L}_L(\psi_L) + \sum_i c_i \frac{\mathcal{O}_i}{\Lambda^{\dim(\mathcal{O}_i)-4}}. \tag{2.2.4}$$

The expansion ensures that each individual term and thus interaction is local. In practice, we work to some fixed order in the expansion and use these new local interactions. The advantage of this expansion is that for a given process at fixed order, only a certain number of the large set of operators will contribute. The

---

[1]There are exceptions to this general idea of separation of scales, notably the Higgs-fermion Yukawa interactions. These interactions do not decouple as their sizes directly affect the size of the scales via the Higgs mechanism.

higher the dimension of the operator $\mathcal{O}_i$, the smaller its contribution to lower-energy observables. Our expansion and truncation relies on terms decreasing in importance with expansion order; this ceases to be the case as we approach the heavy scale Λ. The truncation modifies the high-energy behaviour of the theory and thus the EFT is not valid at and above the heavy scale, which we refer to as the *cut-off*, Λ, of the effective theory. Different UV completions above the cut-off scale generally require different values of the so-called Wilson coefficients, c_i, in the lower-scale effective theory. In Section 2.3, we look at the Standard Model Effective Field Theory (SMEFT), which we use in Chapter 3, including only the dimension-6 contributions.

EFTs are useful for a number of reasons. If the UV theory is known, we can trade the full calculation of higher-energy physics for a number or new or modified interaction vertices, which can greatly simplify calculations. If the UV theory is not known, the presence of non-renormalisable interactions, which can be included in a model-independent way, give us clues for the possible higher-energy physics. As Howard Georgi puts it in his review on EFTs [63], when we don't know what is going on at high energies, EFTs allow us to "parametrise our ignorance in a useful way". We return to this idea in Sections 2.2.2 and 2.3. For more information on EFTs, readers are referred to Ref. [63–65].

2.2.1   Fermi β decay

Let us first consider an example: the Fermi theory of β decay. Fermi proposed a four-point fermion interaction to explain β decay, via the interaction term,

$$\mathcal{L}_{\text{Fermi}} = G_F \mathcal{O}_{\text{Fermi}} \approx G_F [\bar{\psi}_p \gamma^\mu P_L \psi_n][\bar{\psi}_e \gamma_\mu P_L \psi_\nu] \sim G_F \bar{\psi}_p \psi_n \bar{\psi}_e \psi_\nu, \qquad (2.2.5)$$

where G_F is the Fermi constant, $P_L = \frac{1}{2}(1-\gamma^5)$ is the left-handed projection operator and $\psi_{p,n,e,\nu}$ denotes the spinors of the proton, neutron, electron and neutrino. This term and corresponding interaction vertex give good predictions for weak interactions at low energy, despite no involvement of the responsible W boson. This is because, as we shall see, the leading effect of the W boson is absorbed into the Fermi constant. In other words, the effect of higher-energy physics is approximated by leading order corrections to the interactions of the lower-energy field content.

The operator, $\mathcal{O}_{\text{Fermi}}$, in the Fermi interaction term in Eq. 2.2.5 is a dimension-6 operator. Equivalently, the Fermi constant has mass dimension -2. As such, the term is non-renormalisable This is the first clue that there is higher-energy physics at play. We now know that the higher-energy physics is the weak interaction, mediated by the W boson.
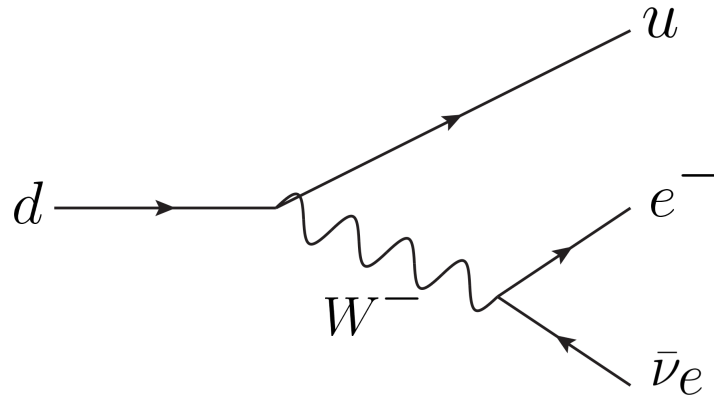
(a) *Full weak theory*
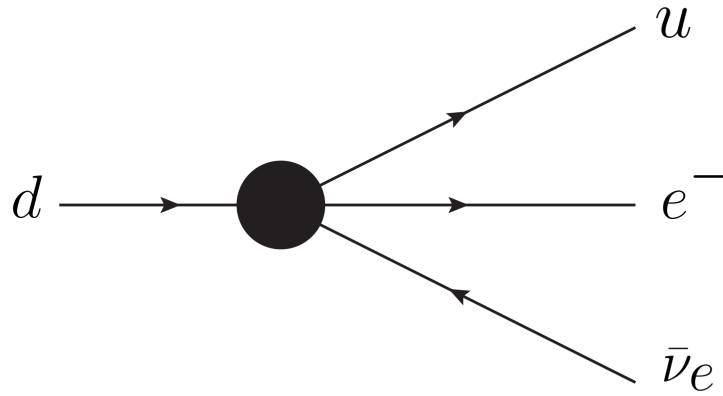
(b) *Fermi theory*

Figure 2.6: *Feynman diagrams for the quark-level beta decay process. The diagram in (a) involves W exchange and uses the full electroweak theory vertex and propagator. The diagram in (b) uses the simplified Fermi four-point interaction (see Eq. 2.2.5). This is an effective vertex and as such is a valid substitution for calculations at scales $E < m_W$. We can see that, pictorially, the substitution is like contracting the W propagator to a point. This is also intuitive given that the effective operators are local whereas the propagator is non-local.*

Consider β decay as the quark-level process $u \to de^+\nu_e$, assuming for simplicity that we only have one lepton flavour and no CKM mixing. The tree-level amplitude for this process, using the Feynman rules of the full electroweak theory, is given by,

$$i\mathcal{M} = \left(\frac{-ig}{\sqrt{2}}\right)^2 [\bar{d}\gamma^\mu P_L u]\frac{-i(g_{\mu\nu} - p_\mu p_\nu/m_W^2)}{p^2 - m_W^2}[\bar{\nu}_e\gamma^\nu P_L e], \tag{2.2.6}$$

with weak coupling g, exchange four-momentum p^μ and projection operator $P_L = \frac{1}{2}(1 - \gamma^5)$ used to extract the left-handed part of the spinors. The contributing tree-level Feynman diagram is shown in Fig. 2.6a.

At scales much lower than the W mass, i.e. $p^2 \ll m_W^2$, this expression can be expanded in powers of $p^2/m_W^2 \ll 1$,

$$\mathcal{M} = -\frac{g^2}{2m_W^2}[\bar{d}\gamma^\mu P_L u][\bar{\nu}_e\gamma_\mu P_L e]\left(1 + \mathcal{O}(p^2/m_W^2)\right). \qquad (2.2.7)$$

We see that the leading order term is in fact the Fermi interaction term in Eq. 2.2.5. Higher order terms are suppressed by powers of $p^2/m_W^2 \ll 1$. The Feynman diagram for this effective interaction is shown in Fig. 2.6b. The overall effect of the leading order approximation can be thought of as contracting the W propagator to a point.

Note the $1/m_W^2$ suppression, ensuring that the overall term is still dimension four, as expected in Eq. 2.2.4. We see by comparison to Eq. 2.2.5, that we have the relation $G_F \sim g^2/m_W^2$ and so the size of the coupling for a non-renormalisable interaction is an indication of the scale of new physics, $\Lambda \sim m_W$. It is also an indication of when our effective theory will break down. As we near $p^2 \sim m_W^2$ we need more and more orders in this expansion to maintain accuracy and the utility of these methods breaks down. Above the new physics scale, $p^2 > m_W^2$, we find unnatural growth and violation of unitarity. This is an artefact of our expansion truncation, which modifies the high-energy behaviour of the theory.

In summary, the Fermi four-point interaction is an effective vertex, which simplifies calculations of low-energy weak observables. The cut-off of the effective theory, Λ, is the scale of new physics, which in this example is the W mass. As long as we stay below this scale, we can trade complex propagators and Feynman rules for a simpler point interaction. For more on β decay, see Ref. [22].

2.2.2 Top down vs bottom up

The example of the Fermi interaction as an effective operator nicely illustrates the potential top down use of effective field theories. We started with the full electroweak theory and integrated out the W boson to get a dimension-six operator that simplifies calculations, provided we are at an appropriate scale. The same ideology is employed in a variety of different contexts, such as the Heavy Quark Effective Theory (HQET) used in flavour physics, in which the heavy b field components are integrated out to simplify calculations of B meson decays (for a recent review see Ref. [66]).

In these top down scenarios, the known UV theory can be evolved down by renormalisation group equations (RGEs) from the UV to the scale of the new physics, say m_W, where we can then match with the effective theory. Upon matching, the effective theory can be evolved down to the scale of interest. The large logarithms

of the scale ratios from the RG running are absorbed into the scale-dependence of the parameters.

Conversely, we can take a bottom up approach. In this approach, we have values for various parameters, measured at some experimentally-available scale. We then use the effective RGEs to evolve their values up to the scale of new physics, where they can be compared to the values expected for any arbitrary UV-complete theory.

Our interest lies in this second approach. With no direct hints as to what the next sector of new physics might be, EFTs provide a general model-independent way to parametrise the effects of higher-energy physics on the physics at our available scales. We can simply ignore the specifics in the UV. We list all the higher-dimensional operators allowed by our symmetries and begin to constrain their Wilson coefficients by experimental measurement of processes with which they interfere. The values of the new effective couplings give an indication of the scale of new physics and can be used to exclude potential UV models. The popular Standard Model Effective Field Theory (SMEFT) is an example of the bottom up approach applied to the Standard Model (SM).

2.3 SMEFT & the Warsaw basis

The fact that LHC has seen no direct signs of new physics suggests that the next new physics may be at a scale $\Lambda \gg m_h$. Therefore, as discussed in Section 2.2, it is useful to parametrise our ignorance of this new physics by measuring its effects on our accessible lower-energy physics. These new physics effects present themselves in the form of new higher-dimension non-renormalisable operators (see Eq. 2.2.4). These operators reliably describe the new physics effects below the scale Λ. The Standard Model Effective Field Theory (SMEFT) offers a standardised parametrisation of new physics effects due to higher-dimension effective operators. Working to dimension-6 and assuming that the discovered scalar boson is indeed the SM Higgs boson, we define,

$$\mathcal{L}_{\text{SMEFT}} = \mathcal{L}_{\text{SM}} + \mathcal{L}^{(6)} = \mathcal{L}_{\text{SM}} + \sum_i \frac{c_i}{\Lambda^2} \mathcal{O}_i, \qquad (2.3.1)$$

where $\mathcal{L}_{\text{SM}}$ is the regular SM Lagrangian (see Chapter 1) and the operators $\mathcal{O}_i$ satisfy the symmetries of the Standard Model. The SMEFT takes a bottom up approach to new physics: we simply use the SM fields to construct all possible operators that satisfy the appropriate symmetries (including baryon and lepton number conservation), and parametrise their presence by their Wilson coefficient, c_i.

The operators appearing in Eq. 2.3.1, $\mathcal{O}_i$, are defined in the unbroken phase, i.e. before electroweak symmetry breaking. Ignoring flavour structure, the number of

independent operators needed to fully describe the allowed dimension-6 operator space is 59, as first shown in Ref. [67]. This is a reduction from the previously established number of 80 in Ref. [68]. The 59 operators are generally presented in eight classes: X^3, H^6, H^4D^2, X^2H^2, ψ^2H^3, ψ^2XH, ψ^2H^2D and ψ^4. Here, $X = G^a_{\mu\nu}, W^a_{\mu\nu}, B_{\mu\nu}$ is a gauge field strength tensor, H is the unbroken Higgs doublet, $\psi = q, u, d, l, e$ is a fermion field and D is the covariant derivative [69]. For the full set of 59 operators, see Table 2.3. This basis is called the Warsaw basis and is the basis we will use in Chapter 3[1]. For three generations of fermions, one finds a total of 2499 hermitian operators: 1350 CP-even and 1149 CP-odd [69].

As mentioned, the operators in the Warsaw basis are defined in the unbroken phase. In phenomenological calculations we generally refer to the broken-phase or *mass basis* interactions. Therefore, we must know how the Wilson coefficients of the unbroken Warsaw operators contribute to the broken-phase interactions. Fortunately, this has been done in meticulous detail for all relevant interactions in Ref. [72]. For a given lower-energy observable, we can find the relevant mass-basis interactions and see how their coupling strengths depend on the unbroken Warsaw Wilson coefficients. This is done for $hVV/hVf\bar{f}$ interactions in Chapter 3, where we use a parametrisation known as the BSM primaries [73]. The move to the mass basis involves some subtleties such as shifts to the Higgs doublet definitions. For discussions on these subtleties, see for example Refs. [69, 74, 75].

A further complication arises if we want to compare experimentally measured Wilson coefficients to those predicted by UV theories. As touched upon in Section 2.2.2, we match the two theories at the new physics scale, Λ. However, any measurements will generally be made at a far lower scale $\sim m_h \ll \Lambda$. Hence, we must evolve the coefficients $c_i(\Lambda)$ at the matching scale down to the experimental scale using the renormalisation group equations (RGEs),

$$\mu \frac{dc_i}{d\mu} = \frac{1}{16\pi^2}\gamma_{ij}c_j, \qquad (2.3.2)$$

where μ is the scale and γ_{ij} is the anomalous dimension matrix, which measures the extent to which the operators mix upon evolution: a diagonal anomalous dimension matrix corresponds to no mixing. We thus expect evolution of the form,

$$c_i(\mu_1) = c_i(\mu_2) - \frac{1}{16\pi^2}\gamma_{ij}c_j(\mu_2)\log\left(\frac{\mu_2}{\mu_1}\right), \qquad (2.3.3)$$

for $\mu_2 > \mu_1$. The anomalous dimension matrix is generally non-diagonal and therefore the operators do mix upon evolution. For more information on the anomalous

---

[1]Other basis choices exist, such as the SILH basis [70] or the HISZ basis [71].

dimension matrix in SMEFT, see Refs. [69, 76]. In our study of $hVV/hVf\bar{f}$ inter-
actions we neglect RG running as our measurements only span an energy range of
approximately 500-1500 GeV. Due to the loop suppression factor and logarithmic
dependence, this corresponds to a negligible factor of $(1/16\pi^2)\log(1.5) \approx 2 \times 10^{-3}$.
Of course, any UV theory predictions for $c_i(\Lambda)$ will still need to be evolved down to
scales $\mu \sim m_h$ before making comparisons.

With collider searches and effective theories introduced, we now move on to their
implementation in constraining $hVV/hVf\bar{f}$ interactions.

<div align="center">

$1 : X^3$ **$2 : H^6$** **$3 : H^4D^2$**
</div>

$\mathcal{O}_G$	$f^{ABC}G_\mu^{A\nu}G_\nu^{B\rho}G_\rho^{C\mu}$	$\mathcal{O}_H$	$(H^\dagger H)^3$
$\mathcal{O}_{\widetilde{G}}$	$f^{ABC}\widetilde{G}_\mu^{A\nu}G_\nu^{B\rho}G_\rho^{C\mu}$	$\mathcal{O}_{H\Box}$	$(H^\dagger H)\Box(H^\dagger H)$
$\mathcal{O}_W$	$\epsilon^{IJK}W_\mu^{I\nu}W_\nu^{J\rho}W_\rho^{K\mu}$	$\mathcal{O}_{HD}$	$\left(H^\dagger D_\mu H\right)^*\left(H^\dagger D_\mu H\right)$
$\mathcal{O}_{\widetilde{W}}$	$\epsilon^{IJK}\widetilde{W}_\mu^{I\nu}W_\nu^{J\rho}W_\rho^{K\mu}$		

<div align="center">

$4 : X^2H^2$ **$6 : \psi^2XH + \text{h.c.}$**   **$7 : \psi^2H^2D$**
</div>

$\mathcal{O}_{HG}$	$H^\dagger H\, G_{\mu\nu}^A G^{A\mu\nu}$	$\mathcal{O}_{eW}$	$(\bar{l}_p\sigma^{\mu\nu}e_r)\sigma^I H W_{\mu\nu}^I$	$\mathcal{O}_{HL}^{(1)}$	$(H^\dagger i\overleftrightarrow{D}_\mu H)(\bar{l}_p\gamma^\mu l_r)$
$\mathcal{O}_{H\widetilde{G}}$	$H^\dagger H\, \widetilde{G}_{\mu\nu}^A G^{A\mu\nu}$	$\mathcal{O}_{eB}$	$(\bar{l}_p\sigma^{\mu\nu}e_r)H B_{\mu\nu}$	$\mathcal{O}_{HL}^{(3)}$	$(H^\dagger i\overleftrightarrow{D}_\mu^I H)(\bar{l}_p\sigma^I\gamma^\mu l_r)$
$\mathcal{O}_{HW}$	$H^\dagger H\, W_{\mu\nu}^I W^{I\mu\nu}$	$\mathcal{O}_{uG}$	$(\bar{q}_p\sigma^{\mu\nu}T^A u_r)\widetilde{H}\, G_{\mu\nu}^A$	$\mathcal{O}_{He}$	$(H^\dagger i\overleftrightarrow{D}_\mu H)(\bar{e}_p\gamma^\mu e_r)$
$\mathcal{O}_{H\widetilde{W}}$	$H^\dagger H\, \widetilde{W}_{\mu\nu}^I W^{I\mu\nu}$	$\mathcal{O}_{uW}$	$(\bar{q}_p\sigma^{\mu\nu}u_r)\sigma^I\widetilde{H}\, W_{\mu\nu}^I$	$\mathcal{O}_{HQ}^{(1)}$	$(H^\dagger i\overleftrightarrow{D}_\mu H)(\bar{q}_p\gamma^\mu q_r)$
$\mathcal{O}_{HB}$	$H^\dagger H\, B_{\mu\nu}B^{\mu\nu}$	$\mathcal{O}_{uB}$	$(\bar{q}_p\sigma^{\mu\nu}u_r)\widetilde{H}\, B_{\mu\nu}$	$\mathcal{O}_{HQ}^{(3)}$	$(H^\dagger i\overleftrightarrow{D}_\mu^I H)(\bar{q}_p\sigma^I\gamma^\mu q_r)$
$\mathcal{O}_{H\widetilde{B}}$	$H^\dagger H\, \widetilde{B}_{\mu\nu}B^{\mu\nu}$	$\mathcal{O}_{dG}$	$(\bar{q}_p\sigma^{\mu\nu}T^A d_r)H\, G_{\mu\nu}^A$	$\mathcal{O}_{Hu}$	$(H^\dagger i\overleftrightarrow{D}_\mu H)(\bar{u}_p\gamma^\mu u_r)$
$\mathcal{O}_{HWB}$	$H^\dagger\sigma^I H\, W_{\mu\nu}^I B^{\mu\nu}$	$\mathcal{O}_{dW}$	$(\bar{q}_p\sigma^{\mu\nu}d_r)\sigma^I H\, W_{\mu\nu}^I$	$\mathcal{O}_{Hd}$	$(H^\dagger i\overleftrightarrow{D}_\mu H)(\bar{d}_p\gamma^\mu d_r)$
$\mathcal{O}_{H\widetilde{W}B}$	$H^\dagger\sigma^I H\, \widetilde{W}_{\mu\nu}^I B^{\mu\nu}$	$\mathcal{O}_{dB}$	$(\bar{q}_p\sigma^{\mu\nu}d_r)H\, B_{\mu\nu}$	$\mathcal{O}_{Hud}+\text{h.c.}$	$i(\widetilde{H}^\dagger D_\mu H)(\bar{u}_p\gamma^\mu d_r)$

<div align="center">

$8 : (\bar{L}L)(\bar{L}L)$ **$8 : (\bar{R}R)(\bar{R}R)$**   **$8 : (\bar{L}L)(\bar{R}R)$**
</div>

$\mathcal{O}_{ll}$	$(\bar{l}_p\gamma_\mu l_r)(\bar{l}_s\gamma^\mu l_t)$	$\mathcal{O}_{ee}$	$(\bar{e}_p\gamma_\mu e_r)(\bar{e}_s\gamma^\mu e_t)$	$\mathcal{O}_{le}$	$(\bar{l}_p\gamma_\mu l_r)(\bar{e}_s\gamma^\mu e_t)$
$\mathcal{O}_{qq}^{(1)}$	$(\bar{q}_p\gamma_\mu q_r)(\bar{q}_s\gamma^\mu q_t)$	$\mathcal{O}_{uu}$	$(\bar{u}_p\gamma_\mu u_r)(\bar{u}_s\gamma^\mu u_t)$	$\mathcal{O}_{lu}$	$(\bar{l}_p\gamma_\mu l_r)(\bar{u}_s\gamma^\mu u_t)$
$\mathcal{O}_{qq}^{(3)}$	$(\bar{q}_p\gamma_\mu\sigma^I q_r)(\bar{q}_s\gamma^\mu\sigma^I q_t)$	$\mathcal{O}_{dd}$	$(\bar{d}_p\gamma_\mu d_r)(\bar{d}_s\gamma^\mu d_t)$	$\mathcal{O}_{ld}$	$(\bar{l}_p\gamma_\mu l_r)(\bar{d}_s\gamma^\mu d_t)$
$\mathcal{O}_{lq}^{(1)}$	$(\bar{l}_p\gamma_\mu l_r)(\bar{q}_s\gamma^\mu q_t)$	$\mathcal{O}_{eu}$	$(\bar{e}_p\gamma_\mu e_r)(\bar{u}_s\gamma^\mu u_t)$	$\mathcal{O}_{qe}$	$(\bar{q}_p\gamma_\mu q_r)(\bar{e}_s\gamma^\mu e_t)$
$\mathcal{O}_{lq}^{(3)}$	$(\bar{l}_p\gamma_\mu\sigma^I l_r)(\bar{q}_s\gamma^\mu\sigma^I q_t)$	$\mathcal{O}_{ed}$	$(\bar{e}_p\gamma_\mu e_r)(\bar{d}_s\gamma^\mu d_t)$	$\mathcal{O}_{qu}^{(1)}$	$(\bar{q}_p\gamma_\mu q_r)(\bar{u}_s\gamma^\mu u_t)$
		$\mathcal{O}_{ud}^{(1)}$	$(\bar{u}_p\gamma_\mu u_r)(\bar{d}_s\gamma^\mu d_t)$	$\mathcal{O}_{qu}^{(8)}$	$(\bar{q}_p\gamma_\mu T^A q_r)(\bar{u}_s\gamma^\mu T^A u_t)$
		$\mathcal{O}_{ud}^{(8)}$	$(\bar{u}_p\gamma_\mu T^A u_r)(\bar{d}_s\gamma^\mu T^A d_t)$	$\mathcal{O}_{qd}^{(1)}$	$(\bar{q}_p\gamma_\mu q_r)(\bar{d}_s\gamma^\mu d_t)$
				$\mathcal{O}_{qd}^{(8)}$	$(\bar{q}_p\gamma_\mu T^A q_r)(\bar{d}_s\gamma^\mu T^A d_t)$

<div align="center">

$5 : \psi^2H^3 + \text{h.c.}$ **$8 : (\bar{L}R)(\bar{R}L) + \text{h.c.}$**   **$8 : (\bar{L}R)(\bar{L}R) + \text{h.c.}$**
</div>

$\mathcal{O}_{eH}$	$(H^\dagger H)(\bar{l}_p e_r H)$	$\mathcal{O}_{ledq}$	$(\bar{l}_p^j e_r)(\bar{d}_s q_{tj})$	$\mathcal{O}_{quqd}^{(1)}$	$(\bar{q}_p^j u_r)\epsilon_{jk}(\bar{q}_s^k d_t)$
$\mathcal{O}_{uH}$	$(H^\dagger H)(\bar{q}_p u_r\widetilde{H})$			$\mathcal{O}_{quqd}^{(8)}$	$(\bar{q}_p^j T^A u_r)\epsilon_{jk}(\bar{q}_s^k T^A d_t)$
$\mathcal{O}_{dH}=\mathcal{O}_{y_d}$	$(H^\dagger H)(\bar{q}_p d_r H)$			$\mathcal{O}_{lequ}^{(1)}$	$(\bar{l}_p^j e_r)\epsilon_{jk}(\bar{q}_s^k u_t)$
				$\mathcal{O}_{lequ}^{(3)}$	$(\bar{l}_p^j\sigma_{\mu\nu}e_r)\epsilon_{jk}(\bar{q}_s^k\sigma^{\mu\nu}u_t)$

Table 2.3: *The Warsaw basis [67, 69, 74, 75] consists of 59 independent baryon-number-conserving dimension-6 operators. Each is constructed from Standard Model fields and their derivatives. The operators are presented in the notation of Ref. [77], with the one exception that the operators are labelled with $\mathcal{O}_i$ in place of the original Q_i, to be consistent with internal notation. The subscripts p, r, s, t are flavour indices, and σ^I are Pauli matrices. Operators relevant to the study in Chapter 3 are highlighted in blue.*

Chapter 3

A Differential Analysis of the SMEFT Vh Mode

3.1 Introduction

The data being collected by the LHC is the first record of interactions of the Higgs and other Standard Model (SM) particles at the sub-attometre (multi-TeV) scale. As long as beyond SM (BSM) physics is significantly heavier than the mass of electroweak particles, these interactions can be described in a model independent way by the Standard Model Effective Field Theory (SMEFT) Lagrangian. The SMEFT Lagrangian is thus a statement of the laws of nature at the most fundamental scale ever probed. The measurement of (or constraints on) the SMEFT parameters [1, 67, 70, 73, 76, 78–104] may well turn out to be the main legacy of the LHC after the Higgs discovery.

It is thus of great importance to maximally exploit all the data that the LHC can provide us. Constraining the SMEFT parameters can be a rather subtle task; it is important to extract the full multi-dimensional differential information available in a process. This is because the effect of new dimension-6 vertex structures is often more pronounced in certain regions of phase space, the most common example being the growth of EFT rates at high energies. In fact, for many processes, the effect of certain vertices is lost completely unless we use a more complex differential analysis. Consider, for example, the operators whose contributions do not interfere with the SM amplitude at the inclusive level [105]. These operators can generate large differential excesses [1, 106–109] in certain regions of the phase space, which are cancelled by corresponding deficits in other regions. These effects are lost unless a sophisticated study is carried out to isolate the appropriate phase space regions. Sometimes, in order to resurrect these interference terms one must go even beyond

differential distributions with respect to a single variable and use multidimensional distributions. More generally, using the full differential information enlarges the list of observables and lifts flat directions in EFT space that can otherwise remain unconstrained. In order to optimally reconstruct the SMEFT Lagrangian, it is thus essential to systematically and completely extract *all* the available differential information.

Experimental measurements are often communicated via presenting only a few intuitively chosen distributions. As such, there is a large reduction in differential information. To estimate this, consider a three body final state where the phase space in the centre of mass frame can be completely described by four variables: an energy variable and three angles. For a given energy, taking for instance 10 bins for each of the angular variables results in 1000 units of data to capture the entire information contained in this process, at this level of experimental precision. However, often individual angles are analysed in isolation and the correlations contained in the full set of data are projected onto only 30 units of data, i.e. 10 for each angle, resulting in a loss of accessible information in the search for new physics contributions.

Interestingly, for many important processes, the multi-differential data (i.e. the 1000 units of data in the above example) contain redundant information. We argue, that with an understanding of the underlying theoretical structure of process, the number of physical quantities required to completely characterise the full differential distribution can be drastically reduced. We utilise the fact that for some of the most important processes in Higgs and electroweak physics, the full angular distribution at a given energy can be expressed as a sum of a fixed number of basis functions (if we limit ourselves to a certain order in the EFT expansion). The reason for this is that only a finite number of helicity amplitudes get corrections up to the given EFT order, see for instance Ref. [110, 111]. Therefore, the coefficients of these basis functions, the so-called *angular moments* [112–115], and their energy dependence, contain the full differential information available in a process. The effect of EFT operators on differential distributions can thus be summarised by their contribution to these angular moments. That is to say, the angular moments can be used to construct any possible differential distribution. As a result, an analysis utilising these angular moments has the potential to reach maximal sensitivity in probing EFT coefficients.

While similar approaches have been used for some isolated studies in Higgs and flavour physics [106, 113–120], we believe the suitability of these techniques in globally constraining the SMEFT Lagrangian have not been sufficiently recognised.

These methods would complement other techniques that aim to employ a maximum-

information approach, for example the matrix element method [121–124] or machine learning techniques that have recently gained popularity [125–129]. One advantage of this approach over other multivariate techniques is its more physical and transparent nature. The angular moments described above can be directly related to physical experimental quantities than the abstract neural network outputs used in machine learning approaches. Another important distinction of the methods proposed here from some multivariate approaches such as the matrix element method, is that the extraction process of the angular moments is hypothesis-independent; for example it is independent of any assumptions about whether electroweak symmetry is linearly or non-linearly realised.

In this chapter we will show how these angular moments can be extracted and mapped back to the EFT Lagrangian. While we will focus on Higgs-strahlung at the LHC as a first example, this approach can be extended to all the important Higgs/electroweak production and decay processes, namely weak boson fusion, Higgs decay to weak bosons and diboson production. For the Higgs-strahlung process at the partonic level there are 9 angular moments, although only a smaller number of these are measurable at the LHC for our final states of interest. We will see that extracting all the experimentally-available angular moments can simultaneously constrain all the possible $hVV^*/hVff$ ($V \equiv Z/W^{\pm}, ff \equiv f\bar{f}/f\bar{f}'$) tensor structures. An essential prerequisite for our methods to be applicable is that the final angular distributions measured by the experiments should preserve, to a large extent, the initial theoretical form of EFT signal governed by the angular moments. To truly establish the usefulness of our methods, we therefore carry out a detailed and realistic collider study. In particular we include differentially[1] QCD NLO effects that can potentially improve partonic contributions to the EFT signal, reducing scale uncertainties. Our final results (see Section 3.6), despite these effects, show a marked improvement in sensitivity compared to existing projections for most of the EFT couplings.

The chapter is divided as follows. In Section 3.2, we write the most general Lagrangian for the $pp \to V(\ell\ell)h(b\bar{b})$ process at Dimension 6 in SMEFT and list the relevant operators in the Warsaw basis. Section 3.3 is dedicated to deriving the most general angular moments for the $pp \to Vh$ processes in the SMEFT. In Section 3.4, we discuss the method of moments, which forms the backbone of this analysis. In Section 3.5, we detail the collider studies that we undertake for the $pp \to Vh$ processes. Finally, the results and conclusions are presented in Section 3.6.

_____

[1]Refers to full NLO treatment rather than using a K-factor.

3.2   The $pp \rightarrow V(\ell\ell)h(b\bar{b})$ process in the dimension 6 SMEFT

We want to study the process $pp \rightarrow V(\ell\ell)h(b\bar{b})$ where $\ell\ell$ denotes $\ell^+\ell^-$ ($\ell^+\nu, \ell^-\bar{\nu}$) for $V = Z$ ($V = W^\pm$). The EFT corrections to $pp \rightarrow V(\ell\ell)h(b\bar{b})$ are either due to corrections to the Vff, $hb\bar{b}$ and $hVV/hZ\gamma$ vertices[1], or due to the new $hVff$ contact terms. In the unitary gauge all these corrections are contained in the following Lagrangian [73, 130],

$$
\begin{aligned}
\Delta\mathcal{L}_6 \supset & \delta\hat{g}^h_{WW} \frac{2m_W^2}{v} hW^{+\mu}W^-_\mu + \delta\hat{g}^h_{ZZ} \frac{2m_Z^2}{v} h\frac{Z^\mu Z_\mu}{2} + \delta g^W_Q (W^+_\mu \bar{u}_L \gamma^\mu d_L + \mathrm{h.c.}) \\
& + \delta g^W_L (W^+_\mu \bar{\nu}_L \gamma^\mu e_L + \mathrm{h.c.}) + g^h_{WL} \frac{h}{v}(W^+_\mu \bar{\nu}_L \gamma^\mu e_L + \mathrm{h.c.}) \\
& + g^h_{WQ} \frac{h}{v}(W^+_\mu \bar{u}_L \gamma^\mu d_L + \mathrm{h.c.}) + \sum_f \delta g^Z_f Z_\mu \bar{f}\gamma^\mu f + \sum_f g^h_{Zf} \frac{h}{v} Z_\mu \bar{f}\gamma^\mu f \\
& + \kappa_{WW} \frac{h}{v} W^{+\mu\nu}W^-_{\mu\nu} + \tilde{\kappa}_{WW} \frac{h}{v} W^{+\mu\nu}\tilde{W}^-_{\mu\nu} + \kappa_{ZZ} \frac{h}{2v} Z^{\mu\nu}Z_{\mu\nu} \\
& + \tilde{\kappa}_{ZZ} \frac{h}{2v} Z^{\mu\nu}\tilde{Z}_{\mu\nu} + \kappa_{Z\gamma} \frac{h}{v} A^{\mu\nu}Z_{\mu\nu} + \tilde{\kappa}_{Z\gamma} \frac{h}{v} A^{\mu\nu}\tilde{Z}_{\mu\nu} + \delta\hat{g}^h_{b\bar{b}} \frac{\sqrt{2}m_b}{v} hb\bar{b}, \quad (3.2.1)
\end{aligned}
$$

where for brevity we have only included the first generation for the couplings involving $W^\pm, Z$ bosons, so that $f = u_L, d_L, u_R, d_R, e_L, e_R, \nu_L^e$; and $F = Q(L)$, the first generation quark (lepton) doublet. We assume that the above Lagrangian is extended to the other generations in such a way that the couplings $\delta g^{Z,W}_f$ and $g^h_{Zf,Wf}$ are flavour diagonal and universal in the interaction basis. This allows us to impose strong constraints on them [131, 132], as we are no longer required to distinguish between the light quarks (u, d, s). It is well motivated theoretically and can be obtained, for instance, by including the leading terms after imposing Minimal Flavour Violation [133]). If we limit ourselves to only universal corrections, the contact terms above must be replaced by $hV_\mu\partial_\nu V^{\mu\nu}$ [2]. The above parametrisation can be used even for non-linearly-realised electroweak symmetry (see for example [134]). For such a non-linearly-realised scenario, all the above couplings should be thought of as independent.

If electroweak symmetry is linearly realised, the above vertices arise in the unitary gauge from electroweak-invariant operators containing the Higgs doublet. For instance, the operators of the Warsaw basis [67] in Table 3.1, give the following

---

[1]The $hZ\gamma$ vertex only exists at loop-level in the SM.

[2]Note that $\partial_\mu hV_\nu V^{\mu\nu}$ is equivalent to this vertex and the $hV_{\mu\nu}V^{\mu\nu}$ vertices via integration by parts.

$$\mathcal{O}_{H\square} = (H^\dagger H)\square(H^\dagger H)$$

$$\mathcal{O}_{HD} = (H^\dagger D_\mu H)^*(H^\dagger D_\mu H)$$

$$\mathcal{O}_{Hu} = iH^\dagger \overset{\leftrightarrow}{D}_\mu H \bar{u}_R \gamma^\mu u_R$$

$$\mathcal{O}_{Hd} = iH^\dagger \overset{\leftrightarrow}{D}_\mu H \bar{d}_R \gamma^\mu d_R$$

$$\mathcal{O}_{He} = iH^\dagger \overset{\leftrightarrow}{D}_\mu H \bar{e}_R \gamma^\mu e_R$$

$$\mathcal{O}_{HQ}^{(1)} = iH^\dagger \overset{\leftrightarrow}{D}_\mu H \bar{Q} \gamma^\mu Q$$

$$\mathcal{O}_{HQ}^{(3)} = iH^\dagger \sigma^a \overset{\leftrightarrow}{D}_\mu H \bar{Q} \sigma^a \gamma^\mu Q$$

$$\mathcal{O}_{HL}^{(1)} = iH^\dagger \overset{\leftrightarrow}{D}_\mu H \bar{L} \gamma^\mu L$$

$$\mathcal{O}_{HL}^{(3)} = iH^\dagger \sigma^a \overset{\leftrightarrow}{D}_\mu H \bar{L} \sigma^a \gamma^\mu L$$

$$\mathcal{O}_{HB} = |H|^2 B_{\mu\nu} B^{\mu\nu}$$

$$\mathcal{O}_{HWB} = H^\dagger \sigma^a H W_{\mu\nu}^a B^{\mu\nu}$$

$$\mathcal{O}_{HW} = |H|^2 W_{\mu\nu} W^{\mu\nu}$$

$$\mathcal{O}_{H\tilde{B}} = |H|^2 B_{\mu\nu} \tilde{B}^{\mu\nu}$$

$$\mathcal{O}_{H\tilde{W}B} = H^\dagger \sigma^a H W_{\mu\nu}^a \tilde{B}^{\mu\nu}$$

$$\mathcal{O}_{H\tilde{W}} = |H|^2 W_{\mu\nu}^a \tilde{W}^{a\mu\nu}$$

$$\mathcal{O}_{y_b} = |H|^2 (\bar{Q}_3 H b_R + h.c).$$

Table 3.1: *Dimension-6 operators in the Warsaw basis that contribute to the anomalous $hVV^*/hV\bar{f}f$ couplings in Eq. 3.2.1. See Table 2.3 for the full set of 59 Warsaw basis operators. Other details regarding the notation can be found in [67].*

contributions to these vertices,

$$\delta g_f^W = \frac{g}{\sqrt{2}} \frac{v^2}{\Lambda^2} c_{HF}^{(3)} + \frac{\delta m_Z^2}{m_Z^2} \frac{\sqrt{2} g c_{\theta_W}^2}{4 s_{\theta_W}^2},$$

$$g_{Wf}^h = \sqrt{2} g \frac{v^2}{\Lambda^2} c_{HF}^{(3)},$$

$$\delta \hat{g}_{WW}^h = \frac{v^2}{\Lambda^2} \left(c_{H\square} - \frac{c_{HD}}{4} \right),$$

$$\kappa_{WW} = \frac{2v^2}{\Lambda^2} c_{HW},$$

$$\tilde{\kappa}_{WW} = \frac{2v^2}{\Lambda^2} c_{H\tilde{W}},$$

$$\delta g_f^Z = -\frac{g Y_f s_{\theta_W}}{c_{\theta_W}^2} \frac{v^2}{\Lambda^2} c_{WB} - \frac{g}{c_{\theta_W}} \frac{v^2}{\Lambda^2} (|T_3^f| c_{HF}^{(1)} - T_3^f c_{HF}^{(3)} + (1/2 - |T_3^f|) c_{Hf})$$

$$+ \frac{\delta m_Z^2}{m_Z^2} \frac{g}{2 c_{\theta_W} s_{\theta_W}^2} (T_3 c_{\theta_W}^2 + Y_f s_{\theta_W}^2),$$

$$\delta \hat{g}_{ZZ}^h = \frac{v^2}{\Lambda^2} \left(c_{H\square} + \frac{c_{HD}}{4} \right),$$

$$g_{Zf}^h = -\frac{2g}{c_{\theta_W}} \frac{v^2}{\Lambda^2} (|T_3^f| c_{HF}^{(1)} - T_3^f c_{HF}^{(3)} + (1/2 - |T_3^f|) c_{Hf}),$$

$$\kappa_{ZZ} = \frac{2v^2}{\Lambda^2} (c_{\theta_W}^2 c_{HW} + s_{\theta_W}^2 c_{HB} + s_{\theta_W} c_{\theta_W} c_{HWB}),$$

$$\tilde{\kappa}_{ZZ} = \frac{2v^2}{\Lambda^2} (c_{\theta_W}^2 c_{H\tilde{W}} + s_{\theta_W}^2 c_{H\tilde{B}} + s_{\theta_W} c_{\theta_W} c_{H\tilde{W}B}),$$

$$\kappa_{Z\gamma} = \frac{v^2}{\Lambda^2}(2c_{\theta_W}s_{\theta_W}(c_{HW} - c_{HB}) + (s_{\theta_W}^2 - c_{\theta_W}^2)c_{HWB}),$$

$$\tilde{\kappa}_{Z\gamma} = \frac{v^2}{\Lambda^2}(2c_{\theta_W}s_{\theta_W}(c_{H\tilde{W}} - c_{H\tilde{B}}) + (s_{\theta_W}^2 - c_{\theta_W}^2)c_{H\tilde{W}B}),$$

$$\delta\hat{g}_{b\bar{b}}^h = -\frac{v^2}{\Lambda^2}\frac{v}{\sqrt{2}m_b}c_{y_b} + \frac{v^2}{\Lambda^2}(c_{H\square} - \frac{c_{HD}}{4}), \qquad (3.2.2)$$

where we have used $(m_W, m_Z, \alpha_{em}, m_b)$ as our input parameters. In the equations for $\delta g_f^{W,Z}$ above, the term,

$$\frac{\delta m_Z^2}{m_Z^2} = \frac{v^2}{\Lambda^2}(2t_{\theta_W}c_{WB} + \frac{c_{HD}}{2}), \qquad (3.2.3)$$

makes explicit the contribution to the shift in the input parameter, m_Z, due to the above operators.

The $pp \to W^\pm(\ell\nu)h(b\bar{b})$ process directly constrains the couplings $\delta\hat{g}_{WW}^h, \kappa_{WW}$ and g_{WQ}^h, whereas the $pp \to Z(l^+l^-)h(b\bar{b})$ process constrains the couplings $\delta\hat{g}_{ZZ}^h$, a linear combination of κ_{ZZ} and $\kappa_{Z\gamma}$, and the following linear combination of the contact terms [101],

$$g_{Z\mathbf{p}}^h = g_{Zu_L}^h - 0.76\ g_{Zd_L}^h - 0.45\ g_{Zu_R}^h + 0.14\ g_{Zd_R}^h. \qquad (3.2.4)$$

This linear combination arises by summing over the polarisations of the initial quarks as well as including the possibility of both up and down-type initial-state quarks, weighted by their respective PDF luminosities. For example, the lower value PDF for the down quark in the proton is reflected in the lower contribution of $g_{Zd_L}^h$ in the linear combination versus $g_{Zu_L}^h$. The precise linear combination changes very little with energy.

For the case of linearly-realised electroweak symmetry, the CP-even couplings involved in $W^\pm h$ production can be correlated to those involved in Zh production, as the same set of operators in Table 3.1 generate all the anomalous couplings (see Eq. 3.2.2). To derive these correlations, we can trade the 13 CP-even Wilson coefficients above for the 13 independent (pseudo-)observables $\delta\hat{g}_{b\bar{b}}^h$, δg_f^Z (7 couplings), g_{WQ}^h, $\delta\hat{g}_{WW}^h$, κ_{WW}, $\kappa_{Z\gamma}$ and $\kappa_{\gamma\gamma}$, the coefficient of $\frac{h}{2v}A_{\mu\nu}A^{\mu\nu}$ [1]. This can be done using the expressions in Eq. 3.2.2 and the corresponding expression for $\kappa_{\gamma\gamma}$,

$$\kappa_{\gamma\gamma} = \frac{2v^2}{\Lambda^2}(s_{\theta_W}^2 c_{HW} + c_{\theta_W}^2 c_{HB} - s_{\theta_W}c_{\theta_W}c_{HWB}). \qquad (3.2.5)$$

Since we have more coupling equations than Wilson coefficients, the rest of the

---

[1]This analysis is in the spirit of Ref. [73] but with a different choice of primary/independent observables. Indeed, we include in our list the anomalous Higgs couplings, g_{WQ}^h and κ_{ZZ}, rather than the anomalous triple gauge couplings (TGC) $\delta\kappa_\gamma$ and δg_1^Z. As we will see, the bounds on the anomalous Higgs couplings are comparable or better than those expected for the TGCs.

anomalous couplings can then be expressed as functions of these independent ones; for example we obtain,

$$
\begin{aligned}
\delta\hat{g}^h_{ZZ} =& \delta\hat{g}^h_{WW} - \left(\kappa_{WW} - \kappa_{\gamma\gamma} - \kappa_{Z\gamma} \frac{c_{\theta_W}}{s_{\theta_W}} \right) \frac{s^2_{\theta_W}}{c^2_{\theta_W}} \\
& + \left(\sqrt{2}c_{\theta_W}(\delta g^Z_{u_L} - \delta g^Z_{d_L}) - g^h_{WQ} \right) \frac{s^2_{\theta_W}}{\sqrt{2}gc^2_{\theta_W}}, \\
\kappa_{ZZ} =& \frac{1}{c^2_{\theta_W}}(\kappa_{WW} - 2c_{\theta_W}s_{\theta_W}\kappa_{Z\gamma} - s^2_{\theta_W}\kappa_{\gamma\gamma}).
\end{aligned}
\tag{3.2.6}
$$

Some of the couplings on the right-hand side of the above equations can be measured extremely precisely. For instance, the two couplings, $\kappa_{Z\gamma}$ and $\kappa_{\gamma\gamma}$, can be bounded very strongly (below per-mille level) by measuring the $h \to \gamma\gamma/\gamma Z$ branching ratios [76, 131] [1]. In addition, the Z-coupling deviations, δg^Z_f, are constrained at the per-mille level by LEP data [132]. As we will see later, studying $W^\pm h$ production at high energies would allow us to constrain g^h_{WQ} at the per-mille level. On the other hand, the couplings κ_{VV} and $\delta\hat{g}^h_{VV}$ can be constrained at most at the 1-10% level. Thus, one can safely ignore the strongly-constrained couplings to obtain the direct relationships,

$$
\begin{aligned}
\delta\hat{g}^h_{ZZ} \approx& \delta\hat{g}^h_{WW} - \frac{s^2_{\theta_W}}{c^2_{\theta_W}}\kappa_{WW}, \\
\kappa_{ZZ} \approx& \frac{\kappa_{WW}}{c^2_{\theta_W}},
\end{aligned}
\tag{3.2.7}
$$

which hold up to a very good approximation. We will utilise these relationships in order to combine our results from $W^\pm h$ and Zh modes to obtain our final bounds on the CP-even vertices.

As well as the CP-even couplings there are four CP-odd couplings, including those corresponding to $\frac{h}{2v}A_{\mu\nu}\tilde{A}^{\mu\nu}$ and $\frac{h}{2v}A_{\mu\nu}\tilde{Z}^{\mu\nu}$. The latter two couplings are, however, not precisely measurable as in the CP-even case [2]. Thus an analogue of the above procedure to correlate $\tilde{\kappa}_{WW}$ and $\tilde{\kappa}_{ZZ}$ is not possible.

Finally, we have the correlation,

$$
\begin{aligned}
g^h_{Zf} =& 2\delta g^Z_f + \frac{2gY_f t^2_{\theta_W}}{c_{\theta_W}} \left(\kappa_{WW} - \kappa_{\gamma\gamma} - \kappa_{Z\gamma} \frac{c_{\theta_W}}{s_{\theta_W}} \right) \\
& - \left(2(\delta g^Z_{u_L} - \delta g^Z_{d_L}) - \frac{\sqrt{2}}{c_{\theta_W}}g^h_{WQ} \right) (T_3 + Y_f t^2_{\theta_W}),
\end{aligned}
\tag{3.2.8}
$$

---

[1]This might seem surprising, as the branching ratios themselves are not constrained at this level. Recall, however, that the SM $h \to \gamma\gamma/\gamma Z$ rates are loop suppressed, so that even an $\mathcal{O}(10\%)$ uncertainty in the branching ratios translate to per-mille level bounds on these couplings.

[2]The CP odd interactions won't interfere with the SM interactions and so won't show in rate information.
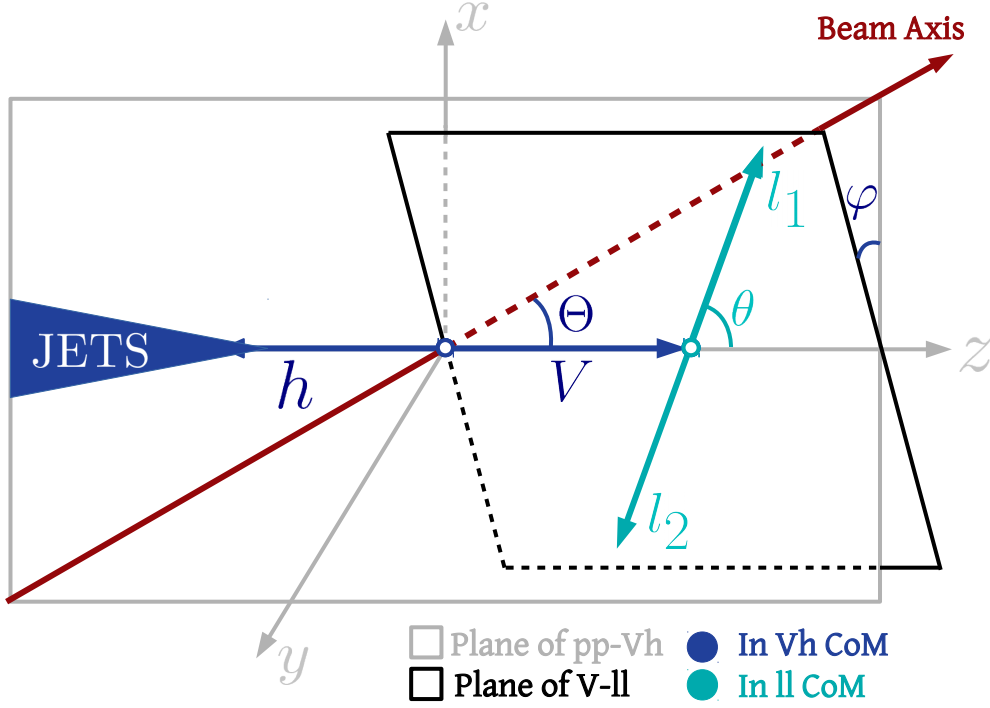
Figure 3.1: *Diagram showing the angles that can completely charac-*
terise our final state. Note the use of two different frames
of reference: the CoM frame of the Vh system (in which φ
and Θ are defined) and the CoM frame of V (in which θ
is defined). The Cartesian axes $\{x, y, z\}$ are defined by the
Vh centre-of-mass frame, with z identified as the direction
of the V-boson; y identified as the normal to the plane of
V and the beam axis; x defined so that it completes the
right-handed set.

which can also be translated to a correlation between the coupling $g_{Z\mathbf{P}}^h$ in Eq. 3.2.4 and those in the right-hand side above.

The operators in Table 3.1 also contribute to anomalous Triple Gauge Couplings (TGCs) as follows,

$$\delta g_1^Z = \frac{1}{2s_{\theta_W}^2} \frac{\delta m_Z^2}{m_Z^2} \, ,$$

$$\delta \kappa_\gamma = \frac{1}{t_{\theta_W}} \frac{v^2}{\Lambda^2} c_{HWB} \, , \tag{3.2.9}$$

where δg_1^Z and $\delta \kappa_\gamma$ appear in the dimension-six Lagrangian as,

$$\Delta \mathcal{L}_6 \supset ig\delta g_1^Z c_{\theta_W}[Z^\mu(W^{+\nu}W_{\mu\nu}^- - W^{-\nu}W_{\mu\nu}^+) + Z^{\mu\nu}W_\mu^+ W_\nu^-]$$

$$+ ig\delta\kappa_\gamma s_{\theta_W}(A^{\mu\nu} - t_{\theta_W}Z^{\mu\nu})W_\mu^+ W_\nu^- \, , \tag{3.2.10}$$

and we have used the correlation $\delta \kappa_Z = \delta g_1^Z - t_{\theta_W}^2 \delta \kappa_\gamma$, which holds at the dimension-six level [76, 135]. Using the above equations together with Eq. 3.2.2 and Eq. 3.2.5 we can obtain the following correlations between the TGCs and the Higgs couplings to gauge bosons,

$$g_{WQ}^h = \sqrt{2} c_{\theta_W} \left(\delta g_{u_L}^Z - \delta g_{d_L}^Z - g c_{\theta_W} \delta g_1^Z \right) , \qquad (3.2.11)$$

$$\kappa_{WW} = \delta \kappa_\gamma + \kappa_{\gamma\gamma} + \kappa_{Z\gamma} \frac{c_{\theta_W}}{s_{\theta_W}} . \qquad (3.2.12)$$

While Wh production at high energies constrains g_{WQ}^h, the linear combination in the right-hand side of Eq. 3.2.11 is precisely the EFT direction constrained by high-energy WZ production. This connection between Wh and WZ production is a consequence of the Goldstone boson equivalence theorem (see Section 1.2.1) as explained in Ref. [136]. In Section 3.6.2 we will use the above relations to compare our bounds with TGC bounds obtained from double gauge boson production.

With the relevant modified and new vertices discussed we move to calculating the matrix element for the process and decompose the resulting expression into angular observables.

3.3   Decomposition into angular observables

In this section we come to the central topic of this work and discuss how the full angular distributions in the $pp \to V(\ell\ell)h(b\bar{b})$ processes, at a given energy, can be expressed in terms of a finite number of basis functions, both in the SM and Dimension-6 (D6) SMEFT. The corresponding coefficients of these functions are the so-called angular moments for these processes. We start at the level of $ff \to V(\ell\ell)h(b\bar{b})$ and then discuss the experimental subtleties that arise in the extraction of these angular moments for $pp \to W^{\pm}(\ell\nu)h(b\bar{b})$ and $pp \to Z(\ell^+\ell^-)h(b\bar{b})$. In our analysis, we will require the two b-jets arising from the Higgs decay to form a fat jet. As such, we will effectively consider the three-body final state of two leptons and the fat jet in this section.

3.3.1   Angular moments at the $ff \to Vh$ level

The helicity amplitude formalism is the most convenient way to arrive at the full angular and energy dependence of the $ff \to V(\ell\ell)h(b\bar{b})$ amplitude. Starting at the 2→2 level, $f(\sigma)\bar{f}(-\sigma) \to Vh$, these helicity amplitudes are given by,

$$\mathcal{M}_\sigma^{\lambda=\pm} = \sigma \frac{1 + \sigma\lambda\cos\Theta}{\sqrt{2}} G_V \frac{m_V}{\sqrt{\hat{s}}} \left[1 + \left(\frac{g_{Vf}^h}{g_f^V} + \hat{\kappa}_{VV} - i\lambda\hat{\tilde{\kappa}}_{VV} \right) \frac{\hat{s}}{2m_V^2} \right],$$

$$\mathcal{M}_{\sigma}^{\lambda=0} = -\frac{\sin\Theta}{2}G_V\left[1 + \delta\hat{g}_{VV}^h + 2\hat{\kappa}_{VV} + \delta g_f^Z + \frac{g_{Vf}^h}{g_f^V}\left(-\frac{1}{2} + \frac{\hat{s}}{2m_V^2}\right)\right], \qquad (3.3.1)$$

where,

$$\begin{aligned}
\hat{\kappa}_{WW} &= \kappa_{WW}, \\
\hat{\kappa}_{ZZ} &= \kappa_{ZZ} + \frac{Q_f e}{g_f^Z}\kappa_{Z\gamma}, \\
\hat{\tilde{\kappa}}_{ZZ} &= \tilde{\kappa}_{ZZ} + \frac{Q_f e}{g_f^Z}\tilde{\kappa}_{Z\gamma}, \qquad\qquad (3.3.2)
\end{aligned}$$

and $G_{Z,W} = \frac{gg_f^Z}{c_{\theta_W}}, \frac{g^2}{\sqrt{2}}$. The helicities of the Z-boson and initial-state fermions are $\lambda = \pm 1$ and $\sigma = \pm 1$, respectively; $g_f^Z = g(T_3^f - Q_f s_{\theta_W}^2)/c_{\theta_W}$ and $g_f^W = g/\sqrt{2}$; $\sqrt{\hat{s}}$ is the partonic centre-of-mass energy. The above expressions hold both for quark and leptonic initial states. In Eq. 3.3.1 above, we have kept only the terms with leading powers of $\sqrt{\hat{s}}/m_V$ both for the SM and D6 SMEFT (the subdominant terms are smaller by, at least, factors of $m_V^2/\hat{s}$). We have, however, retained the next-to-leading EFT contribution for the $\lambda = 0$ mode, as an exception, in order to keep the leading effect amongst the terms proportional to $\delta\hat{g}_{VV}^h$. The full expressions for the helicity amplitudes including the SMEFT corrections can be found in Ref. [137]. The above expressions assume that the momentum of the initial fermion, f, is in the positive z-direction of the lab frame. The expressions for the case where the anti-fermion, $\bar{f}$, has momentum in the positive z-direction can be obtained by making the replacement $\sigma \to -\sigma$. Note that we have not included the effect of a Vff coupling deviation (δg_f^V in Eq. 3.2.1). This effect will be incorporated at the end of this section.

It is worth emphasising that for both the SM and D6 SMEFT, only contributions up to the $J = 1$ helicity amplitude appear. For the SM, this is because the $ff \to Vh$ process is mediated by a spin-1 gauge boson. For the D6 SMEFT, in addition to diagrams with spin-1 exchange, there is also the contribution from the contact term in Eq. 3.2.1. This contact term is exactly the vertex that would arise by integrating out a heavy spin-1 particle. Therefore, even in the D6 SMEFT, only contributions up to $J = 1$ exist. This will no longer be true at higher orders in the EFT expansion, where higher-J amplitudes will also get contributions.

At the $2 \to 3$ level, the amplitude can be most conveniently written in terms of φ and θ, the azimuthal and polar angle of a leptonic daughter particle of the gauge boson, V, in the V rest frame as defined in Fig. 3.1. For consistency, this daughter particle is chosen to be the negatively-charged lepton for $V = W^-, Z$ and the neutrino for

$V = W^+$. Under these definitions, the amplitude reads,

$$\mathcal{A}(\hat{s}, \Theta, \theta, \varphi) = \frac{-i g_\ell^V}{\Gamma_V} \sum_\lambda \mathcal{M}_\sigma^\lambda(\hat{s}, \Theta) d_{\lambda,1}^{J=1}(\theta) e^{i\lambda\hat{\varphi}}, \tag{3.3.3}$$

where g_ℓ^V is defined below Eq. 3.3.1, Γ_V is the V-width, and $d_{\lambda,1}^{J=1}(\hat{\theta})$ are the Wigner functions,

$$d_{\pm 1,1}^{J=1} = \tau \frac{1 \pm \tau \cos\theta}{\sqrt{2}}, \quad d_{0,1}^{J=1} = \sin\theta, \tag{3.3.4}$$

with lepton helicity τ. We have assumed a SM amplitude for the V-decay; modifications due to a $V\ell\ell$ coupling deviation will be included at the end of this section. For $V = W^\pm$, we always have $\tau = -1$. We can now obtain the squared amplitude with the full angular dependence using Eqs. 3.3.1 to 3.3.4,

$$\sum_\tau |\mathcal{A}(\hat{s}, \Theta, \theta, \varphi)|^2 = \sum_i a_i(\hat{s}) f_i(\Theta, \theta, \varphi), \tag{3.3.5}$$

where we have summed over the final-lepton helicity. The nine functions, $f_i(\Theta, \theta, \varphi)$, are obtained by squaring the sum of the three helicity amplitudes in the right-hand side of Eq. 3.3.3, see also [103, 138, 139]. Explicitly, these are,

$$
\begin{aligned}
f_{LL} &= S_\Theta^2 S_\theta^2, \\
f_{TT}^1 &= C_\Theta C_\theta, \\
f_{TT}^2 &= (1 + C_\Theta^2)(1 + C_\theta^2), \\
f_{LT}^1 &= C_\varphi S_\Theta S_\theta, \\
f_{LT}^2 &= C_\varphi S_\Theta S_\theta C_\Theta C_\theta, \\
\tilde{f}_{LT}^1 &= S_\varphi S_\Theta S_\theta, \\
\tilde{f}_{LT}^2 &= S_\varphi S_\Theta S_\theta C_\Theta C_\theta, \\
f_{TT'} &= C_{2\varphi} S_\Theta^2 S_\theta^2, \\
\tilde{f}_{TT'} &= S_{2\varphi} S_\Theta^2 S_\theta^2,
\end{aligned}
\tag{3.3.6}
$$

where $S_\alpha = \sin\alpha$, $C_\alpha = \cos\alpha$. The subscripts of the above functions denote the V-polarisation of the two interfering amplitudes, with TT' denoting the interference of two transverse amplitudes with opposite polarisations. The corresponding coefficients a_i are the so-called angular moments for this process, which completely characterise the multidimensional angular dependence of this process at a given energy, $\hat{s}$. The expressions for these angular moments in terms of the vertex couplings in Eq. 3.2.1 are given in Table 3.2. Note the factor,

$$\epsilon_{RL}^V = \frac{(g_{l_R}^V)^2 - (g_{l_L}^V)^2}{(g_{l_R}^V)^2 + (g_{l_L}^V)^2}, \tag{3.3.7}$$

where $V = Z, W^{\pm}$, which arises in some moments from the sum over final lepton helicity, τ, in Eq. 3.3.5.

It is worth emphasising an important conceptual point here. The cross-helicity moment functions, i.e. the last six functions in Eq. 3.3.6, integrate to zero over the full phase space of the V-decay products. This is to be expected, as the two amplitudes corresponding to different helicities, at the level of the V-boson, cannot interfere. If we look at the phase space of the decay products differentially, however, the corresponding angular moments carry very useful information. For example, one can verify from Table 3.2, that the leading contribution of the κ_{ZZ} ($\tilde{\kappa}_{ZZ}$) coupling is to the moment a_{LT}^2 ($\tilde{a}_{LT}^2$). As pointed out in Ref. [1], this effect can only be recovered if we study the triple differential with respect to all three angles, i.e. an integration over *any* of the three angles makes the basis functions f_{LT}^2 and $\tilde{f}_{LT}^2$ vanish. This is an example of an 'interference resurrection' study, see also Refs. [106–109], where interference terms absent at the inclusive level are 'recovered' by analysing the phase space of the decay products differentially.

It is possible that not all of these angular moments will be relevant or observable for a given initial and final state. Before considering in detail the case of the $pp \to V(ll)h$ process, let us briefly comment on which of these angular moments are accessible to lepton colliders. For the $e^+e^- \to Z(\ell^+\ell^-)h$ process in lepton colliders, all nine angular moments can be measured[1]. However, three of them, namely a_{TT}^1, a_{LT}^1 and $\tilde{a}_{LT}^1$, are suppressed by the factor of $|\epsilon_{RL}^Z| = 0.16$, which is accidentally small due to the numerical closeness of the couplings $g_{l_L}^Z$ and $g_{l_R}^Z$.

3.3.2   Angular moments for the $pp \to Z(\ell\ell)h(b\bar{b})$ process

Our process of interest requires an initial quark-antiquark pair, $q\bar{q}'$. For the Zh mode, $q = q'$. The first thing to note about the LHC is that the direction of the quark, q, is not always in the same direction in the lab frame. The expressions in Table 3.2 are for the case where the quark moves in the positive z-direction. For the other case, where the momentum of the antiquark, $\bar{q}$, is in the z-direction, as stated below Eq. 3.3.3, one can obtain the corresponding expressions for the angular moments by making the substitution $\sigma \to -\sigma$. The angular moments a_{TT}^1, a_{LT}^1 and $\tilde{a}_{LT}^1$ thus vanish once we average over both these possibilities.

We are therefore left with six moments. At high energy, a_{LL} dominates over all other moments in the SM, as it is the only term independent of $\gamma = \sqrt{\hat{s}}/(2m_V)$; all other

---

[1]In Section 3.3.2 we see that ignorance over which of the initial partons, q and $\bar{q}$, is moving in the positive z direction leads to some moments averaging to zero. Knowledge of the e^+ and e^- directions at lepton colliders could reduce this cancellation.

a_{LL}	$\frac{\mathcal{G}_V^2}{4}\left[1 + 2\delta\hat{g}_{VV}^h + 4\hat{\kappa}_{VV} + 2\delta g_f^V + \frac{g_{Vf}^h}{g_f^V}(-1 + 4\gamma^2)\right]$
a_{TT}^1	$\frac{\mathcal{G}_V^2 \sigma \epsilon_{RL}^V}{2\gamma^2}\left[1 + 4\left(\frac{g_{Vf}^h}{g_f^V} + \hat{\kappa}_{VV}\right)\gamma^2\right]$
a_{TT}^2	$\frac{\mathcal{G}_V^2}{8\gamma^2}\left[1 + 4\left(\frac{g_{Vf}^h}{g_f^V} + \hat{\kappa}_{VV}\right)\gamma^2\right]$
a_{LT}^1	$-\frac{\mathcal{G}_V^2 \sigma \epsilon_{RL}^V}{2\gamma}\left[1 + 2\left(\frac{2g_{Vf}^h}{g_f^V} + \hat{\kappa}_{VV}\right)\gamma^2\right]$
a_{LT}^2	$-\frac{\mathcal{G}_V^2}{2\gamma}\left[1 + 2\left(\frac{2g_{Vf}^h}{g_f^V} + \hat{\kappa}_{VV}\right)\gamma^2\right]$
$\tilde{a}_{LT}^1$	$-\mathcal{G}_V^2 \sigma \epsilon_{RL}^V \hat{\tilde{\kappa}}_{VV}\gamma$
$\tilde{a}_{LT}^2$	$-\mathcal{G}_V^2 \hat{\tilde{\kappa}}_{VV}\gamma$
$a_{TT'}$	$\frac{\mathcal{G}_V^2}{8\gamma^2}\left[1 + 4\left(\frac{g_{Vf}^h}{g_f^V} + \kappa\hat{}_{VV}\right)\gamma^2\right]$
$\tilde{a}_{TT'}$	$\frac{\mathcal{G}_V^2}{2}\hat{\tilde{\kappa}}_{VV}$

Table 3.2: *Expressions for the angular moments as a function of the different anomalous couplings in Eq. 3.2.1 up to linear order. Contributions subdominant in $\gamma = \sqrt{\hat{s}}/(2m_V)$ are neglected, with the exception of the next-to-leading EFT contribution to a_{LL}, which has been retained in order to keep the leading effect of the $\delta\hat{g}_{VV}^h$ term. The factor ϵ_{RL}^V is defined in text and $\mathcal{G}_V = gg_f^V\sqrt{(g_{l_L}^V)^2 + (g_{l_R}^V)^2}/(c_{\theta_W}\Gamma_V)$, Γ_V being the V-width. The SM part of our results can also be found in [140].*

SM terms go as γ^{-1} or γ^{-2}. The largest BSM contribution at high energies is also to a_{LL}, from the linear combination $g_{Z\mathbf{p}}^h$ (see Eq. 3.2.4) that arises from averaging over the initial-state flavour and polarisation [101]. The contribution due to $g_{Z\mathbf{p}}^h$ grows quadratically with energy and this coupling can thus be measured very precisely, as we will see in Section 3.6. This was also discussed in detail in Ref. [101].

Once $g_{Z\mathbf{p}}^h$ has been precisely measured, we can use the remaining information in the angular moments to constrain the coupling $\delta\hat{g}_{ZZ}^h$ and the linear combinations,

$$\kappa_{ZZ}^{\mathbf{p}} = \kappa_{ZZ} + 0.3\ \kappa_{Z\gamma}$$
$$\tilde{\kappa}_{ZZ}^{\mathbf{p}} = \tilde{\kappa}_{ZZ} + 0.3\ \tilde{\kappa}_{Z\gamma}, \tag{3.3.8}$$

that enter, respectively, the CP-even and odd angular moments at the $pp \to Z(\ell\ell)h(b\bar{b})$ level. The coefficient of $\kappa_{Z\gamma}$ and $\tilde{\kappa}_{Z\gamma}$ above arise by appropriately averaging Eq. 3.3.2 over the initial-state flavours and polarisations. Recall, however, that there is a very strong bound on $\kappa_{Z\gamma}$ (see Section 3.2) so that the above linear combination effectively reduces to only κ_{ZZ} to a very good approximation.

Consider now the angular moment a_{TT}^2 and the contribution to a_{LL} sub-dominant

(a)

(b)
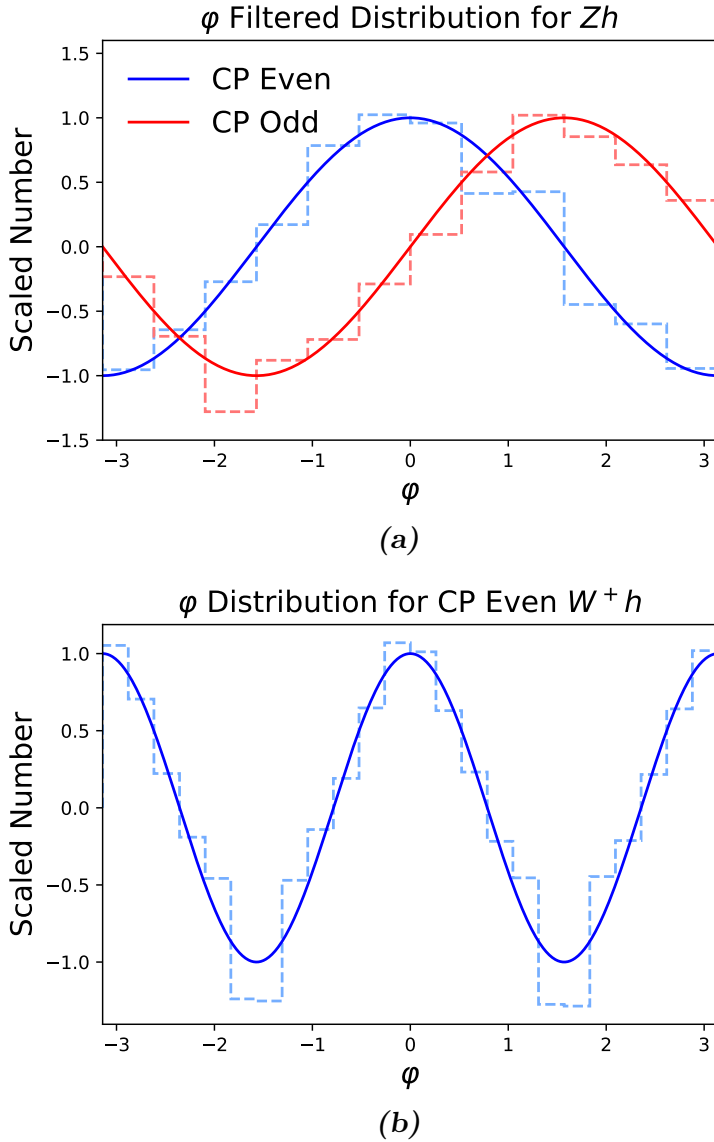
Figure 3.2: *(a) Weighted φ-distributions for two different Monte-Carlo samples for the Zh mode with the EFT couplings, κ_{ZZ} and $\tilde{\kappa}_{ZZ}$, respectively, turned on. The events used include showering and hadronisation and are those passing all selection cuts (see Section 3.5 for details). To show the effect of the angular moments a^1_{LT} and $\tilde{a}^1_{LT}$, we take the weight of each event to be the sign of $\sin(2\theta)\sin(2\Theta)$. We then show the histogram with respect to φ and obtain the expected shapes for the two samples; (b) Regular φ-distributions for a Monte-Carlo sample for the Wh mode with a non-zero value for the EFT coupling κ_{WW}. We see the effect of the angular moment $a_{TT'}$, the only angular moment that survives after integrating over θ and Θ, and averaging over the two solutions. Again, the events used are those passing all cuts. The angular moment $\tilde{a}^1_{LT}$ can also be extracted in Wh production but its effect can only be seen in a weighted distribution like in (a).*

in γ, which is unconstrained even after the strong bound on $g_{Z\mathbf{P}}^h$. First of all, the total rate of the $pp \to Z(l^+l^-)h(b\bar{b})$ process depends only on the two moments a_{LL} and a_{TT}^2 as all other non-vanishing moments are coefficients of cross-helicity terms that vanish upon integration over φ, see Eq. 3.3.6. The rate itself can constrain a linear combination of $\delta\hat{g}_{ZZ}^h$ and $\kappa_{ZZ}^{\mathbf{P}}$. Additionally, these two moments also carry the information of the joint distribution of the events with respect to (θ, Θ), which, along with the total rate, can in principle be used to constrain $\delta\hat{g}_{ZZ}^h$ and $\kappa_{ZZ}^{\mathbf{P}}$ simultaneously. We find in our final analysis, however, that the joint (θ, Θ) distribution in the events surviving our cuts is not very effective in simultaneously constraining these couplings. The main reason for this is that the Θ-distribution gets distorted with respect to the original theoretical form due to the experimental cuts necessary for our boosted Higgs analysis. In particular, we require $p_T^h > 150$ GeV, which eliminates forward events. Another effect that could further distort the distribution is radiation of hard jets[1]. As θ and Θ appear in a correlated way in the amplitude, these effects also deform the θ-distribution, but to a smaller extent. For this reason, as discussed in Section 3.4.2, we will isolate a_{LL} and a_{TT}^2 using only the θ-distribution in our final analysis, in order to obtain better bounds.

Much more reliable are the φ distributions, which preserve their original shape to a large extent. Consider, for example, the moments a_{LT}^2 and $\tilde{a}_{LT}^2$, which contribute terms to the square amplitude,

$$\sum_\tau |\mathcal{A}(\hat{s}, \Theta, \theta, \varphi)|^2 \supset \frac{1}{4}a_{LT}^2 \sin(2\theta)\sin(2\Theta)\cos(\varphi) + \frac{1}{4}\tilde{a}_{LT}^2 \sin(2\theta)\sin(2\Theta)\sin(\varphi). \tag{3.3.9}$$

In Fig. 3.2a we show the φ distributions corresponding to a sample in which these two moments are enhanced, for events that include the effect of jet radiation and pass all experimental cuts to be described in Section 3.5. By multiplying event weights by the sign of $\sin(2\theta)\sin(2\Theta)$ we recover the expected sinusoidal and cosinusoidal φ-dependences despite all these effects.

The information for the φ-dependence is carried by the angular moments a_{LT}^2 and $a_{TT'}$ in the CP-even case, which can be measured to constrain the linear combination $\kappa_{ZZ}^{\mathbf{P}}$, assuming again that g_{Vf}^h is already precisely constrained. Among these, as identified in Ref. [1], the leading contribution is from a_{LT}^2, as it is larger relative to $a_{TT'}$ by a factor of γ, see Table 3.2. This moment provides the strongest bound on the linear combination $\kappa_{ZZ}^{\mathbf{P}}$ in our analysis but can only be accessed by looking at

---

[1]This could have the effect of changing the kinematics from $2 \to 2$ to $3 \to 2$ or so on. If required, this effect can be mended by applying an active boost of the HZ system to be on the collision axis, or by requiring that the transverse momentum of all the final-state particles, excluding additional jets, is small compared to the hard scale of the event. The latter is preferable compared to a jet veto as it avoids jet reconstruction uncertainties [136].

the joint distribution of $(\theta, \Theta, \varphi)$. A standard analysis that integrates over any of these three angles would miss this effect completely.

Finally the CP-odd coupling, $\tilde{\kappa}_{ZZ}^{\mathbf{p}}$, cannot be constrained without using φ information contained in $\tilde{a}_{LT}^2$ and $\tilde{a}_{TT'}$. Again, the leading effect contained in $\tilde{a}_{LT}^2$ is highly non-trivial and can only be accessed by utilising the triple differential distribution with respect to $(\theta, \Theta, \varphi)$.

Before moving to the next subsection, we would like to comment that the distortion of the distribution due to experimental cuts and jet radiation does not invalidate our analysis. That is to say, while these effects perhaps reduce our sensitivity compared to the idealised case, as we will discuss later, these effects will already be factored into our uncertainty estimates. Moreover, our final analysis does not depend too much on the precise shape of the Θ-distribution, as we rely more on the θ and especially φ distributions.

3.3.3   Angular moments for the $pp \rightarrow W(\ell\ell)h(b\bar{b})$ process

Much of the discussion in the previous section is also relevant here. Once again, averaging over the initial quark-antiquark direction causes the angular moments a_{TT}^1, a_{LT}^1 and $\tilde{a}_{LT}^1$ to vanish. The high-energy amplitude is again dominated by a_{LL} both in the SM and EFT. In the EFT case, the contribution from g_{WQ}^h can be strongly constrained due to its quadratic growth. The discussion about the distortion of the Θ-distributions and its effect on extracting the moments a_{LL} and a_{TT}^2 also holds for this case.

The main difference from $pp \rightarrow Z(\ell\ell)h(b\bar{b})$ arises in the φ-distributions. A complication arises from the fact that the neutrino four momentum is experimentally inaccessible. Imposing energy and momentum conservation and assuming an on-shell W-boson yields two possible solutions for the neutrino four momentum, i.e. two solutions for the z-component of the neutrino momentum in the lab frame, the p_T being equal for both solutions (see Appendix A.1 for a brief derivation). While Θ, θ and the final-state invariant mass converge for the two solutions, especially at high energies [108], the values of φ for the two solutions do not converge, and in fact are related to each other as $\varphi_2 = \pi - \varphi_1$ to a very good approximation. In our analysis, we average over Θ, θ and the final-state invariant mass, but keep both φ solutions with equal weight. This has the consequence that the functions $\cos\varphi$ and $\sin 2\varphi$ vanish when averaged over these two possibilities, resulting in the vanishing of the moments a_{LT}^1, a_{LT}^2 and $\tilde{a}_{TT'}$ (see Eq. 3.3.6).

In Figs. 3.3a to 3.3c we show, for the three angles, a scatter plot between the true and reconstructed values obtained after our collider analysis described in Section 3.5. For
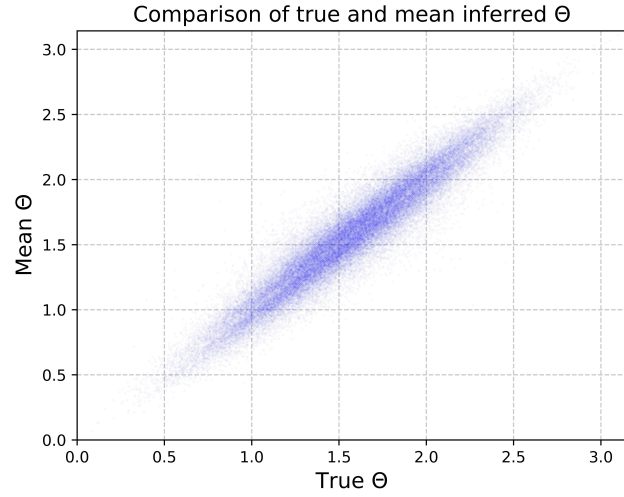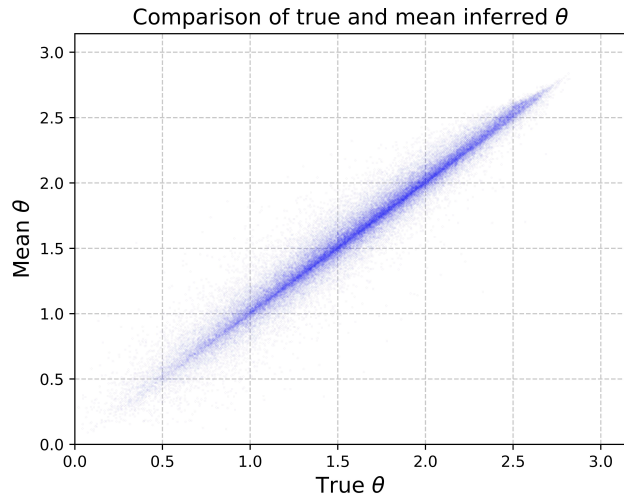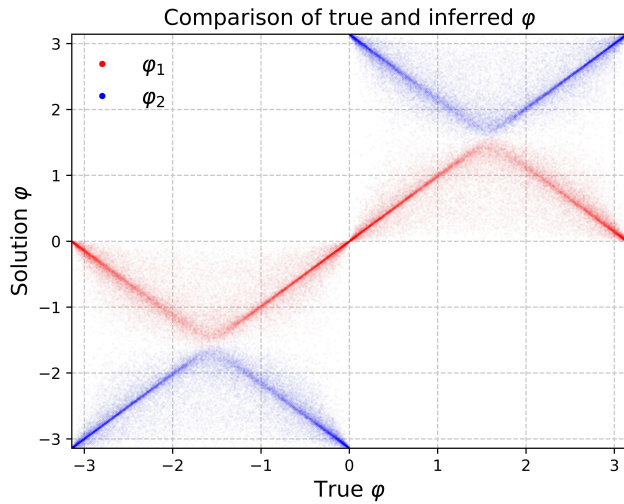
Figure 3.3: *In the $W^{\pm}(l\nu)h(b\bar{b})$ process, the ambiguity in the z momentum of the neutrino leads to two possible values of each of the three angles. Plots (a) and (b) above show the scatter plot for the mean of the solutions for Θ and θ vs the true value. Plot (c) includes two solutions for φ (shown in red and blue) in a scatter plot vs the true value.*

Θ and θ, we use for the reconstructed value the mean of the two solutions, whereas for φ, we populate the scatter plot with both solutions. It is clear from Fig. 3.3c that we have $\varphi_1 + \varphi_2 = \pi$ to a very good approximation. While Figs. 3.3a to 3.3c show that the angles can be reconstructed quite well, the procedure is not exact, as we have assumed that the W boson is on-shell and did not properly take into account radiation of additional hard jets. In fact, for some rare events the virtuality of the W-boson is so high that no real solutions exist for the neutrino p_z, if we assume an on-shell W-boson; we neglect such events in our analysis.

In Fig. 3.2b we show the φ-distribution for EFT events that finally survive the collider analysis discussed in Section 3.5. We again see the expected $\cos(2\varphi)$ shape corresponding to $a_{TT'}$, which is the only moment that survives integration over the other two angles and averaging over the two solutions (see also Ref. [141]). The difference in the true and reconstructed distributions at $\varphi = \pm\pi/2$ is related to fact that we discard events where the neutrino four momentum solutions are complex [108].

So far we have not considered the effect of Vff, Vll and hbb coupling deviations due to D6 operators. All these coupling deviations are like $\delta\hat{g}_{VV}^h$ in Eq. 3.2.1, in that they simply rescale the SM coupling and thus all SM distributions. Their effect can therefore be incorporated by making the replacement in Table 3.2 and elsewhere,

$$\delta\hat{g}_{VV}^h \rightarrow \delta\hat{g}_{VV}^h + \delta\hat{g}_{bb}^h + \frac{2\delta g_f^V}{g_f^V} + \frac{2\delta g_l^V}{g_l^V} \; . \tag{3.3.10}$$

Of the above couplings, while the $\delta g_{f,l}^V$ couplings are very precisely constrained to be close to zero[1], the effect of $\delta\hat{g}_{bb}^h$ cannot be ignored.

3.4   Method of angular moments

3.4.1   Basic idea

As we have seen in Section 3.3, the squared amplitudes for our processes can be decomposed into a set of angular structures, $f_i(\Theta, \theta, \varphi)$, whose contributions are parametrised by the associated coefficients, the so-called angular moments, a_i. We would like to extract these coefficients in a way that best takes advantage of all the available angular information. In principle, this can be done by a full likelihood fit, but here we use the method of moments [112, 114, 115]. This method has its advantages – especially if the number of events is not too large [115]. This method

---

[1] These constraints come from W, Z decays.

involves the use of an analogue of Fourier analysis to extract the angular moments. Essentially, we look for weight functions, $w_i(\Theta, \theta, \varphi)$, that can uniquely extract the coefficients, a_i, i.e.,

$$\int_0^\pi d\theta \int_0^\pi d\Theta \int_0^{2\pi} d\varphi \sum_i (a_i f_i) w_j \sin\theta \sin\Theta = a_j,$$

$$\Rightarrow \qquad \int_0^\pi d\theta \int_0^\pi d\Theta \int_0^{2\pi} d\varphi f_i w_j \sin\theta \sin\Theta = \delta_{ij}. \qquad (3.4.1)$$

Assuming that the weight functions are linear combinations of the original basis functions,

$$w_i = \lambda_{ij} f_j, \qquad (3.4.2)$$

we can use Eq. 3.4.1 to show that the matrix $\lambda_{ij} = M_{ij}^{-1}$, where,

$$M_{ij} = \int_0^\pi d\theta \int_0^\pi d\Theta \int_0^{2\pi} d\varphi f_i f_j \sin\theta \sin\Theta. \qquad (3.4.3)$$

For the set of basis functions in Eq. 3.3.6, the resulting matrix is given by,

$$M = \begin{pmatrix} \frac{512\pi}{225} & 0 & \frac{128\pi}{25} & 0 & 0 & 0 & 0 & 0 & 0 \\ 0 & \frac{8\pi}{9} & 0 & 0 & 0 & 0 & 0 & 0 & 0 \\ \frac{128\pi}{25} & 0 & \frac{6272\pi}{225} & 0 & 0 & 0 & 0 & 0 & 0 \\ 0 & 0 & 0 & \frac{16\pi}{9} & 0 & 0 & 0 & 0 & 0 \\ 0 & 0 & 0 & 0 & \frac{16\pi}{225} & 0 & 0 & 0 & 0 \\ 0 & 0 & 0 & 0 & 0 & \frac{16\pi}{9} & 0 & 0 & 0 \\ 0 & 0 & 0 & 0 & 0 & 0 & \frac{16\pi}{225} & 0 & 0 \\ 0 & 0 & 0 & 0 & 0 & 0 & 0 & \frac{256\pi}{225} & 0 \\ 0 & 0 & 0 & 0 & 0 & 0 & 0 & 0 & \frac{256\pi}{225} \end{pmatrix}, \qquad (3.4.4)$$

where we have organised the basis functions in the order in which they appear in Eq. 3.3.6.

It is convenient to go to a basis such that M_{ij} and thus its inverse λ_{ij}, are diagonal. This can be achieved by an orthogonal rotation,

$$\hat{f}_1 = \cos\beta f_{LL} - \sin\beta f_{TT}^2,$$

$$\hat{f}_3 = \sin\beta f_{LL} + \cos\beta f_{TT}^2, \qquad (3.4.5)$$

by an angle,

$$\tan\beta = -\frac{1}{2}(5 + \sqrt{29}). \qquad (3.4.6)$$

In the new fully-orthogonal basis, $\vec{\hat{f}} = \{\hat{f}_1, f_{TT}^1, \hat{f}_3, f_{LT}^1, f_{LT}^2, \tilde{f}_{LT}^1, \tilde{f}_{LT}^2, f_8, f_9\}$, the

rotated matrix $M \to \hat{M}$ reads,

$$\hat{M} = \mathrm{diag}\left(\frac{64\pi}{225}\xi_+, \frac{8\pi}{9}, \frac{64\pi}{225}\xi_-, \frac{16\pi}{9}, \frac{16\pi}{225}, \frac{16\pi}{9}, \frac{16\pi}{225}, \frac{256\pi}{225}, \frac{256\pi}{225}\right), \qquad (3.4.7)$$

with $\xi_\pm = (53 \pm 9\sqrt{29})$. This is the matrix $\hat{\lambda}_{ij}^{-1}$, so that the weight functions in the rotated basis are,

$$w_i = \hat{M}_{ij}^{-1} f_j. \qquad (3.4.8)$$

We are now able to convolute our event distributions with these weight functions to extract values for the coefficients, $\hat{a}_i$, in the new basis, which can then be rotated back if we are interested in the moments in the original basis.

3.4.2   Alternative weight functions for a_{LL} and a_{TT}^2

The above algorithm to extract the moments systematically generates the set of weight functions, but this set is not unique. For instance, a function proportional to $\cos 2\varphi$ can also be the weight function for $f_{TT'}$. As we mentioned in Section 3.3, the Θ distribution suffers distortions to its original shape due to experimental cuts and other effects. For this reason, the extraction of a_{LL} and a_{TT}^2 using the weight functions derived above does not give optimal results. To avoid this, we can use weight functions only involving θ to extract these two moments.

Let us integrate Eq. 3.3.5 over the Θ and φ to keep only the θ dependence,

$$\int d\varphi d\Theta \sin\Theta \sum_\tau |\mathcal{A}(\hat{s}, \Theta, \theta, \varphi)|^2 = a'_{LL} f'_{LL}(\theta) + a_{TT}^{2'} f_{TT}^{2'}(\theta)$$

$$= a'_{LL} \sin^2\theta + a_{TT}^{2'}(1 + \cos^2\theta), \qquad (3.4.9)$$

where a'_{LL} and $a_{TT}^{2'}$ are related to the original moments a_{LL} and a_{TT}^2 as follows,

$$a'_{LL} = \frac{8\pi}{3}a_{LL}, \qquad a_{TT}^{2'} = \frac{16\pi}{3}a_{TT}^2. \qquad (3.4.10)$$

Now, following the steps in Section 3.4.1, we carry out a rotation,

$$\hat{f}'_1 = \cos\beta' f'_{LL} - \sin\beta' f_{TT}^{2'},$$
$$\hat{f}'_3 = \sin\beta' f'_{LL} + \cos\beta' f_{TT}^{2'}, \qquad (3.4.11)$$

to diagonalise the matrix in Eq. 3.4.3. In this case, the angle of rotation is given by $\tan\beta' = 1$. In this basis, the weight functions are proportional to $\hat{f}'_1$ and $\hat{f}'_3$, given by,

$$\hat{w}'_1(\theta) = \hat{f}'_1(\theta)\frac{3(\sqrt{61} - 9)}{16},$$

$$\hat{w}'_3(\theta) = \hat{f}'_3(\theta)\frac{3(\sqrt{61} + 9)}{16}. \tag{3.4.12}$$

Convoluting the observed distribution with these weight functions yields $\hat{a}'_1$ and $\hat{a}'_3$, which can be rotated back to give a'_{LL} and $\hat{a}^{2'}_{TT}$ and finally a_{LL} and $\hat{a}^2_{TT}$ using Eq. 3.4.10. Using these alternative weight functions is equivalent to using only the information in the θ-distribution to extract these two moments and ignoring the distorted Θ distribution. This will improve the final bounds we obtain in Section 3.6.

For clarity, we denote the final set of weight functions by W_i,

$$\vec{W} = \{\hat{w}'_1, w_2, \hat{w}'_3, w_4, w_5, w_6, w_7, w_8, w_9\}. \tag{3.4.13}$$

In other words, the first and third weight functions have been integrated (such that they only depend on θ) and rotated, as described above; the remaining seven weight functions are unchanged from those defined in Eq. 3.4.8.

3.4.3   Extraction of angular moments and uncertainty estimate

For our simulated samples, which are generated following the procedure detailed in Section 3.5, the convolution in Eq. 3.4.1 becomes a simple summation over all the events in our sample,

$$\alpha_i(M) = \frac{\hat{N}}{N}\sum_{n=1}^{N} W_i(\Theta_n, \theta_n, \varphi_n). \tag{3.4.14}$$

In order to also take energy dependence into account, we have split the events into bins of the final-state invariant mass, with M being the central value of a given bin. Here, $N = N(M)$ is the number of Monte-Carlo events in the sample and $\hat{N} = \hat{N}(M)$ the actual number of events expected, both in the particular invariant-mass bin for a given integrated luminosity. Note that, as such, the set α_i in Eq. 3.4.14 is proportional to the set $\{\hat{a}'_{LL}, a^1_{TT}, \hat{a}^{2'}_{TT}, a^1_{LT}, a^2_{LT}, \tilde{a}^1_{LT}, \tilde{a}^2_{LT}, a_{TT'}, \tilde{a}_{TT'}\}$, normalised such that $\sum_i \alpha_i \hat{f}_i$ now yields the distribution of the actual number of events expected at a certain integrated luminosity and not the squared amplitude integrated over the full phase space as in Eq. 3.3.5. For a sufficiently-large number of events, N, the weight functions, W_i, converge to a multivariate Gaussian distribution with a mean and covariance matrix given by,

$$\bar{W}_i = \frac{1}{N}\sum_{n=1}^{N} W_i(\Theta_n, \theta_n, \varphi_n),$$

$$\sigma_{ij} = \frac{1}{N-1}\sum_{n=1}^{N}\left[W_i - \bar{W}_i\right]\left[W_j - \bar{W}_j\right]. \tag{3.4.15}$$

We find that if we keep increasing N, as soon as it is large enough (say 100), the $\bar{W}_i$ and σ_{ij} approach fixed values. In the orthonormal basis, involving the functions $\hat{f}_i$, we find a covariance matrix that is nearly diagonal.

Assuming a diagonal covariance matrix, the angular moments in the orthonormal basis converge to Gaussians with mean and standard deviation given by,

$$\alpha_i \pm \delta\alpha_i = \hat{N}\bar{W}_i \pm \sqrt{\hat{N}\sigma_{ii}}\,. \tag{3.4.16}$$

As a cross-check, we also computed the second term above, $\delta\alpha_i$, by splitting our Monte-Carlo sample into parts with $\hat{N}$ events each and computing α_i in each case; the standard deviation of the α_i obtained matches the second term above very closely. This way of estimating the error also shows that any deformation of the original angular distribution due to experimental or QCD effects (see Section 3.3.2), has been already factored into our uncertainty estimate. To estimate the uncertainty on the α_i one must also consider the fact that, $\hat{N}$, the expected number of events in the given bin, itself fluctuates statistically. Moreover, there are systematic uncertainties in the value of α_i we obtain in this way. These two effects result in additional uncertainties on the mean value above. Adding all these errors in quadrature we obtain, for the uncertainty in each moment, α_i,

$$\Sigma_i = \sqrt{\left(\left(\frac{\sqrt{\hat{N}}}{\hat{N}}\right)^2 + \kappa_{\text{syst}}^2\right)\alpha_i^2 + \sigma_{ii}}\,, \tag{3.4.17}$$

where κ_{syst} represents the percentage systematic error, which we take to be 0.05 in this work.

3.5 Collider simulation

In this section, we give a explanation of the methodology used to create and analyse our samples. A summary of the overall architecture is presented in Section 3.5.1; the specific subtleties associated with the Zh and Wh channels are addressed in Section 3.5.2 and Section 3.5.3 respectively. The packages (written in SMALL CAPS), algorithms and tools (written in **bold**) mentioned throughout this section are briefly elaborated upon in Appendix A.2, which acts somewhat like a glossary.

3.5.1 Summary of the process

In this study, we take into account next-to-leading order (NLO) QCD effects. This leads to a slight complication of the workflow, as certain new packages and tools

are needed to extend leading order (LO) tools to NLO capability. A pictorial representation of our workflow or 'stack' is shown in Fig. 3.4, with the LO tools shown in black and any extra packages needed to extend to NLO shown in blue.

The process begins with the model. Our model, with its new SMEFT vertices, is defined in FEYNRULES [142], which generates a Universal FeynRules Output (UFO) file. Such UFO files can be used as inputs for event generators. In order to work at NLO, we must use FEYNRULES in conjunction with NLOCT [143]. NLOCT computes the UV and R_2 counterterms, which are required for the one-loop calculations, and adds them to the UFO. When required, we manually insert the R_2 terms in the NLO model as the usage of the publicly available NLOCT version is restricted to renormalisable interactions only.

We then feed our UFO file, along with NNPDF2.3 [144] parton distribution functions (PDFs) into the MADGRAPH (MG5_aMC@NLO [145]) environment. Within this framework, we generate events and perform various other helpful functions. When it comes to the NLO calculations, real emission corrections are performed following the **FKS subtraction** method [146], whereas virtual corrections are done using the **OPP reduction** technique [147]. Furthermore, the MC@NLO formalism [148] takes care of the matching between the LO matrix element and parton shower via the **MLM merging** scheme [149], thus avoiding double counting. Extension to NLO requires that we use MADSPIN [150] to specify the decays of the heavy bosons and retain spin information at tree-level accuracy. The parton showering itself is implemented within the framework using PYTHIA8 [151, 152]. The output of this complex framework of interfaced tools is a High Energy Physics Monte Carlo (HEPMC) file, which stores information about the showered events.

The event information is read into an analysis script, which implements the various demands and selection cuts required to best isolate the desired signal. In our study, this includes triggering, lepton isolation and **jet algorithms** (implemented within FASTJET [153]). Events surviving the desired criteria are stored in a ROOT file for further analysis.

It has been shown in Ref. [101] that a multivariate analysis (MVA) is more effective for our purposes than a simple cut-and-count analysis. We use the TMVA [154] package within the ROOT framework to perform a **BDT** analysis. The BDT training non-linearly selects optimal cuts for various input parameters, in order to best separate background and signal. During the analysis, we use 50% of the samples for training and always ensure that there is no overtraining by requiring that the **Kolmogorov-Smirnov statistic** is at least $\mathcal{O}(0.1)$ [155]. After applying the BDT classification, we obtain our final ROOT file, which now contains MVA information.

This file is the input for the method of moments analysis, which is described in Section 3.4 and used to obtain bounds in Section 3.6.

We now focus on the specifics of applying the above workflow to our two channels of interest: $pp \to Zh$ and $pp \to W^{\pm}h$, with the Higgs decaying to a pair of *b*-quarks and the Z/W decaying leptonically. In other words, for the Zh (Wh) process, we study the $\ell^+\ell^- b\bar{b}$ ($\ell\nu b\bar{b}$) final states, where $\ell = e, \mu, \tau$. The $q\bar{q} \to Zh$ and $q\bar{q}' \to W^{\pm}h$ processes are generated at NLO QCD, whereas the $gg \to Zh$ channel is generated at LO (which is at one loop). The following analyses are performed at 14 TeV centre-of-mass energy and the predictions are shown for the High Luminosity Large Hadron Collider (HL-LHC) projected integrated luminosity of 3 ab^{-1}.

3.5.2   The *Zh* channel

First we outline the generations of the signal and background samples for the $pp \to Zh \to b\bar{b}\ell^+\ell^-$ analysis. While generating the signal samples, *i.e.* $q\bar{q} \to Zh$, we use the aforementioned NLO model file and interface it with PYTHIA8. We choose dynamic renormalisation and factorisation scales, $\mu_F = \mu_R = m_{Zh}$. We choose NNPDF2.3@NLO as our parton distribution function (PDF) for the NLO signal samples. As mentioned above, for the NLO signal samples we use MADSPIN [150] to decay the heavy bosons. This step is done at LO and hence we correct for the branching ratios following the Higgs working group recommendations.

In generating the background samples we follow Refs. [1, 101]. All background samples are generated at LO with NNPDF2.3@LO as the PDF. The dominant backgrounds are the $Zb\bar{b}$ and the irreducible SM Zh production. For the $Zb\bar{b}$ production, we consider the tree-level mode as well as the $gg \to ZZ$ mode at one-loop. Furthermore, we consider reducible backgrounds like $Z+$ jets where the light jets are misidentified as *b*-tagged jets (*c*-jet misidentification is not considered separately), and the fully-leptonic decay of $t\bar{t}$. An example Feynman diagram for each of these signal and background processes is shown in Figs. 3.5a to 3.5d.

Our signal process involves the decay of a Higgs boson to a $b\bar{b}$ pair, which will become jets. Rather than performing a standard resolved analysis, where one would consider two separate narrow *b*-tagged jets, here we require a fat jet with its jet parameter $R = 1.2$. We utilise a modified[1] version of the **BDRS algorithm** [52] in order to maximise sensitivity. This procedure helps us in maximising the signal by retaining extra radiations and in discriminating electroweak-scale resonant signals from strong

---

[1]Our slight modification is the use of the filtered cone radius $R_{\text{filt}} = \max(0.2, R_{b\bar{b}}/2)$ rather than the standard $R_{\text{filt}} = \min(0.3, R_{b\bar{b}}/2)$ used in the original paper [52]. This modification was shown to be effective in Refs. [156, 157].
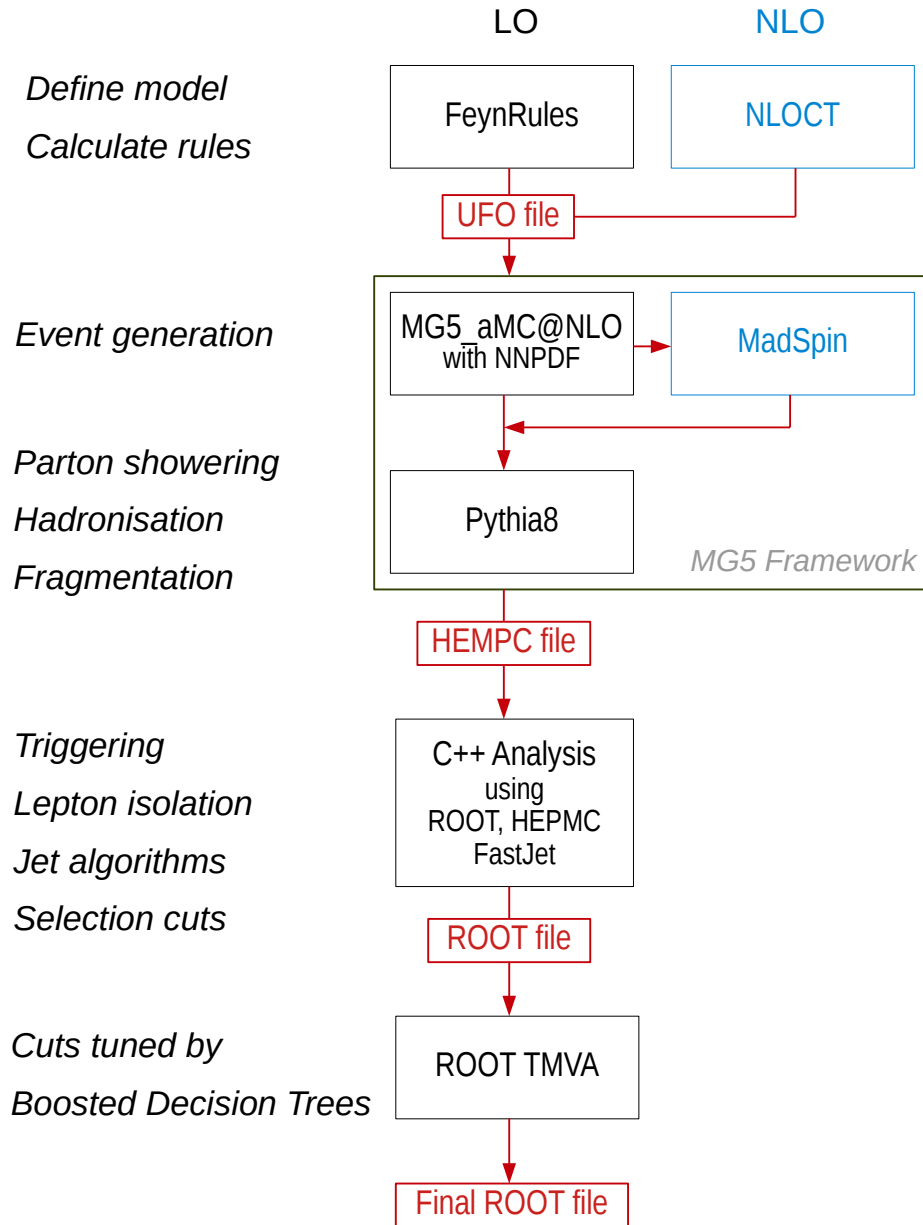
Figure 3.4: *A basic outline of the workflow for creating our samples, including the packages used and their role in the process, as summarised in the text. Blue boxes indicate packages and parts of the process that are only necessary when working at next-to-leading order (NLO). Red boxes indicate input and output files for the various processes. For a brief description of each of these technologies, see Appendix A.2.*

(a) The signal: $pp \rightarrow Zh \rightarrow b\bar{b}\ell^+\ell^-$

(b) $pp \rightarrow Zb\bar{b}$

(c) $gg \rightarrow ZZ$ (one loop)

(d) $gg \rightarrow Zh$ (one loop)
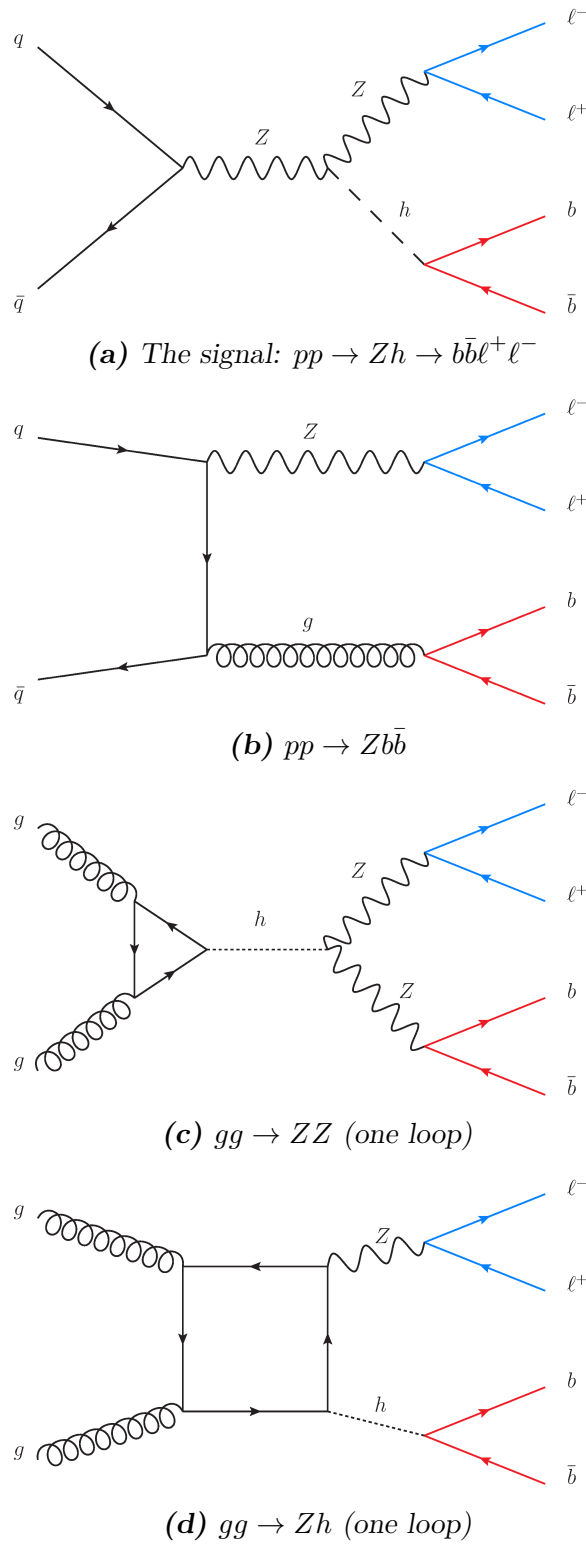
Figure 3.5: *Example Feynman diagrams for each of the signal and background processes considered for the Zh channel (see Section 3.5.2). In each diagram the possible isolated leptons are coloured in blue and the possible b-jet activity is in red. Note that the leading contributions for $gg \rightarrow ZZ$ and $gg \rightarrow Zh$, in (c) and (d) respectively, are from one-loop diagrams. The Z+jets process has essentially the same diagrams as the $Zb\bar{b}$ process in (b), but with, for example, c quarks instead of b quarks, which are later misidentified as b quarks.*

QCD backgrounds, see also [156, 157]. As with the other techniques mentioned, see Appendix A.2 for more details. Finally, we require the hardest-two-filtered subjets to be b-tagged with tagging efficiencies of 70%. Moreover, the misidentification rate of light subjets faking as b-subjets is taken as 2%.

One of our goals is to look for new physics effects in high-energy bins. It is therefore imperative to generate the signal and background samples with certain generation-level cuts in order to improve statistics:

- For the $q\bar{q} \rightarrow Zh$ samples generated at NLO, we require a cut on the p_T of the Higgs boson, $p_{T,h} > 150$ GeV.

- The $Zb\bar{b}$ and $t\bar{t}$ samples are generated with the following cuts: $p_{T,(j,b)} > 15$ GeV, $p_{T,\ell} > 5$ GeV, $|y_j| < 4$, $|y_{b/\ell}| < 3$, $\Delta R_{b\bar{b}/bj/b\ell} > 0.2$ [1], $\Delta R_{\ell\ell} > 0.15$, 70 GeV $< m_{\ell\ell} < 110$ GeV, 75 GeV $< m_{b\bar{b}} < 155$ GeV and $p_{T,\ell\ell} > 150$ GeV. The $Zb\bar{b}$ sample is generated upon merging with an additional matrix element (ME) parton via the **MLM merging** scheme [149].

- For the $Z+$ jets samples, we do not impose any invariant mass cuts in the jets. Furthermore, the sample is merged with three additional partons.

Since the backgrounds are generated at LO, we use flat K-factors to bring them at a similar footing to the signal. For the tree-level $Zb\bar{b}$, one-loop $gg \rightarrow ZZ$, one-loop $gg \rightarrow Zh$ and $Z+$ jets, we respectively use K-factor values of 1.4 (computed within MG5_AMC@NLO), 1.8 [158], 2 [159] and 1.13, computed within MCFM [160–162].

As mentioned earlier, we opt for a multivariate analysis over a simple cut-based analysis. Thus, in this work we do not revisit the cut-and-count analysis and delve directly into the multivariate formulation. In preparation for the BDT optimization, we begin with some basic requirements and cuts:

1. We start by constructing fatjets with cone radii of $R = 1.2$. Furthermore, we require these fatjets to have $p_T > 80$ GeV and to lie within a rapidity, $|y| < 2.5$. We employ FASTJET [153] in constructing the jets.

2. We then isolate the leptons (e, μ) upon demanding that the total hadronic activity deposited around a cone radius of $R = 0.3$ can at most be 10% of its transverse momentum. The leptons are also required to have $p_T > 20$ GeV and have rapidity, $|y| < 2.5$. In our setup, every non-isolated object is considered to be part of the fatjet construction. Before performing the multivariate analysis,

---

[1]Recall that $\Delta R = \sqrt{(\Delta\phi)^2 + (\Delta y)^2}$, where $\Delta\phi$ and Δy are respectively the separation in azimuthal angle and rapidities of the two objects.

we require each event to have exactly two oppositely charged same flavour (OSSF) isolated leptons.

3. We apply loose cuts on certain kinematic variables. We require the invariant mass of the leptons to be in the range 70 GeV $< m_{\ell\ell} <$ 110 GeV, the transverse momentum of the di-lepton system, $p_{T,\ell\ell} > 160$ GeV. We also require $\Delta R_{\ell\ell} > 0.2$, $p_{T,\text{fatjet}} > 60$ GeV, the reconstructed Higgs mass, 95 GeV $< m_h < 155$ GeV, $\Delta R_{b_i,\ell_j} > 0.4$ ($i = 1, 2$) and $\not{E}_T < 30$ GeV. We also require that there is at least one fat jet with at least two B-meson tracks, there are exactly two mass-drop subjets and at least three filtered subjets. We also require that the hardest two filtered subjets are b-tagged.

Owing to the smallness of the $Z+$ jets and $t\bar{t}$ backgrounds compared to $Zb\bar{b}$, we train our **boosted decision tree (BDT)** upon only considering the NLO Zh and the tree-level $Zb\bar{b}$ samples. We use the following variables to train the BDT:

- p_T of both isolated leptons.

- ΔR between the b-subjets and the isolated leptons (four combinations), between the isolated leptons and also between the two b-subjets in the fatjet.

- The reconstructed dilepton mass and its p_T.

- The $\Delta\phi$ separation between the fatjet and the reconstructed dilepton system.

- The missing transverse energy, $\not{E}_T$.

- The mass of the Higgs fatjet and its transverse momentum.

- p_T of the two b-tagged filtered subjets and the ratio of the p_T of these b-tagged subjets.

- The rapidity of the reconstructed Higgs fatjet.

During our training process, we do not require variables that are 100% correlated but retain every other variable. Given that one of our final variables of interest is the reconstructed Zh invariant mass, we refrain from using it as an input variable.

For the BDT analysis, we use 50% of the samples for training and always ensure that there is no overtraining by requiring that the **Kolmogorov-Smirnov statistic** is at least $\mathcal{O}(0.1)$ [155]. After optimising the cut on the BDT variable, one finds that there are around 463 $q\bar{q} \to Zh$ (SM) and 820 $Zb\bar{b}$ events at 3 ab^{-1}, which amounts to the SM $qq \to Zh$ (SM) over rest of the background (B) ratio, $SM/B \sim 0.56$. Using the same training, we have respectively 44, 7 and 57 $Z+$ jets, $gg \to ZZ$ and $gg \to Zb\bar{b}$ background events after the BDT cut. This yields $SM/B \sim 0.5$.

3.5.3   The Wh channel

For the $W^{\pm}h \rightarrow b\bar{b}\ell\nu$ analysis, we follow a very similar methodology as before. The dominant backgrounds are the irreducible SM $W^{\pm}h$ and the reducible $W^{\pm}b\bar{b}$ channels. We also consider the fully and semi-leptonic $t\bar{t}$ events, $W^{\pm}+$ jets and $Z+$ jets, where $Z \rightarrow \ell^+\ell^-$. An example Feynman diagram for each of these processes is shown in Figs. 3.6a to 3.6c.

The $W^{\pm}$ samples, like the Z samples, are generated at NLO QCD. We use the same PDF choice as for the Zh samples and the scales are chosen to be $\mu_F = \mu_R = m_{Wh}$. The backgrounds are generated with the same PDF choice at LO. The scales chosen for the background generation are m_W for the $Wb\bar{b}$ and $W+$ jets samples and $2m_t$ for the $t\bar{t}$ samples.

The $W^{\pm}b\bar{b}$ samples are generated upon merging with an additional parton as described above. Unlike the Zh channel, the $W^{\pm}h$ channel only has quark-initiated production modes. For the Zh channel, it was quite simple to reduce the $t\bar{t}$ background by imposing a lower cut on $\not{E}_T$. For the $W^{\pm}$ study, the signal itself contains a final state with a neutrino and hence demanding a cut on $\not{E}_T$ will not only reduce the $t\bar{t}$ backgrounds but also a significant fraction of the signal.

As in the Zh case, we impose some generation-level cuts:

- The signal samples are generated with $p_{T,h} > 150$ GeV and the invariant mass of the Wh system, $m_{Wh} > 500$ GeV to improve statistics in the high-energy bins.

- The background samples are generated with: $p_{T,(j,b)} > 15$ GeV, $p_{T,\ell} > 5$ GeV, $|y_{b/\ell}| < 3$, $|y_j| < 5$, $\Delta R_{b\bar{b}} > 0.1$, $\Delta R_{b\ell} > 0.2$ and 70 GeV $m_{b\bar{b}} < 155$ GeV. The $W^{\pm}b\bar{b}$ samples are generated upon merging with an additional parton, whereas the $W^{\pm}+$jets samples are merged with up to two additional partons.

For the tree-level $W^+b\bar{b}$, $W^-b\bar{b}$, $t\bar{t}$, W^++jets, W^-+jets and $Z+$ jets, we respectively use K-factor values of 2.68, 2.49, 1.35, 1.23, 1.18 and 1.13, computed within MCFM [160–162].

We separate the Wh analysis into two parts depending on the charge of the isolated lepton. For the analysis, we require one isolated charged lepton. In contrast to the Zh analysis, the $W^{\pm}h$ has a known ambiguity in the form of the p_z component of the neutrino momentum. We deal with this by requiring that the invariant mass of the neutrino and the isolated lepton peaks around the W-boson mass. This gives us two solutions to $p_{z,\nu}$ and we demand that the solutions are always real. We discard

(a) *The signal:* $W^{\pm}h \to b\bar{b}\ell\nu$

(b) $pp \to W^{\pm}b\bar{b}$

(c) $pp \to t\bar{t}$ *semi-leptonic (fully leptonic)*
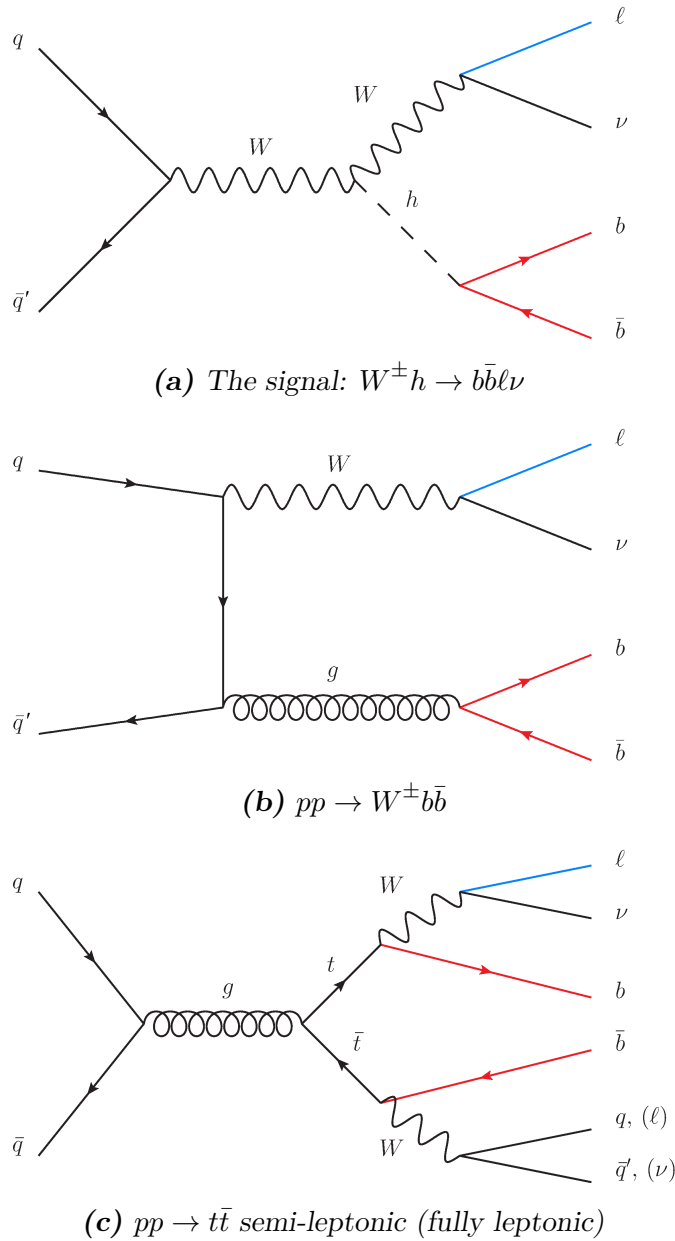
Figure 3.6: *Example Feynman diagrams for each of the signal and background processes considered for the Wh channel (see Section 3.5.3). In each, the vertex $W^{+} \to \ell^{+}\nu$ ($W^{-} \to \ell^{-}\bar{\nu}$) is generically labelled as $W \to \ell\nu$ to cover both cases. In each diagram a possible isolated lepton is coloured in blue and the possible b-jet activity is in red. The $W+$jets process has essentially the same diagrams as the $Wb\bar{b}$ process in (b) but with, for example, c quarks instead of b quarks, which are later misidentified as b quarks. The $Z+$jets process has essentially the same diagrams as the $Zb\bar{b}$ process in Fig. 3.5b but with, for example, c quarks instead of b quarks, which are later misidentified as b quarks; it also must have one missed lepton to match the desired signature for the Wh channel, as must the fully-leptonic $t\bar{t}$ process in (c).*

events where complex solutions are encountered. We construct two invariant masses for the Wh system for the two neutrino p_z solutions, $m_{\text{fatjet}\ell\nu_{1,2}}$.

Before implementing the BDT analysis, as in the Zh case, we make some basic demands and cuts. As before we have a number of fatjets/subjets requirements and search for isolation leptons. We apply the loose cuts: $p_{T,\text{fatjet}} > 150$ GeV, 95 GeV $< m_h < 155$ GeV, $m_{\text{fatjet}\ell\nu_{1,2}} > 500$ GeV and $\Delta R_{b_i,\ell} > 0.4$.

For the BDT analyses (one for W^+h and another for W^-h), we train the samples upon considering the SM Wh sample as the signal and the $Wb\bar{b}$, semi-leptonic and fully-leptonic $t\bar{t}$ samples as backgrounds. Owing to multiple backgrounds, we impose relative weight factors to these backgrounds which are defined as $1/\mathcal{L}_{\text{gen}}$, where $\mathcal{L}_{\text{gen}}$ is the generated luminosity that depends on the production cross-section, including the K-factors, and the number of Monte Carlo generated events. Besides, NLO samples also contain negative weights for certain events, which we include while training the BDT samples. We also find that the effect of including the weight factor in our training is small, owing to the very small number of signal events having negative weights (less than 4% percent).

We optimise the BDT analysis for W^+h (W^-h) and find 1326 (901) events for the signal and 4473 (3476) $W^+b\bar{b}$ ($W^-b\bar{b}$) events at 3 ab^{-1}. The number of surviving events for $t\bar{t}$, $W+$ jets and $Z+$ jets are much smaller. Ultimately, we find $SM/B \sim$ 0.28 (0.24) for W^+h (W^-h).

3.6   Analysis and results

In this section we describe how we obtain our final sensitivity estimates and present our main results. We consider only the interference contribution in this study, which in any case is expected to be dominant piece below the EFT cut-off. There is no conceptual hurdle in also including the squared terms, as Eq. 3.3.5 is still equally valid; the reasons for their omission are purely practical. We first consider the contact terms, g_{Vf}^h, which can be very precisely constrained in the high-energy bins due to their quadratic growth relative to the SM terms. Once these couplings are very precisely constrained, we will turn to the lower-energy bins, where there are a sufficient number of events to carry out an angular moment analysis to constrain the other couplings. All the results presented in this section are for an integrated luminosity of 3 ab^{-1}.

3.6.1 Bounds on contact terms

As already discussed, at high energies the EFT deviations are dominated by the contribution of the contact interactions, g^h_{Vf}, to a_{LL}. Since this contribution grows quadratically with energy relative to the SM Vh contribution, it can be very-precisely constrained by probing high-energy bins. Unfortunately, some of the bins providing maximum sensitivity have too few events for an angular moment analysis. We thus constrain these couplings simply using the final state invariant mass distribution. Following Ref. [101], where this procedure was carried out for the Zh mode, we construct a bin-by-bin χ^2 function; the SM events are used as the expected number and the SMEFT events are used as the observed number. To ensure that we do not violate EFT validity, we neglect any event with a final-state invariant mass above the cut-off. The cut-off is evaluated for a given value of the anomalous couplings, by setting the Wilson coefficients in Eq. 3.2.2 to unity[1]. For an integrated luminosity of 3 ab^{-1}, we obtain the sub-per-mille level bounds at the one sigma level,

$$
\begin{aligned}
|g^h_{WQ}| &< 6 \times 10^{-4}, \\
|g^h_{Z\mathbf{P}}| &< 4 \times 10^{-4}.
\end{aligned}
\tag{3.6.1}
$$

3.6.2 Angular moment analysis

Now that g^h_{WQ} and $g^h_{Z\mathbf{P}}$ are strongly constrained from the higher energy-bins, we turn to the lower-energy bins with enough events to perform an angular moment analysis to constrain the other couplings. Ideally, we should also marginalise over the effect of contact terms in the lower bins. However, as we will see, the expected bounds on the contact terms are almost two orders of magnitude smaller than that of the other couplings, and thus their effect is negligible in the lower-energy bins. We will therefore ignore them in further analysis. We first split our simulated events into 200 GeV bins of the final-state invariant mass. To obtain the angular moments, we first convolute the events in each energy bin with the weight functions using Eq. 3.4.14. Given that the CP-even and odd couplings contribute to a mutually-exclusive set of angular moments, we construct two separate bin-by-bin χ^2 functions as follows,

$$
\begin{aligned}
\chi^2(\delta \hat{g}^h_{VV}, \kappa^{\mathbf{P}}_{VV}) &= \sum_{ij} \frac{\left(\alpha^{EFT}_i(M_j) - \alpha^{SM}_i(M_j)\right)^2}{(\Sigma_i(M_j))^2}, \\
\tilde{\chi}^2(\tilde{\kappa}^{\mathbf{P}}_{VV}) &= \sum_{ij} \frac{\left(\tilde{\alpha}^{EFT}_i(M_j) - \tilde{\alpha}^{SM}_i(M_j)\right)^2}{(\Sigma_i(M_j))^2},
\end{aligned}
\tag{3.6.2}
$$

---

[1]The resultant cut off is usually significantly larger than our invariant mass values and therefore largely irrelevant.

where $\kappa_{VV}^{\mathbf{P}}, \tilde{\kappa}_{VV}^{\mathbf{P}}$ are the same as $\kappa_{WW}, \tilde{\kappa}_{WW}$ for $V = W^{\pm}$ and defined in Eq. 3.3.8 for $V = Z$. In the above equation, we include only the CP-even (CP-odd) angular moments in χ^2 ($\tilde{\chi}^2$); the index i indicates the different moments and M_j labels the invariant-mass bins. The squared error in the denominator is computed using Eq. 3.4.17 on the background sample (which includes the SM Vh contribution), where $\hat{N}$ in this case is the total number of background events in the j-th bin.

Once again, the contributions due to $\kappa_{VV}^{\mathbf{P}}$ and $\tilde{\kappa}_{VV}^{\mathbf{P}}$ grow with energy and one must be careful about EFT validity. For a given value of the coupling we estimate the cut-off Λ using Eq. 3.2.2 with all the Wilson coefficients set to unity. We ignore any event that has final-state invariant mass above 1500 GeV, a value smaller than the cut-off corresponding to the size of the couplings we will eventually constrain. The most sensitive bins for the analysis of the contact term, on the other hand, are bins higher than 1500 GeV. The contribution due to $\hat{g}_{VV}^h$ does not grow with energy with respect to the SM and thus the bounds on this coupling are dominated by contributions from the lowest-energy bins in our analysis.

We now discuss the results for the Zh and $W^{\pm}h$ modes separately, before presenting our combined bounds. The individual bounds are important as they do not assume Eq. 3.2.7, which has been derived assuming that electroweak symmetry is linearly realised. In fact, the independent measurement of couplings involving the Z and W can be used to verify Eq. 3.2.7 as a prediction of linearly-realised electroweak symmetry.

As a final note, the calculations used to obtain our results use the rescaled moments, α_i, defined in Eq. 3.4.14 and used in Eq. 3.6.2. These are simply proportional to the unscaled set $\{\hat{a}'_{LL}, a^1_{TT}, \hat{a}^{2'}_{TT}, a^1_{LT}, a^2_{LT}, \tilde{a}^1_{LT}, \tilde{a}^2_{LT}, a_{TT'}, \tilde{a}_{TT'}\}$. In the remaining sections we use the unscaled names to make referencing tables, checking parametric dependencies and understanding helicity origins easier. These properties are, of course, unchanged by the rescaling.

The Zh mode

Following the discussion in Section 3.3.2, for the CP-even case we include the moments proportional to $\hat{a}'_1, \hat{a}'_3, a^2_{LT}$ and $a_{TT'}$ in our χ^2 (see Eq. 3.6.2). Recall that $\hat{a}'_1$ and $\hat{a}'_3$ are integrated linear combinations of the original angular moments a_{LL} and a^2_{TT} defined in Section 3.4.2. The bound obtained for the two CP-even couplings is shown in Fig. 3.7a. To show the power of our method we show the progression of the bounds obtained as the differential information used is gradually increased. The bound obtained, if one uses only the total rate to constrain a linear combination of the two couplings, $\delta\hat{g}_{ZZ}^h$ and $\kappa_{ZZ}^{\mathbf{P}}$, is shown by the two dashed lines. Next, we include

(a)

(b)
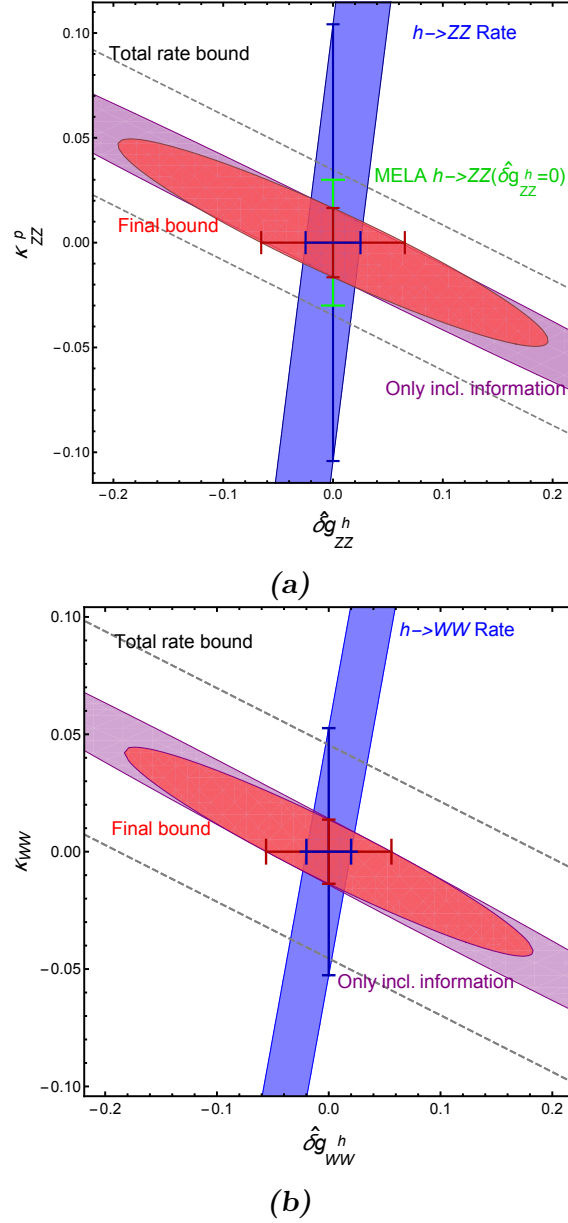
Figure 3.7: (a) Bounds at 65% CL on the CP-even anomalous coup-
lings from Zh production with 3 ab^{-1} integrated luminos-
ity, assuming that the contact term has been very precisely
constrained (see Eq. 3.6.1). We show the improvement of
the bounds as more and more differential information is
included in the fit. The dashed lines show the bound just
from the total rate. The purple region includes differential
information at the level of the Z-boson four momentum,
such as the final-state invariant mass distribution and Θ-
distribution. Finally, the red region includes information
from all the angular moments, including the cross-helicity
interference terms. The blue band shows the bound from
the $h \rightarrow ZZ \rightarrow 4l$ rate, using the results of Ref. [49].
The bars show the bounds on one of the couplings when
the other coupling is 0. The green bar shows the bound
obtained using the Matrix Element Likelihood Analysis
(MELA) in Ref. [163] and assuming $\delta\hat{g}^h_{ZZ} = 0$. (b) Same
as in (a) but for the $W^{\pm}h$ mode where there is no bound
from MELA.

distributions of the final-state invariant mass and other differential information at the level of the Z-boson four momentum (i.e. the decay products of the Z-boson are treated inclusively)[1] and obtain the excluded region shown in purple. The analysis at this stage is comparable to a regular SMEFT analysis that includes a few standard differential distributions. Finally, we include the effects of the angular moments a_{LT}^2 and $a_{TT'}$, and obtain our final bound shown in red. The main improvement in sensitivity in the final bounds comes from a_{LT}^2, the effect of which can be captured only by a careful study of the joint $(\Theta, \theta, \varphi)$ distribution, as pointed out in Ref. [1]. While this is clearly something beyond the scope of a regular cut-based analysis, as one would need to take into account all the correlations of the final-state phase space, the angular moment approach captures it effortlessly.

We show also the projected bounds from the $h \rightarrow ZZ \rightarrow 4l$ process in Fig. 3.7a. The blue band shows the bound from the $h \rightarrow ZZ \rightarrow 4l$ rate, whereas the green bar is the bound obtained using the Matrix Element Likelihood Analysis (MELA) framework [163]. As far as $\kappa_{ZZ}^{\mathbf{p}}$ is concerned, we see that the bound obtained from Zh production using our methods surpass the other existing projections shown in Fig. 3.7a [2]. In the horizontal direction, our bounds might seem redundant once the $h \rightarrow ZZ \rightarrow 4l$ process is taken into account. However, if one allows for hbb coupling deviations our bounds become the measurement of a truly independent effect (see Eq. 3.3.10).

The CP-odd coupling, $\tilde{\kappa}_{ZZ}^{\mathbf{p}}$, is constrained using the function $\tilde{\chi}^2$ in Eq. 3.6.2, which includes the moments $\tilde{a}_{LT}^1$ and $\tilde{a}_{TT'}$. We obtain the one-sigma-level bound,

$$|\tilde{\kappa}_{ZZ}^{\mathbf{p}}| < 0.03. \tag{3.6.3}$$

The $W^{\pm}h$ mode

As discussed in Section 3.3.3, the relevant angular moments for this mode in the CP-even case are a_{LL}, a_{TT}^2 and $a_{TT'}$. Instead of the first two moments, we use the linear combination $\hat{a}_1'$ and $\hat{a}_3'$ described in Section 3.4.2. Again, we show the progression of the bounds at different stages of inclusion of differential information. The dashed lines show bounds from the total rate and the purple region shows the bound obtained

---

[1]For this bound, we include only the angular moments $\hat{a}_1$ and $\hat{a}_3$ (i.e. the rotated a_{LL} and a_{TT}^2), extracted using the weights in Section 3.4.1, as these are the only moments that survive integration over θ and φ. These two angles are inaccessible if the decay products of the Z-boson are treated inclusively.

[2]A bound using the matrix element method for $pp \rightarrow Zh$ may potentially match our bounds but the results in Ref. [163] are unfortunately not comparable to ours as these studies include high-energy phase space regions, where the EFT contribution is many times that of the SM. Therefore, the methodology used to obtain these bounds violates our assumption of $\mathcal{O}(1)$ Wilson coefficients.

by including only the angular moments, a_{LL} and a_{TT}^2, that encapsulate the differential information at the level of the Z boson, treating its decay products inclusively. Our final bound, also including the effect of a_{LT}^1 and $a_{TT'}$, is shown in red. We show also the projected bounds from the $h \to WW \to 2l2\nu$ decay rate in blue, to which our bounds are complementary (recall again that, what our bounds actually probe is a linear combination also involving $hb\bar{b}$ coupling deviations, see Eq. 3.3.10). In this case there is no competing bound on κ_{WW} from the $h \to WW$ mode, presumably because the neutrinos in the final state make much of the differential information inaccessible in this case. Our bound on κ_{WW} from the $pp \to W^\pm h$ process is therefore likely to be the best possible bound on this coupling.

Again, the CP odd coupling, $\tilde{\kappa}_{WW}$, is constrained by including the moment $\tilde{a}_{LT1}$ in the function $\tilde{\chi}^2$ in Eq. 3.6.2. We obtain the one-sigma-level bound,

$$|\tilde{\kappa}_{WW}| < 0.04. \tag{3.6.4}$$

We see that we obtain bounds of similar size from the $pp \to Wh$ and $pp \to Zh$ processes on the respective anomalous couplings. The fact that the couplings can be independently measured is very important, as we can then use these measurements to test the correlations in Eq. 3.2.7, which in turn tests whether or not electroweak symmetry is linearly realised. An alternative approach would be to use the correlations to combine the bounds from Wh and Zh production as we show in the next subsection.

Combination of Zh and Wh modes

In Fig. 3.8, we show the bounds obtained after combining the results using the correlations in Eq. 3.2.7, thus assuming electroweak symmetry is linearly realised. Again, we show the bounds obtained at various levels of inclusion of differential data. The dashed lines show the bound just from the total rate, the purple region includes differential information at the level of the Z/W-boson four momentum and the red region is our final bound including all angular moments. The blue band shows the bound from a combination of the $h \to WW \to 2l2\nu$ and $h \to ZZ \to 4l$ rates. The green bar shows the MELA bound from Ref. [163] on κ_{ZZ}, assuming $\delta\hat{g}_{ZZ}^h = 0$, translated to this plane.

Comparison with bounds from WZ and WW production

If electroweak symmetry is linearly realised, bounds on κ_{WW} and g_{WQ}^h can also be extracted from double gauge boson production using Eqs. 3.2.11 and 3.2.12. For
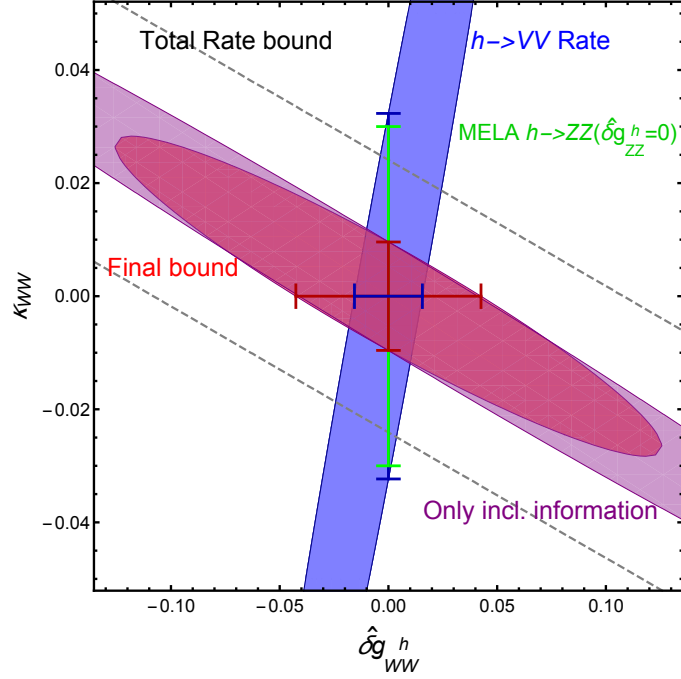
Figure 3.8: *Bounds at 65% CL on the CP-even anomalous couplings, with 3 ab^{-1} integrated luminosity, after combining results from Zh and Wh production using Eq. 3.2.7 and assuming that the contact terms have been very-precisely constrained (see Eq. 3.6.1). Again, we show the progression of the bounds as more and more differential information is included in the fit. The dashed lines show the bound just from the total rate in both processes. The purple region includes differential information at the level of the Z/W-boson four momentum. The red region is our final bound and includes information from all the angular moments. The blue band shows the bound from a combination of the $h \rightarrow WW \rightarrow 2l2\nu$ and $h \rightarrow ZZ \rightarrow 4l$ rates. The bars show the bounds on one of the couplings when the other coupling is 0. The green bar shows the bound implied by the bound on κ_{ZZ}, using the Matrix Element Likelihood Analysis (MELA) in Ref. [163] and assuming $\delta \hat{g}_{ZZ}^h = 0$.*

instance, WZ production at high energies constrains precisely the linear combination of Z-pole couplings and TGCs that appears in the right-hand side of Eq. 3.2.11 at the sub-per-mille level [136]. This bound is of the same size as the one obtained in Eq. 3.6.1 in this work. Combining the two bounds will thus yield a significantly-improved bound compared to each individual bound. This is also true for Eq. 3.2.12, where the least-constrained coupling in the right-hand side, $\delta\kappa_\gamma$, can be bounded at the level of a few percent in WW production [164]. This is comparable to our bound on κ_{WW} in Figs. 3.7b and 3.8 once we marginalise over $\delta\hat{g}_{WW}^h$. This last statement uses the fact that the Z couplings to quarks appearing in the right-hand side of Eq. 3.2.12, which also affect WW production, are measured more precisely at the per-mille level [132].

Alternatively, the fact that the left and right hand sides of Eqs. 3.2.11 and 3.2.12 can be measured with similar precision, in double gauge boson and Higgs-strahlung processes, means that one can actually verify Eq. 3.2.11 as a test of linearly-realised electroweak symmetry at the HL-LHC.

3.6.3   Summary

The precise measurement of Higgs boson properties will be one of the legacies of the LHC's scientific achievements. Potential deformations of the Higgs boson's couplings to other particles compared to Standard Model predictions can be cast into limits on Wilson coefficients of effective operators originating in the SMEFT framework. To obtain predictive limits on the highly-complex system of SMEFT operators, it is necessary to measure Higgs interactions in various production and decay channels. Studying the Higgs boson's couplings to massive gauge bosons, i.e. the W and Z bosons, is key in establishing the nature of its embedding in the scalar sector.

We proposed a novel method to probe the full structure of the Higgs-gauge boson interactions in Higgs-associated production. Using the helicity-amplitude formalism and expanding the squared matrix elements into angular moments, the whole process can be expressed in terms of nine trigonometric functions. This is true not only in the SM but also in the D6 SMEFT. Extracting the coefficients of these functions, the so-called angular moments, is a powerful and predictive way of encapsulating the full differential information of this process. Since differential information can encode signatures of EFT operators in subtle ways, maximally mining the differential information is essential to obtain the best possible bounds on the EFT operators. The actual interpretation of the measurement relies now on a shape analysis of a small number of trigonometric functions. Strong constraints can be obtained, provided experiments publicise measurements of these functions. We therefore encourage

the experimental collaborations to provide such measurements for various Higgs production processes[1].

The success of this method relies on whether the theoretical form of the original angular distribution can be preserved despite effects like experimental cuts, showering and hadronisation. In this study, we carried out a detailed collider simulation of the Higgs-strahlung process, including these effects, before applying the method of angular moments. The results we find are encouraging, indicating that a shape analysis using the trigonometric basis functions can set the most sensitive limits on effective operators within the SMEFT framework. While the high-energy behaviour of the process results in the strongest possible bounds on the $hVff$ contact terms (see Eq. 3.6.1), the full angular moment analysis leads to the strongest reported bounds on the $hV_{\mu\nu}V^{\mu\nu}$ (see Figs. 3.7a, 3.7b and 3.8) and $hV_{\mu\nu}\tilde{V}^{\mu\nu}$ (see Eqs. 3.6.3 and 3.6.4) terms.

There are plans to extend this method to various other Higgs/electroweak production and decay processes such as weak boson fusion, the $h \to ZZ \to 4\ell$ decay and diboson production. One can then perform a full global fit including this enlarged set of observables to obtain the best possible bounds on the SMEFT Lagrangian.

---

[1]The provision of measurements of the moments and basis functions will allow for an ideal approach to perform hypothesis testing for effective operators. As such it will improve on current initiatives of using so-called simplified cross section measurements [165] in global fits.

Part II

The Higgs at High Energies

Chapter 4

Multiparticle Production

We now move away from collider phenomenology to more formal calculations regarding the behaviour of interacting massive scalar bosons, such as the Standard Model Higgs boson, at high energies. In this context, 'high energies' refers to energies higher than those currently probable by experiments. While Part I focused on perturbative interactions of the Higgs with other SM particles, Part II (Chapters 4 to 6) focuses on the non-perturbative effects we might expect due to the Higgs' self-interacting potential.

4.1 Introduction

There is a renewed interest among particle theorists in re-examining our understanding of basic predictions of quantum field theory in the regime where production of a very large number of elementary massive bosons becomes energetically possible. Specifically, in quantum field theoretical models with microscopic massive scalar fields at weak coupling, $\lambda \ll 1$, the regime of interest is characterised by $few \to many$ particle production processes,

$$X \to n \times \phi \,, \tag{4.1.1}$$

at ultra-high centre of mass energies $\sqrt{s} \gg m$. In these reactions, X is the initial state with a small particle number, generally 1 or 2, and the final state is a multiparticle state with $n \propto \sqrt{s}/m \gg 1$ Higgs-like neutral massive scalar particles. For the initial states X being the 2-particle states, the processes in Eq. 4.1.1 correspond to a particle collision.

If X is a single particle state $|1^*\rangle$ with the virtuality $p^2 = s$, Eq. 4.1.1 describes its decay into n-particle final states. The authors of [43] conjectured that the partial

width of X to decay into n relatively soft elementary Higgs-like scalars can become exponentially large above a certain energy scale $s \gtrsim E_*^2$. This scenario is called Higgsplosion [43]. It allows all super-heavy or highly-virtual states to be destroyed via rapid decays into multiple Higgs bosons[1].

The aim of this part is to provide a comprehensive review of the semiclassical calculation of few $\to n$-particle processes in the limit of ultra-high particle multiplicity, n. The underlying semiclassical formalism was originally developed by Son in Ref. [168], and generalised to the $\lambda n \gg 1$ regime in [169, 170]. We will give a detailed justification of the formalism and its derivation, and show its application to non-perturbative calculations in the weakly-coupled high-multiplicity regime.

Scattering processes at very high energies with $n \gg 1$ particles in the final state were studied in depth in the early literature [171–181], and more recently in [182–184]. These papers largely relied on perturbation theory, which is robust in the regime of relatively low multiplicities, $n \ll 1/\lambda$. However, in the regime of interest for Higgsplosion, $n \gtrsim 1/\lambda \gg 1$, perturbative results for n-particle amplitudes and rates can no longer be trusted. Perturbation theory becomes effectively strongly-coupled in terms of the expansion parameter $\lambda n \gtrsim 1$. This calls for a robust non-perturbative formalism. Semiclassical methods [168, 185, 186] provide a way to achieve this in the large λn regime [169, 170]. It is for this reason that the semiclassical method is at the centre of much of these notes.

We consider a real scalar field $\phi(x)$ in $(d + 1)$-dimensional spacetime, with the Lagrangian,

$$\mathcal{L} = \frac{1}{2}(\partial_\mu \phi)^2 - \frac{1}{2}m^2\phi^2 - \mathcal{L}_{\text{int}}(\phi), \qquad (4.1.2)$$

where $\mathcal{L}_{\text{int}}$ is the interaction term. The two simplest examples are the ϕ^4 model in the unbroken phase, with $\mathcal{L}_{\text{int}} = (\lambda/4)\,\phi^4$, and the model with the spontaneously broken Z_2 symmetry,

$$\mathcal{L} = \frac{1}{2}\,\partial^\mu h\,\partial_\mu h \,-\, \frac{\lambda}{4}\left(h^2 - v^2\right)^2. \qquad (4.1.3)$$

The classical equation for the model in Eq. 4.1.3 is the familiar Euler-Lagrange equation,

$$\partial^\mu \partial_\mu h \,+\, \lambda\,h\,(h^2 - v^2) \,=\, 0\,. \qquad (4.1.4)$$

As in Refs. [43, 170], we are ultimately interested in the scalar sector of the Standard

---

[1]Ref. [166] recently expressed concerns about locality of the Quantum Field Theory in such a scenario. These concerns were largely addressed by Ref. [167], which stresses that quantum fields are defined as operator-valued distributions acting on test functions that are localized in finite regions of space-time. The effects of these test functions is briefly mentioned in Sections 6.1.1 and 6.5.

Model, for which we use a simplified description in terms of the model in Eq. 4.1.3.

We will concentrate on the simplest realisation of Higgsplosion where X is a single-particle state $|1^*\rangle$. In high-energy $2 \to n$ scattering processes, the highly-virtual state 1^* would correspond to the s-channel resonance created by two incoming colliding particles. For example in the gluon fusion process, $gg \to h^* \to n \times h$, the highly-virtual Higgs boson h^* is created by the two initial gluons before decaying into n Higgs bosons in the final state. In this example, the $1^* \to n$ decay rate of interest corresponds to the $h^* \to n \times h$ part of the process. We will not discuss the complete $2 \to n$ scattering in this work[1]. This part focuses on explaining how the semiclassical calculation of the n-particle decay rates works. We consider the method itself and its applications, rather than its potential phenomenological implications. The calculation we present is aimed to develop a theoretical foundation for the phenomenon of Higgsplosion [43].

If Higgsplosion can be realised in the Standard Model, its consequences for particle theory would be quite remarkable. Higgsplosion would result in an exponential suppression of quantum fluctuations beyond the Higgsplosion energy scale and have observable consequences at future high-energy colliders and in cosmology, some of which were discussed in [4,42,187–189]. However, of course, the formalism we review is general and not limited to Higgsplosion nor its applications.

This part consists of three chapters. We begin, in this chapter, by recalling the known results for multiparticle scattering rates via tree-level perturbation theory. In Chapter 5 we move on to summarising the basics of coherent states in quantum mechanics and quantum field theory respectively. The coherent state formalism in quantum field theory (for reviews and some applications see [186, 190–192]) forms much of the foundation for the semiclassical method in question. Its summary helps provide context, familiarity and referenceable results for the method's derivation, which is presented at the start of Chapter 6.

The remainder of Chapter 6 focuses on the application of the method. With the necessary tools reviewed, we begin to calculate the rate for the $1^* \to n$ process semiclassically in Section 6.2. The resulting set-up is ideal for using the thin-wall approach, which we develop in Sections 6.2.1 and 6.2.2. In particular, in Section 6.2.1 we recover tree-level results discussed in Section 4.2 along with the prescription for computing the quantum corrections. These quantum contributions to the multiparticle rate are computed in Section 6.2.2 using thin-walled singular classical

---

[1]In particular, we will not attempt to apply the semiclassical approximation for the initial states that are not point-like, for example contributions to scattering processes dominated by exchanges in the t-channel. This is beyond the scope of this work.

solutions. In Section 6.3 we compare the semiclassical method in quantum field theory that we rely upon and use in this work to Landau and Lifshitz' WKB calculation of quasi-classical matrix elements in quantum mechanics [193], and discuss the similarities and differences between these two methods. In Section 6.4 we consider multiparticle processes in less than four spacetime dimensions and provide a successful test for the semiclassical results. Finally, we present our conclusions in Section 6.5.

4.2   First glance at classical solutions for tree-level amplitudes

In later chapters of this part, we will compute the amplitudes and corresponding probabilistic rates for processes involving multiparticle final states in the large λn limit non-perturbatively using a semiclassical approach with no reference to perturbation theory and without artificially separating the result into tree-level and 'quantum corrections' contributions. Their entire combined contribution should emerge from the unified semiclassical algorithm. Before beginning our review of the semiclassical formalism [168, 169, 186], it is worth setting the scene for its application in this computation. In this introductory section our aim is to recall the known properties of the tree-level amplitudes and their relation with certain classical solutions. We will also discuss the ways to analytically continue such classical solutions by complexifying the time variable in Section 4.2.2.

4.2.1   Classical solutions for tree-level amplitudes

Let us begin with tree-level n-point scattering amplitudes computed on the n-particle mass thresholds. This is the kinematic regime where all n final state particles are produced at rest. These amplitudes for all n are conveniently assembled into a single object – the amplitude generating function – which at tree-level is described by a particular solution of the Euler-Lagrange equations. The classical solution, which provides the generating function of tree-level amplitudes on multi-particle mass thresholds for the model in Eq. 4.1.3, is given by [173],

$$h_0(z_0; t) = v \left(\frac{1 + z_0 \, e^{imt}/(2v)}{1 - z_0 \, e^{imt}/(2v)} \right), \quad m = \sqrt{2\lambda} v \,, \qquad (4.2.1)$$

where z_0 is an auxiliary variable. It is easy to check by direct substitution that the expression in Eq. 4.2.1 satisfies the time-dependent ODE,

$$\partial_t^2 h + \lambda h (h^2 - v^2) = 0 \,, \qquad (4.2.2)$$

for any value of the parameter z_0. Since the expression for $h_0(z_0; t)$ is uniform in space, it automatically satisfies the full Euler-Lagrange equation (Eq. 4.1.4). In fact, the configuration in Eq. 4.2.1 is the unique non-trivial solution of Eq. 4.1.4 with only outgoing waves.

It then follows that all $1^* \to n$ tree-level scattering amplitudes on the n-particle mass thresholds are given by the differentiation of $h_0(z_0; t)$ with respect to z_0,

$$\mathcal{A}_{1 \to n} = \langle n | S h(0) | 0 \rangle = \left(\frac{\partial}{\partial z_0} \right)^n h_0 \bigg|_{z_0 = 0} . \qquad (4.2.3)$$

The classical solution in Eq. 4.2.1 is uniquely specified by requiring that it is a holomorphic function of the complex variable $z(t) = z_0 \, e^{imt}$,

$$h_0(z) = v + 2v \sum_{n=1}^{\infty} \left(\frac{z}{2v} \right)^n , \quad z = z(t) = z_0 \, e^{imt} , \qquad (4.2.4)$$

so that the amplitudes in Eq. 4.2.3 are given by the coefficients of the Taylor expansion in Eq. 4.2.4 with a factor of $n!$ from differentiating n times over z,

$$\mathcal{A}_{1 \to n} = \left(\frac{\partial}{\partial z} \right)^n h_0(z) \bigg|_{z=0} = n! \left(\frac{1}{2v} \right)^{n-1} = n! \left(\frac{\lambda}{2m^2} \right)^{\frac{n-1}{2}} . \qquad (4.2.5)$$

The connection between the classical solution $h_0(z_0; t)$ in Eq. 4.2.1 and the $1 \to n$ tree-level amplitudes in Eq. 4.2.5 is nontrivial, but it can be verified that Eq. 4.2.5 is the correct answer following the elegant formalism pioneered by Brown in Ref. [173], for a recent review see section 2 of Ref. [182]. The approach of [173] focuses on solving classical equations of motion and bypasses the summation over individual Feynman diagrams. In the following sections we will see how these (and also more general solutions describing full quantum processes) emerge from the semiclassical approach of [168] which we shall follow. For now we just note the feature of the tree-level expressions expressions in Eq. 4.2.5 that is of greatest interest to us – the factorial growth of n-particle amplitudes, $\mathcal{A}_n \sim \lambda^{n/2} n!$.

Next, we would like to draw the reader's attention to the fact that the classical solution in Eq. 4.2.4 is complex-valued, in spite of the fact that we are working with the real-valued scalar field theory model in Eq. 4.1.3. The classical solution h_0 that generates tree-level amplitudes via Eq. 4.2.5 does not have to be real. In fact it is manifestly complex and this is a consequence of the fact that this solution will
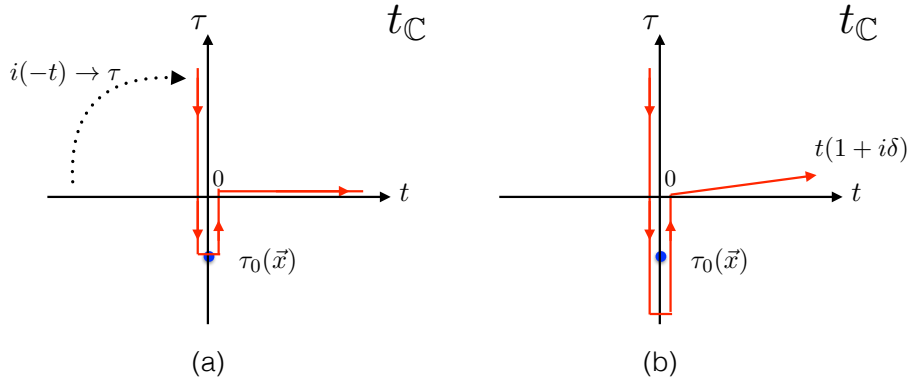
Figure 4.1: *Time evolution contour on the complex time plane $t_{\mathbb{C}}$. Plot (a) shows the contour obtained after deforming the the evolution along the real time axis $-\infty < t < +\infty$ where the early-time ray $-\infty < t < 0$ is rotated by $\pi/2$ into the ray along the vertical axis, $\infty > \tau > \tau_0(\mathbf{x})$ and ending at the singularity surface of the solution $\tau_0(\mathbf{x})$. Plot (b) shows a refinement of this contour: (1) rather than touching the singularity, the contour surrounds it; (2) at late times, the contour approaches $t \to +\infty$ along the ray with an infinitesimally small positive angle δ to the real time axis.*

emerge as an extremum of the action in the path integral using the steepest descent method. In this case, the integration contours in path integrals are deformed to enable them to pass through extrema (or encircle singularities) that are generically complex-valued.

It makes sense however to consider whether one can avoid explicitly deforming the fields as functional integration variables in the functional integral and instead analytically continue the time variable. Such an approach can simplify the calculation if it allows the saddle-point field configuration to be real-valued, even if only for part of its time evolution path. Thus let us consider field configurations that depend on the complexified time $t_{\mathbb{C}}$. We promote the real time variable t into the variable $t_{\mathbb{C}}$ that takes values on the complex time plane,

$$t \longrightarrow t_{\mathbb{C}} = t + i\tau, \tag{4.2.6}$$

where t and τ are real-valued. We will deform the time-evolution contour from the real time axis $-\infty < t < +\infty$ to the contour in the complex $t_{\mathbb{C}}$ plane (depicted in Fig. 4.1) in such a way that the initial time, $t = -\infty$, maps to the imaginary time, $\mathrm{Im}\, t_{\mathbb{C}} = \tau = +\infty$. This corresponds to the $(-t) \times e^{i\pi} = \tau$ rotation,

$$\text{at early times}, \, -\infty < t < 0 : \qquad t \to i\tau. \tag{4.2.7}$$

We also note that τ corresponds to minus the Euclidean time t_E defined by the

standard Wick rotation $t \to -it_E$. The rationale for choosing this slightly bizarre looking 'down-up-right' analytic continuation on the complex plane of $t_{\mathbb{C}}$ – i.e. the contour shown in Fig. 4.1 – will be discussed at the end of this section. First we would like to explain the analytic structure of the field configurations relevant to us with a simple example of the classical solution in Eq. 4.2.1.

Expressed as a function of the complexified time variable, $t_{\mathbb{C}}$, the classical solution in Eq. 4.2.1 reads,

$$h_0(t_{\mathbb{C}}) \; = \; v \left(\frac{1 + e^{im(t_{\mathbb{C}} - i\tau_\infty)}}{1 - e^{im(t_{\mathbb{C}} - i\tau_\infty)}} \right), \tag{4.2.8}$$

where τ_∞ is a constant,

$$\tau_\infty := \frac{1}{m} \log\left(\frac{z_0}{2v} \right), \tag{4.2.9}$$

and parametrises the location (or the centre) of the solution in imaginary time. If the time-evolution contour of the solution in the $t_{\mathbb{C}}$ plane is along the imaginary time axis with real time $t = 0$, the field configuration in Eq. 4.2.8 becomes real-valued,

$$h_0(t_{\mathbb{C}} = i\tau) \; = \; v \left(\frac{1 + e^{-m(\tau - \tau_\infty)}}{1 - e^{-m(\tau - \tau_\infty)}} \right), \tag{4.2.10}$$

and singular at $\tau = \tau_\infty$.

For future reference it will be useful to define the profile function of τ

$$h_{0E}(\tau) \; = \; v \left(\frac{1 + e^{-m\tau}}{1 - e^{-m\tau}} \right), \tag{4.2.11}$$

so that Eq. 4.2.10 becomes $h_0(t_{\mathbb{C}} = i\tau) = h_{0E}(\tau - \tau_\infty)$. By construction, $h_{0E}(\tau)$ is a real-valued function of its argument, is $\mathbf{x}$-independent, and is a solution of the Euclidean-time analogue of the equation of motion (Eq. 4.2.2),

$$-\partial_\tau^2 h_{0E}(\tau) + \lambda \, h_{0E}(\tau) \, (h_{0E}^2(\tau) - v^2) = 0. \tag{4.2.12}$$

The expression on the right-hand side of Eq. 4.2.10 has an obvious interpretation in terms of a singular domain wall, located at $\tau = \tau_\infty$, that separates two domains of the field $h(\tau, \mathbf{x})$ as shown in Fig. 4.2. The domain on the right of the wall $\tau \gg \tau_\infty$ has $h = +v$, and the domain on the left of the wall, $\tau \ll \tau_\infty$, is characterised by $h = -v$. The field configuration is singular at the position of the wall, $\tau = \tau_\infty$, for all values of $\mathbf{x}$, i.e. the singularity surface is flat (or uniform in space). The thickness of the wall is set by the inverse mass $1/m$.
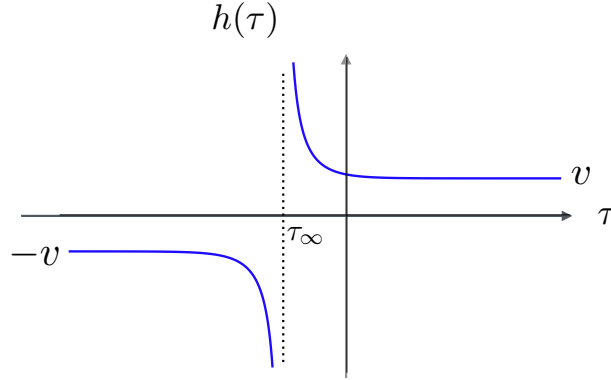
Figure 4.2: *Singular classical solution (Eq. 4.2.10). This configuration defines a uniform-in-space flat singular domain wall located at imaginary time $\tau = \tau_\infty$.*

4.2.2   More on the analytic continuation in time

In the previous section we reviewed two important general features of the classical solution (Eq. 4.2.4) describing simple tree-level scattering amplitudes:

1. The classical solution is complex-valued in real time;

2. It has a singularity on the complex plane located at a point $(t, \tau) = (0, \tau_\infty)$, where τ_∞ is a free parameter (a collective coordinate).

We have also noted that the analytic continuation of h_0 to the imaginary time, $t_{\mathbb{C}} = i\tau$, gives a manifestly real-valued scalar field configuration in Eq. 4.2.10 or equivalently Eq. 4.2.11. As a result, the classical solution is real-valued along the two vertical parts of the red contour in Fig. 4.1. This fact turns out to be a general feature of all saddle-point solutions that will be relevant for our scattering problem, and is a consequence of the initial-time boundary condition, which will be derived in Eq. 6.1.64,

$$\lim_{t \to -\infty} h(x) = v + \int \frac{d^d k}{(2\pi)^{d/2}} \frac{1}{\sqrt{2\omega_{\mathbf{k}}}} a_{\mathbf{k}}^* e^{ik_\mu x^\mu} . \tag{4.2.13}$$

Notice that the $\sim e^{i\omega_{\mathbf{k}} t}$ terms appearing on the right hand side are not accompanied by the opposite-sign frequencies – the latter are not allowed in this expression. Hence, when analytically continued to the imaginary time $t = i\tau$, the above equation gives,

$$\lim_{\tau \to +\infty} h(x) = v + \sim a_{\mathbf{k}}^* e^{-\omega_{\mathbf{k}} \tau} , \tag{4.2.14}$$

which amounts to a real-valued field configuration that is well-behaved at large τ. Time evolving this initial condition along the first (downwards) part of the contour

in Fig. 4.1 results in a real-valued classical solution along the Euclidean time axis $\tau \leq \infty$.

The obvious question is then why should not we just remain in the Euclidean time and define the entire contour as $\int_{+\infty}^{-\infty} d\tau$ instead of the 'up-down-right' zig-zag contour in Fig. 4.1. The reason is that the final-time boundary conditions are also specified for our problem. As we will show in Eq. 6.1.65, in general (i.e. for the saddle-point solution giving a dominant contribution to the functional integral representation for the scattering rate, in the regime where λn is not small) these boundary conditions state:

$$\lim_{t \to +\infty} h(x) \;=\; v \;+\; \int \frac{d^d k}{(2\pi)^{d/2}} \frac{1}{\sqrt{2\omega_{\mathbf{k}}}} \left(c_{\mathbf{k}}\, e^{-ik_\mu x^\mu} \;+\; b_{\mathbf{k}}^*\, e^{ik_\mu x^\mu} \right) . \qquad (4.2.15)$$

The coefficients $c_{\mathbf{k}}$ and $b_{\mathbf{k}}^*$ for both positive and negative frequencies are non-vanishing in the general case, which is incompatible with any naive continuation of the complete solution to $\tau \to -\infty$, as it will diverge,[1]

$$h \to v \;+\; \mathcal{O}(e^{-m\tau}) \;+\; \mathcal{O}(e^{m\tau}) . \qquad (4.2.16)$$

In general, $c_{\mathbf{k}} \neq b_{\mathbf{k}}$, giving a genuinely complex-valued field configuration in Minkowski time.

To implement Section 4.2.2 it is thus unavoidable that the final part of the contour should be along the real time axis – the time variable cannot run to infinite values in any other direction if we are to avoid exponentially-divergent field configurations. On the first two vertical parts of the contour in Fig. 4.1, the solution and its Euclidean action are real-valued quantities. However, on the real-time part of the contour, the classical solution is a complex field.

Finally, the contour should also encounter the singularity of the solution, as shown in Fig. 4.1 a or b. This ensures that the contour cannot be continuously deformed and shifted away to infinite values of $|t_{\mathbb{C}}|$ in the upper-right quadrant of the complex plane. If this were possible, we could keep the contour at infinite values of τ, which would contradict the boundary condition in Eq. 4.2.16. We will see later on that encountering the singularity of the solution on its time evolution trajectory is precisely what allows for the jump in the energy E carried by the solution. The energy changes from $E = 0$ carried by the configuration in Eq. 4.2.13 at early times to $E > 0$ computed at late times from Section 4.2.2.

---

[1]In this respect the simple configuration $h_{0E}(\tau)$ in Eq. 4.2.11 is an exception of the general rule in Section 4.2.2, as it can be written in the form $\lim_{\tau \to \pm\infty} h_{0E}(\tau) = \pm v + \mathcal{O}(e^{-m|\tau|})$ and it appears that only the decaying exponents are present at large positive or large negative values of τ. However, this is an accidental simplification specific to this particularly simple solution describing tree-level amplitudes (i.e. $\lambda n \ll 1$ limit) on the mass thresholds.

A brief summary of the analytic continuation discussion above consists of the following steps. The starting point for the formalism is the functional integral over real-valued fields in Minkowski spacetime. The saddle-point (a.k.a. steepest descent) field configurations always turn out to be complex-valued functions in real time. This fact by itself does not at all contradict the original requirement that the fields we are integrating over in a real scalar field theory are real by definition. The steepest descent saddle-point is simply not on the real-field-valued functional contour and in order to pass through it, one simply deforms the functional integration field variables into complex fields. The main point instead is whether this approach can be simplified by also analytically continuing the time variable for the fields. The answer is 'yes', but only in so far as the standard Wick rotation $t \rightarrow i\tau$ is allowed. We showed that this can be achieved on the first two (vertical) parts of the time-evolution contour in Fig. 4.1. The steepest descent field configurations on these parts of the contour are real and well-defined in the $\tau \rightarrow \infty$ limit. We have thus avoided complex-valued fields and actions on the saddle point – but only for part of the time-evolution contour. We further explained that the last part of the contour cannot be rotated into the imaginary time direction and must remain real or at least run parallel to the real-time axis (we neglect the infinitesimal angle δ in this discussion). This is forced on us by the final-time boundary condition (Section 4.2.2) for the saddle point field. On this final right-most part of the contour in Fig. 4.1, the saddle-point field configuration cannot be made real and remains complex. This does not in any way present an obstacle or an ambiguity for using the steepest descent method. It is more of a technical point to keep in mind: on this final segment of the time evolution, the fields $h(x)$ in the functional integration measure $\mathcal{D}h(x)$ should be analytically continued to allow the integration contour to pass through complex-valued saddle-point field configurations. Incidentally, it will turn out in our calculation that classical action contributions on this part of the time-evolution contour will simply amount to certain boundary terms that will be easy to account for. This summary concludes our discussion of the analytic continuation. We will return to its implementation in Section 6.1.3. Until then we will be following instead the original first-principles formulation in real Minkowski time.

We now move on to reviewing the semiclassical formalism, starting with a brief discussion of coherent states in quantum mechanics, which form the foundation for the coherent state representation used heavily in later sections.

Chapter 5

The Coherent State Formalism

5.1 Coherent states in quantum mechanics

Much of this section is basic quantum mechanics, but we review it nonetheless to ensure that our conventions are clear from the beginning. Furthermore, many of the more complex and notation-heavy equations presented in Section 5.2 can be understood as analogous to the more simple relations discussed here. Thus the formulae below provide a useful reference for the more advanced calculations to come. We begin with a brief summary of coherent states in quantum mechanics, using the familiar canonical example of the quantum harmonic oscillator.

5.1.1 Review of the quantum harmonic oscillator

Consider the 1D quantum harmonic oscillator, with Hamiltonian, $\hat{H}_0$,

$$\hat{H}_0 = \frac{\hat{p}^2}{2} + \frac{1}{2}\omega^2 \hat{q}^2, \tag{5.1.1}$$

where $\hat{p}$ and $\hat{q}$ are the momentum and position operators respectively, satisfying the usual commutation relation, $[\hat{q}, \hat{p}] = i$. The angular frequency of the oscillator is denoted by ω. Note that we set $\hbar = 1$ and choose a unit mass $m = 1$ in this quantum mechanical example.

In quantum mechanics, one seeks the energy spectrum of this system. This is usually

done using the so-called raising and lowering operators, $\hat{\alpha}$ and $\hat{\alpha}^{\dagger}$,[1]

$$\hat{\alpha} = \sqrt{\omega/2}\,(\hat{q} + i\hat{p}/\omega) \qquad \hat{\alpha}^{\dagger} = \sqrt{\omega/2}\,(\hat{q} - i\hat{p}/\omega), \qquad (5.1.2)$$

which satisfy the commutation relation,

$$[\hat{\alpha}, \hat{\alpha}^{\dagger}] = 1, \qquad (5.1.3)$$

and enable the Hamiltonian to be rewritten as,

$$\hat{H}_0 = \omega(\hat{\alpha}^{\dagger}\hat{\alpha} + 1/2) = \omega(\hat{n} + 1/2). \qquad (5.1.4)$$

We find that the stationary states are eigenstates, $|n\rangle$, of the operator $\hat{n} = \hat{\alpha}^{\dagger}\hat{\alpha}$, which is commonly referred to as the occupation number operator, with integer eigenvalues $n \geq 0$. Using the Schrödinger equation, we see that unique energy levels are uniformly separated by intervals $\Delta E = E_n - E_{n-1} = \omega$, with a ground state energy $E_0 = \omega/2$:

$$\hat{H}_0|n\rangle = E_n|n\rangle \qquad E_n = \omega(n + 1/2) \qquad n \in \mathbb{Z} \geq 0. \qquad (5.1.5)$$

A simple consequence of the commutation relations for $\hat{\alpha}^{\dagger}$ and $\hat{\alpha}$ is that,

$$\hat{\alpha}^{\dagger}|n\rangle = \sqrt{n+1}|n+1\rangle \qquad \hat{\alpha}|n\rangle = \sqrt{n}|n-1\rangle, \qquad (5.1.6)$$

and so $\hat{\alpha}^{\dagger}$ increases the energy of a state by ω where $\hat{\alpha}$ decreases it in equal measure. Given the "vacuum" state, $|0\rangle$, for which $\hat{\alpha}|0\rangle = 0$, one can generate the full spectrum using the raising operator,

$$|n\rangle = \frac{(\hat{\alpha}^{\dagger})^n}{\sqrt{n!}}|0\rangle. \qquad (5.1.7)$$

5.1.2   Coherent states as eigenstates of the lowering operator

With the energy spectrum and associated states found, we now want to find eigenstates of the lowering operator $\hat{\alpha}$. These eigenstates are known as coherent states [194–196].

We note that the states $|n\rangle$ form a complete set (since they are the eigenstates of

---

[1]In this section we use Greek letters $\hat{\alpha}$ and $\hat{\alpha}^{\dagger}$ to denote the lowering/raising operators. The complex-number-valued eigenvalue of $\hat{\alpha}$ is denoted by Latin letter a, and its complex conjugate is a^*. When dealing with the QFT generalisation starting from Section 5.2, we will use a more compact notation with Latin letters denoting both the operator-valued expressions and their eigenvalues.

the Hermitian operator $\hat{H}_0$) and thus any state $|\psi\rangle$ can be written as,

$$|\psi\rangle = \sum_{n=0}^{\infty} \psi_n |n\rangle = \sum_{n=0}^{\infty} \psi_n \frac{(\hat{\alpha}^\dagger)^n}{\sqrt{n!}} |0\rangle\,, \qquad \text{with} \qquad \psi_n \in \mathbb{C}. \qquad (5.1.8)$$

From this we can see that an eigenstate of the raising operator is not possible as the lowest n component in the decomposition will not be present after acting with $\hat{\alpha}^\dagger$. However, one can find eigenstates of the lowering operator,

$$\hat{\alpha}|\psi\rangle = \sum_{n=0}^{\infty} \psi_n \hat{\alpha}|n\rangle = \sum_{n=0}^{\infty} \psi_{n+1}\sqrt{n+1}\,|n\rangle := a\,|\psi\rangle\,, \qquad \text{for} \quad \psi_{n+1}\sqrt{n+1} = a\,\psi_n,$$
$$(5.1.9)$$

where a is the eigenvalue of state $|\psi\rangle$ under the action of operator $\hat{\alpha}$. In other words, by iterating the second equation above, we find,

$$\psi_n = a^n \frac{\psi_0}{\sqrt{n!}} \quad \rightarrow \quad |\psi\rangle = \psi_0 \sum_{n=0}^{\infty} \frac{(a\hat{\alpha}^\dagger)^n}{n!}|0\rangle = \psi_0\, e^{a\hat{\alpha}^\dagger}|0\rangle. \qquad (5.1.10)$$

These eigenstates of the lowering operator are known as *coherent states* and will prove to be a powerful tool in the functional integral QFT framework. We treat ψ_0 as an optional normalisation, which we set to 1 in accordance with coherent state convention, despite the state's subsequently non-unit norm. In preparation for the calculations to follow, where many independent sets of coherent states can appear in a single expression it is useful to clearly define a coherent state in terms of one Latin letter a,

$$|a\rangle = e^{a\hat{\alpha}^\dagger}|0\rangle \qquad \hat{\alpha}|a\rangle = a|a\rangle \qquad \langle a| = \langle 0|e^{a^*\hat{\alpha}} \qquad \langle a|\hat{\alpha}^\dagger = a^*\langle a|. \qquad (5.1.11)$$

Note that stars simply indicate a complex conjugate. It is important to distinguish between:

- the quantum state $|a\rangle$ which lives in a Hilbert space,

- the raising and lowering operators $\hat{\alpha}^\dagger$ and $\hat{\alpha}$, which have hats and act on states in this space,

- the complex number a, which is the eigenvalue associated with the action of operator $\hat{\alpha}$ on state $|a\rangle$, and a^* which is the complex conjugate of the eigenvalue a.

With this in mind, one can introduce any number of coherent states $|b\rangle, |c\rangle, ...$, with eigenvalues $\{b, c, ...\}$ under the *same* single set of operators: $\hat{\alpha}^\dagger$ and $\hat{\alpha}$. For example,

$$|b\rangle = e^{b\hat{\alpha}^\dagger}|0\rangle \qquad \hat{\alpha}|b\rangle = b|b\rangle. \qquad (5.1.12)$$

Hence we established a one-to-one correspondence between a complex number $z \in \mathbb{C}$ and a coherent state $|z\rangle$, defined via,

$$|z\rangle = e^{z\hat{\alpha}^\dagger}|0\rangle. \tag{5.1.13}$$

The set of coherent states $\{|a\rangle\}$ obtained by the complex number z spanning the entire complex plane is known to be an over-complete set. Mathematically, this is the statement that,

$$1 = \int \frac{dz^* dz}{2\pi i} \, e^{-z^* z} |z\rangle\langle z|, \tag{5.1.14}$$

where the 2-real-dimensional integral is over the complex plane $z \in \mathbb{C}$. The *over-completeness* of the set manifests itself in the presence of the exponential factor $e^{-z^* z}$ on the right hand side. We will derive Eq. 5.1.14 in the following section, see Eq. 5.1.18 below.

The transition to QFT in Section 5.2 will be achieved by generalising the simple 1-dimensional QM example considered so far, to an infinite number of dimensions (i.e. infinite number of coupled harmonic oscillators). Hence we will need an infinite set of creation and annihilation operators $\hat{\alpha}_{\mathbf{k}}$ and $\hat{\alpha}_{\mathbf{k}}^\dagger$, and correspondingly a set of coherent states $\{|a\rangle\}_{\mathbf{k}}$ parametrised by complex-valued *functions* $a(\mathbf{k}) \equiv a_{\mathbf{k}}$ where $\mathbf{k}$ is the momentum variable.

5.1.3   Properties of coherent states in quantum mechanics

We now discuss some of the useful properties of coherent states, which form the basis of many more complex derivations. As the eigenstates of the lowering operator, one might ask how coherent states are changed by application of the raising operator. It follows directly from the definition, $|a\rangle = e^{a\hat{\alpha}^\dagger}|0\rangle$, that

$$\hat{\alpha}^\dagger|a\rangle = \frac{\partial}{\partial a}|a\rangle. \tag{5.1.15}$$

Next we need the inner product of two coherent states,

$$\langle b|a\rangle = \langle 0|e^{b^*\hat{\alpha}}e^{a\hat{\alpha}^\dagger}|0\rangle = e^{b^* a}. \tag{5.1.16}$$

The expression on the right-hand side was obtained using the Baker-Campbell-Hausdorff (BCH) relation,

$$e^{\hat{A}}e^{\hat{B}} = e^{[\hat{A},\hat{B}]}e^{\hat{B}}e^{\hat{A}}, \tag{5.1.17}$$

which is valid so long as the commutator $[\hat{A}, \hat{B}] \in \mathbb{C}$.

Since a is just a complex number, for a given set of raising and lowering operators there is an infinite set $\{|a\rangle\}$ of coherent states: one for every point in the complex

plane. Accounting for their non-unit norm, the analogue of the completeness relation for coherent states is,

$$1 = \int \frac{da^* da}{2\pi i} \, e^{-a^* a} |a\rangle\langle a| \;:=\; \int d(a^*, a) \, e^{-a^* a} |a\rangle\langle a|. \tag{5.1.18}$$

The identity in Eq. 5.1.18 is often called the over-completeness relation due to the non-trivial exponential factor in the integral, with the basis of coherent states described as over-complete. Also note that Eq. 5.1.16 implies that coherent states are not orthogonal either.

Using the relations in Eqs. 5.1.16 to 5.1.18, one can write quantum-mechanical objects in a coherent state representation, where they appear as functions of one or more of the complex coherent state variables. We define the coherent-state representation of the state $|\psi\rangle$ as $\langle a|\psi\rangle = \psi(a^*)$, from which we find that the inner product of two states,

$$\langle \psi_A | \psi_B \rangle = \int d(a^*, a) \, e^{-a^* a} \psi_A^*(a) \psi_B(a^*), \tag{5.1.19}$$

where $\psi_A^*(a)$ is just $[\psi_A(a^*)]^*$. Similarly, we define the matrix element of an operator $\hat{A}$ between two coherent states as $\langle b|\hat{A}|a\rangle = A(b^*, a)$. The action of such an operator on an arbitrary state $|\psi\rangle$ can be written as,

$$(\hat{A}\psi)(b^*) = \int d(a^*, a) \, e^{-a^* a} A(b^*, a) \psi(a^*). \tag{5.1.20}$$

Furthermore, one can write the matrix element for the product of two operators as,

$$(AB)(b^*, a) = \langle b|\hat{A}\hat{B}|a\rangle = \int d(c^*, c) \, e^{-c^* c} A(b^*, c) B(c^*, a). \tag{5.1.21}$$

The above logic is used extensively in the rest of this section and Section 5.2.

A quantity which will prove to be useful is the coherent state representation of a position eigenstate, $\langle q|a\rangle$. We rewrite the raising operator in the coherent state exponent in terms of the original position and momentum operators, $\hat{q}$ and $\hat{p}$,

$$\langle q|a\rangle = \langle q| \, e^{a\hat{a}^\dagger} |0\rangle = \langle q| \, e^{a\sqrt{\omega/2}\left(\hat{q} - \frac{i\hat{p}}{\omega}\right)} |0\rangle = e^{a\sqrt{\omega/2}\left(q - \frac{1}{\omega}\frac{d}{dq}\right)} \langle q|0\rangle, \tag{5.1.22}$$

where the operators are now in their position-space representations: q and $-id/dq$. It is well-known in quantum mechanics that the vacuum state is a Gaussian distribution centred at the origin of the potential well, $q = 0$,

$$\langle q|0\rangle = \psi_0(q) = N e^{-(q/q_0)^2/2} = N e^{-\omega q^2/2}, \tag{5.1.23}$$

where N is a normalisation constant and $q_0 = \sqrt{1/\omega}$. We now make the substitution

$y = q/q_0$ and use another BCH-like relation,

$$e^{\hat{A}+\hat{B}} = e^{-[\hat{A},\hat{B}]/2} e^{\hat{A}} e^{\hat{B}}, \tag{5.1.24}$$

to show that,

$$\langle q|a \rangle = N \exp\left(-\frac{1}{2}a^2 - \frac{1}{2}\omega q^2 + \sqrt{2\omega}aq\right). \tag{5.1.25}$$

In quantum field theory, where the lowering operator is instead understood as an annihilation operator for quanta of the field, the analogous operator to position $\hat{q}$ will be the real scalar quantum field itself: $\hat{\phi}$.

Finally, consider the action of a time evolution operator, $\hat{U}_0(t) = e^{-i\hat{H}_0 t}$, on a coherent state[1],

$$
\begin{aligned}
\hat{U}_0(t)\,|a\rangle &= e^{-i\hat{H}_0 t} e^{a\hat{\alpha}^\dagger}|0\rangle \;=\; e^{-i\hat{H}_0 t} \sum_{n=0}^{\infty} a^n \frac{(\hat{\alpha}^\dagger)^n}{n!}|0\rangle \\
&= \sum_{n=0}^{\infty} a^n\, e^{-i\hat{H}_0 t}\,|n\rangle\,\frac{1}{\sqrt{n!}} \;=\; \sum_{n=0}^{\infty}(ae^{-i\omega t})^n\,|n\rangle\,\frac{1}{\sqrt{n!}} \\
&= \sum_{n=0}^{\infty}(ae^{-i\omega t})^n \frac{(\hat{\alpha}^\dagger)^n}{n!}|0\rangle \;=\; |ae^{-i\omega t}\rangle .
\end{aligned}
\tag{5.1.26}
$$

We see that time evolution operators simply shift the phase of the coherent state variable associated with the coherent state. This property will be useful in computing the scattering S-matrix operator $\hat{S}$ in Section 5.2.2.

5.2   Coherent state formalism in QFT and the S-matrix

In this section we develop the coherent state formalism for the functional integral representation of the S-matrix in quantum field theory, which is an important ingredient in the formulation of the semi-classical method for computing multiparticle production rates. We begin with the nuances associated with the move from quantum mechanics (QM) to quantum field theory (QFT), where the concept of coherent states is somewhat more abstract. We then explore their use in the calculation of amplitudes via path integrals. Sections 5.2.1 and 5.2.2 outline the coherent-states-based approach for writing matrix elements in QFT that was originally presented in Refs. [186, 191, 192], and in a slightly different formulation, called the holomorphic

---

[1]The subscripts on $\hat{U}_0$ and $\hat{H}_0$ are used to remind us that the Hamiltonian is that of the simple harmonic oscillator, it will play the role of the free part of the Hamiltonian in interacting models, in particular the QFT settings considered in the following section.

representation, in the textbook [190]. In Section 6.1 we will use the results derived here for matrix elements to efficiently implement the phase space integration and thus write down formulae for probabilistic rates for multiparticle production following the semiclassical formalism of Ref. [168].

5.2.1 QFT in $d + 1$ dimensions as the infinite-dimensional QM system

In Section 5.1 we discussed coherent states as eigenstates of the lowering operator for the quantum harmonic oscillator (QHO). Now we instead discuss the real scalar quantum field in $d + 1$ dimensions, which has many mathematical parallels to the harmonic oscillator.

A free real scalar field is described by the Klein-Gordon Lagrangian, which can be manipulated into a Klein-Gordon Hamiltonian H_0,

$$H_0 = \int d^d x\, \mathcal{H}_0\,, \quad \text{where} \quad \mathcal{H}_0 = \frac{1}{2}\pi^2 + \frac{1}{2}|\nabla\phi|^2 + \frac{m^2}{2}\phi^2. \tag{5.2.1}$$

Here $\phi(x)$ is the scalar field, $\pi(x)$ is the momentum conjugate to the field, and ∇ denotes a spatial derivative in d dimensions. The conjugate momentum field $\pi = \partial_t \phi = \dot{\phi}$ is just a change in variable associated with the Legendre transformation linking the Lagrangian and Hamiltonian formalisms. The final term is a mass term; this mass will later be set to unity. When transitioning from classical field theory to quantum field theory, the fields ϕ and π gain operator status. We will always be in the quantum regime and so their hats are omitted. Finally, note that x now represents a $(1, d)$-vector $x = (t, \mathbf{x})$.

The above Hamiltonian already looks similar to that of the QHO but with the so-called generalised coordinate now being a field ϕ rather than a position q. This is made more obvious if we integrate the spatial derivative by parts,

$$\mathcal{H}_0 = \frac{\pi^2}{2} + \frac{1}{2}\phi(m^2 - \nabla^2)\phi, \tag{5.2.2}$$

and so our frequency $\omega^2 = (m^2 - \nabla^2)$ is no longer a constant parameter. In a Fourier expansion, the Laplacian, $-\nabla^2$, will bring out a factor of the squared d-dimensional momentum $\mathbf{k}^2$. We thus expect a dispersion relation: $\omega_{\mathbf{k}}^2 = m^2 + \mathbf{k}^2$. For every d-momentum, $\mathbf{k}$, there is an associated harmonic oscillator with frequency, $\omega_{\mathbf{k}}$, which we can solve by introducing raising and lowering operators, $\hat{a}_{\mathbf{k}}^\dagger$ and $\hat{a}_{\mathbf{k}}$, as shown in

Section 5.1[1],

$$\hat{H}_0 = \int d^d k \, \omega_{\mathbf{k}} \, \hat{a}^\dagger_{\mathbf{k}} \, \hat{a}_{\mathbf{k}} \, + \, \mathcal{V}. \tag{5.2.3}$$

Here, $\mathcal{V}$ is analogous to the ground-state energy in the QHO and can be thought of as the energy of the vacuum. We ignore this term in the rest of this work by assuming the normal ordering prescription $: H_0 :$ as is standard.

The usual interpretation of the free quantum field is that it consists of an infinite number of harmonic oscillators. The raising and lowering operators can now be reinterpreted as creation and annihilation operators: the operator $\hat{a}^\dagger_{\mathbf{k}}$ creates a quantum of the field with d-momentum $\mathbf{k}$, whereas operator $\hat{a}_{\mathbf{k}}$ annihilates it. Considering the parallels with the QHO it should not be surprising that they obey the commutation relation,

$$[\hat{a}_{\mathbf{k}}, \hat{a}^\dagger_{\mathbf{p}}] = (2\pi)^{d/2} \, \delta(\mathbf{k} - \mathbf{p}). \tag{5.2.4}$$

Inverting the definitions of the creation and annihilation operators and accounting for their momentum-space representation, one obtains the definition of the scalar field operator in terms of Fourier modes,

$$\hat{\phi}(x) = \int \frac{d^d k}{(2\pi)^{d/2}} \frac{1}{\sqrt{2\omega_{\mathbf{k}}}} (\hat{a}_{\mathbf{k}} \, e^{-ikx} \, + \, \hat{a}^\dagger_{\mathbf{k}} \, e^{+ikx}), \tag{5.2.5}$$

where $kx = k_0 t - \mathbf{k} \cdot \mathbf{x}$. An on-shell field satisfies the Klein-Gordon equation, implying $k_0 = \omega_{\mathbf{k}} = \sqrt{m^2 + \mathbf{k}^2}$. The coefficients of the modes are the creation and annihilation operators in the quantum theory[2].

In analogy with QM, a coherent state in QFT is a common eigenstate of *all* annihilation operators, with eigenvalues dependent on the momentum $\mathbf{k}$ of the annihilation operator. We follow the notational rationale put forward in Section 5.1, by labelling the coherent state $|\{a\}\rangle$, and denoting its eigenvalue under operator $\hat{a}_{\mathbf{k}}$ as $a_{\mathbf{k}}$,

$$\hat{a}_{\mathbf{k}} |\{a\}\rangle = a_{\mathbf{k}} |\{a\}\rangle \qquad \forall \mathbf{k}. \tag{5.2.6}$$

When converting from QM to QFT we have to take into account that we have moved from one oscillator to an infinite set, indexed by a free d-dimensional momentum $\mathbf{k}$. The curly braces in the state label, $|\{a\}\rangle$, serve as a constant reminder. Therefore,

---

[1]As already mentioned, to avoid overly-complicated notation in QFT, we will now use Latin letters for both the creation/annihilation operators and for their eigenvalues, see Eqs. 5.2.5 and 5.2.6.

[2]We use a non-relativistic normalisation for the integration measure in Eq. 5.2.5. In the relativistic normalisation, $\hat{\phi}(x) = \int \frac{d^d k}{(2\pi)^{d/2}} \frac{1}{2\omega_{\mathbf{k}}} (\hat{a}_{\mathbf{k}} e^{-ikx} + \hat{a}^\dagger_{\mathbf{k}} e^{+ikx})$ and one rescales $\hat{a}_{\mathbf{k}}$ and $\hat{a}^\dagger_{\mathbf{p}}$ such that $[\hat{a}_{\mathbf{k}}, \hat{a}^\dagger_{\mathbf{p}}] = (2\pi)^{d/2} 2\omega_{\mathbf{k}} \delta(\mathbf{k} - \mathbf{p})$.

in terms of the vacuum, our coherent state can be written as,

$$|\{a\}\rangle = e^{\int d\mathbf{k}\, a_{\mathbf{k}} \hat{a}_{\mathbf{k}}^{\dagger}}|0\rangle. \tag{5.2.7}$$

To avoid notational clutter, we use $d\mathbf{k}$ to represent the d-dimensional momentum integration measure,

$$d\mathbf{k} := d^d k. \tag{5.2.8}$$

The Fourier transformation of the field operator is defined via,

$$\tilde{\hat{\phi}}(\mathbf{k}) := \tilde{\hat{\phi}}(t, \mathbf{k}) := \int \frac{d^d x}{(2\pi)^{d/2}} e^{-i\mathbf{k}\cdot\mathbf{x}}\, \hat{\phi}(t, \mathbf{x}), \tag{5.2.9}$$

so that the Fourier transform of the free field in Eq. 5.2.5 becomes simply a linear combination of the annihilation and creation operators with positive and negative frequencies,

$$\tilde{\hat{\phi}}(\mathbf{k}) = \frac{1}{\sqrt{2\omega_{\mathbf{k}}}}(\hat{a}_{\mathbf{k}}\, e^{-i\omega_{\mathbf{k}} t} + \hat{a}_{-\mathbf{k}}^{\dagger}\, e^{i\omega_{\mathbf{k}} t}). \tag{5.2.10}$$

In exact analogy to the operator-valued expressions for the Fourier-transforms in Eqs. 5.2.9 and 5.2.10 we can also define the Fourier transform of the c-valued scalar field $\phi(x)$,

$$\tilde{\phi}(\mathbf{k}) = \frac{1}{\sqrt{2\omega_{\mathbf{k}}}}(a_{\mathbf{k}}\, e^{-i\omega_{\mathbf{k}} t} + a_{-\mathbf{k}}^{*}\, e^{i\omega_{\mathbf{k}} t}). \tag{5.2.11}$$

where in this case the annihilation and creation operators are substituted by the complex-valued eigenfunction $a_{\mathbf{k}}$ and it complex conjugate $a_{\mathbf{k}}^{*}$ as per Eq. 5.2.6. Note that $[\tilde{\phi}(\mathbf{k})]^{*} = \tilde{\phi}(-\mathbf{k})$ because $\phi(t, \mathbf{x}) \in \mathbb{R}$.

As in QM, we can find an inner product of two coherent states,

$$\langle\{b\}|\{a\}\rangle = e^{\int d\mathbf{k}\, b_{\mathbf{k}}^{*} a_{\mathbf{k}}}, \tag{5.2.12}$$

the over-completeness relation reads,

$$1 = \int d(\{a^{*}\}, \{a\}) e^{-\int d\mathbf{k}\, a_{\mathbf{k}}^{*} a_{\mathbf{k}}}|\{a\}\rangle\langle\{a\}|, \tag{5.2.13}$$

and for the inner product between the eigenstate of the field $\tilde{\phi}_{\mathbf{k}}$ and the coherent state we have,

$$\langle\phi|\{a\}\rangle = N \exp\left(-\frac{1}{2}\int d\mathbf{k}\, a_{\mathbf{k}} a_{-\mathbf{k}} - \frac{1}{2}\int d\mathbf{k}\, \omega_{\mathbf{k}}\tilde{\phi}(\mathbf{k})\tilde{\phi}(-\mathbf{k}) + \int d\mathbf{k}\, \sqrt{2\omega_{\mathbf{k}}} a_{\mathbf{k}}\phi(\mathbf{k})\right). \tag{5.2.14}$$

Here N is some constant normalisation factor irrelevant for our purposes. The expression in Eq. 5.2.14 is the generalisation of the quantum mechanical overlap formula (Eq. 5.1.25) to the QFT case at hand, which corresponds to an infinite number of QM oscillator degrees of freedom. We note that the states $\langle\phi|$ and $|\{a\}\rangle$

in the expression in Eq. 5.2.14 are defined as the eigenstates of the operators $\hat{\phi}$ and $\hat{a}$ respectively; with both operators taken at the same time t, which we take to be $t = 0$[1]. Hence the Fourier components of the field $\tilde{\phi}(\mathbf{k})$ are given by the spatial Fourier transform (see Eq. 5.2.9) of $\phi(t, \mathbf{x})$ at $t = 0$. For completeness of our presentation, the formula in Eq. 5.2.14 is derived in Appendix B.1.

5.2.2   Application to path integrals and amplitude calculation

We now consider an interacting quantum field theory in $d + 1$ dimensions with the Hamiltonian H. The object central to scattering theory is the S-matrix. Given an initial state, $|\phi_i(t_i)\rangle$, the S-matrix defines the probability amplitude of arriving at a final state, $|\phi_f(t_f)\rangle$.

In the interaction picture, where we split the Hamiltonian into the free part H_0, and the interacting part V,

$$\hat{H} = \hat{H}_0 + \hat{V}, \tag{5.2.15}$$

the S-matrix S_{fi} is defined as,

$$S_{fi} = \langle \phi_f | \hat{S} | \phi_i \rangle = \lim_{t_f, t_i \to \pm\infty} \langle \phi_f | e^{i\hat{H}_0 t_f} \hat{U}(t_f, t_i) e^{-i\hat{H}_0 t_i} | \phi_i \rangle, \tag{5.2.16}$$

where $|\phi_f\rangle$ and $|\phi_i\rangle$ are free states, i.e. eigenstates of the free Hamiltonian $\hat{H}_0$, prepared at the times $t = t_f$ and $t = t_i$ respectively. The S-matrix operator, appearing on the right-hand side of Eq. 5.2.16,

$$\hat{S} = \lim_{t_f, t_i \to \pm\infty} e^{i\hat{H}_0 t_f} \hat{U}(t_f, t_i) e^{-i\hat{H}_0 t_i}, \tag{5.2.17}$$

implements the time-evolution of the interaction-picture-state $|\phi_i\rangle$ from t_i to t_f where it is contracted with the final state $|\phi_f\rangle$. The operator $U(t_f, t_i)$ in Eq. 5.2.17 is the time-evolution operator for the Heisenberg fields,

$$\hat{U}(t_f, t_i) = \mathcal{T} \exp\left(-i \int_{t_i}^{t_f} \hat{H} dt\right), \tag{5.2.18}$$

with $\mathcal{T}$ denoting a time-ordered product. Given that the fields in the interaction picture are free fields, one has,

$$|\phi(t')\rangle = e^{-i\hat{H}_0(t'-t)} |\phi(t)\rangle, \tag{5.2.19}$$

---

[1]The operators $\hat{\phi}$ and $\hat{a}$ are defined in a theory with the Hamiltonian H_0, and it is straightforward to time-evolve them from $t = 0$ to any t with $e^{\pm iH_0 t}$. This will be done in Eq. 5.2.29 in the next section, but in Eq. 5.2.14 we use $t = 0$.

which explains the $e^{i\hat{H}_0 t_f}$ and $e^{-i\hat{H}_0 t_i}$ factors in Eq. 5.2.17.

In the infinite future and past, the initial and final particles are sufficiently separated in the d-dimensional space so as not to experience interactions (apart from the effects accounted for by UV renormalisation of fields and parameters of the theory). Thus, by taking the limit $\lim_{t_f, t_i \to \pm\infty}$, the free Hamiltonian eigenstates in Eq. 5.2.16 are a good approximation to the actual initial and final states.

Of course, for a non-interacting theory, $\hat{S}$ is simply the identity operator. More generally, $\hat{S} = 1 + i\hat{T}$ and we define the matrix element, $\mathcal{M}$, by the relation,

$$\langle \phi_f | \hat{S} - 1 | \phi_i \rangle = \langle \phi_f | i\hat{T} | \phi_i \rangle = (2\pi)^4 \delta^{(d+1)} \left(\sum k_f - \sum k_i \right) i\mathcal{M}, \qquad (5.2.20)$$

where the delta function simply enforces momentum conservation.

We now want to express the S-matrix (see Eq. 5.2.17) in the basis of coherent states. The kernel of the S-matrix is given by,

$$S(b^*, a) := \lim_{t_f, t_i \to \pm\infty} \langle \{b\} | e^{i\hat{H}_0 t_f} \hat{U}(t_f, t_i) e^{-i\hat{H}_0 t_i} | \{a\} \rangle. \qquad (5.2.21)$$

Eq. 5.1.26 implies that the free evolution operators simply shift the phase of the coherent states, giving,

$$S(b^*, a) := \lim_{t_f, t_i \to \pm\infty} \langle \{be^{-i\omega t_f}\} | \hat{U}(t_f, t_i) | \{ae^{-i\omega t_i}\} \rangle. \qquad (5.2.22)$$

Note that $|\{ae^{-i\omega t_i}\}\rangle$ refers to a coherent state much like $|\{a\}\rangle$ but with $a_{\mathbf{k}} \to a_{\mathbf{k}} e^{-i\omega_{\mathbf{k}} t_i}$ for all $\mathbf{k}$.

The derivation of the S-matrix kernel will closely follow that presented in [191, 192]. Using the completeness relation,

$$1 = \int d\phi_f |\phi_f\rangle \langle \phi_f|, \qquad (5.2.23)$$

and similarly for ϕ_i, we can re-write Eq. 5.2.22 as,

$$S(b^*, a) = \lim_{t_f, t_i \to \pm\infty} \int d\phi_f d\phi_i \langle \{be^{-i\omega t_f}\} | \phi_f \rangle \langle \phi_f | \hat{U}(t_f, t_i) | \phi_i \rangle \langle \phi_i | \{ae^{-i\omega t_i}\} \rangle. \qquad (5.2.24)$$

We recognise $\langle \phi_f | \hat{U}(t_f, t_i) | \phi_i \rangle$ as the Feynman path integral,

$$\langle \phi_f | \hat{U}(t_f, t_i) | \phi_i \rangle = \int \mathcal{D}\phi \, e^{iS[\phi]_{t_i}^{t_f}}, \qquad (5.2.25)$$

over the fields satisfying the boundary conditions,

$$\phi(t_i) = \phi_i, \quad \phi(t_f) = \phi_f, \qquad (5.2.26)$$

where $S[\phi]_{t_i}^{t_f}$ is the action,

$$S[\phi]_{t_i}^{t_f} = \int\limits_{t_i}^{t_f} dt \int d^d x \, \mathcal{L}(\phi). \tag{5.2.27}$$

Inserting the projections of the initial and final states in the coherent state basis (see Eq. 5.2.14), we arrive at the following result,

$$S(b^*, a) = \lim_{t_f, t_i \to \pm\infty} \int d\phi_f \, d\phi_i \, e^{B_i(\phi_i; a) + B_f(\phi_f; b^*)} \int \mathcal{D}\phi \, e^{iS[\phi]_{t_i}^{t_f}}. \tag{5.2.28}$$

Here the boundary terms, $\exp[B_i(\phi_i; a)] = \langle \phi_i | \{ae^{-i\omega t_i}\}\rangle$ and $\exp[B_f(\phi_f; b^*)] = \langle \{be^{-i\omega t_f}\} | \phi_f \rangle$, are given by (*cf.* Eq. 5.2.14),

$$B_i(\phi_i; a) = -\frac{1}{2} \int d\mathbf{k} \, a_{\mathbf{k}} a_{-\mathbf{k}} e^{-2i\omega_k t_i} - \frac{1}{2} \int d\mathbf{k} \, \omega_{\mathbf{k}} \tilde{\phi}_i(\mathbf{k}) \tilde{\phi}_i(-\mathbf{k}) + \int d\mathbf{k} \sqrt{2\omega_{\mathbf{k}}} a_{\mathbf{k}} \tilde{\phi}_i(\mathbf{k}) e^{-i\omega_{\mathbf{k}} t_i},$$

$$B_f(\phi_f; b^*) = -\frac{1}{2} \int d\mathbf{k} \, b_{\mathbf{k}}^* b_{-\mathbf{k}}^* e^{2i\omega_k t_f} - \frac{1}{2} \int d\mathbf{k} \, \omega_{\mathbf{k}} \tilde{\phi}_f(\mathbf{k}) \tilde{\phi}_f(-\mathbf{k}) + \int d\mathbf{k} \sqrt{2\omega_{\mathbf{k}}} b_{\mathbf{k}}^* \tilde{\phi}_f(-\mathbf{k}) e^{i\omega_{\mathbf{k}} t_f}. \tag{5.2.29}$$

In these expressions, $\tilde{\phi}_i(\mathbf{k})$ and $\tilde{\phi}_f(\mathbf{k})$ are the d-dimensional Fourier transforms of the boundary fields, $\phi_i(\mathbf{x}) = \phi(t_i, \mathbf{x})$ and $\phi_f(\mathbf{x}) = \phi(t_f, \mathbf{x})$, so that,

$$\begin{aligned} \tilde{\phi}_i(\mathbf{k}) &= \int d\mathbf{x} \, e^{-i\mathbf{k}\cdot\mathbf{x}} \, \phi(t_i, \mathbf{x}), \\ \tilde{\phi}_f(\mathbf{k}) &= \int d\mathbf{x} \, e^{-i\mathbf{k}\cdot\mathbf{x}} \, \phi(t_f, \mathbf{x}), \end{aligned} \tag{5.2.30}$$

where, in analogy with Eq. 5.2.8, the d-dimensional coordinate integration measure is defined as,

$$d\mathbf{x} := d^d x \,. \tag{5.2.31}$$

Thus in comparison to the simple overlaps in Eq. 5.2.14 at $t = 0$, the boundary terms in Eq. 5.2.29 contain the dependence on t_i or t_f via the phase factors accompanying the a and b^* in Eq. 5.2.29, as well as in the definitions of the boundary fields in Eq. 5.2.30.

Before concluding this section, we mention a particularly useful property of the coherent state basis for scattering theory: it allows one to circumvent the LSZ reduction formulae. The kernel, $A(b^*, a) = \langle b | \hat{A} | a \rangle$, of any operator $\hat{A}$ in the coherent state representation is the generating functional for the same operator in the Fock space,

$$\langle q_1 ... q_m | \hat{A} | p_1 ... p_n \rangle = \frac{\partial}{\partial b_{\mathbf{q}_1}^*} ... \frac{\partial}{\partial b_{\mathbf{q}_m}^*} \frac{\partial}{\partial a_{\mathbf{p}_1}} ... \frac{\partial}{\partial a_{\mathbf{p}_n}} A(b^*, a)|_{a = b^* = 0}, \tag{5.2.32}$$

where $|p_1 ... p_n\rangle$ is an n-particle state with particle d-momenta $\mathbf{p}_i$, $i = 1, \ldots, n$. This

formula follows immediately from the definition of the coherent state in Eq. 5.2.7, since

$$\frac{\partial}{\partial a_{\mathbf{p}_1}} \cdots \frac{\partial}{\partial a_{\mathbf{p}_n}} \, e^{\int d\mathbf{k} \, a_{\mathbf{k}} \hat{a}_{\mathbf{k}}^{\dagger}} |0\rangle|_{a=0} \;=\; |p_1...p_n\rangle . \tag{5.2.33}$$

Applying this to the S-matrix operator we find,

$$\langle q_1...q_m|S|p_1...p_n\rangle \;=\; \frac{\partial}{\partial b_{\mathbf{q}_1}^*} \cdots \frac{\partial}{\partial b_{\mathbf{q}_m}^*} \frac{\partial}{\partial a_{\mathbf{p}_1}} \cdots \frac{\partial}{\partial a_{\mathbf{p}_n}} \, S(b^*, a)|_{a=b^*=0}. \tag{5.2.34}$$

The left-hand side is just the S-matrix element for the $n \to m$ process. Hence, we can calculate any scattering amplitude directly from the kernel of the S-matrix by simply differentiating with respect to coherent state variables. Thus the coherent state representation allows one to bypass the LSZ reduction formulae, by simply differentiating the path integral for the kernel of the S-matrix. This coherent state formulation is of course equivalent to the LSZ procedure[1], but gives a more direct route for semiclassical applications, given the exponential nature of $S(b^*, a)$.

---

[1] In our derivation we have neglected the Z factors arising from the wave-function renormalisation. Of course they can be painstakingly restored, but this will not be required for our applications of the semiclassical approach.

Chapter 6

The Semiclassical Method

6.1 The semiclassical method for multi-particle production

In this section we review the semiclassical method of Son [168] for calculating probabilistic rates or cross sections for the processes given in Eq. 4.1.1. There are two types of initial states X that are of particular interest,

$$\text{Scattering}: \qquad |X(\sqrt{s})\rangle = |2\rangle \ \rightarrow \ |n\rangle \quad \Rightarrow \quad \text{cross section } \sigma_n(\sqrt{s})\,, \qquad (6.1.1)$$

$$\text{Resonance}: \qquad |X(\sqrt{s})\rangle = |1^*\rangle \rightarrow \ |n\rangle \quad \Rightarrow \quad \text{partial width } \Gamma_n(s)\,. \qquad (6.1.2)$$

For the 2-particle initial state, the n-particle production process in Eq. 6.1.1 is characterised by the cross section $\sigma_n(\sqrt{s})$; for the single-particle state of virtuality $p^2 = s$ in Eq. 6.1.2, the relevant quantity is the partial decay width $\Gamma_n(s)$. Final states contain a large number $n \gtrsim 1/(\text{coupling constant}) \gg 1$ of elementary Higgs-like scalar particles of mass m.

As we already mentioned in the Introduction, this work concentrates primarily on the process shown in Eq. 6.1.2 to simplify the presentation. Formally, the processes in Eqs. 6.1.1 and 6.1.2 can both be treated simultaneously in the semiclassical approach of Son [168], where the initial state X is approximated by a local operator $\mathcal{O}(x)$ acting on the vacuum state. In $|2\rangle \rightarrow |n\rangle$ scattering with n large, the original 2 particles exchange large momentum and thus come within a short distance of one another. This justifies a description with a local operator source[1].

---

[1]The effect of smearing of the local operator would be important in the description of $2 \rightarrow n$ processes in order to account for the effect of a finite impact parameter between the two incoming particles in the collision and to maintain unitarity in the asymptotic high-energy regime, $\sqrt{s} \rightarrow \infty$, with fixed coupling constant $\lambda = \text{fixed} \ll 1$.

We will use the notation $|1^*\rangle \to |n\rangle$ for the process in Eq. 6.1.2, where $|1^*\rangle$ denotes a highly-virtual particle that, for example, can be produced as an intermediate state in a high-energy collision, and $|n\rangle$ denotes an n-particle final state. We are interested in the regime of high-multiplicity ($n \gg 1$) in a weakly coupled theory ($\lambda \ll 1$) with λn held at a fixed value that we ultimately take to be large.

Our discussion in this section follows the construction in [168] and also borrows from Refs. [186, 192, 197, 198].

6.1.1   Setting up the problem

Consider a real scalar field $\phi(x)$ in $(d+1)$-dimensional spacetime, with the Lagrangian,

$$\mathcal{L}(\phi) = \frac{1}{2}(\partial_\mu \phi)^2 - \frac{1}{2}m^2\phi^2 - \mathcal{L}_{\text{int}}(\phi), \qquad (6.1.3)$$

where $\mathcal{L}_{\text{int}}$ is the interaction term. The two simplest examples are the ϕ^4 model in the unbroken phase, with $\mathcal{L}_{\text{int}} = \frac{\lambda}{4}\phi^4$, and the theory in Eq. 4.1.3 with the spontaneously-broken Z_2 symmetry,

$$\mathcal{L} = \frac{1}{2}\partial^\mu h \, \partial_\mu h - \frac{\lambda}{4}\left(h^2 - v^2\right)^2. \qquad (6.1.4)$$

The theory in Eq. 6.1.4 has a non-zero vacuum expectation value $\langle h \rangle = v$ and we introduce the shifted field of mass $m = \sqrt{2\lambda}\,v$,

$$\phi(x) = h(x) - v, \qquad m = \sqrt{2\lambda}\,v. \qquad (6.1.5)$$

Our considerations in this section are general and the expressions that follow, unless stated otherwise, will be written in terms of the manifestly VEV-less field ϕ with the Lagrangian in Eq. 6.1.3. If the VEV is non-zero, as in the model in Eq. 6.1.4, the ϕ field is defined by subtracting the VEV from the original field via Eq. 6.1.5.

Our main goal is to derive the probability rate or the 'cross section' for the process where a single highly-virtual off-shell particle is produced as an intermediate state in a high-energy collision, or alternatively a few energetic on-shell particles in the initial state $|\phi_i\rangle$, produce an n-particle final state with $n \gg 1$. Most importantly, this probability rate should be written in a form suitable for a semiclassical treatment. In other words, the functional integral representation for the multiparticle rate should be calculable by some appropriate incarnation of the steepest descent method.

We begin by specifying the initial state. Instead of using the coherent state $|\{a\}\rangle$ as we have done in the previous section, we now assume that the initial state is

prepared by acting with a certain local operator $\hat{\mathcal{O}}(x)$ on the vacuum,

$$|\phi_i\rangle = \hat{\mathcal{O}}(x)|0\rangle. \tag{6.1.6}$$

We will see that the operator $\hat{\mathcal{O}}(x)$ will act as a local injection of energy (or more precisely the virtuality characterising the off-shell state $|\phi_i\rangle$) into the vacuum state $|0\rangle$ at the spacetime point x. From now on, and without loss of generality, we will place the operator insertion point x at the origin, $x = 0$.

In a general local QFT, any field $\mathcal{O}(x)$ that is sharply defined at a point x is in fact an operator-valued distribution. In order to define an operator one has to smear the field with a test function that belongs to an appropriate set of well-behaved smooth functions with finite support in spacetime [199]. This implies that $\mathcal{O}(x)$ in Eq. 6.1.30 should be averaged with a test function $g(x)$. The operator localised in the vicinity of a point x is,

$$\mathcal{O}_g(x) = \int d^4x' \, g(x' - x) \, \mathcal{O}(x'), \tag{6.1.7}$$

and the prescription in Eq. 6.1.6 for defining the initial state should be refined [167] using,

$$|\phi_i\rangle = \mathcal{O}_g(0)|0\rangle = \int d^4x' \, g(x') \, \mathcal{O}(x')|0\rangle. \tag{6.1.8}$$

This gives a well-defined state in the Hilbert space. For the rest of this section we will ignore the averaging of the operators with the test functions. Their effect can be recovered from the distribution-valued rate $\mathcal{R}_n(\sqrt{s} = E)$ that we will concentrate on from now on and refer the reader to [167] for more details on the topic of the operator smearing.

For a given final state, $|\phi_f\rangle$, one can isolate the parts with the desired energy and multiplicity using projection operators $\hat{P}_E$ and $\hat{P}_n$ on states with the fixed energy E and particle number n. The probability rate $\mathcal{R}_n(E)$ for a transition between the initial state and the final state with the energy E and particle number n is given by the square of the matrix element of the S-matrix with the projection operators $\hat{P}_E$ and $\hat{P}_n$,

$$\langle\phi_f|\hat{P}_E\hat{P}_n\hat{S}|\phi_i\rangle = \langle\phi_f|\hat{P}_E\hat{P}_n\hat{S}\hat{\mathcal{O}}|0\rangle, \tag{6.1.9}$$

integrated over the final states phase space, $\int d\phi_f \, |\phi_f\rangle\langle\phi_f|$, to give

$$\begin{aligned}\mathcal{R}_n(E) &= \int d\phi_f \, \langle0|\hat{\mathcal{O}}^\dagger\hat{S}^\dagger\hat{P}_E\hat{P}_n|\phi_f\rangle\langle\phi_f|\hat{P}_E\hat{P}_n\hat{S}\hat{\mathcal{O}}|0\rangle \\ &= \langle0|\hat{\mathcal{O}}^\dagger\hat{S}^\dagger\hat{P}_E\hat{P}_n\hat{S}\hat{\mathcal{O}}|0\rangle.\end{aligned} \tag{6.1.10}$$

It is clear that neither the initial state $|\phi_i\rangle = \hat{\mathcal{O}}|0\rangle$ nor the final state $\langle\phi_f|$ in the matrix element in Eq. 6.1.9 are states of definite energy. The projection operator $\hat{P}_E$ resolves this problem by projecting onto the fixed energy states. This applies to

both, the initial and the final states, since the energy E is conserved in the transition amplitude and hence is the same in the initial and the final states. This implies that $\hat{P}_E\hat{\mathcal{O}}\,|0\rangle$ selects the initial state with the energy equal to E that is injected into the vacuum state by the operator $\hat{P}_E\hat{\mathcal{O}}$ at the point $x = 0$ – in agreement with what we have already stated above.

The particle number, on the other hand, is not a conserved quantity, it is computed only for asymptotic free states and is equal to n in the final state $\langle\phi_f|\,\hat{P}_n$. In the initial state we want to have the particle number n_i to be small, 1 or 2, to correspond a scattering process 'few $\rightarrow$ many'. The selection of n_i is achieved by a judicious choice of the operator $\mathcal{O}$ in the definition of the initial state. We will see below that the requirement that the semiclassical approximation is applicable to the functional integral representation of the transition rate in Eq. 6.1.10 will allow for the operators of the form,

$$\hat{\mathcal{O}} \;=\; j^{-1}\,e^{j\phi(0)}\,, \tag{6.1.11}$$

where j is a constant. To select the single-particle initial state $\langle 0|\phi(0)$, the limit $j \rightarrow 0$ will ultimately be taken in the computation of the probability rate in Eq. 6.1.10, along with the semiclassical limit $\lambda \rightarrow 0$.[1] Eq. 6.1.11 defines the local operator used by Son in [168], which we too will use (we will have more to say about this prescription in Section 6.1.2).

To proceed with the determination of the multiparticle rate in Eq. 6.1.10, we need expressions for the projection operators $\hat{P}_E$ and $\hat{P}_n$. This is where the coherent states formalism is useful. The kernel of $\hat{P}_E$ is given by,

$$P_E(b^*, a) := \langle\{b\}|\hat{P}_E|\{a\}\rangle \;=\; \int \frac{d\xi}{2\pi}\,\exp\left[-iE\xi + \int d\mathbf{k}\,b_\mathbf{k}^* a_\mathbf{k} e^{i\omega_\mathbf{k}\xi}\right]. \tag{6.1.12}$$

To derive this expression, consider applying the delta function,

$$\delta(\hat{H}_0 - E) \;=\; \int \frac{d\xi}{2\pi}\,e^{i(\hat{H}_0 - E)\xi}\,, \tag{6.1.13}$$

to the coherent state $|\{a\}\rangle$,

$$\delta(\hat{H}_0 - E)\,|\{a\}\rangle \;=\; \int \frac{d\xi}{2\pi}\,e^{-iE\xi}\,|\{ae^{i\omega\xi}\}\rangle \tag{6.1.14}$$

and then convoluting this with the state $\langle\{b\}|$. Using Eq. 5.2.12 we find,

$$\langle\{b\}|\delta(\hat{H}_0 - E)|\{a\}\rangle \;=\; \int \frac{d\xi}{2\pi}\,\exp\left[-iE\xi + \int d\mathbf{k}\,b_\mathbf{k}^* a_\mathbf{k} e^{i\omega_\mathbf{k}\xi}\right], \tag{6.1.15}$$

---

[1]We will explain in Section 6.1.2 in the discussion below Eq. 6.1.29 that the $j \rightarrow 0$ limit should be taken such that $j/\lambda \sim 1$ to guarantee that the number of initial particles is ~ 1 while the number of final state particles is $n \sim 1/\lambda$.

which is equivalent to Eq. 6.1.12.

Using the same line of reasoning we also get the kernel of the projection operator $\hat{P}_n$,

$$P_n(b^*, a) := \langle\{b\}|\hat{P}_n|\{a\}\rangle = \int \frac{d\eta}{2\pi} \exp\left[-in\eta + \int d\mathbf{k}\, b_\mathbf{k}^* a_\mathbf{k} e^{i\eta}\right]. \qquad (6.1.16)$$

As seen in Eq. 5.1.21, the kernel of a product of two operators is the convolution of their individual kernels, such that the combined energy and multiplicity projector is given by,

$$
\begin{aligned}
P_E P_n(b^*, a) &= \int d(\{c^*\}, \{c\})\, e^{-\int d\mathbf{k}\, c_\mathbf{k}^* c_\mathbf{k}} P_E(b^*, c) P_n(c^*, a) \\
&= \int d(\{c^*\}, \{c\}) \frac{d\xi}{2\pi}\frac{d\eta}{2\pi} e^{-iE\xi - in\eta} \exp\left[\int d\mathbf{k}\left(-c_\mathbf{k}^*(c_\mathbf{k} - a_\mathbf{k}\, e^{i\eta}) + b_\mathbf{k}^* c_\mathbf{k} e^{i\omega_\mathbf{k}\xi}\right)\right] \\
&= \int d(\{c\}) \frac{d\xi}{2\pi}\frac{d\eta}{2\pi} e^{-iE\xi - in\eta}\delta(\{c\} - \{ae^{i\eta}\}) \exp\left[\int d\mathbf{k}\, b_\mathbf{k}^* c_\mathbf{k} e^{i\omega_\mathbf{k}\xi}\right] \\
&= \int \frac{d\xi}{2\pi}\frac{d\eta}{2\pi} \exp\left[-iE\xi - in\eta + \int d\mathbf{k}\, b_\mathbf{k}^* a_\mathbf{k} e^{i\omega_\mathbf{k}\xi + i\eta}\right],
\end{aligned}
$$
$$(6.1.17)$$

where the delta function $\delta(\{c\} - \{ae^{i\eta}\})$ is shorthand for an infinite product of delta functions for the infinite set $\{c\}$ such that, after integration, $c_\mathbf{k} \to a_\mathbf{k} e^{i\eta}$ for all $\mathbf{k}$. The expression on the last line of Eq. 6.1.17 can also be derived instantly without considering the convolution of two individual kernels, by inserting the product of the two delta functions into the overlap $\langle\{b\}|\{a\}\rangle$.

After inserting the coherent state (over-)completeness relation (see Eq. 5.2.13), the last line of our expression for the rate in Eq. 6.1.10 gives,

$$
\begin{aligned}
\mathcal{R}_n(E) &= \int d(\{b^*\}, \{b\})e^{-\int d\mathbf{k}\, b_\mathbf{k}^* b_\mathbf{k}} \langle 0|\hat{\mathcal{O}}^\dagger \hat{S}^\dagger|\{b\}\rangle\langle\{b\}|\hat{P}_E \hat{P}_n \hat{S}\hat{\mathcal{O}}|0\rangle \\
&= \int d(\{b^*\}, \{b\})e^{-\int d\mathbf{k}\, b_\mathbf{k}^* b_\mathbf{k}} \\
&\quad \times [S\mathcal{O}(b^*, 0)]^* \\
&\quad \times P_E P_n S\mathcal{O}(b^*, 0),
\end{aligned}
$$
$$(6.1.18)$$

where we have identified the two matrix elements as kernels of product operators in the coherent state formalism.

Given that $\hat{\mathcal{O}} = \hat{\mathcal{O}}[\hat{\phi}(0)]$, we can simply absorb it into the path integral during the derivation of $S(b^*, a)$ seen in Section 5.2.2,

$$S\mathcal{O}(b^*, a) = \lim_{t_f, t_i \to \pm\infty} \int d\phi_f d\phi_i e^{B_i(\phi_i; a) + B_f(\phi_f; b^*)} \int \mathcal{D}\phi\, \mathcal{O}[\phi]\, e^{iS[\phi]_{t_i}^{t_f}}. \qquad (6.1.19)$$

As in Section 5.2.2, the functional integral satisfies the boundary conditions in Eq. 5.2.26. The definitions of $B_i(\phi_i; a)$ and $B_f(\phi_f; b^*)$ are given in Eq. 5.2.29.

We now turn to the incorporation of the projection operators. Following the logic used in deriving the product kernel $P_E P_n(b^*, a)$ in Eq. 6.1.17, we deduce,

$$
\begin{aligned}
P_E P_n S\mathcal{O}(b^*, a) &= \int d(\{c^*\}, \{c\}) e^{-\int d\mathbf{k}\, c_{\mathbf{k}}^* c_{\mathbf{k}}} P_E P_n(b^*, c) S\mathcal{O}(c^*, a) \\
&= \int d(\{c^*\}) \frac{d\xi}{2\pi} \frac{d\eta}{2\pi} e^{-iE\xi - in\eta} \delta(\{c^*\} - \{b^* e^{i\omega_{\mathbf{k}}\xi + i\eta}\}) S\mathcal{O}(c^*, a) \\
&= \int \frac{d\xi}{2\pi} \frac{d\eta}{2\pi} e^{-iE\xi - in\eta} S\mathcal{O}(b^* e^{i\omega_{\mathbf{k}}\xi + i\eta}, a).
\end{aligned}
$$

(6.1.20)

We now have all the ingredients needed to write the master equation for $\mathcal{R}(n, E)$. Combining Eqs. 6.1.18 and 6.1.20, we find,

$$
\begin{aligned}
\mathcal{R}(n, E) = \int d(\{b^*\}, \{b\}) \frac{d\xi}{2\pi} \frac{d\eta}{2\pi} \\
\times \exp\left[-iE\xi - in\eta - \int d\mathbf{k}\, b_{\mathbf{k}}^* b_{\mathbf{k}}\right] \\
\times [S\mathcal{O}]^*(b, 0) \\
\times S\mathcal{O}(b^* e^{i\omega_{\mathbf{k}}\xi + i\eta}, 0),
\end{aligned}
$$

(6.1.21)

where we have set $a = 0$ to reduce the coherent state $|\{a\}\rangle$ to the vacuum as required by Eq. 6.1.18. Making changes of variable,

$$
b_{\mathbf{k}}^* \to b_{\mathbf{k}}^* e^{-i\omega_{\mathbf{k}}\xi - i\eta}, \qquad \xi \to -\xi, \qquad \eta \to -\eta,
$$

(6.1.22)

gives,

$$
\begin{aligned}
\mathcal{R}(n, E) = \int d(\{b^*\}, \{b\}) \frac{d\xi}{2\pi} \frac{d\eta}{2\pi} \\
\times \exp\left[iE\xi + in\eta - \int d\mathbf{k}\, b_{\mathbf{k}}^* b_{\mathbf{k}} e^{i\omega_{\mathbf{k}}\xi + i\eta}\right] \\
\times [S\mathcal{O}]^*(b, 0) \\
\times S\mathcal{O}(b^*, 0).
\end{aligned}
$$

(6.1.23)

Inserting the definition of $S\mathcal{O}(b^*, 0)$ and the choice of operator $\hat{\mathcal{O}}$ in Eq. 6.1.19 finally yields the master equation for $\mathcal{R}(n, E)$ in the form given in [168], which we write below specifying all integration variables in the functional integrals (and dropping factors of $1/(2\pi)$ and $1/j$):

$$
\begin{aligned}
\mathcal{R}(n, E) = \lim_{t_f, t_i \to \pm\infty} \int d\xi d\eta\, db_{\mathbf{k}}^*\, db_{\mathbf{k}}\, d\phi_i(\mathbf{x})\, d\phi_f(\mathbf{x})\, \mathcal{D}\phi(\mathbf{x}, t)\, d\varphi_i(\mathbf{x})\, d\varphi_f(\mathbf{x})\, \mathcal{D}\varphi(\mathbf{x}, t) \\
\times \exp\left[iE\xi + in\eta - \int d\mathbf{k}\, b_{\mathbf{k}}^* b_{\mathbf{k}} e^{i\omega_{\mathbf{k}}\xi + i\eta} + \Xi\right],
\end{aligned}
$$

(6.1.24)

with the functional $\Xi = \Xi(\phi_i, \phi_f, \phi; \varphi_i, \varphi_f, \varphi; b_{\mathbf{k}}^*, b_{\mathbf{k}}; t_i, t_f)$ defined by,

$$
\begin{aligned}
\Xi = B_i(\phi_i; 0) + B_f(\phi_f; b^*) + [B_i(\varphi_i; 0)]^* + [B_f(\varphi_f; b^*)]^* \\
+ iS[\phi]_{t_i}^{t_f} - iS[\varphi]_{t_i}^{t_f} + j\phi(0) + j\varphi(0).
\end{aligned}
\tag{6.1.25}
$$

Eqs. 6.1.24 and 6.1.25 specify the multi-dimensional (functional and ordinary) integral we need to compute or estimate in order to determine the rate for multiparticle production processes. We will do so by method of steepest descent, i.e. the semi-classical approximation, and its validity will be justified in the following section by bringing the large parameter (the equivalent of $1/\hbar$ in the simple WKB method) out in front of all terms appearing in the exponent in Eqs. 6.1.24 and 6.1.25.

It will be useful to keep in mind the explicit forms of the four boundary terms. These follow from Eq. 5.2.29 and are given below,

$$
\begin{aligned}
B_i(\phi_i; 0) &= -\frac{1}{2} \int d\mathbf{k}\, \omega_{\mathbf{k}} \tilde{\phi}_i(\mathbf{k}) \tilde{\phi}_i(-\mathbf{k}), \\
B_f(\phi_f; b^*) &= -\frac{1}{2} \int d\mathbf{k}\, b_{\mathbf{k}}^* b_{-\mathbf{k}}^* e^{2i\omega_{\mathbf{k}} t_f} - \frac{1}{2} \int d\mathbf{k}\, \omega_{\mathbf{k}} \tilde{\phi}_f(\mathbf{k}) \tilde{\phi}_f(-\mathbf{k}) + \int d\mathbf{k}\, \sqrt{2\omega_{\mathbf{k}}} b_{\mathbf{k}}^* \tilde{\phi}_f(\mathbf{k}) e^{i\omega_{\mathbf{k}} t_f}, \\
[B_i(\varphi_i; 0)]^* &= -\frac{1}{2} \int d\mathbf{k}\, \omega_{\mathbf{k}} \tilde{\varphi}_i(\mathbf{k}) \tilde{\varphi}_i(-\mathbf{k}), \\
[B_f(\varphi_f; b^*)]^* &= -\frac{1}{2} \int d\mathbf{k}\, b_{\mathbf{k}} b_{-\mathbf{k}} e^{-2i\omega_{\mathbf{k}} t_f} - \frac{1}{2} \int d\mathbf{k}\, \omega_{\mathbf{k}} \tilde{\varphi}_f(\mathbf{k}) \tilde{\varphi}_f(-\mathbf{k}) \\
&\quad + \int d\mathbf{k}\, \sqrt{2\omega_{\mathbf{k}}} b_{\mathbf{k}} \tilde{\varphi}_f(-\mathbf{k}) e^{-i\omega_{\mathbf{k}} t_f}.
\end{aligned}
\tag{6.1.26}
$$

Recall that tildes denote the spatial Fourier transformations of the fields defined in Eq. 5.2.30.

6.1.2 Application of steepest-descent method

Discussion of the validity of steepest descent/semiclassical approach

In quantum mechanics, steepest descent methods are very useful, as one often obtains integrals of exponentials with a $1/\hbar$ prefactor in the exponent. The key to the validity of the method is that one can consider the $\hbar \to 0$ limit. Of course $\hbar$ is a dimensionful parameter and one needs to identify the appropriate large dimensionless factor in front of the functions in the exponent that goes as $1/\hbar$.

In quantum field theory, the semiclassical approximation in the simplest scenarios is achieved by rescaling all fields in the action S such that $S \propto 1/\lambda$ where λ is the coupling constant. The relevant limit is the weak-coupling limit $\lambda \to 0$. This reasoning holds for instanton calculations of Green functions and amplitudes in

gauge theories [200, 201]. In this case one rescales the gauge fields $A_\mu \to g A_\mu$, where g is the gauge coupling and, as a result, the microscopic action of the theory $S = \frac{1}{g^2} \int d^4 x \, \mathrm{tr} F_{\mu\nu} F^{\mu\nu} \propto \frac{1}{g^2}$, which is the equivalent of $1/\lambda$. If scalar fields are also present in the theory, then one rescales them with $\sqrt{\lambda}$ and the relevant terms in the action scale as $1/\lambda$, which is taken to be $\propto 1/g^2$ in the common weak-coupling limit $\lambda \to 0$, $g^2 \to 0$.

The main lesson concerning the applicability of the steepest descent approximation to the multiple integrals we want to evaluate, is that one needs to arrange for all relevant terms appearing in the exponent of the integrand to contain the same large multiplicative factor. By *relevant* terms we mean the terms that have a potential to influence the saddle-point solution, which will provide the dominant contribution to the integral. To be on the safe side, we can demand that *all* terms in the exponent contain this large factor. Once this is achieved, we search for an extremum of the function in the exponent – called the stationary solution or the the saddle-point – and expand all the integration variables in the integrand around this extremum. Following such an expansion, one would usually compute the integral by integrating over the fluctuations around this extremum. This is equivalent to using a background perturbation theory in the background of the saddle-point solution. In reality, to obtain the leading-order result, it is sufficient to just compute the exponent of the integrand on the saddle-point configuration. The leading-order corrections come from integrating over quadratic fluctuations around the saddle-point. These are Gaussian integrals and determine the prefactor in front of the exponent. Each subsequent order in fluctuations is suppressed by an extra power of $(\mathrm{large \, parameter})^{-1/2} \ll 1$ on general dimensional grounds.

In our case we have, *a priori*, three large dimensionless parameters, $1/\lambda$, n and E/m. The first one is an internal parameter of the theory, while the second and the third are process-dependent – they arise from specifying the final state to contain $n \gg 1$ particles at high energies $E \gg m$. In a sense, the entire rationale for developing the coherent state approach that led to the expression for the rate in the form shown in Eq. 6.1.24 was to pull the dependence on n and E from the final state into the exponent of the rate. Essentially, the quantity in the exponent on the second line of Eq. 6.1.24 can be thought of as an effective action which depends on three large parameters, $1/\lambda$, n and E. Most important for the validity of the steepest descent approach, is that no n- and E-dependence appears elsewhere, in particular not in the integration variables: the number of integrations (functional and ordinary ones) is fixed and independent of n, E or λ.

Now, for the application of the steepest descent method we need to have just one large parameter. For that reason the appropriate semiclassical limit is defined where

n and $1/\lambda$ are of the same order, such that their ratio is held fixed in the limit $n \to \infty$. Indeed, it is easy to see that $n = \lambda n/\lambda$ is $\sim 1/\lambda$ for $\lambda n = $ fixed. Similarly we have to hold $n \propto E/m$. Thus the steepest descent approximation to the integral in Eq. 6.1.24 is justified in the weak-coupling – large-n – high-E semiclassical limit:

$$\lambda \to 0\,, \quad n \to \infty\,, \quad \text{with} \quad \lambda n = \text{fixed}\,, \quad \varepsilon = \text{fixed}\,. \qquad (6.1.27)$$

Here ε denotes the average kinetic energy per particle per mass in the final state,

$$\varepsilon = (E - nm)/(nm)\,. \qquad (6.1.28)$$

Holding ε fixed implies that in the large-n limit we are raising the total energy linearly with n. Note that there is no $E \to \infty$ appearing in the limit in Eq. 6.1.27. The variable $E/(nm)$ is traded for ε using Eq. 6.1.28 and held fixed.

We further note that the perturbation theory in the background of the saddle-point solution has conceptually-different conclusions from the usual perturbation theory in a trivial background. Even though the perturbative corrections in both cases are suppressed by powers of λ, in the case of the steepest descent method, these corrections cannot be enhanced by powers of n. As we mentioned already, in our approach n and E/m are large parameters of the same order as $1/\lambda$, and the hypothetical contribution $\sim \lambda n$ cannot appear as a perturbative order-λ correction – it should instead be a part of the leading-order result. This is different from the usual perturbation theory in which n can arise as a combinatorial enhancement of the order-λ perturbative corrections. So it should not come as a surprise that the steepest descent, or equivalently the semiclassical method, is a non-perturbative computation, with controlled corrections in the semiclassical limit that are suppressed by powers of $1/n$, λ and m/E.

We now finally discuss the scaling of the exponent in Eq. 6.1.24 with the large parameter. For the semiclassical method to be applicable, all terms in the exponent must be the same order in $1/\lambda$ in the limit in Eq. 6.1.27. To achieve this we rescale the fields and coherent state variables, as well as the source j coming from the operator $\mathcal{O}$ insertion by $1/\sqrt{\lambda}$,

$$\{\phi, \varphi, b_{\mathbf{k}}^*, b_{\mathbf{k}}, j\} \to \frac{1}{\sqrt{\lambda}}\{\phi, \varphi, b_{\mathbf{k}}^*, b_{\mathbf{k}}, j\}. \qquad (6.1.29)$$

Taking into account that $n \sim E \sim 1/\lambda$, we see that the entire exponent in Eq. 6.1.24 now scales as $1/\lambda$ in the limit in Eq. 6.1.27 as required for the validity of the steepest descent approach. However, this scaling implies that the source term in the operator

in Eq. 6.1.11 used to produce the initial state is $j/\sqrt{\lambda}$ and,

$$|\phi_i\rangle \,=\, e^{\frac{j}{\sqrt{\lambda}}\frac{\phi(0)}{\sqrt{\lambda}}}\,|0\rangle \,=\, e^{\frac{j}{\sqrt{\lambda}}\phi(0)_{\text{rescaled}}}\,|0\rangle\;. \qquad (6.1.30)$$

This is somewhat problematic as the operator in terms of the rescaled ϕ now explicitly depends on λ. The initial state is some semiclassical state with the mean particle number $\langle n_i\rangle \sim j/\lambda$ rather than being a single-particle state. As noted in the original papers [168, 197] that were developing this approach, this is the consequence of the non-semiclassical nature of the initial state with a single particle or with few highly energetic particles rather than a large number of soft ones. The resolution of the problem proposed in [168, 186, 197] is to continue applying the semiclassical i.e. the steepest descent approach to the integral in Eq. 6.1.24 with the source $j/\sqrt{\lambda}$ where j is a constant, and only after establishing the saddle-point equations take the limit $j \to 0$. In this case we effectively return to the single-particle initial state with $j/\lambda \sim 1$, but at the same time, the semiclassical method continues to be justified. Of course, this line of reasoning is not a proof, but at least it provides an unambiguous procedure for computation. Furthermore, in this limit one ends up with an operator $\mathcal{O}$ that does not depend on λ (or on $\hbar$ in quantum mechanics). In the quantum mechanical case, it is known that the analogous semiclassical computation – using the Landau WKB formulation – gives the semiclassical exponent of the rate, $W = \log \mathcal{R}$, which does not depend on the form of the operator used, in so far as the operator does not depend on $\hbar$ explicitly.

Perhaps the most important existing verification of this procedure is that, following it, Son has successfully reproduced in [168] the known results for the multiparticle rate at tree-level [179] and in the resummed one-loop approximation [176, 177, 179] with no use of perturbation theory. It was also demonstrated in [180] based on a few calculable examples for $1 \to n$ and $2 \to n$ processes, that the semiclassical exponent $W = \log \mathcal{R}$ does not depend on the construction of the initial state and that the multiparticle amplitudes should be the same – at the level of the exponent – for all few-particle initial states.

These computations were carried out in the regime of relatively low multiplicities where the fixed value of λn in Eq. 6.1.27 is taken to be small. This is the regime where the comparison of the semiclassical method results [168, 180] with the tree-level and leading-order loop corrections in ordinary perturbation theory [176, 177, 179] is meaningful. Of course the real usefulness of the semiclassical approach lies in applying it to the opposite regime of high multiplicities, where the rescaled multiplicity λn is taken to be large. This is the non-perturbative regime where currently no other predictions for the multiparticle rates are known in QFT in 4 dimensions. Nevertheless, the semiclassical approach in the large λn limit can

still be successfully tested in $(2+1)$ dimensions against the known RG-resummed perturbative results [202] in a regime where both approaches are valid. This was shown in [169] and will be reviewed in Section 6.4.

From now on, we will take the $j \to 0$ prescription as a constructive approach for applying the semiclassical method to the calculation of the $1 \to n$ processes following [168]. In summary: the semiclassical formalism is fully self-consistent for computing the multi-particle rate in Eq. 6.1.24 with the initial state defined by Eq. 6.1.30. To obtain the result for the probability rate of the $1 \to n$ processes we will take the limit $j \to 0$ after writing down the saddle-point equations that will follow from extremising the exponent in Eq. 6.1.24 in the next section.

Finding the saddle-point

With all terms in the exponent in Eq. 6.1.24 being of the same order with respect to the large semiclassical parameter $1/\lambda$, we are ready to proceed with deriving the equations for its extremum. It is no longer necessary to use the rescaled fields in Eq. 6.1.29, as we are primarily interested in the leading-order semiclassical expression for the rate. Hence we will use the integral representation of the rate in the original form in Eq. 6.1.24. We also note that the saddle-point trajectory in the steepest descent method allows $\phi(x)$ to be complex, so from this point on we will have to take a little more care with the relationships between ϕ and ϕ^* in position and momentum space.

Applying the steepest descent approach to the integral in Eq. 6.1.29, we search for an extremum of,

$$ W = iE\xi + in\eta - \int d\mathbf{k}\, b_{\mathbf{k}}^* b_{\mathbf{k}} e^{i\omega_{\mathbf{k}}\xi + i\eta} + \Xi(\phi_i, \phi_f, \phi; \varphi_i, \varphi_f, \varphi; b_{\mathbf{k}}^*, b_{\mathbf{k}}). \qquad (6.1.31) $$

In principle, we should look for all extrema of this expression and then select the one which gives the dominant (i.e largest) contribution to $\mathcal{R}_n(E)$ – normally, this would be the one with the maximal value of W. More generally, one would sum over the contributions to $\mathcal{R}_n(E) \propto e^W$ from all extrema. In what follows we will end up selecting a particular stationary point solution: the one with the highest symmetry between ϕ and φ components, whose contribution gives the lower bound to the total rate $\mathcal{R}_n(E)$.

The extrema or saddle-points are solutions of the equations $\delta_\chi W = 0$, where the set $\chi = \{\xi, \eta, \phi(\mathbf{x},t), \phi_i(\mathbf{x}), \phi_f(\mathbf{x}), \varphi(\mathbf{x},t), \varphi_i(\mathbf{x}), \varphi_f(\mathbf{x}), b_{\mathbf{k}}^*, b_{\mathbf{k}}\}$ denotes all integration variables.

Following Ref. [168] we will look for a saddle-point solution for which ξ and η are purely imaginary (this corresponds to deforming the integration contours in ξ and

η to pass through this complex saddle-point configuration – the standard practice required in steepest descent). Keeping with Son's notation we change variables,

$$\xi = -iT, \qquad \eta = i\theta, \tag{6.1.32}$$

and treat T and θ as real variables. We now vary W,

$$W = ET - n\theta - \int d\mathbf{k}\, b_{\mathbf{k}}^* b_{\mathbf{k}} e^{\omega_{\mathbf{k}} T - \theta} + \Xi(\phi_i, \phi_f, \phi; \varphi_i, \varphi_f, \varphi; b_{\mathbf{k}}^*, b_{\mathbf{k}}), \tag{6.1.33}$$

with respect to,

$$\chi = \{T, \theta, \phi(\mathbf{x}, t), \phi_i(\mathbf{x}), \phi_f(\mathbf{x}), \varphi(\mathbf{x}, t), \varphi_i(\mathbf{x}), \varphi_f(\mathbf{x}), b_{\mathbf{k}}^*, b_{\mathbf{k}}\}, \quad \frac{\delta W}{\delta \chi} = 0. \tag{6.1.34}$$

Variations with respect to variables in Eq. 6.1.32, T and θ, give the equations for the E and n,

$$\partial_T W : \qquad E = \int d\mathbf{k}\, \omega_{\mathbf{k}} b_{\mathbf{k}}^* b_{\mathbf{k}} e^{\omega_{\mathbf{k}} T - \theta} \tag{6.1.35}$$

$$\partial_\theta W : \qquad n = \int d\mathbf{k}\, b_{\mathbf{k}}^* b_{\mathbf{k}} e^{\omega_{\mathbf{k}} - \theta}. \tag{6.1.36}$$

Next we obtain the saddle-point equations for ϕ, $\tilde{\phi}_i$, $\tilde{\phi}_f$ and $b_{\mathbf{k}}^*$,

$$\frac{\delta W}{\delta \phi(x)} : \qquad \frac{\delta S}{\delta \phi(x)} = ij\delta^{d+1}(x) \tag{6.1.37}$$

$$\frac{\delta W}{\delta \tilde{\phi}_i(-\mathbf{k})} : \qquad i\partial_{t_i} \tilde{\phi}_i(\mathbf{k}) + \omega_{\mathbf{k}} \tilde{\phi}_i(\mathbf{k}) = 0 \tag{6.1.38}$$

$$\frac{\delta W}{\delta \tilde{\phi}_f(-\mathbf{k})} : \qquad i\partial_{t_f} \tilde{\phi}_f(\mathbf{k}) - \omega_{\mathbf{k}} \tilde{\phi}_f(\mathbf{k}) + \sqrt{2\omega_{\mathbf{k}}}\, b_{-\mathbf{k}}^* e^{i\omega_{\mathbf{k}} t_f} = 0 \tag{6.1.39}$$

$$\frac{\delta W}{\delta b_{\mathbf{k}}^*} : \qquad -b_{\mathbf{k}} e^{\omega_{\mathbf{k}} T - \theta} - b_{-\mathbf{k}}^* e^{2i\omega_{\mathbf{k}} t_f} + \sqrt{2\omega_{\mathbf{k}}}\, \tilde{\phi}_f(\mathbf{k}) e^{i\omega_{\mathbf{k}} t_f} = 0. \tag{6.1.40}$$

The first terms in Eqs. 6.1.38 and 6.1.39 come from the boundary contributions to the action S from total derivatives,

$$S_{\text{Boundary}}[\phi_i, \phi_f] = \frac{1}{2} \int_{t_i}^{t_f} dt \int d^d x\, \partial_t(\phi\, \partial_t \phi) = \frac{1}{2} \int d^d x\, (\phi_f \partial_t \phi_f - \phi_i \partial_t \phi_i), \tag{6.1.41}$$

as explained in Appendix C.1 in more detail. The other terms arise rather straightforwardly from the rest of the expression in Eq. 6.1.33

Unsurprisingly, equations analogous to Eqs. 6.1.37 to 6.1.40 exist for φ, $\tilde{\varphi}_i$, $\tilde{\varphi}_f$ and $(b_{\mathbf{k}}^*)^*$. Note that, *a priori*, there is no need for $b_{\mathbf{k}}$ and $b_{\mathbf{k}}^*$ to be complex conjugates, nor is there any constraint on the complex phases of ξ and η. Nevertheless, there exists a saddle-point for which $(b_{\mathbf{k}})^* = b_{\mathbf{k}}^*$, and ξ and η are purely imaginary (and thus T and θ are purely real). We focus on this scenario, as Son does [168]. With these

assignments in mind, the final group of saddle-point equations give the equations for the remaining field variables, φ, $\tilde{\varphi}_i$, $\tilde{\varphi}_f$ and $b_{\mathbf{k}}$,

$$\frac{\delta W}{\delta \varphi(x)} : \qquad \frac{\delta S}{\delta \varphi(x)} = -ij\delta^{d+1}(x) \tag{6.1.42}$$

$$\frac{\delta}{\delta \tilde{\varphi}_i(-\mathbf{k})} : \qquad -i\partial_{t_i}\tilde{\varphi}_i(\mathbf{k}) + \omega_{\mathbf{k}}\tilde{\varphi}_i(\mathbf{k}) = 0 \tag{6.1.43}$$

$$\frac{\delta W}{\delta \tilde{\varphi}_f(-\mathbf{k})} : \qquad -i\partial_{t_f}\tilde{\varphi}_f(\mathbf{k}) - \omega_{\mathbf{k}}\tilde{\varphi}_f(\mathbf{k}) + \sqrt{2\omega_{\mathbf{k}}}\, b_{\mathbf{k}} e^{-i\omega_{\mathbf{k}}t_f} = 0 \tag{6.1.44}$$

$$\frac{\delta W}{\delta b_{\mathbf{k}}} : \qquad -b_{\mathbf{k}}^* e^{\omega_{\mathbf{k}}T-\theta} - b_{-\mathbf{k}} e^{-2i\omega_{\mathbf{k}}t_f} + \sqrt{2\omega_{\mathbf{k}}}\, \tilde{\varphi}_f(-\mathbf{k}) e^{-i\omega_{\mathbf{k}}t_f} = 0. \tag{6.1.45}$$

It is not difficult to see that these equations (Eqs. 6.1.42 to 6.1.45) are satisfied by,

$$\varphi(t,\mathbf{x}) = [\phi(t,\mathbf{x})]^* \quad \longrightarrow \quad \tilde{\varphi}(\mathbf{k}) = [\tilde{\phi}(-\mathbf{k})]^*, \tag{6.1.46}$$

if ϕ satisfies its saddle-point equations (Eqs. 6.1.37 to 6.1.40). We will focus on solutions for which Eq. 6.1.46 holds from here on, which implies that we only need to solve the field equations (Eqs. 6.1.37 to 6.1.40), and then trade the Lagrange multiplied variables T and θ for the final state energy and multiplicity, E and n, using Eqs. 6.1.35 and 6.1.36. For a discussion on more general saddle points, see Appendix C.2.

Let us consider what the saddle-point equations imply for our scalar field, $\phi(x)$. Eq. 6.1.37 gives the classical field equations with a singular point-like source at the origin $x = 0$. We are searching for classical solutions in a $(d+1)$-dimensional theory that become free fields at $t \to \pm\infty$ and thus the classical field in these limits must be a superposition of plane waves.

Solving Eq. 6.1.38 gives $\tilde{\phi}_i(\mathbf{k}) \sim e^{i\omega_{\mathbf{k}}t_i}$ with no $e^{-i\omega_{\mathbf{k}}t_i}$ components allowed. Using Eq. 5.2.11 to recover the coefficient in front of $e^{i\omega_{\mathbf{k}}t_i}$ we find,

$$\tilde{\phi}_i(\mathbf{k}) = \frac{1}{\sqrt{2\omega_{\mathbf{k}}}}\, a_{-\mathbf{k}}^* \, e^{i\omega_{\mathbf{k}}t_i}, \qquad t_i \to -\infty. \tag{6.1.47}$$

This is the behaviour of $\tilde{\phi}(t,\mathbf{k})$ in the infinite past. The coefficient $a_{-\mathbf{k}}^*$ is an arbitrary Fourier component. Rearranging Eq. 6.1.40 gives the behaviour in the infinite future,

$$\tilde{\phi}_f(\mathbf{k}) = \frac{1}{\sqrt{2\omega_{\mathbf{k}}}}(b_{\mathbf{k}} e^{\omega_{\mathbf{k}}T-\theta-i\omega_{\mathbf{k}}t_f} + b_{-\mathbf{k}}^* e^{i\omega_{\mathbf{k}}t_f}), \qquad t_f \to +\infty, \tag{6.1.48}$$

which, as one would expect, satisfies Eq. 6.1.39. Thus Eqs. 6.1.38 to 6.1.40 have simply provided boundary conditions at t_i and t_f for the solution $\phi(x)$ of the Euler-Lagrange equation in Eq. 6.1.37. Both boundary conditions correspond to a complex-valued saddle-point solution for $\phi(x)$, since the first condition (see Eq. 6.1.47) has $a_{\mathbf{k}}^* = 0$, while the second boundary condition (see Eq. 6.1.48) contains the factor

$e^{\omega_{\mathbf{k}} T - \theta}$ accompanying $b_{\mathbf{k}}$ that prevents the coefficients of $e^{\pm i \omega_{\mathbf{k}} t_f}$ from being complex conjugates of each other.

We can now compute the energy and the particle number on the saddle-point solution from its $t \to \pm \infty$ asymptotics in Eqs. 6.1.47 and 6.1.48. At $t \to -\infty$ the energy and the particle number are vanishing since the corresponding solution contains only the $e^{i\omega_{\mathbf{k}} t}$ harmonics. On the other hand at $t \to +\infty$, using the free-field solution in Eq. 6.1.48, we find,

$$E = \int d\mathbf{k} \; \omega_{\mathbf{k}} \, b_{\mathbf{k}}^* \, b_{\mathbf{k}} \, e^{\omega_{\mathbf{k}} T - \theta}, \qquad n = \int d\mathbf{k} \; b_{\mathbf{k}}^* \, b_{\mathbf{k}} \, e^{\omega_{\mathbf{k}} T - \theta}. \qquad (6.1.49)$$

These are precisely the saddle-point equations in Eqs. 6.1.35 and 6.1.36. The energy of course is conserved by regular solutions at $t < 0$ and at $t > 0$ and changes discontinuously from 0 to E at the singularity at the origin $t = 0 = \mathbf{x}$ induced by the δ-function source in Eq. 6.1.37.

In other words, E and n are the energy and multiplicity of the solution ϕ for $t > 0$. In the absence of the source, one expects the energy of the field to be conserved. Indeed, energy is conserved individually in the regions $t < 0$ and $t > 0$, where solutions contain no singularities and there is no source. However, at $t = 0$, the point source will give a discontinuous jump in energy. This can be seen by looking at Eq. 6.1.37. The left-hand side reduces to an Euler-Lagrange term and so we have a second-order partial differential equation with a point source. We know from Green's function theory that we should expect the solution, ϕ, to have a discontinuity in its first derivative in some direction at $x = 0$. Suppose that this direction is the time direction such that by integrating Eq. 6.1.37 over the region $-\epsilon \leq t \leq \epsilon$ for small ϵ,

$$\int\limits_{-\epsilon}^{+\epsilon} dt \frac{\delta S[\phi]}{\delta \phi(x)} = \left[\frac{\partial \mathcal{L}}{\partial (\partial_t \phi)} \right]_{-\epsilon}^{+\epsilon} = (\partial_t \phi)_{+\epsilon} - (\partial_t \phi)_{-\epsilon} = \delta \dot{\phi}(0, \mathbf{x}) = ij\delta^d(\mathbf{x}), \qquad (6.1.50)$$

with a dot indicating a time derivative, $\dot{\phi} = \partial_t \phi$. This gives an energy jump,

$$\begin{aligned} \delta E =& \delta \left(\frac{1}{2} \int d^d x \dot{\phi}^2 \right) = \frac{1}{2} \int d^d x ([\dot{\phi}(+\epsilon, \mathbf{x})]^2 - [\dot{\phi}(-\epsilon, \mathbf{x})]^2) \\ =& \frac{1}{2} \int d^d x (\dot{\phi}_+ - \dot{\phi}_-)(\dot{\phi}_+ + \dot{\phi}_-) = \int d^d x \dot{\phi}(0, \mathbf{x}) \delta \dot{\phi}(0, \mathbf{x}) = ij\dot{\phi}(0), \end{aligned} \qquad (6.1.51)$$

where $\dot{\phi}(0, \mathbf{x})$ is strictly the mean of the $t = \pm \epsilon$ values and the last step follows from Eq. 6.1.50. Recall that the early-time asymptote in Eq. 6.1.47 has only positive frequency components and thus has zero energy. Therefore, the energy associated with the saddle-point field configuration undergoes a discontinuous jump from 0 to $E = \delta E = ij\dot{\phi}(0)$, when crossing $t = 0$.

The $j \to 0$ limit

After having found the defining equations for the saddle-point, we now want to take the $j \to 0$ limit in order to obtain the rate for the $1^* \to n$ processes, as explained in Section 6.1.2.

Taking this limit amounts to more than just setting the source term to zero in the non-linear equations shown in Eqs. 6.1.37 and 6.1.42. In fact, the solutions of the Euler-Lagrange equations without the source term must now become singular at the point $x = 0$ in order to ensure the jump in energy from $E = 0$ at $t < 0$ to $E \neq 0$ at $t > 0$. This singular behaviour of the saddle-point solution is not an additional requirement, but a direct consequence of the saddle-point equations, which require the asymptotic behaviour shown in Eqs. 6.1.47 and 6.1.48, with the jump in energy by E in Eq. 6.1.49. It follows from Eq. 6.1.51 that the late-time energy is $E = ij\dot{\phi}(0)$. For E to be fixed and non-vanishing, as is required for the scattering process of interest, we must require $\dot{\phi}(0) \to \infty$. In other words, the classical solution at the point $x = 0$, as well as its derivative, are singular to ensure that,

$$E = ij\dot{\phi}(x)|_{x=0} = \text{fixed}, \quad \text{for} \quad j \to 0 \quad \text{with} \quad \dot{\phi}(x)|_{x=0} \to \infty. \tag{6.1.52}$$

With these considerations in mind, we now take the limit $j \to 0$ in the saddle-point equations and in the exponent of the rate in Eqs. 6.1.25 and 6.1.33.

Evaluation of integrand at saddle-point

With the saddle-point equations found, we move onto imposing the saddle-point behaviour on the exponent of the rate in Eq. 6.1.24. The function in the exponent can be written as (*cf.* Eqs. 6.1.25 and 6.1.33),

$$W = ET - n\theta + iS[\phi] - iS[\varphi] \tag{6.1.53}$$
$$+ B_i(\phi_i; 0) + B_f(\phi_f; b^*) + [B_i(\varphi_i; 0)]^* + [B_f(\varphi_f; b^*)]^* - \int d\mathbf{k}\, b_\mathbf{k}^* b_\mathbf{k}\, e^{\omega_\mathbf{k} T - \theta}.$$

We now show that the sum of the terms appearing on the second line in Eq. 6.1.53 is vanishing when evaluated on the saddle-point solution for ϕ_i and ϕ_f given in Eqs. 6.1.47 and 6.1.48, in the limit $t_i \to -\infty$ and $t_f \to +\infty$. Indeed,

$$B_i(\phi_i; 0) = -\frac{1}{2} \int d\mathbf{k}\, \omega_\mathbf{k} \tilde{\phi}_i(\mathbf{k}) \tilde{\phi}_i(-\mathbf{k}) = \lim_{t_i \to -\infty} \left(-\frac{1}{4} \int d\mathbf{k}\, a_{-\mathbf{k}}^* a_\mathbf{k}^* e^{2i\omega_\mathbf{k} t_i} \right) = 0,$$
$$\tag{6.1.54}$$

since only the negative frequency plane wave components are present in $\tilde{\phi}_i$. We now evaluate the boundary term $B_f(\phi_f; b^*)$ at t_f in the $t_f \to +\infty$ limit,

$$
\begin{aligned}
B_f(\phi_f; b^*) &= -\frac{1}{2} \int d\mathbf{k}\, b_{\mathbf{k}}^* b_{-\mathbf{k}}^* e^{2i\omega_{\mathbf{k}} t_f} - \frac{1}{2} \int d\mathbf{k}\, \omega_{\mathbf{k}} \tilde{\phi}_f(\mathbf{k}) \tilde{\phi}_f(-\mathbf{k}) + \int d\mathbf{k} \sqrt{2\omega_{\mathbf{k}}}\, b_{\mathbf{k}}^* \tilde{\phi}_f(\mathbf{k}) e^{i\omega_{\mathbf{k}} t_f} \\
&\to 0 - \frac{1}{2} \int d\mathbf{k}\, \frac{\omega_{\mathbf{k}}}{2\omega_{\mathbf{k}}} 2 b_{\mathbf{k}} e^{\omega_{\mathbf{k}} T - \theta} b_{\mathbf{k}}^* + \int d\mathbf{k} \sqrt{2\omega_{\mathbf{k}}}\, b_{\mathbf{k}}^* \frac{1}{\sqrt{2\omega_{\mathbf{k}}}} b_{\mathbf{k}} e^{\omega_{\mathbf{k}} T - \theta} \\
&= \frac{1}{2} \int d\mathbf{k}\, b_{\mathbf{k}} b_{\mathbf{k}}^* e^{\omega_{\mathbf{k}} T - \theta}, \qquad\qquad\qquad\qquad\qquad\qquad\qquad (6.1.55)
\end{aligned}
$$

and similarly, for $[B_i(\varphi_i; 0)]^*$ we have the same result,

$$
[B_i(\varphi_i; 0)]^* = \frac{1}{2} \int d\mathbf{k}\, b_{\mathbf{k}} b_{\mathbf{k}}^* e^{\omega_{\mathbf{k}} T - \theta}. \qquad\qquad (6.1.56)
$$

This implies that the sum of the boundary terms on the second line in Eq. 6.1.53 is vanishing, as already stated,

$$
B_i(\phi_i; 0) + B_f(\phi_f; b^*) + [B_i(\varphi_i; 0)]^* + [B_f(\varphi_f; b^*)]^* - \int d\mathbf{k}\, b_{\mathbf{k}}^* b_{\mathbf{k}}\, e^{\omega_{\mathbf{k}} T - \theta} = 0. \qquad (6.1.57)
$$

Thus the expression in Eq. 6.1.53, evaluated on the saddle-point solution, simplifies to,

$$
W = ET - n\theta + iS[\phi] - iS[\phi]^*, \qquad\qquad (6.1.58)
$$

where we have identified $iS[\varphi] = iS[\phi]^*$ on our saddle-point solution.

Ultimately, as soon as the saddle-point solution $\phi(x)$ is found for all values of t, we obtain the saddle-point value of $\mathcal{R}_n(E)$ to exponential accuracy,

$$
\mathcal{R}_n(E) = e^{W(E,n)}, \qquad\qquad (6.1.59)
$$

with,

$$
W(E, n) = ET - n\theta - 2\mathrm{Im}S[\phi]. \qquad\qquad (6.1.60)
$$

Here the constant parameters T and θ are the solutions of the corresponding saddle-point equations (Eqs. 6.1.35 and 6.1.36), and $\phi(x)$ is the solution of the sourceless Euler-Lagrange equation, $\delta S/\delta\phi = 0$, with the (initial and final) boundary conditions in Eqs. 6.1.47 and 6.1.48.

It is also worth noting that the function $W(E, n)$ in Eq. 6.1.60 is a function of E and n and does not depend explicitly on the T and θ parameters. $W(E, n)$ is in fact the Legendre transformation of $2\mathrm{Im}S(T, \theta)$, where,

$$
E = \frac{\partial\, 2\mathrm{Im}S}{\partial T}, \qquad n = -\frac{\partial\, 2\mathrm{Im}S}{\partial \theta}, \qquad\qquad (6.1.61)
$$

and,

$$\frac{\partial W}{\partial E} = T, \qquad -\frac{\partial W}{\partial n} = \theta. \tag{6.1.62}$$

The relations in Eq. 6.1.61 defining E and n in terms of derivatives of the action of the classical field are in fact equivalent to the already familiar equations for E and n in Eq. 6.1.49 computed on the asymptotics of ϕ at $t \to +\infty$.

Summary of the approach in Minkowski spacetime

After the somewhat lengthy derivations in the previous sections it is worth summarising the resulting algorithm to compute the semiclassical rate [168] in the context of the model in Eq. 4.1.3 with spontaneous symmetry breaking:

1. Solve the classical equation without the source-term,

$$\frac{\delta S}{\delta h(x)} = 0, \tag{6.1.63}$$

   by finding a complex-valued solution $h(x)$ with a point-like singularity at the origin $x^\mu = 0$ and regular everywhere else in Minkowski space. The singularity at the origin is selected by the location of the operator $\mathcal{O}(x = 0)$.

2. Impose the initial and final-time boundary conditions,

$$\lim_{t \to -\infty} h(x) = v + \int \frac{d^d k}{(2\pi)^{d/2}} \frac{1}{\sqrt{2\omega_{\mathbf{k}}}} \, a_{\mathbf{k}}^* \, e^{ik_\mu x^\mu}, \tag{6.1.64}$$

$$\lim_{t \to +\infty} h(x) = v + \int \frac{d^d k}{(2\pi)^{d/2}} \frac{1}{\sqrt{2\omega_{\mathbf{k}}}} \left(b_{\mathbf{k}} \, e^{\omega_{\mathbf{k}} T - \theta} \, e^{-ik_\mu x^\mu} + b_{\mathbf{k}}^* \, e^{ik_\mu x^\mu} \right). \tag{6.1.65}$$

3. Compute the energy and the particle number using the $t \to +\infty$ asymptotics of $h(x)$,

$$E = \int d^d k \, \omega_{\mathbf{k}} \, b_{\mathbf{k}}^* \, b_{\mathbf{k}} \, e^{\omega_{\mathbf{k}} T - \theta}, \qquad n = \int d^d k \, b_{\mathbf{k}}^* \, b_{\mathbf{k}} \, e^{\omega_{\mathbf{k}} T - \theta}. \tag{6.1.66}$$

   At $t \to -\infty$ the energy and the particle number are vanishing. The energy is conserved by regular solutions and changes discontinuously from 0 to E at the singularity at $t = 0$.

4. Eliminate the T and θ parameters in favour of E and n using the expressions above. Finally, compute the function $W(E, n)$

$$W(E, n) = ET - n\theta - 2\mathrm{Im}S[h] \tag{6.1.67}$$

   on the set $\{h(x), T, \theta\}$ to obtain the semiclassical rate $\mathcal{R}_n(E) = \exp[W(E, n)]$.
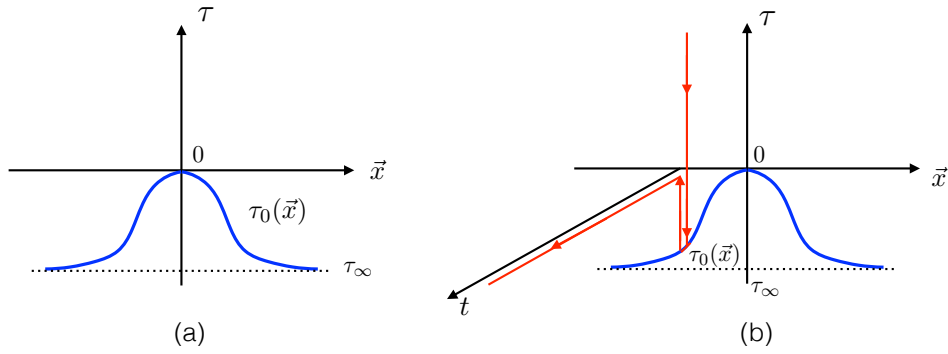
Figure 6.1: *Plot (a): The shape of the singularity surface $\tau = \tau_0(\mathbf{x})$ of the field configuration $h(x)$ is shown in blue. Plot (b) shows the time evolution contour of Fig. 4.1 (a), depicted in red, in the coordinate system $(t, \tau; \mathbf{x})$.*

6.1.3   Reformulation of the boundary value problem

To keep our discussion general, at the start of this section we do not necessarily assume the existence of a spontaneously broken symmetry and return to a generic QFT case with the scalar field denoted by $\phi(x)$. Then, at the end of this section, we summarise the findings in the context of the theory of the scalar field $h(x)$ with the VEV. This follows the same presentational pattern as in the preceding section, where Section 6.1.2 used a generic scalar $\phi(x)$ before presenting a summary at the end in terms of $h(x)$.

Extension to complex time

In Minkowski space, we require that ϕ is regular everywhere except for the singularity at $x = 0$. Ref. [168] complexifies the time coordinate, allowing for imaginary times, τ, so that a general complex time, $t_{\mathbb{C}}$, can be written as $t + i\tau$. Now, $t = 0$ is a $(d+1)$-plane in the $(d+2)$-dimensional $(t_{\mathbb{C}}, \mathbf{x})$ space. As such, the point singularity at $(0, \mathbf{0})$ is in general extended to a d-dimensional singularity surface, A, parametrised as $(i\tau_0(\mathbf{x}), \mathbf{x})$, with the constraint that $\tau_0(\mathbf{0}) = 0$. This constraint ensures that the correct Minkowski singularity structure is maintained. The time-evolution contour on the complex time plane is shown in red in Figs. 4.1 and 6.1 (b). The d-dimensional singularity surface is shown in blue in Fig. 6.1 (a) in the $(d+1)$-dimensional Euclidean spacetime, and in the $(t, \tau, \mathbf{x})$ $(d+2)$-coordinates in Fig. 6.1 (b).

We now look for the field configuration that satisfies the field equation and is singular on A. Following Ref. [168], we will search for the solution by breaking it into two parts: ϕ_1 and ϕ_2. Each of these is a classical solution that satisfies one of the boundary conditions in Eqs. 6.1.47 and 6.1.48. The first part satisfies the Euclidean

asymptotics,

$$\tilde{\phi}_1(\mathbf{k}) = \frac{1}{\sqrt{2\omega_{\mathbf{k}}}} a^*_{-\mathbf{k}} e^{-\omega_{\mathbf{k}}\tau} \to 0, \qquad \tau \to +\infty, \qquad (6.1.68)$$

whereas the second part satisfies the original Minkowski late-time limit,

$$\tilde{\phi}_2(\mathbf{k}) = \frac{1}{\sqrt{2\omega_{\mathbf{k}}}} (b_{\mathbf{k}} e^{\omega_{\mathbf{k}}T - \theta - i\omega_{\mathbf{k}}t} + b^*_{-\mathbf{k}} e^{i\omega_{\mathbf{k}}t}), \qquad t \to +\infty. \qquad (6.1.69)$$

For a given $\mathbf{x}$, we consider the time evolution of the solution along the contour C in complex time, which has three distinct parts in red in Figs. 4.1 and 6.1 (b):

1. $(i\infty, i\tau_0(\mathbf{x}))$: contour begins at infinite Euclidean time and comes down to meet the singularity surface, A.

2. $(i\tau_0(\mathbf{x}), 0)$: after point contact with A, return back to Minkowski time axis. Note that for $\mathbf{x} = \mathbf{0}$, this step vanishes as $\tau_0(\mathbf{0}) = 0$.

3. $(0, \infty)$: travel along Minkowski-time axis to late times.

The first component, ϕ_1, is defined on part (1) of the contour. It is a classical solution, satisfying the initial-time boundary condition in Eq. 6.1.68 at $\tau = +\infty$ and is singular at $\tau = \tau_0(\mathbf{x})$. The solution ϕ_1, and the Euclidean action evaluated on it at this segment of the contour, are real-valued. Indeed, as we already noted in Section 4.2.2, classical evolution of the real-valued initial condition in Eq. 6.1.68 along the τ axis results in a manifestly-real field configuration along the first segment of the contour.

The second component, ϕ_2, is a classical solution defined on the parts (2) and (3) of the contour in Fig. 4.1. It is singular at $\tau = \tau_0(\mathbf{x})$, where it is equal to ϕ_1, and satisfies the final-time boundary condition in Eq. 6.1.69. As explained in Section 4.2.2, the boundary condition in Eq. 6.1.69 requires that we keep the final segment (3) of the contour along the Minkowski time axis t, and the solution is necessarily complex-valued on this segment.

Both ϕ_1 and ϕ_2 can be obtained by starting from the boundary conditions in Eqs. 6.1.68 and 6.1.69 respectively; evolving them forward and backward in time, by solving the sourceless classical equations $\delta S/\delta\phi_{1,2} = 0$; and formally matching $\phi_1(\mathbf{x})$ to $\phi_2(\mathbf{x})$ at some *a priori* arbitrary surface A (defined as $\tau = \tau_0(\mathbf{x})$) where both $\phi_1(\mathbf{x})$ and $\phi_2(\mathbf{x})$ become singular. However, the combined field configuration $\phi(x) = (\phi_1(x), \phi_2(x))$ on the contour C is not yet the solution to the saddle-point equations.

Note that there is a non-vanishing overlap in the range $(0 \leq \tau \leq \tau_0(\mathbf{x}))$ at $t = 0$, where both ϕ_1 and ϕ_2 are defined. For a general surface A, the field configuration ϕ

can still be discontinuous for all $\mathbf{x}$ at $t = 0$. However, we are interested specifically in the case where ϕ is only discontinuous at $\mathbf{x} = \mathbf{0}$, $t = 0$, which is the location of the source term and is the only source of the singularity/discontinuity of the field. That is, we require that,

$$\phi_1(0, \mathbf{x}) = \phi_2(0, \mathbf{x}), \qquad \forall \mathbf{x} \neq \mathbf{0}. \tag{6.1.70}$$

If we can choose the surface A such that this condition is satisfied, the combined field $\phi(x)$ will be the solution to the saddle-point equations. Our next task is to explain how this can be achieved by extremising the action $S[\phi]$ over the singular surfaces. We will show that on the extremal surface, the requirement in Eq. 6.1.70 will be automatically satisfied, see Eq. 6.1.79 below.

The total action $iS[\phi]$, which (by standard convention) we write as the Euclidean action with a minus sign, $iS[\phi] = -S_E[\phi]$, is the sum of the contributions from the three parts of the contour defined above,

$$\begin{aligned} iS[\phi] = &-S_E[\phi] = -S_E^{(1)}[\phi_1] - S_E^{(2)}[\phi_2] + iS^{(3)}[\phi_2] \\ = &\int d^d x \int_{+\infty}^{\tau_0(\mathbf{x})} d\tau\, \mathcal{L}_E(\phi_1) + \int d^d x \int_{\tau_0(\mathbf{x})}^{0} d\tau\, \mathcal{L}_E(\phi_2) + i\int d^d x \int_{0}^{+\infty} dt\, \mathcal{L}(\phi_2), \end{aligned}$$
$$\tag{6.1.71}$$

where $\mathcal{L}(\phi)$ is the usual Lagrangian as defined in Eq. 6.1.3 and,

$$\mathcal{L}_E(\phi) = \frac{1}{2}(\partial_\tau \phi)^2 + \frac{1}{2}|\nabla\phi|^2 + \frac{1}{2}m^2\phi^2 + \mathcal{L}_{\text{int}} = \frac{1}{2}(\partial_\tau \phi)^2 + \frac{1}{2}|\nabla\phi|^2 + V(\phi), \tag{6.1.72}$$

is its Euclidean counterpart. Note that though $S_E^{(1)}$ and $S_E^{(2)}$ are infinite on the singularity surface, i.e. at $\tau = \tau_0(\mathbf{x})$, their sum can be finite (at least on some surfaces) due to the differing integration directions for $S_E^{(1)}$ and $S_E^{(2)}$ in the vicinity of the singularity.

The imaginary part of the Minkowski action appearing in the expression for the rate in Eq. 6.1.67, becomes the real part of the Euclidean action,

$$\operatorname{Im} S = \frac{1}{2i}\left(S - S^*\right) = \frac{1}{2}\left(-iS + iS^*\right) = \frac{1}{2}\left(S_E - S_E^*\right) = \operatorname{Re} S_E. \tag{6.1.73}$$

Extremisation over singularity surfaces

Here we will show that extremising the real part of the Euclidean action over all appropriate singularity surfaces will single out the desired singularity surface (i.e. that which satisfies the condition in Eq. 6.1.70) and consequently yield the solution

to the original boundary-value problem. By "appropriate" we simply mean that A must include the point $\tau = |\mathbf{x}| = 0$ as previously stated. This reduction of the problem of finding the solution to the saddle-point equations to the extremisation over singular surfaces is a key element in the approach of Ref. [168].

To set up the problem we take the following steps:

- Since ϕ is infinite on the singularity surface, we regularise it by setting $\phi_1 = \phi_2 = \phi_0$ everywhere on A, with ϕ_0 large but for now kept finite.

- Note that since ϕ_1 and ϕ_2 are different solutions (carrying different energies), their form in the vicinity of A will be different. As such, we can denote the difference

$$\partial_n(\phi_1 - \phi_2) = J(s_i), \qquad (6.1.74)$$

in terms of a function $J(s_i)$ defined on A. Here ∂_n is the derivative in the direction normal to the singularity surface A, and s_i (with $i = 1, \ldots, d$) are coordinates on A, described by $x^\mu = x^\mu(s_i)$.

- Since the source-term $J(s_i)$ in Eq. 6.1.74 is distributed over the surface, it follows that ϕ is actually the solution to,

$$\frac{\delta S_E[\phi]}{\delta \phi(x)} = J(x) = \int_A ds_i J(s_i) \delta(x^\mu - x^\mu(s_i)). \qquad (6.1.75)$$

In other words, the source term is zero except for points $x^\mu(s_i)$ on the singularity surface, where it is given by the distribution $J(s_i)$.

With this framework in mind, we consider deforming the surface $A \to A'$ such that $x^\mu(s_i) \to x^\mu(s_i) + \delta x^\mu(s_i)$, with $\delta x^\mu(s_i) = n^\mu \delta x(s_i)$ and n^μ a unit normal vector. To match our boundary conditions we require that $x = 0$ is included in both A and A', i.e. $\delta x^\mu|_{x=0} = 0$.

We can now compute the variation of the real part of the action in Eq. 6.1.71 arising from varying the surface $A \to A'$. It is given by the following simple formula [168] (which is derived in Appendix C.3),

$$\delta \operatorname{Re} S_E[\phi] = \frac{1}{2} \int_A ds \left((\partial_n \phi_1)^2 - (\partial_n \phi_2)^2 \right) \delta x(s). \qquad (6.1.76)$$

We now rearrange the expression in Eq. 6.1.76 to the form,

$$\delta \operatorname{Re} S_E[\phi] = \frac{1}{2} \int_A ds [\partial_n(\phi_1 + \phi_2)][\partial_n(\phi_1 - \phi_2)] \delta x(s), \qquad (6.1.77)$$

and recognising $\partial_n(\phi_1 - \phi_2)$ as $J(s)$ in Eq. 6.1.74 and labelling $\phi = (\phi_1 + \phi_2)/2$, we arrive at,

$$\delta \operatorname{Re} S_E[\phi] \;=\; \int_A ds (\partial_n \phi) J(s) \delta x(s). \tag{6.1.78}$$

On the extremised surface we have $\delta \operatorname{Re} S_E[\phi] = 0$. Given that $\delta x|_{x^\mu = 0} = 0$, this is achieved by $J(x^\mu) = j_0 \delta(x^\mu)$. In other words, the source becomes infinitely localised at $x = 0$ and it follows from Eq. 6.1.74 that,

$$\partial_n(\phi_1 - \phi_2) \propto \delta^{(d+1)}(x), \tag{6.1.79}$$

which satisfies the requirement in Eq. 6.1.70. In fact, as noted in [168], it follows from Eq. 6.1.79 and the fact that $\phi_1 = \phi_2$ on A, that when A is the extremal surface, the two parts of the solution coincide on the entire range of the common domain, $\tau_0(\mathbf{x}) < \tau < 0$, with the exception of the point at the origin $\tau = 0 = \mathbf{x}$.

This concludes the proof that the boundary-value problem is solved by extremising the real part of the Euclidean action over all singularity surfaces that include the point $\tau = |\mathbf{x}| = 0$. The solution $\phi(x)$ is obtained from the two branches, ϕ_1 and ϕ_2 that are matched on the extremal singular surface. We also note that the matching condition in Eq. 6.1.70 implies that the Euclidean action integrals are real-valued (and positive) on both Euclidean segments (1) and (2) of the contour.

Summary of the surface extremisation approach in complex time

Here we summarise the steps involved in solving the boundary value problem approach via extremisation over singular surfaces [168] in the context of the $(d+1)$-dimensional model in Eq. 6.1.4 with SSB. Note that all our considerations are general and that the expressions in the summary below can also be written in terms of the manifestly VEV-less field ϕ with the Lagrangian in Eq. 6.1.3 using $\phi(x) = h(x) - v$.

1. Select a trial singularity surface located at $\tau = \tau_0(\mathbf{x})$. The surface profile $\tau_0(\mathbf{x})$ is an $\mathcal{O}(d)$ symmetric function of $\mathbf{x}$ and is given by a local deformation of the flat singularity domain wall at τ_∞ with the single maximum touching the origin $(\tau, \mathbf{x}) = 0$ as shown in blue in Fig. 6.1 (a). Minkowski space is the $\tau = 0$ slice of the $(t, \tau; \mathbf{x})$ space; it intersects the singularity surface at a point located at the origin. Hence in Minkowski space the singularity of the field configuration h is point-like and located at $t = 0 = \tau$ and $\mathbf{x} = 0$ as required.

2. Deform the time evolution contour such that the paths in the Feynman path integral follow the contour on the complex plane (t, τ),

$$[(0, \infty) \to (0, \tau_0(\mathbf{x}))] \,\oplus\, [(0, \tau_0(\mathbf{x})) \to (0, 0)] \,\oplus\, [(0, 0) \to (\infty, 0)]\,, \tag{6.1.80}$$

as shown in Figs. 4.1 (a) and 6.1 (b).

3. Find a classical trajectory $h_1(\tau, \mathbf{x})$ on the first segment, $+\infty > \tau > \tau_0(\mathbf{x})$, of the contour in Eq. 6.1.80 that satisfies the initial-time (vanishing) boundary condition in Eq. 6.1.64,

$$\lim_{\tau \to +\infty} h_1(\tau, \mathbf{x}) - v \to 0, \tag{6.1.81}$$

and becomes singular as $\tau \to \tau_0(\mathbf{x})$ so that $h_1(\tau, \mathbf{x})|_{\tau \to \tau_0(\mathbf{x})} \equiv \phi_0 \to \infty$.

4. Find another classical solution $h_2(\tau, \mathbf{x})$ on the remaining part of the contour in Eq. 6.1.64, that satisfies the final time boundary condition in Eq. 6.1.65,

$$\lim_{t \to +\infty} h_2(t, \mathbf{x}) - v = \int \frac{d^d k}{(2\pi)^{d/2}} \frac{1}{\sqrt{2\omega_{\mathbf{k}}}} \left(b_{\mathbf{k}} \, e^{\omega_{\mathbf{k}} T - \theta} \, e^{-ik_\mu x^\mu} + b_{\mathbf{k}}^* \, e^{ik_\mu x^\mu} \right), \tag{6.1.82}$$

and require that at $\tau \to \tau_0(\mathbf{x})$ the solution $h_2(\tau, \mathbf{x})$ is singular and matches with h_1,

$$h_2(\tau_0, \mathbf{x}) = h_1(\tau_0, \mathbf{x}) = \phi_0 \to \infty. \tag{6.1.83}$$

5. For the combined configuration $h(x)$ to solve the classical equation in Eq. 6.1.63 on the entire contour in Eq. 6.1.80, including at $\tau = \tau_0(\mathbf{x})$, we need to extremise the action,

$$iS[h] = \int d^d x \left(\int_{+\infty}^{\tau_0(\mathbf{x})} d\tau \, \mathcal{L}_E(h_1) + \int_{\tau_0(\mathbf{x})}^{0} d\tau \, \mathcal{L}_E(h_2) + i \int_0^{\infty} dt \, \mathcal{L}(h_2) \right) \tag{6.1.84}$$

over all singularity surfaces $\tau = \tau_0(\mathbf{x})$ containing the point $t = 0 = \mathbf{x}$. This determines the extremal surface $\tau = \tau_0(\mathbf{x})$.

6. Finally, determine the semiclassical rate by evaluating

$$W(E, n) = ET - n\theta - 2\mathrm{Re}\, S_E[h] \tag{6.1.85}$$

on the solution, using Eq. 6.1.84 for the action, and expressions for T and θ in terms of of E and n found from Eq. 6.1.66 as before.

This is the general outcome of the semiclassical construction of Ref. [168]. One starts with the two individual solutions satisfying the boundary conditions in Eqs. 6.1.81 to 6.1.83 and then varies over the profiles of the singular matching surface $\tau_0(\mathbf{x})$ to find an extremum of the imaginary part of the action in Eq. 6.1.84. On the extremal surface, the field configurations and their normal derivatives match, $\partial_n(h_1 - h_2) = 0$, at all $\mathbf{x}$ except $\mathbf{x} = 0$. This implies that $h_1 = h_2$ on the entire slice of the spacetime

where they are both defined, i.e. for τ in the interval $[0, \tau_0]$, except at the point at the origin. Restricting to the Minkowski space slice, i.e. at $\tau = 0$, this implies $h_1(0, \mathbf{x}) = h_2(0, \mathbf{x})$, as it should be. It does not mean however that the real part of the action in Eq. 6.1.84 vanishes, as the sum of the first two integrals can be viewed as encircling the singularity of the solution at τ_0.

In summary, the highly non-trivial problem of searching for the appropriate singular field solutions $h(x)$ is reduced to a geometrical problem – extremisation over the surface shapes $\tau_0(\mathbf{x})$ and accounting for the appropriate boundary conditions in Eqs. 6.1.81 to 6.1.83. This formulation of the problem is now well-suited for using the thin-wall approximation that will be described in Section 6.2.2 and will allow us to address the large λn regime, following [169, 170], where quantum non-perturbative effects become important.

We proceed with the practical implementation of the steps 1-6 for the model in Eq. 4.1.3 in the following sections.

6.2   Computation of the semiclassical rate

We will now concentrate on the scalar field theory model with a non-vanishing vacuum expectation value (see Eq. 4.1.3) in 3+1 dimensions. Some of the material presented below, such as the general aspects of the approach, the computation of tree-level contributions, and the computation of quantum effects at $\lambda n \ll 1$, can be carried out in any scalar QFT with only minor modifications. The case of the unbroken ϕ^4 theory has already been addressed in Ref. [168], while we are predominantly interested in the broken theory (see Eq. 4.1.3), where the applications of the semiclassical method at small λn are new, though the resulting expressions are closely related to those derived by Son in the unbroken theory.

In Sections 6.2.2 and 6.2.3 we focus on the $\lambda n \gg 1$ regime (previously unexplored in [168]), where quantum corrections provide the *dominant* contribution to the multiparticle rate. The computation we will present follows [169] and is specific to the model of the type shown in Eq. 4.1.3 with spontaneous symmetry breaking [170, 185]. In this case, the singular domain wall semiclassical configuration corresponds to a local minimum of the action (rather than a local maximum or a saddle-point) and this will play a role in our construction.

6.2.1   Setting up the computation

In this section, we will specify and solve the boundary conditions in Eqs. 6.1.81 and 6.1.82 at the initial and final times, deriving the coefficient functions $b_{\mathbf{k}}^*$ and $b_{\mathbf{k}} \, e^{\omega_{\mathbf{k}} T - \theta}$ in Eq. 6.1.82. We will then determine the T and θ parameters and compute the general expression for the exponent of the rate $W(E, n)$ in Eq. 6.1.67.

In the limit $\varepsilon = 0$, the scattering amplitude is on the multiparticle threshold, the final-state momenta are vanishing and one would naively assume that the classical solution describing this limit is uniform in space. This is correct for the tree-level solution but not for the solution incorporating quantum effects. In the latter case, the correct and less restrictive assumption is that the presence of the singularity at $x = 0$ deforms the flat surface of singularities near its location, as shown in Fig. 6.1. From now on we will concentrate on the physical case where ε is non-vanishing and non-relativistic, $0 < \varepsilon \ll 1$. At the same time, the parameter λn is held fixed and arbitrary. It will ultimately be taken to be large.

The initial-time boundary condition in Eq. 6.1.81 dictates that the solution $h_1(t_{\mathbb{C}} = i\tau, \mathbf{x}) - v$ must vanish with exponential accuracy as $e^{-m\tau}$ in the limit $\tau \to \infty$. The final-time boundary condition in Eq. 6.1.82 of the finite-energy solution $h_2(x)$ requires the solution to be singular on the singularity surface $\tau_0(\mathbf{x})$. Following Son, without loss of generality, we can search for h_2 in the form,

$$h_2(t_{\mathbb{C}}, \mathbf{x}) = v \left(\frac{1 + e^{im(t_{\mathbb{C}} - i\tau_\infty)}}{1 - e^{im(t_{\mathbb{C}} - i\tau_\infty)}} \right) + \tilde{\phi}(t_{\mathbb{C}}, \mathbf{x}) \,. \tag{6.2.1}$$

The first term on the right-hand side is the $\mathbf{x}$-independent field configuration $h_0(t_{\mathbb{C}})$ that we discussed in Section 4.2.1. It is an exact classical solution (see Eq. 4.2.8) with the surface of singularities at $t_{\mathbb{C}} = i\tau_\infty$, which is a 3-dimensional plane spanned by $\mathbf{x}$, as shown in Fig. 4.2. The second term, $\tilde{\phi}(t_{\mathbb{C}}, \mathbf{x})$, describes the deviation of the singular surface from the τ_∞-plane. This deviation, $\tau_0(\mathbf{x}) - \tau_\infty$, is locally non-trivial around $\mathbf{x} = 0$ and vanishes at $\mathbf{x} \to \infty$. There is no loss of generality in Eq. 6.2.1 because the configuration $\tilde{\phi}(t_{\mathbb{C}}, \mathbf{x})$ is so far completely unconstrained.

Now we can start imposing the boundary conditions in Eq. 6.1.82 at $t \to +\infty$ on the expression in Eq. 6.2.1. On the final segment of the time evolution contour, $t(1 + i\delta_+)$ as $t \to +\infty$, the first term in Eq. 6.2.1 can be Taylor-expanded in powers of $e^{imt(1+i\delta_+)}$ and linearised (since δ_+ is positive) giving,

$$\lim_{t \to +\infty} h_0(x) - v = 2v \, e^{m\tau_\infty} \, e^{imt} \,. \tag{6.2.2}$$

For the second term in Eq. 6.2.1 we write the general expression involving the

positive-frequency and the negative frequency components in the Fourier transform,

$$\lim_{t\to+\infty} \tilde{\phi}(t,\mathbf{k}) = \frac{1}{\sqrt{2\omega_\mathbf{k}}} \left(f_\mathbf{k}\, e^{-i\omega_\mathbf{k}t} + g_{-\mathbf{k}}\, e^{i\omega_\mathbf{k}t} \right). \tag{6.2.3}$$

We will now show that for the solution in the non-relativistic limit, $\epsilon \ll 1$, the boundary conditions in Eq. 6.1.82 will require that $g_{-\mathbf{k}} = 0$ and impose a constraint on the coefficient function $f_\mathbf{k}$, so that,

$$g_{-\mathbf{k}} = 0\,, \tag{6.2.4}$$

$$f_{\mathbf{k}=\mathbf{0}} = \frac{n\sqrt{\lambda}}{(2\pi m)^{3/2}}\, e^{-m\tau_\infty}\,. \tag{6.2.5}$$

To derive Eqs. 6.2.4 and 6.2.5 we proceed by combining the asymptotics in Eq. 6.2.3 with the Fourier transform of Eq. 6.2.2 and write down the full solution in Eq. 6.2.1 in the form,

$$\lim_{t\to+\infty} h_2(t,\mathbf{k}) - v = \frac{1}{\sqrt{2\omega_\mathbf{k}}} \left(f_\mathbf{k}\, e^{-i\omega_\mathbf{k}t} + \left\{ g_{-\mathbf{k}} + 2v\sqrt{2\omega_\mathbf{k}}\, e^{m\tau_\infty} (2\pi)^{3/2}\, \delta^{(3)}(\mathbf{k}) \right\} e^{i\omega_\mathbf{k}t} \right). \tag{6.2.6}$$

Comparing with the the final-time boundary condition Eq. 6.1.82 we read off the expressions for the coefficient functions,

$$b_\mathbf{k}\, e^{\omega_\mathbf{k}T-\theta} = f_\mathbf{k} \tag{6.2.7}$$

$$b_\mathbf{k}^* = g_{-\mathbf{k}} + 2v\sqrt{2m}\, e^{m\tau_\infty} (2\pi)^{3/2}\, \delta^{(3)}(\mathbf{k})\,. \tag{6.2.8}$$

We will now make an educated guess that the parameter T will be infinite in the limit $\varepsilon \to 0$. In fact we will soon derive that $T = 3/(2m\varepsilon)$, so this assumption will be justified *a posteriori*. We can then re-write Eq. 6.2.7 as,

$$b_\mathbf{k} = f_\mathbf{0}\, e^{-\omega_\mathbf{k}T}\, e^\theta\,. \tag{6.2.9}$$

In the limit where $\varepsilon \to 0$ (and thus $T \to \infty$) the factor $e^{-\omega_\mathbf{k}T}$ can be thought of as the regularisation of a momentum-space delta-function: it cuts-off all non-vanishing values of $\mathbf{k}$ by minimising $\omega_\mathbf{k}$, thus reducing $\mathbf{k}$ to zero. Therefore, we set $f_\mathbf{k}$ to $f_\mathbf{0}$ in the equation above.

Furthermore, since the function $b_\mathbf{k}$ is proportional to the (regularised) delta-function, its complex conjugate $b_\mathbf{k}^*$ must be too. This implies that the coefficient function $g_{-\mathbf{k}}$ in Eq. 6.2.8 must be zero [168], which verifies Eq. 6.2.4, so that Eq. 6.2.3 becomes,

$$\lim_{t\to+\infty} \tilde{\phi}(t,\mathbf{k}) = \frac{1}{\sqrt{2\omega_\mathbf{k}}}\, f_\mathbf{k}\, e^{-i\omega_\mathbf{k}t}\,. \tag{6.2.10}$$

We have obtained the expression for the coefficient function $b_\mathbf{k}$ (and its complex

conjugate) and also obtained a symbolic identity involving the parameters T, θ and the delta-function,

$$b_{\mathbf{k}} \;=\; f_{\mathbf{0}}\, e^{-\omega_{\mathbf{k}} T}\, e^{\theta} \;=\; 2v\sqrt{2m}\, e^{m\tau_{\infty}}\,(2\pi)^{3/2}\,\delta^{(3)}(\mathbf{k}) \;=\; b_{\mathbf{k}}^{*}\,. \qquad (6.2.11)$$

This symbolic identity should be interpreted as follows. In the limit of strictly vanishing ε, all these terms are proportional to the delta-function. Away from this limit, i.e. in the case of processes near the multiparticle threshold where $0 < \varepsilon \ll 1$, the function $\delta^{(3)}(\mathbf{k})$ appearing in the third term above is not the strict delta-function, but a narrow peak with the singularity regulated by ε. This can be derived by allowing the surface τ_{∞} in the first term in Eq. 6.2.1 to not be completely flat at small non-vanishing ε, but to have a tiny curvature $2\varepsilon/3 \ll 1$ [168], thus leading to a regularised expression for $\delta^{(3)}(\mathbf{k})$ in the final term in Eq. 6.2.6.

To proceed, we integrate the two middle terms in Eq. 6.2.11 over d^3k,

$$f_{\mathbf{0}}\, e^{\theta} \int d^3k\, e^{-\omega_{\mathbf{k}} T} \;=\; 2v\sqrt{2m}\, e^{m\tau_{\infty}}\,(2\pi)^{3/2}\,. \qquad (6.2.12)$$

The integral on the left hand side of Eq. 6.2.12,

$$\int d^3k\, e^{-\omega_{\mathbf{k}} T} \;=\; 4\pi\, m^3\, e^{-mT} \int_{0}^{\infty} dx\, x^2\, e^{-mT(\sqrt{1+x^2}-1)}\,, \qquad (6.2.13)$$

where $x = k/m$. Note that this integral is dominated by $x \sim mT$, which at large T allows us to simplify this as,

$$4\pi\, m^3\, e^{-mT} \int_{0}^{\infty} dx\, x^2\, e^{-mTx^2/2} \;=\; 4\pi\, m^3\, e^{-mT}\, \frac{\sqrt{\pi/2}}{(mT)^{3/2}}\,. \qquad (6.2.14)$$

We can now solve Eq. 6.2.12 for $f_{\mathbf{0}}$ and find that at large T,

$$f_{\mathbf{0}} \;=\; \frac{2}{\sqrt{\lambda}}\,(T)^{3/2}\, e^{mT-\theta+m\tau_{\infty}}\,. \qquad (6.2.15)$$

We can now compute the particle number n and the energy E in the final state using Eq. 6.1.66 and the now known coefficient functions in Eq. 6.2.11 along with Eq. 6.2.15. We find,

$$n = \int d^3k\, b_{\mathbf{k}}^{*}\, b_{\mathbf{k}}\, e^{\omega_{\mathbf{k}} T-\theta} = \int d^3k\, b_{\mathbf{k}}^{*}\, f_{\mathbf{0}} = \frac{4}{\lambda}\,(2\pi mT)^{3/2}\, e^{mT-\theta+2m\tau_{\infty}}, \qquad (6.2.16)$$

and

$$\begin{aligned} mn\varepsilon = E - mn &= \int d^3k\, \frac{\mathbf{k}^2}{2m}\, b_{\mathbf{k}}^{*}\, b_{\mathbf{k}}\, e^{\omega_{\mathbf{k}} T-\theta} \\ &= \int d^3k\, \frac{\mathbf{k}^2}{2m}\, b_{\mathbf{k}}^{*}\, f_{\mathbf{0}} = \frac{4}{\lambda}\,(2\pi mT)^{3/2}\, e^{mT-\theta+2m\tau_{\infty}}\, \frac{3}{2T}\,. \end{aligned} \qquad (6.2.17)$$

It turns out that it was sufficient to know just the value of $f_{\mathbf{k}}$ at $\mathbf{k} = 0$ to evaluate the integrals above, due to the fact that $b_{\mathbf{k}}^*$ and $b_{\mathbf{k}}$ are sharply peaked at $\mathbf{k} = 0$ as dictated by Eq. 6.2.11.

Dividing the expression on the right hand side of Eq. 6.2.17 by the expression in Eq. 6.2.16 we find,

$$T = \frac{1}{m}\frac{3}{2}\frac{1}{\varepsilon}. \tag{6.2.18}$$

The second parameter θ is found to be,

$$\theta = -\log\frac{\lambda n}{4} + \frac{3}{2}\log\frac{3\pi}{\varepsilon} + 2m\tau_\infty + \frac{3}{2}\frac{1}{\varepsilon}. \tag{6.2.19}$$

We now finally substitute these parameters into Eq. 6.1.85 for the 'holy grail' function $W(E,n)$, and find,

$$W(E,n) = ET - n\theta - 2\mathrm{Re}S_E[h] = mn(1+\varepsilon)T - n\theta - 2\mathrm{Re}S_E[h]$$

$$= n\log\frac{\lambda n}{4} + \frac{3n}{2}\left(1 + \log\frac{\varepsilon}{3\pi}\right) - 2nm\,\tau_\infty - 2\mathrm{Re}S_E[h]. \tag{6.2.20}$$

We also note that the expression for $f_{\mathbf{0}}$ found in Eq. 6.2.15 evaluated with T and θ given by Eqs. 6.2.18 and 6.2.19, reproduces Eq. 6.2.5, which was our second constraint on the general form of the solution $h_2(t_\mathbb{C}, \mathbf{x})$ in Eq. 6.2.1.

Before interpreting the expression in Eq. 6.2.20 for the 'holy grail' function, we would like to separate the terms appearing on the right-hand side into those that depend on the location and shape of the singularity surface $\tau_0(\mathbf{x})$, and those that do not. The first two terms in Eq. 6.2.20 have no dependence on the singularity surface; the third term, $2nm\,\tau_\infty$, depends on its location at τ_∞. The final term, $2\mathrm{Re}S_E$, is obtained by taking the real part of the three integrals appearing in Eq. 6.1.84. The first two integrals are along the Euclidean time τ segments of the contour and are real-valued,

$$2\mathrm{Re}\,S_E^{(1,2)} = 2\int d^3x\left[-\int\limits_{+\infty}^{\tau_0(\mathbf{x})} d\tau\,\mathcal{L}_E(h_1) - \int\limits_{\tau_0(\mathbf{x})}^{0} d\tau\,\mathcal{L}_E(h_2)\right], \tag{6.2.21}$$

while the remaining integral along the third segment of the contour appears to be purely imaginary. This last statement is almost correct, as it applies to the bulk contribution of the Minkowski-time integral $\int_0^\infty dt\,\mathcal{L}(h_2)$, but not to the boundary contribution at $t \to \infty$. The full contribution from the third segment of the contour

is[1],

$$2\operatorname{Re} S_E^{(3)} = 2\operatorname{Re}\left[-i\int\limits_0^\infty dt \int d^3x\, \partial_t\left(\tilde\phi\,\partial_t h_2\right)\right]$$

$$= -\int d^3k\, b_{\mathbf{k}}^* b_{\mathbf{k}}\, e^{\omega_{\mathbf{k}}T-\theta}\ =\ -n\,. \qquad (6.2.22)$$

Accounting for the effect of the boundary contribution in Eq. 6.2.22 we can write the expression for the rate in Eq. 6.2.20 in the form:

$$W(E,n) = n\left(\log\frac{\lambda n}{4} + \frac{3}{2}\log\frac{\varepsilon}{3\pi} + \frac{1}{2}\right) - 2nm\,\tau_\infty - 2\operatorname{Re}S_E^{(1,2)}(\tau_0)\,. \qquad (6.2.23)$$

This is a remarkable formula in the sense that the expression on the right-hand side of Eq. 6.2.23 cleanly separates into two parts. The first part, $n\left(\log\frac{\lambda n}{4} + \frac{3}{2}\log\frac{\varepsilon}{3\pi} + \frac{1}{2}\right)$, does not depend on the shape of the singularity surface $\tau_0(\mathbf{x})$ and coincides with the known tree-level result for the scattering rate in the non-relativistic limit $0 < \varepsilon \ll 1$, as we will demonstrate below. The entire dependence of $W(E,n)$ on $\tau_0(\mathbf{x})$ is contained in the last two terms in Eq. 6.2.23, which correspond to the purely quantum contribution in the $\varepsilon \to 0$ limit.

The tree-level contribution to W is well-known; it was computed using the resummation of Feynman diagrams by solving the tree-level recursion relations [179] and integrating over the phase-space. In the model shown in Eq. 4.1.3, the tree-level result to linear order in ϵ was derived in Ref. [183] and reads,

$$W(E,n;\lambda)^{\text{tree}} = n\left(f_1(\lambda n) + f_2(\varepsilon)\right)\,, \qquad (6.2.24)$$

where

$$f_1(\lambda n) = \log\left(\frac{\lambda n}{4}\right) - 1\,, \qquad (6.2.25)$$

$$f_2(\varepsilon)|_{\varepsilon\to 0} \to f_2(\varepsilon)^{\text{asympt}} = \frac{3}{2}\left(\log\left(\frac{\varepsilon}{3\pi}\right) + 1\right) - \frac{25}{12}\,\varepsilon\,. \qquad (6.2.26)$$

First, ignoring the $\mathcal{O}(\varepsilon)$ terms in the tree-level contribution, we see that the perturbative result is correctly reproduced by the first two terms in the semiclassical expression on the right-hand side of Eq. 6.2.23,

$$W(E,n)^{\text{tree}} = n\left(\log\frac{\lambda n}{4} - 1\right) + \frac{3n}{2}\left(\log\frac{\varepsilon}{3\pi} + 1\right)\,. \qquad (6.2.27)$$

Schematically, the contribution $n\log\lambda n \subset W^{\text{tree}}$ comes from squaring the tree-level

---

[1]The expression in Eq. 6.2.22 for the boundary contribution to the Minkowski action is also in agreement with the construction in [168] and [186].

amplitude on threshold and dividing by the Bose symmetry factor, $\frac{1}{n!}\left(n!\lambda^{n/2}\right)^2 \sim$ $n!\lambda^n \sim e^{n\log\lambda n}$, while the contribution $\frac{3}{2}n\log\varepsilon$ comes from the non-relativistic n-particle phase space volume factor $\varepsilon^{\frac{3n}{2}} \sim e^{\frac{3}{2}n\log\varepsilon}$. [1]

The apparent agreement between the first term in the expression on the right-hand side of Eq. 6.2.23 and the result of an independent tree-level perturbative calculation in Eq. 6.2.27, provides a non-trivial consistency check of the semiclassical formalism that led us to Eq. 6.2.23.

Furthermore, it was shown in [168] that the tree-level results are also correctly reproduced by the semiclassical result to $\mathcal{O}(\varepsilon)$. It would also be interesting to pursue such terms at the quantum level, but this is beyond the scope of this work. We will neglect all $\mathcal{O}(\varepsilon)$ terms as they are vanishing in the $\varepsilon \to 0$ limit.

We can finally re-write the expression in Eq. 6.2.23 for the rate $W(E,n)$ in the form [168],

$$W(E,n) = W(E,n;\lambda)^{\text{tree}} + \Delta W(E,n;\lambda)^{\text{quant}}, \qquad (6.2.28)$$

where the quantum contribution is given by

$$\begin{aligned}\Delta W^{\text{quant}} &= -2nm\,\tau_\infty - 2\text{Re}\,S_E^{(1,2)}\\ &= 2nm\,|\tau_\infty| + 2\int d^3x\left[\int_{+\infty}^{\tau_0(\mathbf{x})} d\tau\,\mathcal{L}_E(h_1) + \int_{\tau_0(\mathbf{x})}^{0} d\tau\,\mathcal{L}_E(h_2)\right] \qquad (6.2.29)\\ &= 2nm\,|\tau_\infty| - 2\int d^3x\left[\int_{\tau_0(\mathbf{x})}^{+\infty} d\tau\,\mathcal{L}_E(h_1) - \int_{\tau_0(\mathbf{x})}^{0} d\tau\,\mathcal{L}_E(h_2)\right].\end{aligned}$$

Here we have used the fact that τ_∞ is manifestly negative (as the singularity surface away at $\mathbf{x} \neq 0$ is by construction assumed to be located at negative τ) to indicate that $-2nm\,\tau_\infty$ is a positive-valued contribution $+2nm\,|\tau_\infty|$.

The problem of finding the singularity surface $\tau_0(\mathbf{x})$ that extremises the expression in Eq. 6.2.29 has a simple physical interpretation [168, 170, 185]: it is equivalent to finding the shape of the membrane $\tau_0(\mathbf{x})$ at equilibrium, which has the surface energy $\text{Re}\,S_E^{(1,2)}$ and is pulled at the point $\mathbf{x} = 0$ by a constant force equal to nm. Note that even before the extremisation of Eq. 6.2.29 with respect to $\tau_0(\mathbf{x})$, both configurations $h_1(x)$ and $h_2(x)$ are tightly constrained. They are required to be solutions of the classical equations; they have to have satisfy the correct boundary conditions in time, and consequentially, their energy is fixed: h_1 has $E = 0$ and h_2 has $E = nm$ (in the $\varepsilon \to 0$ limit). These conditions constrain the extremisation of Eq. 6.2.29 with respect to $\tau_0(\mathbf{x})$.

---

[1]We refer the interested reader to Refs. [179,183] for more details on the derivation of $W(E,n)^{\text{tree}}$ directly in perturbation theory.

6.2.2   Computation of quantum effects at large λn

In this and the following sections we will closely follow the calculation in Ref. [169]. We view the saddle-point field configuration in the model in Eq. 4.1.3 as a domain wall solution separating vacua with different VEVs ($h \to \pm v$) on different sides of the wall. Our scalar theory with spontaneous symmetry breaking clearly supports such field configurations. The solution is singular on the surface of the wall, which has thickness $\sim 1/m$. The effect of the 'force' nm applied to the domain wall is to pull the centre of the wall upwards and gives it a profile $\tau_0(\mathbf{x})$, as depicted in Fig. 6.1. The Euclidean action on the solution characterised by the domain wall at $\tau_0(\mathbf{x})$, becomes a functional of the surface function, $S_E[\tau_0(\mathbf{x})]$. The shape of the surface will be straightforward to determine by extremising the action $S_E[\tau_0(\mathbf{x})]$, which we will compute in the thin-wall approximation, over all surface profile functions $\tau_0(\mathbf{x})$. The validity of the thin-wall approximation will be be justified in the limit $\lambda n \to \infty$. The idea of using the thin-wall approximation in the large λn limit was pursued earlier by Gorsky and Voloshin in Ref. [185], where it was applied to the standard regular bubbles of the false vacuum. These were interpreted as intermediate physical bubble states in the process $1^* \to \text{Bubble} \to n$. Conceptually, this is different from our approach, where the thin-wall solutions are singular points on the deformed contours of the path integral in Euclidean time. In our setting they cannot be interpreted as physical macroscopic states in real Minkowski time representing an intermediate state in the $1^* \to n$ process.

From now on we concentrate on the large λn regime, where the semiclassical rate is non-perturbative.

Classical fields and singularity surfaces

Our first task is to implement the realisation of the singular field configuration $h(x)$ in terms of domain walls with thin-wall singular surfaces. The h_1 branch of the solution is defined on the first part of the time-evolution contour, i.e. the imaginary time interval $+\infty > \tau \geq \tau_0(\mathbf{x})$. It is given by,

$$h_1(\tau, \mathbf{x}) = h_{0E}(\tau - \tau_0(\mathbf{x})) + \delta h_1(\tau, \mathbf{x}). \qquad (6.2.30)$$

The first term on the right-hand side of Eq. 6.2.30 is the familiar singular domain wall,

$$h_{0E}(\tau - \tau_0(\mathbf{x})) = v \left(\frac{1 + e^{-m(\tau - \tau_0(\mathbf{x}))}}{1 - e^{-m(\tau - \tau_0(\mathbf{x}))}} \right), \qquad (6.2.31)$$

with its centre (or position) at $\tau = \tau_0(\mathbf{x})$. This profile is similar to the one depicted in Fig. 4.2. The field configuration interpolates between $h = +v$ at $\tau \gg \tau_0(\mathbf{x})$ and $h = -v$ at $\tau \ll \tau_0(\mathbf{x})$, and is singular on the 3-dimensional surface $\tau = \tau_0(\mathbf{x})$. Since $\tau_0(\mathbf{x})$ depends on the spatial variable, the correction $\delta h_1(\tau, \mathbf{x})$ is required in Eq. 6.2.30 to ensure that the entire field configuration $h_1(x)$ satisfies the classical equations. The δh_1 term vanishes on the singularity surface; in fact it is straightforward to show that $\delta h_1 \sim (\tau - \tau_0(\mathbf{x}))^3$ near the singularity surface by solving the linearised classical equations for δh_1 in the background of the singular h_0 [168]. The initial-time condition on h_1 is

$$\lim_{\tau \to \infty} h_1(x) \;=\; v + \mathcal{O}(e^{-m\tau}) \,, \tag{6.2.32}$$

which also guarantees that $\delta h_1(x) \to 0$ exponentially fast at large τ. Hence, in computing the action integral of $h_1(x)$ in the thin-wall approximation, where the main contribution comes from τ in the vicinity of $\tau_0(\mathbf{x})$, it will be a good approximation to neglect $\delta h_1(x)$ and use,

$$\text{thin wall}: \quad h_1(\tau, \mathbf{x}) \approx h_{0E}(\tau - \tau_0(\mathbf{x})) \,. \tag{6.2.33}$$

Now consider the second branch of the solution, $h_2(x)$. We search for solutions of the form required by Eq. 6.2.1,

$$h_2(t_{\mathbb{C}}, \mathbf{x}) \;=\; h_0(t_{\mathbb{C}}) + \tilde{\phi}(t_{\mathbb{C}}, \mathbf{x}) \,, \tag{6.2.34}$$

The first term on the right-hand side of Eq. 6.2.34 is the classical configuration, which is uniform in space and singular on the plane $\tau = \tau_\infty$,

$$h_0(t_{\mathbb{C}}) \;=\; v \left(\frac{1 + e^{im(t_{\mathbb{C}} - i\tau_\infty)}}{1 - e^{im(t_{\mathbb{C}} - i\tau_\infty)}} \right) \,. \tag{6.2.35}$$

In the previous section we derived the asymptotic form for the second term, $\tilde{\phi}(t_{\mathbb{C}}, \mathbf{x})$, appearing on the right-hand side of Eq. 6.2.34: for the final part of the time-evolution contour, where $t_{\mathbb{C}} = t \to +\infty$ we have,

$$\lim_{t \to +\infty} \tilde{\phi}(t, \mathbf{x}) \;=\; \int \frac{d^3 k}{(2\pi)^{3/2}} \frac{1}{\sqrt{2\omega_{\mathbf{k}}}} \, f_{\mathbf{k}} \, e^{-i\omega_{\mathbf{k}} t} \,. \tag{6.2.36}$$

This is in agreement with Eqs. 6.2.2 and 6.2.10 and its characteristic feature is that it contains only the negative frequency components (at large t). The coefficients of positive frequency components that were present in $\tilde{\phi}(t, \mathbf{x})$ at earlier times, closer to the origin at $t \sim 0$ become suppressed as the real time variable t grows and ultimately disappear for a sufficiently large positive t. We are now going to assume that the asymptotic expression in Eq. 6.2.36, which is valid in the $mt \gg 1$ regime on or near the real time axis, in fact also continues to hold when $\tilde{\phi}(t + i\tau, \mathbf{x})$ moves
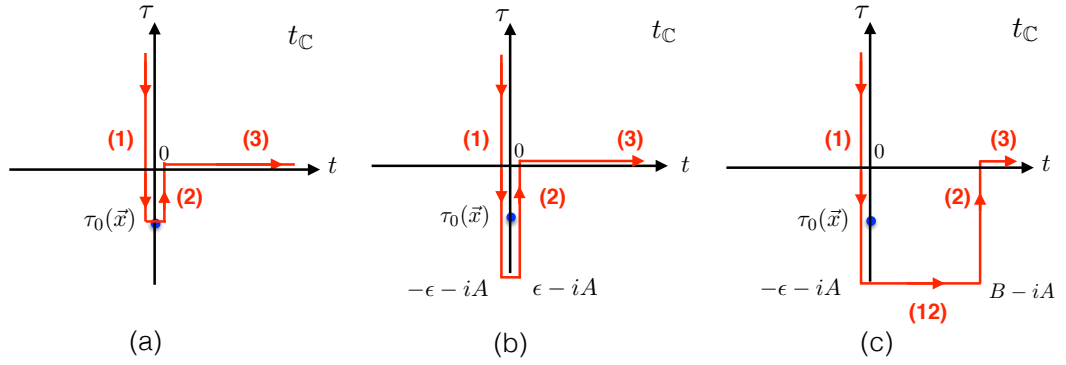
Figure 6.2: _Deformations of the time evolution contour in $t_{\mathbb{C}}$. Plot (a) shows the original contour that touches the singularity located at $t = 0$, $\tau = \tau_0(\mathbf{x})$. Plot (b) gives the resolved contour, now surrounding the singularity with the vertical segments of the contour shifted infinitesimally by $\pm i\epsilon$ and descending to $\tau = -A$. Plot (c) shows now a finite deformation of the vertical part (2) of the contour to the right. We use large shift values, $-A \gg 1/m$ and $B \gg 1/m$ to justify the thin-wall approximation. Consecutive contour segments are denoted (1), (12), (2) and (3)._

in the τ direction, i.e. perpendicular to the real time contour at large fixed value of t. More precisely, we expect that Eq. 6.2.36 generalises to the complex time variable $t_{\mathbb{C}}$ and holds as long as the real time coordinate t is large ($t \gg 1/m$),

$$\lim_{t \to +\infty} \tilde{\phi}(t_{\mathbb{C}}, \mathbf{k}) = \frac{1}{\sqrt{2\omega_{\mathbf{k}}}} \, f_{\mathbf{k}} \, e^{-i\omega_{\mathbf{k}} t_{\mathbb{C}}} = \frac{1}{\sqrt{2\omega_{\mathbf{k}}}} \, f_{\mathbf{k}} \, e^{\omega_{\mathbf{k}}\tau} \, e^{-i\omega_{\mathbf{k}} t} \,. \tag{6.2.37}$$

As always, $t_{\mathbb{C}} = t + i\tau$, and for concreteness we will take the τ component to be negative, i.e. we will only need this expression for shifting downwards from the real time contour at large t.

We now turn to the evaluation of the Euclidean action integrals appearing in Eqs. 6.2.21 and 6.2.29. On the first segment of the contour, indicated as (1) in Fig. 6.2 (a), the classical field configuration is $h_1(x)$, while on the segment (2) of the contour in Fig. 6.2 (a), the field is $h_2(x)$, hence,

$$\text{Fig. 6.2 (a):} \quad -\operatorname{Re} S_E^{(1,2)} = \int d^3x \left[\int_{+\infty}^{\tau_0(\mathbf{x})} d\tau \, \mathcal{L}_E(h_1) + \int_{\tau_0(\mathbf{x})}^{0} d\tau \, \mathcal{L}_E(h_2) \right]. \tag{6.2.38}$$

The two individual integrals in Eq. 6.2.38 are singular at the integration limit $\tau = \tau_0(\mathbf{x})$. However, their sum is expected to be finite, which is also known from the Landau-WKB approach in quantum mechanics [203].

Instead of reaching the singularity and then cancelling the resulting infinite contributions at $\tau \to \tau_0(\mathbf{x})$, we advocate a more practical approach and deform the

integration contour to encircle the singularity, as shown in the contour deformation from Fig. 6.2 (a) to Fig. 6.2 (b). The contour is shifted infinitesimally by $t = -\epsilon$ in the first integral in Eq. 6.2.38 and by $t = +\epsilon$ in the second. Since the integration contour in Fig. 6.2 (b) passes on either side of the singularity at $\tau = \tau_0(\mathbf{x})$, the action integrals and the solutions themselves are finite. One can extend the integration contours down to $\tau = -\infty$ or to any arbitrary large negative value $\tau = -A$. At $\tau = -A$, where τ is well below the final singularity surface τ_∞, the two contours are joined. As a result, the action integrals now read:

$$\text{Fig. 6.2 (b)}: \quad -\operatorname{Re} S_E^{(1,2)} = \int\limits_{+\infty-i\epsilon}^{-A-i\epsilon} d\tau\, L_E[h_1] + \int\limits_{-A+i\epsilon}^{0+i\epsilon} d\tau\, L_E[h_2], \qquad (6.2.39)$$

where $L_E = \int d^3x\, \mathcal{L}_E$, and each of the two integrals in Eq. 6.2.39 is finite. The first integral in Eq. 6.2.39 depends on the classical branch $h_1(x)$, and in the thin-wall approximation (see Eq. 6.2.33) we will be able to evaluate it as the functional of the surface $\tau_0(\mathbf{x})$ using the h_{0E} profile in Eq. 6.2.31.

The second integral in Eq. 6.2.39 is evaluated on the classical configuration $h_2(x)$. It is given by Eq. 6.2.34, where the correction $\tilde{\phi}(t_\mathbb{C}, \mathbf{x})$ to the classical profile $h_0(t_\mathbb{C})$ in Eq. 6.2.35 is known at large values of t, see Eq. 6.2.37. To make use of these expressions for $h_2(x)$ we continue shifting the contour to the right by a constant value B as shown in Fig. 6.2 (c). The resulting contributions to the Euclidean action from the integration contour in Fig. 6.2 (c) are given by the following integrals,

$$\text{Fig. 6.2 (c)}: \quad -\operatorname{Re} S_E^{(1,12,2)} = \int\limits_{+\infty-i\epsilon}^{-A-i\epsilon} d\tau\, L_E[h_1] + i\int\limits_{(12)} dt\, L[h_2] + \int\limits_{-A+iB}^{0+iB} d\tau\, L_E[h_2].$$
$$(6.2.40)$$

An obvious consequence of the thin-wall approximation is that the middle integral on the right hand side of Eq. 6.2.40 vanishes for A sufficiently far below τ_∞ since in this case we are sufficiently deep into the $h_2 = -v$ domain, the field configuration is constant there and the action on the (12) segment of the contour vanishes, $\int_{(12)} dt\, L[h_2] = 0$.

Next, we can readily evaluate the last integral in Eq. 6.2.40. It arises from segment (2) of the contour in Fig. 6.2 (c), which is the integral over the imaginary time component $d\tau$ and is situated at a fixed value of real time at $\operatorname{Re} t_\mathbb{C} = B \gg 1/m$. Hence we can use the asymptotic expression in Eq. 6.2.37 for $\tilde{\phi}(t_\mathbb{C}, \mathbf{x})$ on this segment of the contour, so that the entire solution $h_2(x)$ is given by,

$$h_2^{\text{segment (2)}} = v\left(\frac{e^{-imB-m(|\tau|-|\tau_\infty|)} + 1}{e^{-imB-m(|\tau|-|\tau_\infty|)} - 1} \right) + \int \frac{d^3k}{(2\pi)^{3/2}} \frac{1}{\sqrt{2\omega_\mathbf{k}}}\, f_\mathbf{k}\, e^{-\omega_\mathbf{k}|\tau|}\, e^{-i\omega_\mathbf{k}B}.$$
$$(6.2.41)$$

Figure 6.3: *The same complex-time evolution contour as in Fig. 6.2 (c). The boundary separating the domains $h(x) \to +v$ and $h(x) \to -v$ for the classical solution in a thin-wall approximation is shown as the dotted blue line. The singularity of the solution is at the point $t = 0$, $\tau = \tau_0(\mathbf{x})$, as depicted by a blue blob on the dotted line of the inter-domain boundary.*

Note that on this segment of the contour $t = B$, $-A \leq \tau \leq 0$, hence $0 \leq |\tau| \leq A$ and $0 < |\tau_\infty| \ll A$. In the large λn limit, we will find in the following section that in fact $0 \ll |\tau_\infty|$, and that the only non-trivial contribution in the thin-wall limit on this segment of the contour will come from the first term on the right hand side of Eq. 6.2.41. The location of the wall separating the two $\pm v$ domains of the field configuration is depicted in Fig. 6.3. Recall that away from $t = 0$, the domain wall is regular and not singular. The $\tilde{\phi}$ term on its own cannot contribute to the action integral since it contains only the negative frequencies. Furthermore, its overlap with the h_0 configuration at $\tau \approx \tau_\infty$ is exponentially suppressed by $e^{-m|\tau|_\infty} \ll 1$. Hence we are left with,

$$\text{thin wall}: \quad h_2(\tau, \mathbf{x}) \approx h_{0E}(\tau - \tau_\infty). \tag{6.2.42}$$

This equation is applicable on segment (2) of the contour in Fig. 6.2 (c), where the argument τ of both functions in Eq. 6.2.42 is understood as $\tau - iB$.

Eqs. 6.2.33 and 6.2.42 give us the required precise implementation of the thin-wall approximation that we will apply in what follows. In both cases, the field configurations (h_1 in Eq. 6.2.33 and h_2 in Eq. 6.2.33) are approximated in the thin-wall approach by the Brown's solution profile h_{0E}. The important difference between the two cases, however, is that the domain wall in Eq. 6.2.33 is the $\mathbf{x}$-dependent surface $\tau_0(\mathbf{x})$, while in the case of the h_2 configuration in Eq. 6.2.42, the domain wall is at τ_∞ and is spatially-independent. As the result, the the first integral on the right hand side of our expression for the action in Eq. 6.2.40, is a functional of the

domain-wall surface $\tau_0(\mathbf{x})$,

$$S_E^{(1)} = \int_{-A-i\epsilon}^{+\infty-i\epsilon} d\tau \, L_E[h_1] = S_E[\tau_0((\mathbf{x})]\,, \tag{6.2.43}$$

while the the third integral in Eq. 6.2.40 is evaluated on the uniform in space solution (see Eq. 6.2.42) and is a constant,

$$S_E^{(2)} = -\int_{-A+iB}^{0+iB} d\tau \, L_E[h_2] = -\,\text{const}\,. \tag{6.2.44}$$

In both cases, on segment (1) and segment (2) of the contour, the field configurations are regular, since, by construction, the contour avoids the singularity by the $-i\epsilon$ shift in the first integral and by the $+iB$ shift in the second.

We now proceed to compute the integral in Eq. 6.2.44. This integral is evaluated on the field configuration,

$$h_2(\tau + iB) = v\left(\frac{1 + e^{-m(\tau-\tau_\infty+iB)}}{1 - e^{-m(\tau-\tau_\infty+iB)}}\right)\,, \tag{6.2.45}$$

and can be calculated exactly[1], giving,

$$\int_{-\infty+iB}^{+\infty+iB} d\tau \int d^3x \mathcal{L}_E(h_2) = \mu \int_0^R 4\pi r^2 dr = \mu\,\frac{4\pi}{3}\,R^3\,. \tag{6.2.46}$$

Since the field is uniform in space, to ensure that the $\int d^3x$ is finite, we used the finite volume regularisation with finite spatial radius R. The infinite-volume limit, $R \to \infty$, will be taken at the end of the calculation, after combining the two action integrals in Eqs. 6.2.43 and 6.2.46. The parameter μ appearing on the right-hand side of Eq. 6.2.46 is the surface tension on the bubble solution in Eq. 6.2.45,

$$\mu = \int_{-\infty+i\epsilon}^{+\infty+i\epsilon} d\tau \left(\frac{1}{2}\left(\frac{dh}{d\tau}\right)^2 + \frac{\lambda}{4}\left(h^2 - v^2\right)^2\right) = \frac{m^3}{3\lambda}\,. \tag{6.2.47}$$

It can easily be checked (e.g. by use of the residue theorem) that the value of μ does not depend on the numerical value of iB in the shift of the integration contour: any value of $iB \neq 0$ that shifts the contour such that it does not pass directly through the singularity at τ_∞ will suffice. This shift-independence argument also applies to the integral on the first segment of the contour where the shift is $-i\epsilon$.

Let us summarise our construction up to this point. We have derived the expression

---

[1]For simplicity we extend the integration limits along the vertical axis to $\pm\infty$. Given the narrow width of the wall, any changes due to this extension are negligible.

for the contribution of quantum effects in Eq. 6.2.29 to the semiclassical rate W in Eq. 6.2.28, in the form,

$$\frac{1}{2}\Delta W^{\text{quant}} = nm\,|\tau_\infty| - \underbrace{\int_{-\infty-i\epsilon}^{+\infty+i\epsilon} d\tau\,L_E(h_1;\tau_0(\mathbf{x}))}_{\equiv\, S_E[\tau_0(\mathbf{x})]} + \frac{4\pi}{3}\,\mu R^3\,. \tag{6.2.48}$$

We note that no extremisation of the rate with respect to the surface $\tau = \tau_0(\mathbf{x})$ has been carried out so far. The expression in Eq. 6.2.48 is the general formula equivalent to the expression in Eq. 6.2.29. It will be now extremised with respect to the domain wall surface $\tau_0(\mathbf{x})$. The constant term $\frac{4\pi}{3}\,\mu R^3$ will be cancelled with its counterpart arising from the action integral in Eq. 6.2.48 before the infinite-volume limit is taken.

Following from the discussion at the end of Section 6.2.1, the shape of the singular surface, $\tau_0(\mathbf{x})$, should be determined by extremising the function ΔW^{quant} in the exponent of the multiparticle probability rate. This is equivalent to searching for a stationary (i.e. equilibrium surface) configuration described by the 'surface energy' functional, given by the right hand side of Eq. 6.2.48. Finding the stationary point corresponds to balancing the surface energy of the stretched surface, given by the integral $S_E[\tau_0(\mathbf{x})]$ in Eq. 6.2.48, against the force nm that stretches the surface $\tau_0(\mathbf{x})$ by the amount $|\tau_\infty|$. The third term on the right hand side of Eq. 6.2.48 plays no role in the extremisation procedure over $\tau_0(\mathbf{x})$ and gives a positive-valued constant contribution to $\frac{1}{2}\Delta W^{\text{quant}}$ that will be cancelled against its counterpart in $S_E[\tau_0(\mathbf{x})]$. The overall result will be finite, as expected in the infinite volume limit.

Extremal singular surface in the thin-wall approximation

The action $S_E[\tau_0(\mathbf{x})]$ can now be written as an integral over the domain-wall surface $\tau_0(\mathbf{x})$ in the thin-wall approximation. This is equivalent to stating that the action is simply the surface tension of the domain wall μ, as computed in Eq. 6.2.47, multiplied by the area. The 3-dimensional area of a curved surface in 3+1 dimensions has infinitesimal element $4\pi\mu\,r^2\sqrt{(d\tau)^2 + (dr)^2}$. Hence, the action reads,

$$S_E[\tau_0(r)] = \int_{\tau_\infty}^{0} d\tau\,4\pi\mu\,r^2\sqrt{1+\dot{r}^2} \equiv \int_{\tau_\infty}^{0} d\tau\,L(r,\dot{r})\,, \tag{6.2.49}$$

where $r = |\mathbf{x}|$ and $\dot{r} = dr/d\tau$. The integral depends on the choice of the domain wall surface $\tau_0(\mathbf{x})$ implicitly via the τ-dependence of $r(\tau)$ and $\dot{r}(\tau)$, which are computed on the domain wall.

Since $L(r, \dot{r})$ can be interpreted as the Lagrangian, one can introduce the Hamiltonian function defined in the standard way[1] as the Legendre transformation,

$$H(p, r) \;=\; L(r, \dot{r}) \,-\, p\,\dot{r}\,, \tag{6.2.50}$$

where the momentum p, conjugate to the coordinate r, is

$$p \;=\; \frac{\partial L(r, \dot{r})}{\partial \dot{r}} \;=\; 4\pi\,\mu\,\frac{r^2 \dot{r}}{\sqrt{1 + \dot{r}^2}}\,. \tag{6.2.51}$$

On a classical trajectory $r = r(\tau)$ that satisfies the Euler-Lagrange equations for $L(r, \dot{r})$, the Hamiltonian is time-independent $(dH/d\tau = 0)$ and is given by the energy E of said classical trajectory[2]. Hence, on a stationary point of $S_E[\tau_0(r)]$ with energy E, we can rewrite the action as,

$$S_E[\tau_0(r)]_{\text{stationary}} \;=\; -\tau_\infty\,E + \int\limits_{\tau_\infty}^{0} d\tau\,(L - H) \;=\; -E\tau_\infty + \int\limits_{R}^{0} p(E)\,dr\,. \tag{6.2.52}$$

In the equation above we have added and subtracted the constant energy of the solution $(E = H)$ and used the fact that $L - H = p\dot{r}$. The lower and upper integration limits are consequently set to $r(\tau_\infty) = R$ and $r(0) = 0$. The expression above gives us the action functional $S_E[\tau_0(r)]$ on a trajectory $r(\tau)$, or equivalently $\tau = \tau_0(r)$, which is a classical trajectory (i.e. an extremum of the action for a fixed energy E). Equivalently, for the stationary point of the expression in Eq. 6.2.48 we have,

$$\frac{1}{2}\Delta W^{\text{quant}} \;=\; (E - nm)\tau_\infty - \int\limits_{R}^{0} p(E)\,dr \;+\; \frac{4\pi}{3}\,\mu R^3\,. \tag{6.2.53}$$

Extremisation of this expression with respect to the parameter τ_∞ gives $E = nm$, thus selecting this energy for the classical trajectory as required,

$$\frac{1}{2}\Delta W^{\text{quant}}_{\text{stationary}} \;=\; -\int\limits_{R}^{0} p(E)\,dr \;+\; \frac{4\pi}{3}\,\mu R^3\,, \qquad E = nm\,. \tag{6.2.54}$$

To evaluate Eq. 6.2.54, we need to determine the dependence of the momentum of the classical trajectory on its energy. To find $p(E)$, we start by writing the expression

---

[1] In Euclidean space $L = -K - V$ and $H = -K + V$, where K and V are the kinetic and potential energies respectively.

[2] One should not confuse the energy of the classical trajectory $r = r(\tau)$ – which is essentially the Euclidean surface energy of the domain wall – with the energy of the classical solutions h_1 and h_2. Both energy variables are denoted as E, but the energy of the domain wall at the stationary point will turn out to be $E = mn$, while the energy of the corresponding field configuration h_1 was $E = 0$.

for the energy, $E = L - p\dot{r}$, in the form,

$$E = 4\pi\mu\, r^2 \sqrt{1 + \dot{r}^2} - 4\pi\,\mu \frac{r^2 \dot{r}}{\sqrt{1 + \dot{r}^2}} = 4\pi\,\mu \frac{r^2}{\sqrt{1 + \dot{r}^2}}, \qquad (6.2.55)$$

and then compute the combination $E^2 + p^2$ using the above expression and Eq. 6.2.51,

$$E^2 + p^2 = \left(4\pi\mu\, r^2\right)^2 \left(\frac{1}{1 + \dot{r}^2} + \frac{\dot{r}^2}{1 + \dot{r}^2}\right) = \left(4\pi\mu\, r^2\right)^2. \qquad (6.2.56)$$

This gives the desired expression for the momentum $p = p(E, r)$,

$$p(E, r) = -4\pi\,\mu \sqrt{r^4 - \left(\frac{E}{4\pi\mu}\right)^2}, \qquad (6.2.57)$$

where we have selected the negative root for the momentum in accordance with the fact that $p(\tau) \propto \dot{r}$ (as follows from Eq. 6.2.51) and that $r(\tau)$ is a monotonically decreasing function.

Substituting this into Eq. 6.2.54 we have,

$$\frac{1}{2}\Delta W^{\text{quant}} = -\int_R^{r_0} p(E)\, dr + \frac{4\pi}{3}\mu R^3 = -\int_{r_0}^R 4\pi\,\mu \sqrt{r^4 - r_0^4}\, dr + \frac{4\pi}{3}\mu R^3. \qquad (6.2.58)$$

The minimal value of the momentum (and the lower bound of the integral in Eq. 6.2.58) is cut off at the critical radius r_0,

$$r_0^2 = \frac{E}{4\pi\mu}. \qquad (6.2.59)$$

Note that the contribution to the integral in Eq. 6.2.58 on the interval $0 \leq r \leq r_0$ will be considered in Section 6.2.3; let us temporarily ignore it.

The integral on the right-hand side of Eq. 6.2.58 is evaluated as follows,

$$\int_1^{R/r_0} \sqrt{x^4 - 1}\, dx = \left[\frac{1}{3}x\sqrt{x^4 - 1} - \frac{2}{3}i\,\text{EllipticF}[\text{ArcSin}(x), -1]\right]_{x=1}^{x=R/r_0}$$

where the *Mathematica* function EllipticF$[z, m]$ is also known as the elliptic integral of the first kind, $F(z|m)$. In the $R/r_0 \to \infty$ limit, the integral simplifies to,

$$(-4\pi\mu r_0^3) \int_1^{R/r_0} \sqrt{x^4 - 1}\, dx \to -\frac{4\pi}{3}\mu R^3 + 4\pi\mu r_0^3 \sqrt{4\pi}\,\frac{1}{3}\frac{\Gamma(5/4)}{\Gamma(3/4)}$$

$$= -\frac{4\pi}{3}\mu R^3 + \frac{E^{3/2}}{\sqrt{\mu}}\frac{1}{3}\frac{\Gamma(5/4)}{\Gamma(3/4)}. \qquad (6.2.60)$$

Note that,

$$4\pi\mu r_0^3 \;=\; \frac{E^{3/2}}{\sqrt{\mu}}\frac{1}{\sqrt{4\pi}} \;=\; n\sqrt{\lambda n}\,\frac{\sqrt{3}}{\sqrt{4\pi}}\,. \tag{6.2.61}$$

We see that the large volume constant term $\frac{4\pi}{3}\,\mu R^3$ cancels between the expressions in Eq. 6.2.60 and Eq. 6.2.58, as expected. The final result for the thin-wall trajectory contribution to the quantum rate is given by,

$$\Delta W^{\text{quant}} \;=\; \frac{E^{3/2}}{\sqrt{\mu}}\frac{2}{3}\frac{\Gamma(5/4)}{\Gamma(3/4)} \;=\; \frac{1}{\lambda}\,(\lambda n)^{3/2}\,\frac{2}{\sqrt{3}}\frac{\Gamma(5/4)}{\Gamma(3/4)} \;\simeq\; 0.854\,n\sqrt{\lambda n}\,. \tag{6.2.62}$$

We note that this expression is positive-valued, that it grows in the limit of $\lambda n \to \infty$, and that it has the correct scaling properties for the semiclassical result, i.e. it is of the form $1/\lambda$ times a function of λn.

Our result in Eq. 6.2.62 and the derivation we presented, followed closely the construction in [169, 170]. The expression in Eq. 6.2.62 is also in agreement with the formula derived much earlier in Ref. [185], based on a somewhat different semiclassical reasoning involving regular thin-wall bubble configurations in Euclidean and Minkowski time.

Importantly, the thin-wall approximation is justified in the $\lambda n \gg 1$ limit on the extremal surface in the regime where $r(\tau) > r_0$, as originally noted in [185]. The thin-wall regime corresponds to the spatial radius of the bubble (i.e. the spatial extent of the $O(3)$-symmetric configuration at a fixed τ) being much greater than the thickness of the wall, $r \gg 1/m$. For the classical configuration at hand, the radius is always greater than the critical radius,

$$rm \;\geq\; r_0 m \;=\; m\left(\frac{E}{4\pi\mu}\right)^{1/2} \;\propto\; \left(\frac{\lambda E}{m}\right)^{1/2} \;=\; \sqrt{\lambda n} \;\gg\; 1\,, \tag{6.2.63}$$

where we have used the value for the energy $E = nm$ on our solution. Essentially, our thin-wall approach is justified until we near the top of the deformation of the singular surface, at $t = \tau = x = 0$, where the spatial radius of the bubble decreases towards zero.

6.2.3   Singular surfaces at $r \leq r_0$: beyond thin walls

What happens with the extremal surface in the regime $0 \leq r(\tau) \leq r_0$? To address this question, first let us determine the classical trajectory $r(\tau)$ – or equivalently the wall profile $\tau = \tau_0(r)$ of the saddle-point solution – on which the rate W was computed in Eq. 6.2.62. To find it, we simply integrate the equation for the conserved
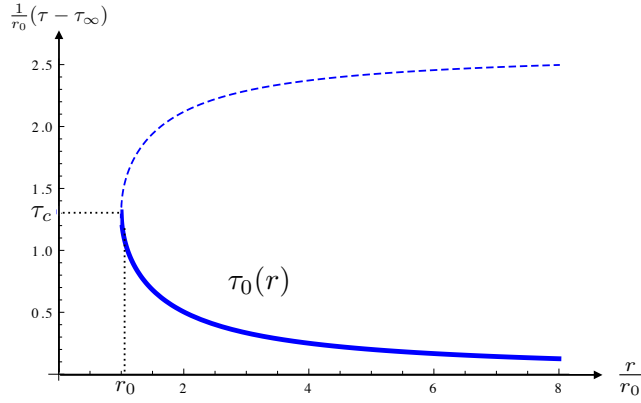
Figure 6.4: *Extremal surface $\tau = \tau_0(r)$ of the thin-wall bubble solution in Eq. 6.2.66. Solid line denotes the bubble wall profile of the bubble radius r above the critical radius r_0. The dashed line corresponds to the branch of the classical trajectory beyond the turning point at r_0.*

energy (see Eq. 6.2.55) on our classical solution,

$$E \; = \; 4\pi\,\mu\,\frac{r^2}{\sqrt{1+\dot{r}^2}}\,, \tag{6.2.64}$$

or, equivalently, the expression $(r/r_0)^4 \; = \; 1 + \dot{r}^2$. One finds,

$$\int_{\tau_\infty}^{\tau} d\tau \; = \; -\int_{R}^{r} \frac{dr}{\sqrt{\left(\frac{r}{r_0}\right)^4 - 1}}\,, \tag{6.2.65}$$

which after integration can be expressed in the form,

$$\tau(r) \; = \; \tau_\infty \; + \; r_0\left(\frac{\Gamma^2(1/4)}{4\sqrt{2\pi}} \; + \; \mathrm{Im}\left(\mathrm{EllipticF}[\mathrm{ArcSin}(r/r_0), -1]\right)\right). \tag{6.2.66}$$

This classical trajectory gives the thin-wall bubble classical profile for $r_0 < r(\tau) < \infty$, which is the result in Eq. 6.2.62 for the quantum contribution to the rate $\Delta W^{\mathrm{quant}}$. This trajectory is plotted in Fig. 6.4.

What happens when the radius of the bubble $r(\tau)$ approaches the critical radius r_0 in Eq. 6.2.59, where the momentum (see Eq. 6.2.57) vanishes? Recall that in the language of a mechanical analogy we are searching for an equilibrium (i.e. the stationary point solution) where the surface $\tau_0(r)$ is pulled upwards (in the direction of τ) by a constant force $E = nm$ acting at the point $r = 0$. This corresponds to finding an extremum – in our case the true minimum – of the expression in Eq. 6.2.48,

which we rewrite now in the form,

$$\frac{1}{2}\Delta W^{\text{quant}} \;=\; \underbrace{E\,|\tau_\infty|}_{\text{force}\times\text{height}} \;-\; \underbrace{\mu \int d^{2+1}\text{Area}}_{\text{surface energy}}\,. \tag{6.2.67}$$

Sufficiently far away from the origin (where the force acts), the surface is nearly flat and does not extend in the τ direction. As r approaches the origin from larger values, the surface becomes increasingly stretched in the τ direction. At the critical radius r_0, the surface approaches the shape of a cylinder $R^1 \times S^2$, with R^1 along the τ direction.

Up to the critical point τ_c where $r = r_0$, the force and the surface tension must balance each other,

$$E\,|\tau_\infty - \tau_c| \;-\; \left(\int_{\tau_\infty}^{\tau_c} d\tau\, 4\pi\mu\, r^2 \sqrt{1+\dot r^2} \;-\; \frac{4\pi}{3}\,\mu R^3 \right) = 0\,. \tag{6.2.68}$$

The right-hand side was of course calculated in Eqs. 6.2.58 and 6.2.62. However, when the critical point r_0 is reached at τ_c, the balance of forces becomes trivial,

$$E\,|\tau_c| \;-\; 4\pi\,\mu\, r_0^2\,|\tau_c| \;=\; 0\,. \tag{6.2.69}$$

Clearly, the branch of the classical trajectory shown as the dashed line in Fig. 6.4 is unphysical in the sense that it does not describe the membrane pulled upwards with the force $E = mn$. Furthermore, the membrane surface does not satisfy the boundary condition that $\tau_0 = 0$ at $r = 0$ since it currently does not even extend to $r < r_0$. The vanishing of the expression in Eq. 6.2.69 is the consequence of the definition of the critical radius in Eq. 6.2.59. As soon as the radius $r(\tau)$ approaches the critical radius r_0, the radius freezes (since $p \propto d_\tau r = 0$); the two terms in Eq. 6.2.69 become equal, $E = \mu\, 4\pi\, r_0^2$, and remain so at all times above the critical time τ_c. The thin-wall profile becomes an infinitely stretchable cylinder, as shown in Fig. 6.5 (a), giving no additional contribution to ΔW^{quant} on top of Eq. 6.2.68.

The freely-stretched cylinder in Fig. 6.5 (a) is an idealised approximation to the more realistic configuration that would be realised in practice in our mechanical analogy. One can consider what this realistic mechanical solution would look like. Let us define the quantity $d(r)$,

$$d = \tau + |\tau_\infty|\,, \qquad 0 \le d \le |\tau_\infty|\,. \tag{6.2.70}$$

as the coordinate along the vertical axis in Ref. Fig. 6.5 measuring the height of the surface stretched by the 'force' $E|\tau_\infty|$ as a function of r. At the base of the surface
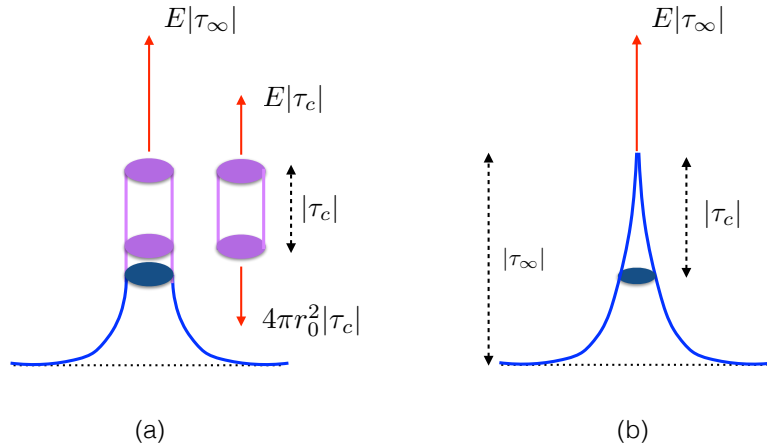
Figure 6.5: *Stationary surface configuration obtained by gluing two branches. Plot (a) shows the surface in the thin-wall approximation, which glues the original solution in Eq. 6.2.66 to the infinitely stretchable cylinder solution of Eq. 6.2.68. Plot (b) depicts its more realistic implementation where the infinite cylinder is replaced by a cone as a consequence of allowing the surface tension μ to increase with $|\tau|$ in the regime where the highly stretched surface effectively becomes a 1-dimensional spring.*

we have[1] $d \simeq 0$. The surface wall profile is nearly flat in the τ direction. As d increases from 0, the radius $r(\tau)$ grows smaller, following the profile of the thin-wall solution contour in the lower part of Fig. 6.5. As r approaches the critical radius r_0, the surface becomes almost parallel to the d (or τ) direction. Such a surface behaves more like a spring along the τ coordinate. For the strict thin-wall approximation, the surface tension μ is assumed to be a constant. However, in the case of the spring, it should instead be the Young's elastic modulus, k_{Young} that takes a constant value. Hence, for a highly-stretched surface in the τ direction, we should introduce some dependence on d (see Eq. 6.2.70) into the surface tension via,

$$\mu(d) = \mu_0 \left(1 + \hat{k}\, d \right), \tag{6.2.71}$$

where $\hat{k} \ll 1$ is a constant such that the product $\hat{k}d$ is dimensionless. In the limit $d \to 0$, the surface tension $\mu(d) \to \mu_0$, where $\mu_0 = \frac{m^3}{3\lambda}$ is the same constant contribution to the surface tension as we computed earlier in Eq. 6.2.47 in the strict thin-wall case. The corresponding Young's modulus of the stretched surface would be $k_{\text{Young}} = \mu_0\, \hat{k}$. Eq. 6.2.71 describes a small deviation from the standard thin-wall approximation, where the surface tension is now dependent on the stretching of the surface. This expression can be thought of as the zeroth and first order terms in the

---

[1]Recall that the tip of the surface is at $\tau = 0$, where $d = |\tau_\infty|$, and that the surface's base is at a negative $\tau = \tau_\infty = -|\tau_\infty|$, which corresponds to $d = 0$.
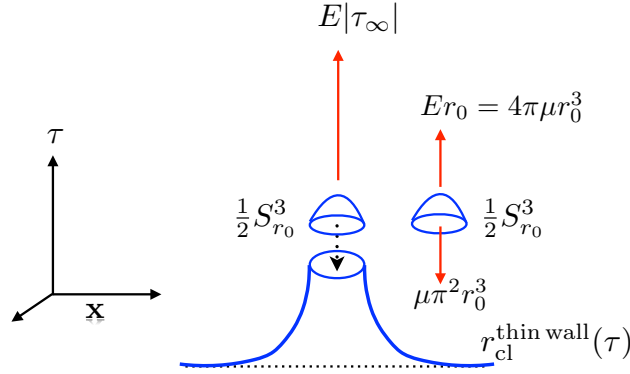
Figure 6.6: *Surface obtained by 'completing' the thin-wall classical solution $r_{\text{cl}}^{\text{thin wall}}$ with the upper half of a three-sphere $S_{r_0}^3$, of radius r_0 in $(\mathbf{x}, \tau)$, at $0 \leq |\mathbf{x}| \leq r_0$. The force stretching the surface is $E = 4\pi\mu r_0^2$.*

Taylor expansion of the function $\mu(\tau + \tau_\infty)$.

The result of this improvement of μ is that the balance between the two terms in Eq. 6.2.69 continues to hold. However, for an adiabatic approximation of nearly constant μ, with $\hat{k}d \ll 1$, it is now in the form,

$$\left(E - \mu(d) \cdot 4\pi\, r(d)^2\right) d = 0\,, \quad \text{where } d \geq |\tau_c|\,. \tag{6.2.72}$$

For every infinitesimal increase in the vertical coordinate d above $|\tau_c|$, the radius $r(d)$ becomes a little smaller than its value r_0 at the base of the cylinder in Fig. 6.5 (a). As a result, the cylinder gets narrower as d increases and turns into the cone-like shape shown in Fig. 6.5 (b). The actual choice of the modification of the surface tension expression, such as in Eq. 6.2.71, is of course determined by the field configurations themselves; it can be seen as a part of the extremisation procedure. For an adiabatically-slowly varying μ (such that the contribution from the cone to W is negligible), the overall contribution ΔW^{quant} is dominated by the surface at $r > r_0$ in the large λn limit. In this case we conclude that,

$$\Delta W^{\text{quant}} = \frac{1}{\lambda} (\lambda n)^{3/2} \frac{2}{\sqrt{3}} \frac{\Gamma(5/4)}{\Gamma(3/4)} \simeq 0.854\, n\sqrt{\lambda n}\,. \tag{6.2.73}$$

Further discussion of $r \leq r_0$ region

Let us discuss the apparent loss of the classical strictly-thin-wall solution at $r < r_0$ in a little more detail. An important point we want to emphasise is that in our model with spontaneous symmetry breaking, the d-dimensional domain wall surface separating two distinct vacuum domains at $\pm v$, is a local *minimum* of the Euclidean

action. The infinite extent of the surface, which reaches the boundary of space ($r \to R$ or $r \to \infty$ when the cut-off R is removed), is important. It is different from the Coleman's bounce solution [204], which is known to be a local maximum, or more precisely the saddle-point of the action. The bounce has a membrane of finite extent; in the $O(4)$-symmetric case, it is the surface of the S^3 spherical bubble separating $h \simeq \pm v$ on the inside/outside of the sphere, and the radius of the bubble is the negative mode for the bounce solution. However, in the case of the infinite domain wall surface, the domain wall is a topologically-stable configuration and hence a local minimum[1]. While the action on the wall with infinite extent in d dimensions contains an infinite constant, $S = \frac{4\pi}{3}R^3 \to \infty$, this contribution is subtracted in our construction, as dictated by Eq. 6.2.48. The force being applied to the domain wall in the τ-direction stretches and curves the surface of the wall to balance the action of the force. The resulting stationary solution for the stretched surface in this mechanical analogy is a stable solution when the required boundary conditions, $\tau_0(r = R) = \tau_\infty$ and $\tau_0(r = 0) = 0$, are satisfied.

We conclude that there must exist a stable classical solution for the domain wall surface with the boundary conditions imposed at infinite and zero radii. But what we have learned from Figs. 6.4 and 6.5 (a) is that this solution can be described by the strict thin-wall configuration only for $r > r_0$. At the values of $r(\tau)$ below the critical radius r_0, the solution corresponding to the minimum of the action requires a deviation from the strict thin-wall limit. One approach to achieve this is to allow for the τ-dependent surface tension, as we already explained. Alternatively, we can continue using the thin-wall configurations with constant μ and attempt to complete our solution at $0 \leq r(\tau) \leq r_0$. We treat these completions as *trial configurations* approximating the true minimal solution. The benefit of this approximation is that it does not require any precise knowledge of how the deviation from the thin wall regime is realised.

A simple completion of the solution is to add the surface of an upper half of the three-sphere $S^3_{r_0}$, of radius r_0, to our thin-wall classical solution,

$$r^{\text{thin wall}}_{\text{trial}}(\tau) = \begin{cases} r^{\text{thin wall}}_{\text{cl}}(\tau) & : \text{ for } r_0 \leq r < \infty \\ \frac{1}{2}\, S^3_{r_0}(\mathbf{x}, \tau) & : \text{ for } 0 \leq r \leq r_0 \,, \end{cases} \qquad (6.2.74)$$

as shown in Fig. 6.6. It is easy to deduce the contribution to the semiclassical rate from the surface of $\frac{1}{2}\, S^3_{r_0}$; it is given by,

$$(1/2)\, \delta W^{\text{quant}}_{\frac{1}{2}S^3} = E r_0 - \mu \pi^2 r_0^3 = 4\pi \mu r_0^3 \left(1 - \pi/4\right) \simeq 0.1\, n\sqrt{\lambda n}\,. \qquad (6.2.75)$$

---

[1]A recent discussion of domain walls and their stability can be found in the textbook [205].

The force E is expressed in terms of the critical radius, as before, $E = 4\pi\mu r_0^2$. The extent of the $S_{r_0}^3$ half sphere in the τ-direction is r_0, and the action of this surface is,

$$\frac{1}{2} S[S_{r_0}^3] = \frac{1}{2} 2\pi^2 r_0^3 = \pi^2 r_0^3, \tag{6.2.76}$$

which, together with the identity in Eq. 6.2.61, justifies the formula in Eq. 6.2.75.

The contribution in Eq. 6.2.75 should be added to the expression for $\Delta W^{\mathrm{quant}}$ in Eq. 6.2.73 that came from the thin-wall classical solution at $r > r_0$. We note that the expression in Eq. 6.2.75 is positive, signalling that the force gives a slightly greater contribution than the surface energy of the half-sphere, increasing the overall rate in Eq. 6.2.75.

In general, the completion of the classical solution by the $O(4)$-symmetric thin-wall surface in Eq. 6.2.75 does not give the minimum of the action but rather a trial configuration. For the true minimum, the rate $\Delta W^{\mathrm{quant}}$ would only be larger. For example a cone-like $O(3)$-symmetric completion, such as the one depicted in Fig. 6.5 (b) would give an even larger contribution. However, to evaluate it, one would be required to use a beyond-the-thin-wall description of the surface. For our purposes, it is sufficient to approximate the true classical stationary point by the thin-wall configuration in Eq. 6.2.74 with the rate given by Eq. 6.2.73 with a small positive correction (see Eq. 6.2.75) arising from the $O(4)$ completion of the classical surface at $0 \leq r \leq r_0$. In total we have,

$$\Delta W^{\mathrm{quant}} = 0.854\, n\sqrt{\lambda n} + \delta W^{\mathrm{quant}} > 1 \cdot n\sqrt{\lambda n}. \tag{6.2.77}$$

Eq. 6.2.77 is the main result of this section. To be on the conservative side we can always ignore the positive $\delta W^{\mathrm{quant}}$ contribution and continue using the expression in Eq. 6.2.73 for the contribution of quantum effects to the function W in the exponent of the semiclassical rate. In summary, our result for the semiclassical approximation to the rate reads,

$$\mathcal{R}_n(E) = e^{W(E,n)}, \quad W \simeq n\left(\log\frac{\lambda n}{4} - 1\right) + \frac{3n}{2}\left(\log\frac{\varepsilon}{3\pi} + 1\right) + 0.854\, n\sqrt{\lambda n}, \tag{6.2.78}$$

reproducing the result in [169, 170]. The expression in Eq. 6.2.78 was derived in the near-threshold high-energy high-multiplicity limit,

$$\lambda \to 0, \quad n \to \infty, \quad \text{with} \quad \lambda n = \text{fixed} \gg 1, \quad \varepsilon = \text{fixed} \ll 1, \tag{6.2.79}$$

where final state particles are non-relativistic so that ε is treated as a fixed number much smaller than one. The overall energy and the final state multiplicity are related linearly via $E/m = (1+\varepsilon)\, n \simeq n \gg 1$. Clearly, for any small fixed value of ε one can

choose a sufficiently large value of λn, such that the function $W(\lambda n, \varepsilon)$ in Eq. 6.2.78 is positive. These semiclassical expressions imply that at sufficiently large particle multiplicities, the expression $\mathcal{R}_n(E)$ grows exponentially with n and consequentially with the energy E.

6.3 Comparison with the Landau WKB method in QM

The semiclassical approach in quantum mechanics (QM) is known as the WKB method. It is commonly used and provides a powerful non-perturbative formalism for solving quantum mechanics problems. In their classic volume [203], Landau and Lifshitz formulate the WKB approach using singular classical solutions analytically-continued to complex space. In this sense the Landau WKB approach in QM [193, 203] has many similarities with the semiclassical approach in quantum field theory [168] that we are using in this work. Considerations in early literature of various generalisations of the Landau-WKB singular configurations approach to multi-dimensional systems can be found in Refs. [185, 186, 206–209].

The main purpose of this section is to compare the the semiclassical approach in quantum field theory, covered in Sections 6.1 and 6.2, to the Landau WKB in quantum mechanics, and to discuss the differences between these two semiclassical realisations.

6.3.1 Matrix elements in the Landau WKB formulation

Landau and Lifshitz consider a matrix element of some physical operator, $\hat{\mathcal{O}}(\hat{q})$, where $\hat{q}$ is the position operator for a 1-dimensional quantum system with potential $U(q)$. Such a system is of course governed by the time-independent Schrödinger equation,

$$-\frac{\hbar^2}{2m}\frac{d^2}{dq^2}\psi(q) + U(q)\psi(q) = E\psi(q), \tag{6.3.1}$$

where m is the mass and E is the energy associated with positional wavefunction $\psi(q)$. The matrix element of $\hat{\mathcal{O}}$ between two states of energy E_1 and E_2 can be written as,

$$O_{12} = \langle E_1|\hat{\mathcal{O}}|E_2\rangle = \int\limits_{-\infty}^{\infty} \psi_1^*(q)\,\hat{\mathcal{O}}(\hat{q})\,\psi_2(q)dq. \tag{6.3.2}$$
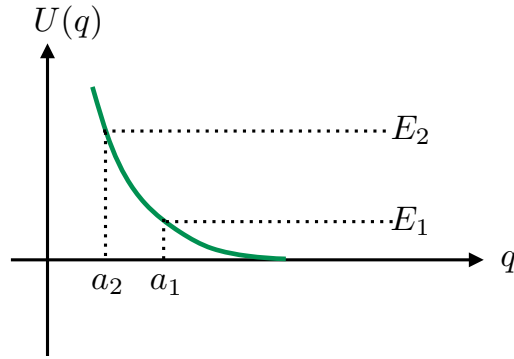
Figure 6.7: *Quantum mechanical potential $U(q)$ with two energy eigenstates $E_2 > E_1$. The turning points are $q = a_1$ and $q = a_2$ where $U(q_i) = E_i$. The wavefunctions $\psi_1(q)$ and $\psi_2(q)$ are given in Eqs. 6.3.3 and 6.3.4 in the classically forbidden regions $q < a_1$ and $q < a_2$ to the left of the potential barrier.*

When the potential varies on length scales much larger than a wavelength, WKB methods can be used to approximate the wavefunctions, ψ_i, for the states of energies E_i by solving the Schrödinger equation by iterations in the small parameter $\hbar$. At the leading WKB order the wavefunctions are given by [203],

$$\psi_1(q) \simeq \frac{C_1}{2\sqrt{|p_1|}}\, e^{-\frac{1}{\hbar}\left|\int_{a_1}^q p_1 dq\right|}, \qquad \text{for } q < a_1, \qquad (6.3.3)$$

$$\psi_2(q) \simeq \frac{iC_2}{2\sqrt{|p_2|}}\, e^{+\frac{1}{\hbar}\left|\int_{a_2}^q p_2 dq\right|}, \qquad \text{for } q < a_2, \qquad (6.3.4)$$

where we have assumed the ordering of the energies, $E_1 < E_2$ to select the signs of the roots in the exponents. In the above expressions p_i denote the classical momenta,

$$p_i = \sqrt{(2m)(E_i - U(q))}, \qquad (6.3.5)$$

and $C_{1,2}$ are constants. The expressions in Eqs. 6.3.3 and 6.3.4 are written in the classically-forbidden regions, $q < a_1$ and $q < a_2$ for the wavefunctions $\psi_1(q)$ and $\psi_2(q)$ respectively, where a_1 and a_2 are the turning points, $U(a_i) = E_i$ as shown in Fig. 6.7. Importantly, the roots of the wavefunctions are selected in such a way that the wavefunction ψ_1 with the smaller energy, $E_1 < E_2$, has the negative-valued exponent, while the wavefunction ψ_2 with the higher energy has the positive exponent.

These approximations (see Eqs. 6.3.3 and 6.3.4) break down in the vicinity of the classical turning points $q \simeq a_1$. Landau and Lifshitz explain how to avoid these regions by deforming the integration contour into the upper half plane of complex q, away from the classical turning points. Then it follows from Eqs. 6.3.2 to 6.3.4

that the matrix element is dominated by the contribution from the singularity of the potential: i.e. the point, q_0, where $U(q_0) \to \infty$,

$$O_{12} \simeq \exp \left\{ -\frac{1}{\hbar} \left| \int^{q_0} p_1 dq \right| + \frac{1}{\hbar} \left| \int^{q_0} p_2 dq \right| \right\}. \qquad (6.3.6)$$

This WKB formula is often presented in the form [203],

$$O_{12} \simeq \exp \left\{ -\frac{1}{\hbar} \text{Im} \left[\int^{q_0} \sqrt{2m(E_2 - U(q))} dq - \int^{q_0} \sqrt{2m(E_1 - U(q))} dq \right] \right\}, \qquad (6.3.7)$$

which requires an additional clarification for selecting the sign of the imaginary part, or equivalently of the square roots in Eq. 6.3.7.

The lower limits of the q integrations in the expressions in Eqs. 6.3.6 and 6.3.7 are unimportant to the leading WKB accuracy as the dominant contributions come from the vicinity of the singularity at $q \sim q_0$ near the upper limit of the integrals.

Notice that the WKB exponent has no dependence on the operator $\hat{\mathcal{O}}$. Indeed the precise form of $\hat{\mathcal{O}}$ may change the overall prefactor, but it does not affect the bulk behaviour. The above estimate is derived for *generic* operators that contain no explicit dependence on $\hbar$. Furthermore, the generic operators above should not include 'bad' choices of $\hat{\mathcal{O}}$ that would give an unusually small coefficient in front of the exponent in Eq. 6.3.7. A simple example is $\hat{\mathcal{O}} = \text{constant}$, for which O_{12} vanishes due to the orthogonality of ψ_1 and ψ_2.

It will be useful to summarise the characteristic features of the WKB result in Eq. 6.3.6:

1. The WKB matrix element is dominated by the singularity of the potential, $U(q) \to \infty$ as $q \to q_0$. Since the energies $E_{1,2}$ are finite, the singularity is located in the classically forbidden region $U(q) > E_{1,2}$, where the coordinates q are analytically-continued on deformed contours and momenta p are complex-valued.

2. For generic operators with no exponential dependence on $\hbar$, the leading order WKB expression for their matrix elements in Eq. 6.3.6 does not depend on the specific choice of the operator.

   However, this is where the similarities between the QM WKB and the QFT semiclassical methods end.

3. The sign prescription in the definition of the imaginary part in the WKB exponent in Eq. 6.3.7 is fixed by the expression in Eq. 6.3.6. It is easy to

verify that for every q in the classically forbidden region, the absolute value of the complex momentum $|p_1|$ is always greater than $|p_2|$ since $U(q) - E_1 > U(q) - E_2$ for the energy ordering $E_1 < E_2$. Hence the resulting matrix elements computed using the WKB approximation in quantum mechanics (see Eqs. 6.3.6 and 6.3.7) are always exponentially suppressed, unlike what we saw in the QFT calculation in the previous section.

`Example`: Landau-Lifshitz Section 51 Problem 1 [203].

Calculate the exponential factor of the matrix elements in the potential $U(q) = U_0 e^{-\alpha q}$.

Solution: $U(q)$ becomes infinite only for $q \to -\infty$, hence the singularity is the point $q = q_0 = -\infty$. Using Eq. 6.3.6 we write

$$
O_{12} \simeq \exp\left\{ -\frac{1}{\hbar}\left| \int_{a_1}^{-\infty} \sqrt{2m(U-E_1)}\, dq \right| + \frac{1}{\hbar}\left| \int_{a_2}^{-\infty} \sqrt{2m(U-E_2)}\, dq \right| \right\}
$$

$$
= \exp\left\{ +\frac{1}{\hbar} \int_{a_1}^{-\infty} \sqrt{2m(U_0 e^{-\alpha q}-E_1)}\, dq - \frac{1}{\hbar} \int_{a_2}^{-\infty} \sqrt{2m(U_0 e^{-\alpha q}-E_2)}\, dq \right\},
$$

$$
\tag{6.3.8}
$$

where a_1 and a_2 are the turning points, $a_1 > a_2 > q_0 = -\infty$, similar to what is shown in Fig. 6.7. It is convenient to introduce the velocity variables v_1 and v_2 and use them instead of the energies E_1 and E_2,

$$
v_1^2 = \frac{2E_1}{m}, \qquad v_2^2 = \frac{2E_2}{m}, \tag{6.3.9}
$$

and rewrite the integrals on the right-hand side of Eq. 6.3.8 ($i = 1, 2$) as

$$
\frac{1}{\hbar} \int_{a_i}^{-\infty} dq \sqrt{2m(U_0 e^{-\alpha q}-E_i)} = \frac{mv_i}{\hbar} \int_{a_i}^{-\infty} dq \sqrt{\frac{2U_0}{m^2 v_i^2} e^{-\alpha q} - 1}. \tag{6.3.10}
$$

Making the change of integration variables from q to y via,

$$
y = -\alpha q + \log \frac{2U_0}{m^2 v_i^2}, \tag{6.3.11}
$$

the integral in Eq. 6.3.10 becomes

$$
-\frac{m}{\hbar}\frac{v_i}{\alpha} \int_0^{+\infty} dy \sqrt{e^y - 1} = -\frac{2m}{\hbar}\frac{v_i}{\alpha}\left(\sqrt{e^{y_0}-1} - \mathrm{Arctan}\left(\sqrt{e^{y_0}-1}\right) \right)|_{y_0 \to \infty}
$$

$$
= -\frac{2\sqrt{2U_0}}{\hbar\alpha} \exp\left[\frac{\alpha}{2}|q_0|\right]|_{|q_0|\to\infty} + \frac{\pi m}{\hbar\alpha} v_i. \tag{6.3.12}
$$

Finally, we note that in the difference between the two integrals in Eq. 6.3.8 the infinite terms cancel and we are left with the finite contribution coming from the second term in Eq. 6.3.12 for $i = 1, 2$. The WKB result for the matrix element to exponential accuracy reads,

$$O_{12} \simeq e^{-\frac{\pi m}{\hbar \alpha}(v_2 - v_1)} . \tag{6.3.13}$$

Since the velocities are ordered in the same way as the energies, $v_2 > v_1$, we conclude that the matrix element is exponentially-suppressed. We also note that the exponent in Eq. 6.3.13 is independent of the choice of the operator $\hat{\mathcal{O}}(q)$.

This example confirms the general conclusion we already reached in item (3.) above: that in quantum mechanics the WKB approximation, by construction, can only result in exponentially-suppressed matrix elements and can never give exponentially-growing probability rates. This is of course fully expected: given that ordinary quantum mechanics with a Hermitian Hamiltonian is a unitary theory, probabilities must be conserved and cannot exceed unity.

What is then the technical difference between the WKB formulation in quantum mechanics and the semiclassical method in quantum field theory? Both formalisms compute matrix elements of certain operators and both use singular complex-valued configurations to find the dominant contributions. Nevertheless the field-theoretical formulation does not have a built-in restriction to disallow positive-valued functions W in the exponent of the semiclassical rate. This is evidenced by the function W in our result (see Eq. 6.2.78), becoming positive at sufficiently-large values of λn. The critical difference between the QM and QFT formulations is that in QFT we have an entire *surface* of singularities rather than isolated singular point(s) in QM.

6.3.2   The role of the singular surface in QFT

For concreteness, when discussing the semiclassical method in quantum field theory we will continue using the model in Eq. 4.1.3 with SSB, which in terms of the shifted field $\phi(x) = h(x) - v$ in $(d + 1)$ dimensions has the Lagrangian description,

$$\mathcal{L}(\phi) = \frac{1}{2} \partial^\mu \phi \, \partial_\mu \phi - \frac{1}{2} m^2 \phi^2 - \lambda v \phi^3 - \frac{\lambda}{4} \phi^4 , \tag{6.3.14}$$

with the mass $m = \sqrt{2\lambda}v$. It is also useful to denote the potential energy density as $\mathcal{V}(\phi)$, and its interacting part as $\mathcal{V}_{\text{int}}(\phi)$,

$$
\begin{aligned}
\mathcal{V}(\phi) &= \frac{1}{2}m^2\phi^2 + \lambda v\phi^3 + \frac{\lambda}{4}\phi^4\,, \\
\mathcal{V}_{\text{int}}(\phi) &= \lambda v\phi^3 + \frac{\lambda}{4}\phi^4\,.
\end{aligned}
\tag{6.3.15}
$$

We recall that the classical trajectory $\phi(x) = h(x) - v$ used in the semiclassical method in Sections 6.1 and 6.2 is infinite on a d-dimensional singularity surface in $(\tau, \mathbf{x})$ that touches the origin $x = 0$ in Minkowski space. Correspondingly, the value of the potential $\mathcal{V}(\phi)$ also becomes infinite at the singularity, which is analogous to the statement about the singularity of the potential $U(q)$ in quantum mechanics,

$$
\begin{aligned}
\text{QFT}: \quad & \lim_{\tau \to \tau_0(\mathbf{x})} \mathcal{V}(\phi(x)) = \infty\,, \\
\text{QM}: \quad & \lim_{q \to q_0} U(q) = \infty\,.
\end{aligned}
\tag{6.3.16}
$$

However, the potential in QFT is singular on the d-dimensional surface, $\tau = \tau_0(\mathbf{x})$, found by extremising the Euclidean action over all appropriate shapes of trial singular surfaces. In QM there are no spatial dimensions; q is a function of time only, $q = q(\tau)$, and the potential $U(q)$ is singular at a point[1] $q(0) \equiv q_0$. Hence, there are no surfaces to extremise over in QM and consequently no dependence on the surface shape $\tau_0(\mathbf{x})$ or the value of $|\tau_\infty|$, which were of critical importance in QFT, as manifested by Eqs. 6.2.29 and 6.2.48,

$$
\frac{1}{2}\Delta W^{\text{quant}} = nm\,|\tau_\infty| - S_E[\tau_0(\mathbf{x})] + S_E[\text{flat}]\,.
\tag{6.3.17}
$$

In fact, the very reason why the contributions of quantum corrections to the rate in the field theory case are not forced to be exponentially-suppressed is due to the positive-valued contribution of the term $nm\,|\tau_\infty|$ on the right-hand side of Eq. 6.3.17. It is easy to verify that the action integral of the surface stretched in the τ-direction (*cf.* Eq. 6.2.49),

$$
S_E[\tau_0(r)] = \int_{\tau_\infty}^{0} d\tau\, 4\pi\mu\, r^2\sqrt{1 + \dot{r}^2} = \int dr\, 4\pi\mu\, r^2\sqrt{(d\tau/dr)^2 + 1}\,,
\tag{6.3.18}
$$

is always greater in absolute value than the action of the flat surface (*cf.* Eq. 6.2.46),

$$
S_E[\text{flat}] = \mu\int_{0}^{R} 4\pi r^2 dr = \mu\,\frac{4\pi}{3}\,R^3\,,
\tag{6.3.19}
$$

[1] Without loss of generality we can use translational invariance to set it at the time $\tau = 0$.

and the semiclassical exponent of the rate $\frac{1}{2}\Delta W^{\text{quant}}$ in Eq. 6.3.17 can be positive only because of the presence of the contribution $nm\,|\tau_\infty|$, which is large and positive in the high multiplicities limit $\lambda n \gg 1$ thanks to the non-trivial stretching of the surface $|\tau_\infty| \neq 0$. As we already explained, this effect is impossible in ordinary quantum mechanics.

Before concluding this section we would like to list the differences between the semi-classical method we are using in the $(d+1)$-dimensional QFT model (see Eq. 6.3.14) and a naive attempt to apply the same method to a quantum mechanical model with the same Lagrangian in $(0+1)$ dimensions.

1. As there are no spatial degrees of freedom in $(0+1)$ dimensions, there is no phase space to integrate over. Hence, one would need to compute just the square of the matrix element. One can continue using the coherent state representation for the final states, as in Eq. 6.1.18, but the integration over the final states $1 = \int d(\{b^*\}, \{b\})e^{-b^*b}$ involves the ordinary rather than functional integrals over b and b^*.

2. With no phase space for final states in QM, it is impossible to project simultaneously on states of fixed energy E and fixed occupation number n. In QM unlike QFT, E and n are related,

$$E_n = nm(1 + \varepsilon_n)\,, \qquad (6.3.20)$$

where the quantity ε_n is fixed in a given QM model and is not a free parameter. As a result, the non-relativistic limit $\varepsilon \ll 1$ that we used in QFT is not something we are free to impose in QM. Therefore, one should impose only a single projector, $\hat{P}_E$ on the matrix elements in Eq. 6.1.18,

$$\langle b| \hat{P}_E \hat{S} \hat{\mathcal{O}} |0\rangle\,. \qquad (6.3.21)$$

One should also keep in mind that an anharmonic quantum potential with a non-vanishing λ has energy levels E_n that are spaced more densely than the energy states of the harmonic oscillator. Hence ε_n are negative-valued, and the 'decays' $E_n \to nm$ are kinematically forbidden in QM. In comparison, in QFT such decays are only disfavoured by the vanishing phase space and become possible after allowing for arbitrary small particle momenta in the final state, leading to a small positive ε.

3. Importantly, in QM one should distinguish between projecting with $\hat{P}_E$ on the eigenstates of the full Hamiltonian with the potential $U(q)$ given by $\mathcal{V}(\phi)$ in Eq. 6.3.15, and the projection on the eigenstates of the Hamiltonian of the

harmonic oscillator. In QFT with $d \geq 2$ spatial dimensions, the field solutions of the Euler-Lagrange equations dissipate in space. Therefore, they become solutions of free equations at early and late times $t \to \pm\infty$. This is not the case in QM. Energy eigenstates in the full quantum mechanical potential of an anharmonic oscillator are trapped in the potential well and do not linearise[1]. Hence, projecting onto the eigenstates of the harmonic oscillator Hamiltonian H_0 as we have done in Eq. 6.1.12 becomes problematic in QM.

4. In QM, the integral analogous to the one in Eqs. 6.1.24 and 6.1.25 over $\{\xi, \phi_i, \phi_f, \varphi_i, \varphi_f, b^*, b\}$, is an ordinary non-functional integral. Only the $(0+1)$-dimensional fields $\phi(t)$ and $\varphi(t)$, playing the role of QM coordinates, are functions. Hence, proceeding formally in QM, we can write down saddle-point equations resulting from the steepest-descent approximation of the integral in Eq. 6.1.24. However, we cannot expect that the solutions at asymptotic times linearise and thus we cannot write down boundary conditions analogous to Eqs. 6.1.47 and 6.1.48 for $q(t)$. Furthermore, the energy E cannot be computed from the late-time asymptotics in analogy to Eq. 6.1.49.

5. With no meaningful boundary-value problem in the $(0+1)$-dimensional QM model, one cannot proceed to derive the formulae in Eqs. 6.2.29 and 6.2.48, for quantum contributions to the semiclassical rate. As we have already noted earlier, there is no analogue in QM of the QFT expression in Eq. 6.3.17, which was instrumental in obtaining unsuppressed QFT rates due to a non-trivial stretching of the singularity surface $|\tau_\infty|$ by the force nm.

6.4 Semiclassical rate in (2+1) dimensions

Loop contributions to the multiparticle amplitudes at threshold in 1 and 2 spatial dimensions are infrared divergent. In the (2+1)-dimensional theory at small but non-vanishing ε, the terms of order $(\lambda \log \varepsilon)^k$ appear at k loops in perturbation theory. These terms were summed up using the renormalisation group technique

---

[1]One can of course always proceed with the WKB computation of matrix elements between the energy eigenstates in a different QM model – one with a potential barrier as in Fig. 6.7. We have analysed this situation in the example of $U(q) = U_0 e^{-\alpha q}$ considered in the previous section. In this case, classical trajectories do indeed become free far away from the barrier at asymptotic times. This however is different from our model in Eq. 6.3.14. Free states that are of interest for us are analogues of particle states in QFT, i.e. those described by the harmonic oscillator potential $m^2 q^2/2$ in Eq. 6.3.14 rather than the states in the asymptotically-vanishing potential.

in [202] in the limit where [179],

$$\lambda \to 0\,, \quad n = \text{fixed}\,, \quad \varepsilon \to 0 \quad \text{with} \quad \lambda \log \varepsilon = \text{fixed}\,. \qquad (6.4.1)$$

In this section we will explain that this resummation in fact provides a non-trivial verification of the Higgsploding rate predicted in the 2+1 dimensional theory by the semiclassical approach.

All our 4-dimensional QFT calculations in in Sections 6.1 and 6.2 can be straightforwardly generalised to any number of dimensions $(d+1)$. Consider once more the scalar QFT model in Eq. 4.1.3 with the VEV $v \neq 0$.

The expression $W(E, N)_d$ in the exponent of the multiparticle rate $\mathcal{R}_n(E)$ has the same general decomposition into tree-level and quantum parts as before,

$$W(E, n)_d = W(E, n; \lambda)_d^{\text{tree}} + \Delta W(E, n; \lambda)_d^{\text{quant}}\,, \qquad (6.4.2)$$

where the tree-level expression in $(d+1)$ dimensions reads (*cf.* Eq. 6.2.27),

$$W(E, n)_d^{\text{tree}} = n \left(\log \frac{\lambda n}{4} - 1 \right) + \frac{dn}{2} \left(\log \frac{\varepsilon}{d\pi} + 1 \right)\,, \qquad (6.4.3)$$

and the quantum contribution is given by,

$$\Delta W_d^{\text{quant}} = 2nm\,|\tau_\infty| + 2 \int d^d x \left[\int_{\tau_0(\mathbf{x})}^{+\infty} d\tau\, \mathcal{L}_E(h_1) - \int_{\tau_0(\mathbf{x})}^{0} d\tau\, \mathcal{L}_E(h_2) \right], \qquad (6.4.4)$$

extremised over the singularity surfaces $\tau_0(\mathbf{x})$ in complete analogy with Eq. 6.2.29.

For the rest of this section we we will consider the case of $d = 2$ spatial dimensions and will concentrate on the contribution of the stationary surface to the quantity $\frac{1}{2}\Delta W_{d=2}^{\text{quant}}$, which we write as,

$$\frac{1}{2}\Delta W_d^{\text{quant}} = E\,|\tau_\infty| - 2\pi\mu \left(\int_{r_0}^{R} r\sqrt{1+\dot{r}}\, dr - \int_{0}^{R} r\, dr \right). \qquad (6.4.5)$$

The surface tension is $\mu = m^3/\lambda$ as before and the critical radius in $d = 2$ is given by $r_0 = E/(2\pi m)$. Proceeding with the evaluation of Eq. 6.4.5 on the classical trajectory $r(\tau)$, analogously to the calculation in the previous section, we get,

$$\frac{1}{2}\Delta W_d^{\text{quant}} = -\int_{r_0}^{R} 2\pi\,\mu\,\sqrt{r^2 - r_0^2}\, dr + 2\pi\,\mu R^2\,. \qquad (6.4.6)$$

In the $Rm \to \infty$ limit this becomes,

$$\simeq \frac{n^2\lambda}{m}\frac{3}{4\pi}\left(\log(Rm) + \frac{1}{2} + \log\left(\frac{2\pi}{3}\frac{m}{\lambda n}\right) + \mathcal{O}\left(\frac{1}{Rm}\frac{\lambda n}{m}\right)\right). \qquad (6.4.7)$$

Adopting the infinite volume limit, in which the limit $Rm \to \infty$ is taken first while the quantity $\frac{n\lambda}{m}$ is held fixed, we can drop the R-independent and $1/R$-suppressed terms, leaving only the logarithmically divergent contribution,

$$\frac{1}{2}\Delta W_d^{\text{quant}} \simeq \frac{3}{4\pi}\frac{n^2\lambda}{m}\log(Rm). \qquad (6.4.8)$$

We see that all power-like divergent terms in mR have cancelled in the expressions in Eqs. 6.4.6 and 6.4.8, but the logarithmic divergence remains. This result is not surprising in $d < 3$ dimensions and is the consequence of the infrared divergences in the amplitudes at thresholds due to the rescattering effects of final particles. In fact, the appropriate coupling constant in the lower-dimensional theory is not the bare coupling λ but the running quantity λt, where t is the logarithm of the characteristic momentum scale in the final state. In our case we can set,

$$t = \log(Rm), \qquad (6.4.9)$$

and treat R as the reciprocal of the average momentum scale in the final state, i.e. $Rm = 1/\varepsilon^{1/2}$.

The semiclassical result obtained in Eq. 6.4.8 encodes the effect of taking into account quantum corrections to the scattering amplitudes into n-particle states near their threshold, and implies,

$$A_n \simeq A_n^{\text{tree}}\exp\left(\frac{3n^2\lambda t}{4\pi m}\right). \qquad (6.4.10)$$

It is important to recall that the semiclassical limit is assumed in the derivation of the above expression. As always, this is the weak-coupling large-multiplicity limit, such that[1]

$$\text{dimensionless running coupling}: \ \frac{\lambda t}{m} \to 0 \qquad \text{and multiplicity}: \ n \to \infty, \ (6.4.11)$$

with the quantity $n\frac{\lambda t}{m}$ held fixed (and ultimately large) and $t = -1/2\log\varepsilon \to 0$. This enforces the non-relativistic limit, which selects the amplitudes close to their multiparticle thresholds.

It is important that it is the running coupling λt that is required to be small in

---

[1]Recall that in $(2+1)$ dimensions, λ has dimensions of mass.

the semiclassical exponent[1]. This implies that the semiclassical expression would in general include unknown corrections,

$$A_n \simeq A_n^{\text{tree}} \exp\left(\frac{3n^2\lambda t}{4\pi m} \left(1 + \sum_{k=1}^{\infty} c_k \left(\frac{\lambda t}{m} \right)^k \right) \right) , \qquad (6.4.12)$$

parametrised by the sum $\sum_{k=1} c_k \left(\frac{\lambda t}{m} \right)^k$. Of course, there is a well-defined regime corresponding to the small values of the effective coupling λt where these corrections are negligible and the leading order semiclassical result in Eq. 6.4.10 is justified.

Remarkably, the semiclassical formula in Eq. 6.4.10 can be tested against an independent computation of quantum effects in the $(2+1)$-dimensional theory, obtained in [179, 202] using the renormalisation group (RG) resummation of perturbative diagrams. The result is,

$$A_n^{\text{RG}} = A_n^{\text{tree}} \left(1 - \frac{3\lambda t}{2\pi m} \right)^{-\frac{n(n-1)}{2}} . \qquad (6.4.13)$$

This expression is supposed to be valid for any value of n in the regime where the effective coupling λt is in the interval,

$$0 \leq \frac{\lambda t}{m} \lesssim 1 . \qquad (6.4.14)$$

Now, taking the large-n limit, the RG-technique-based result of [179, 202] gives,

$$A_n^{\text{RG}} = A_n^{\text{tree}} \exp\left(\frac{3n^2\lambda t}{4\pi m} \left(1 + \sum_{k=1}^{\infty} \frac{1}{k+1} \left(\frac{3\lambda t}{2\pi m} \right)^k \right) \right) . \qquad (6.4.15)$$

It is a nice test of the semiclassical approach that the leading-order terms in the exponent in both expressions (see Eqs. 6.4.12 and 6.4.15) are exactly the same and given by $\frac{3n^2\lambda t}{4\pi m}$. An equally-important observation is that the subleading terms are of the form $\sum_{k=1} c_k \left(\frac{\lambda t}{m} \right)^k$, which is suppressed in the semiclassical limit $\lambda t \to 0$. There is no contradiction between the two expressions in the regime where the semiclassical approach is justified.

It thus follows that there is a regime in the $(2+1)$-dimensional theory where the multiparticle amplitudes near their thresholds, and consequently the probabilistic rates $\mathcal{R}_n(E)$, become large. In the case of the RG expression in Eq. 6.4.13, this is the consequence of taking a large negative power $-n^2/2$ of the term that is smaller than 1.

---

[1]For example, it is completely analogous to the instanton action $S_{\text{inst}} = \frac{8\pi^2}{g^2(t)}$ in Yang-Mills theory, where the inclusion of quantum corrections from the determinants into the instanton measure in the path integral ensures that S_{inst} in the exponent depends on the correct RG coupling $g^2(t)$ and not the unphysical bare coupling g_{bare}^2.

This implies that there is room for realising Higgsplosion in this $(2+1)$-dimensional model in the broken phase.

In the case of a much simpler model – the quantum mechanical anharmonic oscillator in the unbroken phase – it was shown in Refs. [210, 211] that the rates remain exponentially suppressed in accordance with what would be expected from unitarity in QM.

6.5   Summary

In Chapters 4 to 6 we have provided a detailed derivation of the semiclassical exponent for the multi-particle production rate in the Higgsplosion limit, along with a review of the semiclassical method used to compute it. The derivation holds in the high-particle-number $\lambda n \gg 1$ limit, in the kinematic regime where the final-state particles are produced near their mass thresholds. This corresponds to the limit,

$$\lambda \to 0 \,, \quad n \to \infty \,, \quad \text{with} \quad \lambda n = \text{fixed} \gg 1 \,, \quad \varepsilon = \text{fixed} \ll 1 \,. \qquad (6.5.1)$$

Combining the tree-level (see Eq. 6.2.27) and quantum effects (see Eq. 6.2.73) contributions,

$$W(E, n) = W(E, n; \lambda)^{\text{tree}} + \Delta W(E, n; \lambda)^{\text{quant}} \,, \qquad (6.5.2)$$

we can write down the full semiclassical rate,

$$\mathcal{R}_n(E) = e^{W(E,n)} = \exp\left[n\left(\log\frac{\lambda n}{4} + 0.85\sqrt{\lambda n} + \frac{3}{2}\log\frac{\varepsilon}{3\pi} + \frac{1}{2}\right)\right], \quad (6.5.3)$$

computed in the high-multiplicity non-relativistic limit in Eq. 6.5.1. This expression for the multi-particle rates was first written down in the precursor of this work [170], and was used in Refs. [42, 43] and subsequent papers to introduce and motivate the Higgsplosion mechanism.

The energy in the initial state and the final-state multiplicity are related linearly via,

$$E/m = (1 + \varepsilon)\, n \,. \qquad (6.5.4)$$

Hence, for any fixed non-vanishing value of ε, one can raise the energy to achieve any desired large value of n and consequentially a large $\sqrt{\lambda n}$. Clearly, at the strictly-vanishing value of ε, the phase-space volume is zero and the entire rate in Eq. 6.5.3 vanishes. Then, by increasing ε to positive but still small values, the rate increases. The competition is between the negative $\log\varepsilon$ term and the positive $\sqrt{\lambda n}$ term in Eq. 6.5.3; there is always a range of sufficiently-high multiplicities where
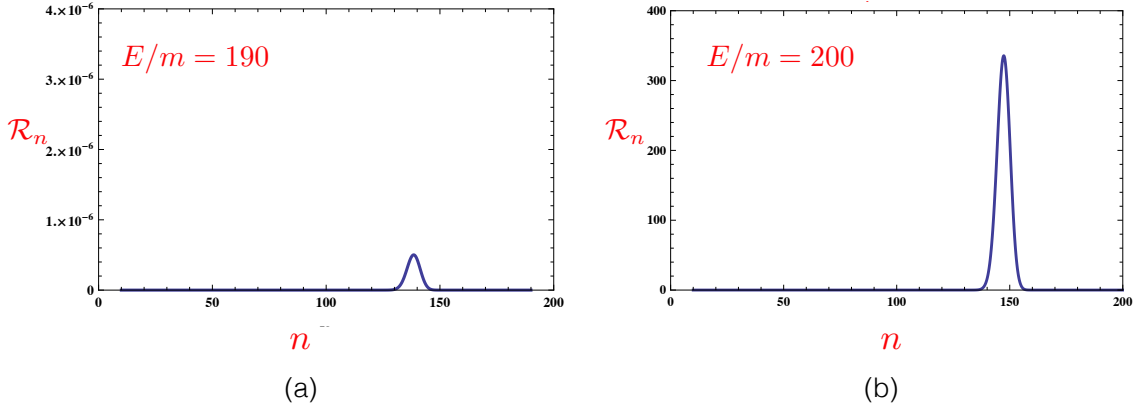
Figure 6.8: *Plots of the semiclassical rate $\mathcal{R}_n$ in Eq. 6.5.3 as a function of n for values of the energy/virtuality E fixed at 190m and at 200m. We chose $\lambda = 1/8$. There is a sharp exponential dependence of the peak rate on the energy. The peak multiplicities $n \sim 150$ in these examples are not far below the maximal values $n_{\max} = E/m$ allowed by kinematics.*

$\sqrt{\lambda n}$ overtakes the logarithmic term $\log \varepsilon$ for any fixed (however small) value of ε. This leads to the exponentially-growing multi-particle rates above a certain critical energy, which in the case described by the expression in Eq. 6.5.3 is in the regime of $E_c \sim 200\,m$. The associated semiclassical rates for $E_c \sim 190\,m,\ 200\,m$ are shown in Fig. 6.8. We see that the multiplicity at which the rate peaks is not far below the maximum kinematically-allowed value, E/m.

The expression for the multi-particle rate in Eq. 6.5.3 is a leading order semiclassical approximation and should of course not be taken as anything more than a rough estimate of the Higgsplosion rate. We have already emphasised that this result is an approximation derived in the simplified scalar model (see Eq. 4.1.3) and in the simplifying non-relativistic limit. Specifically, our result $\Delta W^{\mathrm{quant}}$ for quantum contributions to W in Eq. 6.2.73 was derived on the multi-particle threshold, i.e. at $\varepsilon = 0$. Hence the higher-order corrections in ε will be present in the expression for the rate in the λn limit. Let us estimate these corrections following the discussion in Section 5 of Ref. [170].

Denote these unknown corrections $f_{\lambda n;\varepsilon}(\lambda n, \varepsilon)$, so that

$$\Delta W_{\mathrm{new}} = \frac{\lambda n}{\lambda}\, f_{\lambda n;\varepsilon}(\lambda n, \varepsilon)\,, \qquad (6.5.5)$$

and the now modified rate becomes,

$$\mathcal{R}_n(E) \sim \int\limits_0^{\varepsilon_{nr}} d\varepsilon \left(\frac{\varepsilon}{3\pi}\right)^{\frac{3n}{2}} \exp\left[n\left(0.85\sqrt{\lambda n} + \log \lambda n + f_{\lambda n;\varepsilon}(\lambda n, \varepsilon) + c\right)\right], \quad (6.5.6)$$

where we have included the new correction $\sim n f_{\lambda n;\varepsilon}(\lambda n, \varepsilon)$ and have also made

explicit the fact that the $3n/2 \log \varepsilon /(3\pi)$ factor in the exponent of the rate in Eq. 6.5.3 originated from the integration over the non-relativistic n-particle phase space with a cut-off at $\varepsilon_{nr} < 1$. The constant c absorbs various constant factors appearing in the original rate.

The integral above is of course meant to be computed in the large-n limit by finding the saddle-point value $\varepsilon = \varepsilon_\star$. The main point of the exercise is to determine (1) whether there is a regime where $\varepsilon_\star \ll 1$ so that our near-the-threshold approach is justified, and (2) whether the saddle-point value of the rate itself is large. These requirements should tell us something about the function $f_{\lambda n;\varepsilon}$.

Let us assume that the correction to our result has the form,

$$f_{\lambda n;\varepsilon}(\lambda n, \varepsilon) \; = \; -a\,\varepsilon\,(\lambda n)^p\,, \tag{6.5.7}$$

where a and p are constants. This function is supposed to represent the higher-order in ε correction to our result in the small-ε, large-λn limit. The integral we have to compute is,

$$\mathcal{R}_n \;\sim\; e^{n\left(0.85\sqrt{\lambda n} + \log \lambda n + \tilde{c}\right)} \int d\varepsilon\, e^{n\left(\frac{3}{2}\log\varepsilon - a\varepsilon\,(\lambda n)^p\right)}\,. \tag{6.5.8}$$

Denoting the ε-dependent function in the exponent $s(\varepsilon)$,

$$s(\varepsilon) \;=\; \frac{3}{2}\log\varepsilon \;-\; a\,\varepsilon\,(\lambda n)^p\,, \tag{6.5.9}$$

we can compute the saddle-point,

$$\frac{\partial s(\varepsilon)}{\partial \varepsilon} \;=\; 0 \quad\Rightarrow\quad \varepsilon_\star \;=\; \frac{3}{2}\frac{1}{a}\frac{1}{(\lambda n)^p}\,, \tag{6.5.10}$$

and the value of the function s at the saddle-point,

$$s(\varepsilon_\star) \;=\; -\frac{3}{2}\left(p\log\lambda n \;+\; 1 \;-\; \log\frac{3}{2a}\right)\,. \tag{6.5.11}$$

Combining this with the function in the exponent in front of the integral in Eq. 6.5.8 we find the saddle-point value of the rate,

$$\mathcal{R}_n(\varepsilon_\star) \;\sim\; \exp\left[n\left(0.85\sqrt{\lambda n} - \left(\frac{3p}{2}-1\right)\log\lambda n \;+\; \text{const}\right)\right]\,. \tag{6.5.12}$$

This is the value of the rate at the local maximum, and since the factor of $\sqrt{\lambda n}$ grows faster than the $-\log\lambda n$ term, the peak value of the rate is exponentially-large in the limit of $\sqrt{\lambda n} \to \infty$. It is also easy to verify that this conclusion is consistent within the validity of the non-relativistic limit. In fact, the value of ε at the saddle-point is non-relativistic,

$$\varepsilon_\star \;=\; \frac{3}{2}\frac{1}{a}\frac{1}{(\lambda n)^p} \;\to\; 0\,, \quad \text{as} \quad \lambda n \to \infty\,. \tag{6.5.13}$$

We thus conclude that the appearance of the higher-order ε corrections to our result in the form of Eq. 6.5.7 do not prevent the eventual Higgsplosion in this model at least in the formal limit $\sqrt{\lambda n} \to \infty$ where we have found that,

$$\mathcal{R}_n(\varepsilon_\star) \gg 1 \,. \tag{6.5.14}$$

The growth persists for any constant values of a and p. In fact, if a were negative, the growth would only be enhanced. In Eq. 6.5.7 we have assumed that the function goes as ε to the first power. The higher powers would not change the conclusion, while the effect of $\sim \varepsilon^0$ is what is already taken into account in Eq. 6.2.73.

We now also recall from our earlier discussion that the expression for $\mathcal{R}_n(E)$ in Eq. 6.5.3 is in fact a distribution-valued function. To obtain the proper n-particle production rate one needs to account for the operator-smearing effect in the definition of the initial state in Eq. 6.1.8. The result of this is that the Higgsplosion rate becomes $|\tilde{g}(p)|^2 \, \mathcal{R}_n(\sqrt{s})$ where $\tilde{g}(p)$ is the momentum space Fourier transform of the spacetime test function $g(x')$. This implies that the Higgsplosion rate can be written in the form [167],

$$R_g(n, \sqrt{s}) \,=\, |\tilde{g}(\sqrt{s})|^2 \, \mathcal{R}_n(\sqrt{s}) \,=\, |\tilde{g}(\sqrt{s})|^2 \, e^{\, n \, F(\lambda n, \varepsilon)} \,, \tag{6.5.15}$$

by dressing the leading order semiclassical result $\mathcal{R}_n(\sqrt{s})$ with the smearing function $|\tilde{g}(\sqrt{s})|^2$. This smearing will also ensure an acceptable behaviour of the physical production rate at asymptotically high centre-of-mass energies for $2 \to n$ processes, in accordance with unitarity.

Finally, we note that our discussion concentrated entirely on a simple scalar QFT model. If more degrees of freedom were included, for example the W and Z vector bosons and the SM fermions, new coupling parameters (such as the gauge coupling and the Yukawas) would appear in the expression for the rate along with the final state particle multiplicities. As there are more parameters, the simple scaling properties of $\mathcal{R}_n$ in the pure scalar theory will be modified. Understanding how this would work in practice and investigating the appropriate semiclassical limits is one (of the admittedly many) tasks for future work on exploring realisations of Higgsplosion in particle physics.

Part III

The Higgs in the Early Universe

Chapter 7

Problems & Solutions in Fundamental Physics

With our discussion on the Higgs boson's possible non-perturbative behaviour at high energies concluded, we change pace and move on to looking at its cosmological evolution. As we have noted in many parts of this thesis thus far, the Standard Model is a very successful theory. However, there are several questions and observations that, in its current state, it fails to answer. This motivates us to look for ways to extend the SM in such a way as to address as many of these problems as possible. Many proposed solutions to these problems involve considerations of how the physics of the universe may change over the course of its cosmological evolution.

In this chapter, we briefly look at four of the current problems in fundamental physics and give an example of a proposed solution for each. In Chapter 8, we present a *relaxion* model [44], which aims to solve the four aforementioned problems, as well as the hierarchy problem discussed in Section 1.2.2. Though other possible solutions are mentioned, the example solutions presented in this chapter are chosen to be the ones utilised in the model presented in Chapter 8. The exception is the strong CP problem, for which two solutions are presented: the QCD axion [212] and the Nelson-Barr mechanism [213–215]. The Nelson-Barr mechanism is indeed used in the combined relaxion model, while the discussion of the QCD axion will prove useful when explaining the relaxion mechanism in Section 8.2. Hence, this chapter lays the necessary foundations for the discussions in Chapter 8.

7.1   The strong CP problem

The strong CP problem concerns a CP-violating term in quantum chromodynamics (QCD) that is allowed by the symmetries of the Lagrangian [212],

$$\mathcal{L}_{\text{strongCP}} = \theta \frac{\alpha_s}{8\pi} G_{a\mu\nu} \tilde{G}_a^{\mu\nu}, \qquad (7.1.1)$$

where $\tilde{G}_a^{\mu\nu} = \epsilon^{\mu\nu\alpha\beta} G_{a\alpha\beta}$, $G_{a\mu\nu}$ is the gluon field strength tensor and α_s is the strong coupling. The parameter θ dictates the size of this term and, consequentially, the extent of CP violation. Without a mechanism to suppress its size, it causes a large neutron electric dipole moment, d_n.

In general, there are in fact two contributions to this CP violation: the $G\tilde{G}$ term above and the phase of the quark mass matrix. The combined effect of these contributions can be expressed by $\bar{\theta}$,

$$\bar{\theta} = \theta + \text{Arg}(\det M), \qquad (7.1.2)$$

where θ is the size of the $G\tilde{G}$ term and M is the quark mass matrix. These two contributions are in fact connected. The phase of the mass matrix can be changed by chiral rotations of the fields, but due to the anomalous nature of the associated chiral symmetry, this comes at the cost of producing a $G\tilde{G}$ term [212]. Therefore, chiral rotations can be used to change the values of θ and $\text{Arg}(\det M)$ but their sum, $\bar{\theta}$, remains constant. It is this combined quantity, $\bar{\theta}$, that is experimentally accessible. Current experimental bounds on the neutron electric dipole moment [216–218] require that $\bar{\theta} \leq 10^{-9}$.

In the Standard Model there is no reason for the strong CP angle, $\bar{\theta}$, to be small. This has motivated extensions that give a natural suppression to this term, such as the axion and the Nelson-Barr mechanism considered below.

7.1.1   The QCD axion & ALPs

A popular solution to the strong CP problem is the axion or *chiral* solution [212, 219, 220]. This solution involves the introduction of a new global chiral symmetry, $U(1)_{PQ}$, which is spontaneously broken and dynamically drives $\bar{\theta}$ to zero. A consequence of the breaking is the presence of a new associated pseudo Nambu-Goldstone boson, the axion $a(x)$, with Lagrangian,

$$\mathcal{L}_{\text{axion}} = \frac{1}{2}(\partial_\mu a)^2 + \frac{a(x)}{f_a} \frac{\alpha_s}{8\pi} G\tilde{G}, \qquad (7.1.3)$$

where f_a is the scale of the breaking. Note that the strong CP parameter is now a dynamic quantity,

$$\bar{\theta}_{\text{eff}}(x) = \bar{\theta} + \frac{a(x)}{f_a}. \tag{7.1.4}$$

As QCD becomes strongly-coupled at low energies, non-perturbative effects break the axion shift symmetry and give it an effective potential,

$$V_{\text{eff}}(a) = -m_u f_\pi^3 \cos(\bar{\theta} + a(x)/f_a), \tag{7.1.5}$$

where m_u is the up-quark mass and f_π is the decay constant of the pions [221]. Minimisation of this potential forces the axion VEV to,

$$\langle a \rangle = -f_a \bar{\theta}, \tag{7.1.6}$$

such that $\bar{\theta}_{\text{eff}} = 0$. This solves the strong CP problem.

Note that if the axion Lagrangian in Eq. 7.1.3 had an explicit mass term $\sim m^2 a^2$, the minimum of the potential would be shifted and the strong CP problem would return. This is why it is problematic for the relaxion discussed in Section 8.2 to be the QCD axion. This restriction is lifted in some other models with axion-like particles (ALPs), where the axion is of some new gauge group and not intended to solve the strong CP problem. This is the case in the model we present in Chapter 8, where we have an axion of a new gauge group with new field content. The associated non-perturbatively generated potential gives the important backreaction (see Section 8.3.3) required for the relaxion mechanism described in Section 8.2.

7.1.2 The Nelson-Barr mechanism

The Nelson-Barr (NB) mechanism [213–215] provides an alternative solution to the strong CP problem. We assume CP is a good symmetry that is spontaneously broken in such a way as to ensure a small $\bar{\theta}_{\text{eff}}$ while also maintaining an $\mathcal{O}(1)$ CKM phase. If CP were to remain unbroken, this phase would vanish, which is in conflict with observed CP violation in flavour physics [222].

Consider a NB sector inspired by Refs. [223, 224], with a new vector-like quark ψ that extends the Standard Model 'up' sector, $\{u, c, t\}$,

$$\mathcal{L}_{\text{NB}} = \left[y_i^\psi \chi + \tilde{y}_i^\psi \chi^* \right] \psi u_i^c + \mu_\psi \psi \psi^c + \text{h.c.}, \tag{7.1.7}$$

where χ is a new complex scalar field, which gets a complex VEV and spontaneously breaks CP. All couplings are real and ψ (ψ^c) are fundamental (anti-fundamental) under $SU(3)_C$ and have hypercharges $\pm 2/3$. An additional Z_2 symmetry is imposed

under which χ, ψ and ψ^c are charged such that the terms $\chi\psi\psi^c$ and $HQ\psi^c$ are forbidden. This symmetry is also spontaneously broken when χ gets a VEV.

When χ gets a complex VEV $\langle\chi\rangle = fe^{i\eta}$, the Lagrangian for the expanded up sector becomes,

$$\mathcal{L}_{\text{up+NB}} = Y_{ij}HQ_iu_j^c + B_i\psi u_i^c + \mu\psi\psi^c + \text{h.c.}, \tag{7.1.8}$$

with $B_i = f\left[y_i^\psi e^{i\eta} + \tilde{y}_i^\psi e^{-i\eta}\right]$. As a result, the tree-level 4×4 quark mass matrix for the expanded sector reads,

$$M^u = \begin{pmatrix} (\mu)_{1\times 1} & (B)_{1\times 3} \\ (0)_{3\times 1} & (vY^u)_{3\times 3} \end{pmatrix}, \tag{7.1.9}$$

and subsequently at tree level,

$$\bar{\theta}_{\text{eff}} = \text{Arg}(\det(M^d)) + \text{Arg}(\mu\det(vY^u)) = 0. \tag{7.1.10}$$

The only non-real values appear in B, which doesn't contribute to the determinant. If we look at the effective 3×3 mass squared matrix and its diagonalization, we see that in order to maintain a CKM phase $\delta_{\text{CKM}} \sim \mathcal{O}(1)$ we require $y_i^\psi \sim \tilde{y}_i^\psi \sim y^\psi$ for all i. The requirement that radiative corrections to $\bar{\theta}_{\text{eff}}$ are sufficiently small places a model-dependent upper bound on y^ψ. With these conditions respected, the strong CP problem is solved.

The Nelson Barr mechanism will be used in the model presented in Chapter 8 to solve the strong CP problem. The new interactions will also be responsible for generating the required rolling potential for the relaxion mechanism described in Section 8.2.

7.2   Neutrino masses

In the Standard Model, neutrinos, ν_ℓ appear as part of a left-handed $SU(2)_L$ doublet paired with a charged lepton ℓ,

$$L_\ell = \begin{pmatrix} \nu_\ell \\ \ell \end{pmatrix}_L. \tag{7.2.1}$$

They are uncharged with respect to the strong $SU(3)_C$ and electromagnetic $U(1)_{\text{EM}}$ symmetries and as such are only produced by weak interactions. In the SM, fermion masses are generated by the Higgs mechanism, as described in Chapter 1. This mechanism reduces part of a Yukawa interaction involving the Higgs doublet and a fermion left-right pair into a mass term. Such a Yukawa term for leptons consists of the left-handed doublet L_ℓ and a right-handed charged lepton field ℓ_R. However, the

SM contains no such right-handed neutrino fields and thus neutrinos are expected to be massless[1].

A result of non-zero neutrino masses is a misalignment between flavour and mass bases, such that neutrino flavour is not conserved in propagation. This gives rise to neutrino oscillations [222, 225–227]. The frequencies of these oscillations are proportional to the differences between the squared masses, $\Delta m_{ij}^2 = m_i^2 - m_j^2$. Observations of neutrino oscillation by the Super-Kamiokande Collaboration [228] and Sudbury Neutrino Observatory Collaboration [229, 230] therefore provide strong evidence for massive neutrinos.

The most common way to introduce neutrino masses is to add new field content in the form of right-handed *sterile* neutrinos. Here, sterile refers to the fact that they must have no SM gauge interactions: they are SM singlets. Many models involve the introduction of sterile neutrinos but differ in the way they obtain the small masses required by experimental bounds.

When adding N sterile neutrinos, n_i, we have two possible mass terms,

$$-\mathcal{L}_{\nu,n} \supset M_{Dij}\bar{n}_i\nu_\ell + \frac{1}{2}M_n\bar{n}n^c + \text{h.c.}\,, \tag{7.2.2}$$

where n^c is the charge conjugate sterile neutrino field. The first term is the familiar Dirac mass term stemming from the Higgs mechanism, which introduces a coupling between the SM neutrino fields and the new sterile fields. The second term is the Majorana term, which forbidden for SM fields as it violates gauge invariance. The sterile neutrinos are gauge singlets and evade this restriction.

The Dirac and Majorana components give a combined mass matrix for the neutrinos, which can then be diagonalised to find the neutrino mass eigenstates in terms of the weak eigenstates. This generally leads to three light neutrinos with masses $\sim M_D^2/M_n$ and N heavy neutrinos with masses $\sim M_n$, where it is assumed that M_n is some large mass scale [231]. This behaviour has come to be known as the *see-saw* mechanism[2] and can be found in many BSM models (see for example Refs. [222, 232–234]). The see-saw mechanism simultaneously explains the low observed neutrino masses and the inaccessibility of the heavier neutrino states: the SM is a lower-energy effective theory largely unaffected by the heavier states. For more on effective theories, see Chapter 2.

In the model we present in Chapter 8, we introduce three sterile neutrinos to not only provide neutrino mass but also facilitate spontaneous baryogenesis (see Sections 7.3.1

---

[1]Loop-level contributions to neutrino masses are strongly constrained by symmetries [225].

[2]The example shown is specifically a type 1 see-saw, involving the introduction of a fermionic singlet. Other see-saw models with different field content in different representations exist. See, for example, Ref. [232].

and 8.3.2). This will ultimately place an upper bound on the Majorana mass, M_n, such that a conventional see-saw mechanism is not possible; we will need to augment it with some other scale-separating mechanism. We turn to a possible solution with roots in flavour physics: the Froggatt-Nielsen mechanism [235].

7.2.1   The Froggatt-Nielsen mechanism

The Froggatt-Nielsen mechanism [235] was originally proposed as a solution to the flavour problem. The flavour problem concerns the origin of the hierarchy in Yukawa couplings in the quark and lepton sectors. The approach of Froggatt and Nielsen involves the introduction of a new $U(1)_f$ flavour symmetry, which is broken when the new *flavon* field, S, acquires a VEV. The flavon is generally a scalar SM singlet with flavour charge -1.

All SM fermions have different charges under this new flavour symmetry such that the SM Yukawa terms are interpreted as broken higher-dimensional effective operators. Consider, for example, the charged-lepton Yukawa interactions after flavour symmetry breaking,

$$\mathcal{L}_{\mathrm{FN}} \supset \Upsilon_{ij} \left(\frac{S}{\Lambda_{\mathrm{FN}}} \right)^{q_i + q_j} \bar{L}_i H e_j \; \to \; \Upsilon_{ij} (\epsilon_{\mathrm{FN}})^{q_i + q_j} \bar{L}_i H e_j, \qquad (7.2.3)$$

where $\epsilon_{\mathrm{FN}} = \langle S \rangle / \Lambda_{\mathrm{FN}}$, q_i is the flavour charge of the ith species and Λ_{FN} is some UV scale associated with some heavy field content that has been integrated out. The balancing of the different flavour charges of the fermions results in different powers of the flavour symmetry-breaking parameter, ϵ_{FN}. This leads to an effective Yukawa matrix, $Y_{ij} = \Upsilon_{ij} (\epsilon_{\mathrm{FN}})^{q_i + q_j}$. Therefore, if ϵ_{FN} is small, a large hierarchy of effective Yukawa couplings is generated. For more thorough examples, see Refs. [31, 236].

As stated previously, we use the Froggatt-Nielsen mechanism in Chapter 8 to extend the separation between the light and heavy neutrino states beyond the limitations imposed by baryogenesis considerations in Section 8.3.2.

7.3   Baryon asymmetry

Baryon asymmetry refers to the fact that the universe seems to contain more matter than antimatter. All Standard Model interactions produce matter and antimatter in equal measure, so one would expect to see equal amounts of each. There is the possibility that there are patches of the universe where matter dominates and patches where antimatter dominates. However, such patches would exhibit high emissions

from annihilations at their interfaces and thus the lack of such observations suggests a patch size larger than the observable universe. Similarly, baryon asymmetry as an initial condition of the universe does not work with our modern inflationary view of cosmic evolution. The summary of baryogenesis presented here borrows aspects from the review by Cline [237].

The baryon asymmetry is generally parametrised by the ratio η,

$$\eta = \frac{n_B - n_{\bar{B}}}{s}\,, \tag{7.3.1}$$

where n_i is the number density of species i and s is the entropy density. This ratio is used so that η remains constant with the expansion of the universe. The value of η has been inferred from Big Bang Nucleosynthesis [238] and the Cosmic Microwave Background [239] to be $\sim 10^{-10}$. This is orders of magnitude larger than the value expected for a baryon-symmetric homogeneous universe [240], $\sim 10^{-21}$.

Sakharov suggested a dynamic creation of this asymmetry: *baryogenesis* [241]. The Sakharov conditions, which must be satisfied for baryogenesis to occur, are:

1. B number violation

2. C and CP violation

3. Loss of thermal equilibrium (in a CPT invariant theory)

B number violation occurs in the Standard Model due to the anomalous nature of the B+L symmetry. The richer vacuum structure of non-Abelian gauge theories, such as the $SU(2)_L$ group of the Standard Model, allow for multiple valid perturbative vacua. Transitions between these stable vacua cause B number violation. Such transitions can occur in two ways: either by tunnelling (*instantons* [242]) or by getting over an energy barrier (*sphalerons* [243]). One finds that the probabilistic timescale of tunnelling is much larger than the age of the universe. Sphalerons transitions are highly-suppressed at low temperatures but become active at $T \gtrsim 100$ GeV due to availability of thermal energy. Models that produce a lepton asymmetry rely on sphalerons to convert this asymmetry to a baryon asymmetry. This idea is called Leptogenesis; for a review see Ref. [244].

CP violation exists in the SM via the CKM matrix. However, it can be shown that this effect is too small to account for the observed asymmetry [245]. Similarly, as discussed in Section 7.1, any strong CP violation is strongly constrained by measurements of the neutron electric dipole moment.

The method of baryogenesis we employ in Chapter 8 evades the need for loss of thermal equilibrium by spontaneously breaking CPT symmetry. This method is dubbed *spontaneous* baryogenesis [246–249].

7.3.1   Spontaneous baryogenesis

Spontaneous baryogenesis [246, 247] is different to most other mechanisms of baryo-genesis[1] in that the baryon asymmetry is produced in equilibrium. The requirement for departure from equilibrium is sidestepped by incorporating a temporary dynamic violation of CPT invariance [240]. This ultimately has the effect of shifting the chemical potentials of baryons relative to antibaryons, giving a non-zero asymmetry in thermal equilibrium. For a recent review, see Ref. [249].

The key to this mechanism is the presence of some new scalar field, ϕ, that is derivatively coupled to a matter current such as $J^\mu = \bar{\psi}\gamma^\mu\psi$. In general, it can couple to the currents of several species, giving the Lagrangian term,

$$\mathcal{L}_{\text{SB}} \supset -\sum_i c_i \frac{\partial_\mu \phi}{f} J_i^\mu, \tag{7.3.2}$$

where the sum is over particle species and it is understood that this is an effective operator from some physics at high-energy scale f. This term, when non-zero, will violate CPT. Consider the case where ϕ varies with time but is spatially constant. Recalling that J_i^0 is simply the difference in particle/anti-particle number densities, $n_i - \bar{n}_i$, we find,

$$c_i \frac{\partial_\mu \phi}{f} J_i^\mu = \frac{c_i}{f} \dot{\phi}(n_i - \bar{n}_i). \tag{7.3.3}$$

Considerations of the effect of this term on the stress-energy tensor (for details see Ref. [249]) show that the coupling in Eq. 7.3.2 gives a contribution to the energy density such that each particle (anti-particle) gets an additional energy of,

$$\pm \Delta E_i = \mp \frac{c_i}{f} \dot{\phi}, \tag{7.3.4}$$

which, in equilibrium, can be interpreted as a corresponding shift in chemical potential,

$$\hat{\mu}_i \equiv \Delta \mu_i = -\Delta \bar{\mu}_i = \frac{c_i}{f} \dot{\phi}. \tag{7.3.5}$$

In the limiting case of one baryonic species with degrees of freedom g_B, we substitute the Fermi-Dirac distribution for fermions into Eq. 7.3.1 to find a baryon asymmetry,

$$\eta s = n_B - \bar{n}_B \approx g_B \hat{\mu}_B \frac{T^2}{6} \sim \dot{\phi}\frac{T^2}{f}. \tag{7.3.6}$$

Note the dependence on the field velocity $\dot{\phi}$. The scalar field ϕ in spontaneous baryo-genesis models is generally rolling towards some minimum, where $\dot{\phi}$ will ultimately

---

[1]An example of a popular non-equilibrium mechanism is electroweak baryogenesis, in which a sufficiently-first-order electroweak phase transition can provide out-of-equilibrium conditions and allow the production of a baryon asymmetry. See Refs. [237, 250].

reach zero. One might therefore expect that the asymmetry to vanish too. However, we recall that for this asymmetry to be communicated, we require B-violating processes (specifically sphalerons) to be in thermal equilibrium. Hence, it is the value of $\dot{\phi}$ at the sphaleron decoupling temperature, $T = T_{\mathrm{sph}}$, that is of importance. The value of η freezes at T_{sph}, leaving a residual baryon asymmetry regardless of any further evolution of the field ϕ. As such, a temporary dynamic breaking of CPT has generated a baryon asymmetry in thermal equilibrium.

Parts of these calculations are extended to more complex scenarios in Section 8.3.2, where we explain how couplings of the relaxion to non-baryonic currents can still translate into baryon asymmetries via considerations of B-L conservation. The model presented in Chapter 8 will use a clockwork system and sterile neutrinos to generate the required operator in Eq. 7.3.2.

7.4   Dark matter

Measurements of galactic rotation velocities [251–253] and gravitational lensing [254] are in conflict with the gravitational behaviour we expect for the baryonic[1] matter content of the universe. In general there are two schools of thought for this problem: either our theory of gravity is wrong or we have misunderstood the full matter content of the universe. Considerations into the formation of large structures [255, 256], observations in lensing [257], measurements of the Cosmic Microwave Background (CMB) [258–260], investigations regarding Big Bang Nucleosynthesis (BBN) [261], and recent observations of gravitational waves [262, 263] have somewhat pushed the scientific community in the direction of the latter.

We postulate that there is some source of matter that is not currently accounted for, and that is crucial to binding cosmological structures. Constraints on the contributions from Primordial Black Holes[2] (PBHs) [265, 266], MAssive Compact Halo Objects (MACHOs) [267, 268] and other astrophysical objects suggest that a new particle source of matter is required for consistency with observation. We call this new matter *dark matter*. For a more detailed account on the history of dark matter, see the review in Ref. [269]. Current measurements suggest that dark matter contributes five times more to the energy budget of the universe than regular baryonic

---

[1]In the context of dark matter and energy budgets, the term 'baryonic' is used a little loosely to refer to any matter content from the Standard Model.

[2]Conventional studies of PBHs, concerning a single PBH mass, fail to account for the entire dark matter quota. Some more recent studies suggest that some mass distributions could account for all dark matter and evade current experimental constraints. See, for example, Ref. [264]

matter [258–260]. Specifically, measurements point to a dark matter abundance,

$$\Omega_{\text{DM}}h^2 \simeq 0.12, \tag{7.4.1}$$

where h is Hubble's constant in units of 100 km s^{-1} Mpc^{-1}.

Since the advent of dark matter, any new theory of the universe has been expected to present a suitable candidate. In the twentieth century, developments in theories like supersymmetry motivated a class of candidates with mass and coupling strengths in line with the SM weak sector [270, 271]. The lack of such particle discoveries at the Large Hadron Collider [272] and direct/indirect detection programmes [273, 274] has reignited interest into a wider array of possible candidates and generation mechanisms. The model presented in Chapter 8 uses a mechanism with origins in axion physics to produce the required dark matter abundance via potential misalignment.

7.4.1   Misalignment dark matter

Misalignment dark matter production is a non-thermal production mechanism [240, 275]. It is traditionally seen in models with axions, axion-like particles (ALPs) or other light scalar particles. Here, we consider the QCD axion already mentioned in Section 7.1.1.

Recall that the axion has no explicit mass term and is thus massless at temperatures greater than Λ_{QCD}. As the temperatures lower, non-perturbative instanton effects in QCD generate a cosine potential, giving mass to the axion. This potential is minimised by setting the QCD angle to zero. However, at high temperatures there is no preferred angle. Therefore, as the universe cools and the non-perturbative potential is activated, the axion may well be misaligned from the subsequent minimum. In such a scenario, we expect the axion to roll towards the minimum and overshoot, leading to cosmic oscillations of the axion field.

The oscillations of the axion field close to the potential minimum follow damped harmonic motion but with some complications associated with the temperature dependence of both the axion mass and Hubble friction [276],

$$\ddot{\phi} + 3H(T)\dot{\phi} + m_a(T)\phi = 0 \,, \tag{7.4.2}$$

where ϕ is the perturbation of the field from the minimum. When the axion mass exceeds the expansion rate of the universe, the damping decreases and the field begins to oscillate with energy density,

$$\rho_a \propto \frac{m_a(T)}{R^3} \,, \tag{7.4.3}$$

where R is the scale factor. In other words, once the mass of the axion stabilises at lower temperatures, $T \ll \Lambda_{\mathrm{QCD}}$, the energy density goes as R^{-3} and the oscillations behave like cold[1] non-relativistic matter [240], making the axion a suitable dark matter candidate. We obtain a conserved number of axions per comoving volume, from which one can calculate present day density.

The precise calculations of relic abundance associated with the misalignment mechanism vary from model to model but the conceptual basis is the same. In Chapter 8, the light scalar of interest is the relaxion field, which is the light axion of a new strong group. The details of how the misalignment is obtained and the resultant contribution to the relic dark matter abundance are discussed in Section 8.3.3.

With the relevant problems and solutions discussed, we are ready to discuss the "all-in-one" relaxion model [5] with a good contextual foundation. In this model, all the aforementioned problems are addressed, as well as the Higgs hierarchy problem described in Section 1.2.2.

---

[1]Note that this is in contrast to thermal production mechanisms, where light particles such as axions would be produced with highly-relativistic velocities. Relativistic or 'hot' dark matter candidates are disfavoured by simulations of structure formation [277].

Chapter 8

The All-in-one Relaxion

8.1 Introduction

Recently, particle physics research has been driven to a large extent by the expectation of physics beyond the Standard Model (BSM) at the TeV scale. As was discussed in Chapter 7, there are many theoretical and observational reasons to extend the Standard Model (SM) – such as Higgs mass naturalness, dark matter, matter-antimatter asymmetry, neutrino masses and the strong CP problem. However, only the first of these issues necessarily requires TeV-scale new physics. In fact, if Higgs mass naturalness is ignored and new physics scales far beyond the TeV scale are allowed, the other issues can be solved by very minimal extensions of the SM [278–283].

It is arguably far more challenging to find an explanation (apart from tuning or anthropics) for a light Higgs mass with a high new physics scale. While conventional wisdom says this is impossible, the recently-proposed cosmological relaxation (or relaxion) models [44] aim to find just such an explanation. In these models the rolling of the so-called relaxion field during inflation leads to a scanning of the the squared Higgs mass from positive to negative values. Once the Higgs mass squared becomes negative it triggers a backreaction potential that stops the scanning soon after, at a value much smaller than the new physics scale.

We show in this chapter that the relaxion construction has many interesting built-in features that can provide solutions to multiple other BSM puzzles in a way that is completely different from the other examples referred to above. These features are: spontaneous CPT violation during its rolling; spontaneous CP violation when it stops; and oscillations about its stopping point after reheating. The spontaneous CPT violation leads to spontaneous baryogenesis during the rolling of the relaxion

after reheating [284]; the spontaneous CP violation leads to a Nelson-Barr solution [213, 285] of the strong CP problem [224, 286]; and the relaxion oscillations generate the observed dark matter abundance [287]. The spontaneous baryogenesis mechanism requires that baryons and/or leptons are charged under the relaxion shift symmetry. In this work the relaxion shift symmetry is identified with a Froggatt-Nielsen symmetry [235], under which three new right-handed (RH) neutrino states (but no SM states) are charged. This satisfies the requirement of spontaneous baryogenesis while also giving an explanation for the smallness of neutrino masses.

Thus, we achieve a unified solution to five BSM puzzles, namely the lightness of the Higgs boson in the absence of TeV scale new physics, dark matter, matter-antimatter asymmetry, neutrino masses and the strong CP problem. Four of these puzzles were discussed in Chapter 7. The lightness of the Higgs boson, also known as the hierarchy problem, was discussed in Section 1.2.2.

We begin in Section 8.2 with an overview of the relaxion mechanism, which underpins the motivation for the other parts of the model. We also outline the conditions required for successful cosmic evolution of our combined model. In Section 8.3, we look at the content of the model, the clockwork setup and the features of its three non-trivial nodes. We then combine the constraints of each sector in Section 8.4 and discuss the available parameter space. Finally, our conclusions are presented in Section 8.5.

8.2   The relaxion mechanism and evolution

In relaxion models, the Higgs mass squared parameter is promoted to a dynamical quantity $\mu^2(\phi)$, which varies due to its couplings to the relaxion field, ϕ,

$$V_{\text{roll}} = \mu^2(\phi)H^\dagger H + \lambda_H(H^\dagger H)^2 - r_{\text{roll}}^2 M^4 \cos\frac{\phi}{F}, \qquad (8.2.1)$$

with,

$$\mu^2(\phi) = \kappa M^2 - M^2 \cos\frac{\phi}{F}. \qquad (8.2.2)$$

Here, H is the SM Higgs doublet, λ_H is its quartic coupling, M is the UV cut-off of the Higgs effective theory and $\kappa \lesssim 1$ [1]. The origin of this rolling potential is generally not discussed; in this model it can be generated by the Nelson-Barr sector discussed in Section 8.3.4.

---

[1]The periodicity F is large such that the cosine is locally linear in ϕ. By expanding the cosine terms about an arbitrary point, the polynomial terms of the original work [44] can be recovered with $g \sim M^2/F$.
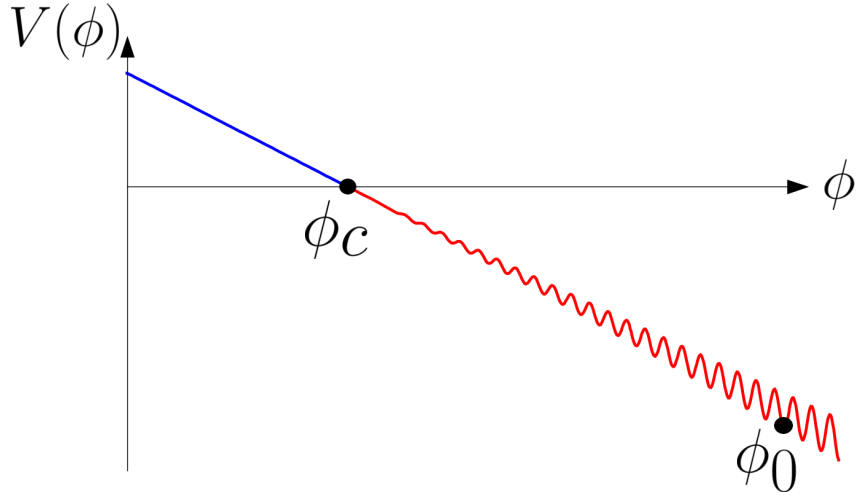
Figure 8.1: *A pictorial representation of the relaxion field evolution during inflation; not to scale. The backreaction is not present until the relaxion crosses $\phi = \phi_c$, at which point $\mu^2(\phi)$ becomes negative, triggering electroweak symmetry breaking. This in turn triggers the backreaction and ultimately traps the relaxion field in a local minimum at $\phi = \phi_0$, such that the $\mu^2(\phi_0) = \mu^2_{\mathrm{SM}}$. The relaxion field will remain in this local minimum throughout the rest of its cosmic evolution, as depicted in Fig. 8.2.*

The rolling starts from a relaxion field value, $\phi < \phi_c = -|F \cos^{-1} \kappa|$, such that $\mu^2 > 0$. After crossing the point $\phi = \phi_c$, μ^2 becomes negative, prompting electroweak symmetry breaking. This in turn activates the backreaction potential, which induces periodic 'wiggles' on top of the linear envelope,

$$V_{\mathrm{br}} = \Lambda_c^4 \cos \frac{\phi}{f_k}. \tag{8.2.3}$$

Here, $\Lambda_c^4(\phi) = m^n v(\phi)^{4-n}$, is an increasing function of the Higgs vacuum expectation value (VEV), where m is some mass scale. The wiggle height increases with evolution of ϕ until the slope of the backreaction matches the slope of the rolling potential, at $\phi = \phi_0$,

$$r_{\mathrm{roll}}^2 M^4 / F \sim \Lambda_c^4(\phi_0) / f_k. \tag{8.2.4}$$

The rolling then stops and the relaxion halts in a local minimum[1], such that the Higgs square mass takes its Standard Model value $\mu^2(\phi_0) = \mu^2_{\mathrm{SM}}$. This evolution is depicted in Fig. 8.1.

---

[1] In reality, we expect the relaxion to be spread over several adjacent minima, allowing for different patches of the universe with different μ^2 values. After inflation these patches are expected to be larger than the observable universe [44].

This generates a large hierarchy between the Higgs VEV and the cut-off M. As discussed in [44], the cut-off, M, cannot be raised to an arbitrarily high value because of cosmological requirements. This stems from three required conditions for successful relaxion evolution during inflation[1]:

1. The vacuum energy during inflation must not be dominated by the relaxion potential. This translates into a bound on the Hubble scale of inflation,

$$H_i > r_{\text{roll}} M^2 / M_P. \tag{8.2.5}$$

2. We require that the evolution of the relaxion is dominated by classical rolling, which places a complimentary bound on the inflationary Hubble scale,

$$H_i < (r_{\text{roll}}^2 M^4 / F)^{1/3}. \tag{8.2.6}$$

3. For the rolling to stop we require that the slope of the barriers in the backreaction can match the slope of the roll potential, see Eq. 8.2.4.

These conditions combine to give an upper bound on the cut-off,

$$M \lesssim \left(\frac{M_P}{r_{\text{roll}}}\right)^{1/2} \left(\frac{\Lambda_c^4}{f_k}\right)^{1/6}. \tag{8.2.7}$$

The relaxion mechanism must be complemented by a new mechanism at the scale M (e.g. supersymmetry [288] or Higgs compositeness [289]) to solve the full hierarchy problem up to the Planck scale, M_P.

Let us now discuss what happens after inflation. Suppose that in reheating, the temperature exceeds some critical temperature, T_c, such that the backreaction vanishes. The wiggles disappear and the relaxion enters a second phase of rolling. When the universe cools below T_c again, the backreaction potential reappears and the rolling eventually stops provided,

$$m_\phi \lesssim 5H(T_c). \tag{8.2.8}$$

This condition is obtained by demanding that the relaxion does not have enough kinetic energy to overshoot the barriers once the backreaction potential reappears [287, 290, 291]. If satisfied, the relaxion enters a slow-roll-like regime with,

$$V'(\phi) = 5H\dot{\phi}. \tag{8.2.9}$$

It is this second phase of rolling that can lead to a generation of both the observed dark matter abundance (discussed in Section 8.3.3) as well as the baryon asymmetry

---

[1]For a more detailed discussion of this evolution, see Ref. [44]

(discussed in Section 8.3.2). We will see that in order for spontaneous baryogenesis to be successful, the relaxion must still be rolling when the sphaleron processes decouple at $T = T_{\rm sph}$. In other words, we require that the backreaction is activated at a temperature lower than the sphaleron-decoupling temperature, $T_c < T_{\rm sph}$. Furthermore, misalignment dark matter production can only occur once this backreaction is present. As a result, we require that the temperature at which oscillation becomes possible is lower than the critical temperature $T_{\rm osc} < T_c$.

In summary, successful cosmic evolution of the relaxion is shown pictorially in Fig. 8.2 and described by the following steps:

1. The relaxion rolls down the rolling potential (Eq. 8.2.1) during inflation until settling in a local wiggle minimum, such that $\mu^2(\phi) = \mu_{\rm SM}^2$ (see Fig. 8.1). Reheating raises the temperature to $T_r > T_c$, such that the backreaction vanishes; a second phase of rolling commences.

2. The relaxion rolls as the universe cools to $T_{\rm sph}$, when the sphalerons decouple, freezing in a non-zero baryon asymmetry (see Section 8.3.2).

3. The universe cools further to T_c, when the backreaction is reactivated and the wiggles reappear. It can be shown that the 'distance' rolled in the second phase of rolling is shorter than the wiggle scale [287], such that the relaxion is still in the same wiggle but misaligned from its original stopping point, provided it doesn't overshoot (see Eq. 8.2.8).

4. The universe continues to cool, with the relaxion experiencing damped motion toward the local minimum.

5. At $T = T_{\rm osc}$, the relaxion mass exceeds the Hubble friction and oscillations of the field about the local minimum commence. These oscillations produce a cold dark matter candidate that can account for the measured relic abundance (see Section 8.3.3).

With the mechanism and evolution outlined, we now look at the specific setup and content of the all-in-one model and the way in which the solutions to the five BSM puzzles are implemented.

8.3   The all-in-one setup

8.3.1   The clockwork & content

As we will see in Section 8.3.2, generation of the observed baryon asymmetry requires a hierarchy $f \ll f_k$, where f is the scale associated with the operator $\mathcal{O}_{\rm SB}$ required
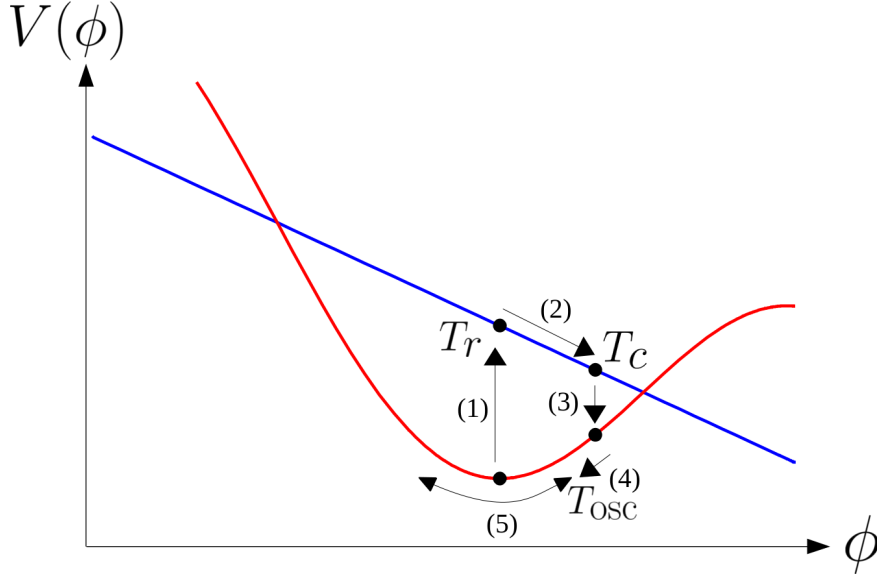
$V(\phi)$

Figure 8.2: *Schematic plot of the relaxion field's evolution. Progress in time is indicated by the numbered arrows, with corresponding numbered explanations in the text. The red (blue) curve is the relaxion's potential with the backreaction turned on (off). The initial relaxion mechanism chooses the appropriate local minimum such that $\mu^2(\phi) = \mu_{\rm SM}^2$. The temperature at various stages of the evolution are shown. We see that all cosmic evolution of the field from the subsequent reheating onwards is localised to this one wiggle. Note that this diagram is not to scale and that transitions are pictured as instantaneous for simplicity.*

for spontaneous baryogenesis. This and the fact that the relaxion, in any case, requires a large hierarchy between f_k and its field excursion during rolling, $f_k \ll F$, are problematic as explained in [292]. The solution to generating the latter hierarchy is to embed the relaxion construction in a so-called clockwork model [293–295]; this can easily be extended to also generate the former hierarchy, giving $f \ll f_k \ll F$.

Clockwork models introduce a system of $N + 1$ interacting complex scalars, Φ_i, all of which get a complex VEV such that,

$$\langle \Phi_i \rangle = \frac{f}{\sqrt{2}} e^{i\pi_i/f} \,. \tag{8.3.1}$$

There is an approximate Abelian symmetry, $\mathrm{U}(1)_i$, at each site, which is spontaneously broken to give rise to a corresponding pseudo-Goldstone mode π_i. Explicit breaking effects give the angular fields, π_i, a mass matrix such that the lightest state is a massless (Goldstone) mode given by,

$$\phi \propto \sum_{j=0}^{N} \frac{\pi_j}{3^j} = \pi_0 + \frac{\pi_1}{3} + ... + \frac{\pi_N}{3^N} \,. \tag{8.3.2}$$

Given that the mixing angle $\langle \pi_k | \phi \rangle \sim 3^{-k}$, any Lagrangian term where the angular field π_k couples with a decay constant f translates to an interaction of ϕ with an exponentially-enhanced effective decay constant, $3^k f$, in the mass basis.

Coming back to our set-up, the hierarchy $f \ll f_k \ll F$ can be obtained by having the operator, $\mathcal{O}_{SB}$, at the 0th site, the backreaction sector at the intermediate kth site and the rolling potential at the Nth site, such that $f_k = 3^k f$ and $F = 3^N f$. This is schematically shown in Fig. 8.3. The rolling and backreaction potentials eventually lift the flat direction in Eq. 8.3.2, giving a mass to the relaxion.

Each of these three non-trivial nodes of the clockwork and their associated sectors will be described in turn in the following sections.

8.3.2   Site 0: neutrino masses & baryogenesis

It was shown in [284] that with just one additional ingredient, the second phase of relaxion rolling can also give spontaneous relaxion baryogenesis (SRB). One requires that some fermions with $B + L$ charge are charged under the relaxion shift symmetry. This leads to the presence of the operator, $\partial_\mu \phi J^\mu / f$, where J^μ contains the $B + L$ current. This operator generates a chemical potential for $B + L$ violation once the second phase of relaxion rolling results in a CPT-breaking expectation value for $\partial_\mu \phi$. A baryon asymmetry is consequentially generated via $(B + L)$-violating sphaleron transitions.

This SRB set-up in [284] is incomplete in two respects: the operator, $\mathcal{O}_{SB}$, and the rolling potential are non-renormalisable and are introduced in a somewhat ad hoc way. While $\mathcal{O}_{SB}$ arises naturally if baryons and/or lepton are charged under the Abelian symmetry of which the relaxion is a Goldstone boson, charging the SM fermions seems to have no purpose other than generating $\mathcal{O}_{SB}$. Furthermore, the charge assignments have to be carefully chosen such that they are anomaly-free with respect to QCD (to avoid generating a strong CP phase) and preferably also with respect to electromagnetism (to avoid the generation of a $\phi\gamma\gamma$ coupling that rules out most of the parameter space in this set-up [284]).

Here we complete the SRB set-up as follows:

1. Instead of introducing the operator, $\mathcal{O}_{SB}$, by hand, we propose a simple neutrino mass model at site 0, which generates this operator with a current containing only three new right-handed (RH) neutrino fields. The operator arises because the RH fields are charged under the relaxion shift symmetry, which in turn is identified with a Froggatt-Nielsen symmetry. This also explains the observed smallness of neutrino masses. Only the SM-singlet RH neutrinos
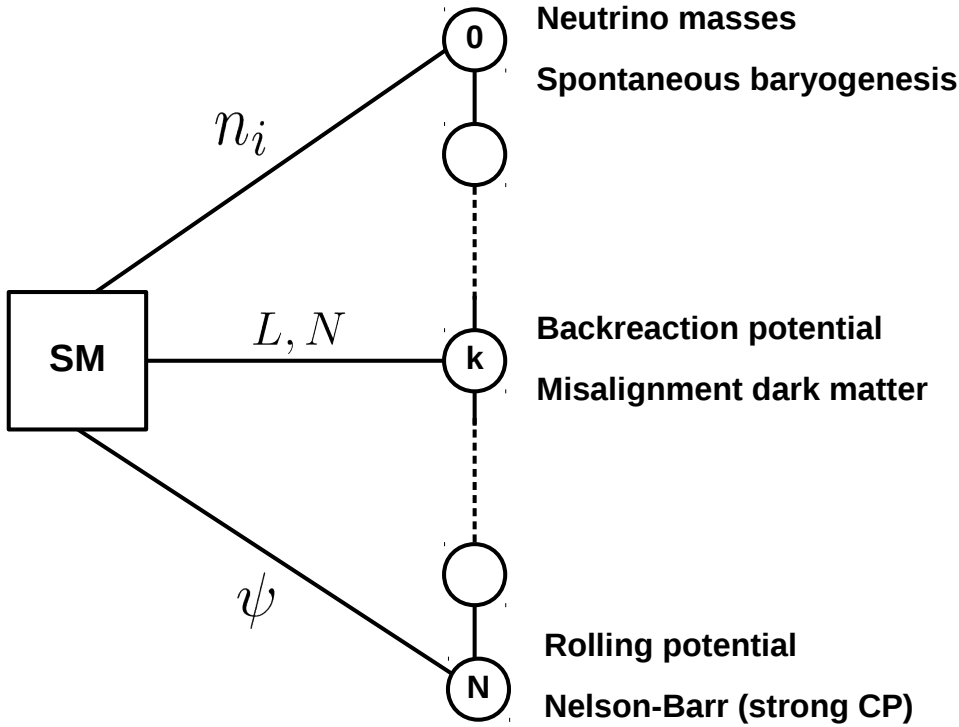
Figure 8.3: *Schematic representation of our set-up with the vertical line representing the clockwork system. The three right-handed neutrinos at the 0th site, n_i, couple to the SM in the usual way, generating neutrino masses; they also provide the current in the all-important operator for spontaneous baryogenesis, $\mathcal{O}_{SB} = (\partial_\mu \phi) J^\mu$. At the kth site we introduce a new strong sector, which couples to SM via its new fermionic matter content, $\{L, L^c, N, N^c\}$. This sector generates the backreaction wiggles; relaxion oscillations inside these wiggles generate the observed dark matter abundance. Finally, at site N there is a Nelson-Barr sector that radiatively generates the rolling potential while also providing a solution to the strong CP problem. This sector couples to the SM up sector via a new vector-like quark pair (ψ, ψ^c).*

are charged under the relaxion shift symmetry, which is thus automatically anomaly-free with respect to both QCD and electromagnetism.

2. We show that the rolling potential can be generated by the addition of a single up-type vector-like pair at site N. This modification can also solve the strong CP problem via the Nelson-Barr mechanism [213, 285]. In Nelson-Barr models, CP is a good symmetry in the UV and is spontaneously broken at an intermediate scale to generate an $\mathcal{O}(1)$ CKM phase but a much smaller strong CP phase (within allowed constraints). We borrow the Nelson-Barr relaxion sector from [224], where , upon stopping, the relaxion phase results in an $\mathcal{O}(1)$

CKM phase. The Nelson-Barr sector and generation of the rolling potential at site N are discussed in Section 8.3.4.

It is also worth noting that spontaneous baryogenesis is an attractive feature from the point of view of the Nelson-Barr relaxion model, as it does not require explicit CP violation. Recall that the Nelson-Barr mechanism requires that CP is a good symmetry that is later spontaneously broken.

Getting the operator $\mathcal{O}_{SB}$

At site 0, we introduce a sector that simultaneously generates small neutrino masses and an operator suitable for spontaneous baryogenesis. We introduce three right-handed (RH) sterile neutrinos, n_i, that are charged under the 0th site Abelian symmetry, $U(1)_0$. We fix the charge of Φ_0 to be -1 under this symmetry and take all SM fields to be neutral.

The Lagrangian for the couplings of these RH neutrinos is given by,

$$\mathcal{L}_{\text{FN}} \supset y_n^{ij} \left(\frac{\Phi_0}{\Lambda_{FN}} \right)^{q_{n_j}} l_i^\dagger H n_j + \left(\frac{\Phi_0}{\Lambda_{FN}} \right)^{q_{n_i}+q_{n_j}} \hat{M}_n^{ij} n_i n_j, \tag{8.3.3}$$

where $l_i^\dagger$ are right-handed spinors denoting the SM lepton doublets, q_{n_j} are the Abelian charges for the sterile neutrinos and M_n^{ij} is the Majorana mass matrix. Given that we will eventually use the Nelson-Barr solution to the strong CP problem, we impose CP as an exact symmetry of the Lagrangian so that all couplings above are real.

Substituting, $\langle \Phi_0 \rangle = \frac{f}{\sqrt{2}} e^{i\pi_0/f}$, we obtain exponentially-suppressed effective Yukawa couplings and Majorana masses, $Y_n^{ij} = y_n^{ij} (\epsilon_{FN})^{q_{n_j}}$ and $M_n^{ij} = \hat{M}_n^{ij} (\epsilon_{FN})^{q_{n_i}+q_{n_j}}$, where $\epsilon_{FN} = f/\sqrt{2}\Lambda_{FN} < 1$.

Factors of $e^{i\pi_0/f}$, that appear upon substitution of Φ_0 in Eq. 8.3.3, can be rotated away by the field redefinition $n_j \to n_j e^{-i\pi_0 q_{n_j}/f}$, which, through the redefinition of the kinetic terms for the RH neutrinos, yields the desired operator, $\mathcal{O}_{SB}$,

$$\frac{q_{n_i}}{f} (\partial_\mu \pi_0) n_i^\dagger \bar{\sigma}^\mu n_i \to \frac{q_{n_i}}{f} (\partial_\mu \phi) n_i^\dagger \bar{\sigma}^\mu n_i, \tag{8.3.4}$$

where we ignore an $\mathcal{O}(1)$ factor corresponding to $\langle \pi_0 | \phi \rangle$.

Getting a baryon asymmetry from $\mathcal{O}_{SB}$

The presence of the operator $\mathcal{O}_{SB}$ can lead to spontaneous baryogenesis, as discussed in Section 7.3.1. The essential feature of this mechanism is the presence of a rolling field that breaks CPT, a role played here by the relaxion [284].

During the second phase of the rolling, the operator $\mathcal{O}_{SB}$ causes equal and opposite shifts in the energies of particles versus antiparticles, implying,

$$\mu_i = -\bar{\mu}_i \;=\; q_i \dot{\phi}/f + (B_i - L_i)\mu_{B-L} + Q_i \mu_Q + T_{3i}\mu_{T_3} \;,$$

where μ_i ($\bar{\mu}_i$) is the chemical potential for (anti-) particles of the ith species; q_i is its charge under $U(1)_0$ (which is non-zero only for the RH neutrinos); Q_i is the electromagnetic charge; T_{3i} is the charge corresponding to the diagonal generator of $SU(2)_L$; and the chemical potentials $\mu_{Q,T_3,B-L}$ have been introduced to enforce conservation of Q, T_3 and $B - L$. In the presence of $(B + L)$-violating sphaleron processes, we find,

$$\Delta n_i \equiv n_i - \bar{n}_i \;=\; f(T, \mu) - f(T, \bar{\mu}) \tag{8.3.5}$$
$$=\; g_i \mu_i \frac{T^2}{6}, \;\; g_i \mu_i \frac{T^2}{3},$$

for fermions and bosons respectively, where $f(T, \mu)$ is the Fermi-Dirac (Bose-Einstein) distribution for fermions (bosons). We have taken $\mu \ll T$ and the factor g_i denotes the number of degrees of freedom for each species. The quantities $\mu_{T_3,Q,B-L}$ can be obtained by imposing $n_Q = n_{B-L} = n_{T_3} = 0$, where,

$$n_Q = \sum_i Q_i \Delta n_i \,, \tag{8.3.6}$$

and similarly for n_{B-L}, n_{T_3}. For temperatures above the critical temperature for the electroweak phase transition, we obtain the following chemical potentials,

$$\mu_Q = -\frac{3}{14}\frac{Q_n \dot{\phi}}{f} \quad \mu_{T_3} = \frac{3}{14}\frac{Q_n \dot{\phi}}{f} \quad \mu_{B-L} = \frac{33}{112}\frac{Q_n \dot{\phi}}{f}, \tag{8.3.7}$$

taking all the $q_{n_i} = Q_n$. We subsequently obtain a baryon number density,

$$n_B = -n_L = g_{\rm SB}\frac{\dot{\phi}}{f}\frac{T^2}{6}, \tag{8.3.8}$$

where $g_{\rm SB} = 3\,Q_n/4$. Finally, we obtain its ratio with the entropy density,

$$\eta \equiv \frac{n_B}{s} \;=\; g_{\rm SB}\frac{\dot{\phi}}{f}\frac{T^2}{6} \times \left(\frac{2\pi^2 g_* T^3}{45}\right)^{-1} \;=\; \frac{15}{4\pi^2}\frac{g_{\rm SB}}{g_*}\frac{\dot{\phi}}{fT}\,. \tag{8.3.9}$$

The equilibrium distribution changes after electroweak symmetry breaking, when there is no longer a need to conserve T_3. This gives $\mu_Q = -(4/11)\mu_{B-L} = -Q_n\dot{\phi}/12f$ and, once again, $g_{\rm SB} = 3Q_n/4$. However, species such as the RH fermions, which are coupled very weakly to the thermal plasma, would not be able to re-equilibrate on the time scale of the electroweak phase transition. The precise value of $g_{\rm SB}$ is thus

hard to compute without considering the full dynamics of the process and may be different from the value obtained above. Given that these subtleties only lead to an $\mathcal{O}(1)$ ambiguity in $g_{\rm SB}$, for definiteness we stick to the value derived in Eq. 8.3.8.

The value of η is frozen at $T = T_{sph} = 130$ GeV, the temperature at which the sphaleron processes decouple [296]. Demanding the observed baryon asymmetry, $\eta_0 = 8.7 \times 10^{-11}$, we obtain,

$$\frac{f_k}{f} = \sqrt{\frac{2}{5}} \frac{2\pi^3}{9} \frac{g_*^{3/2}}{g_{SB}} \frac{\eta_0 T_{sph}^3}{m_\phi^2 M_P} \sim 10^9 \left(\frac{m_\phi}{10^{-5} \text{eV}}\right)^{-2} , \qquad (8.3.10)$$

using $V' = 5H\dot{\phi} \sim \Lambda_c^4/f_k$ (see Section 8.2). It is crucial that the relaxion is rolling with a non-zero $\dot{\phi}$ when the value of η is frozen at $T = T_{sph}$. To ensure this, we require that the critical temperature for the phase transition of the strong sector, T_c, is lower than T_{sph}, as outlined in Section 8.2.

We have assumed so far that the RH neutrinos are relativistic and in equilibrium at the temperatures relevant to the calculation. The first condition requires that the see-saw scale, $M_n \lesssim T_{sph}$, where $M_n^{ij} \sim M_n$. The second requirement implies that the interaction rate of n_i with SM particles satisfies, $\Gamma(n) > H(T_{sph})$. Taking $\Gamma(n) \sim g^2 Y_n^2 T$ [297], where g is the weak coupling and $Y_n^{ij} \sim Y_n$ and imposing this second condition, $\Gamma(n) > H(T_{sph})$, we find that,

$$Y_n \gtrsim 10^{-8} . \qquad (8.3.11)$$

Neutrino masses

The Lagrangian in Eq. 8.3.3 generates masses for the SM neutrinos $m_\nu \sim Y_n^2 v^2 / M_n \lesssim 0.1$ eV. Given that spontaneous baryogenesis demands $M_n \lesssim T_{sph}$, we require small effective Yukawas $Y_n \lesssim 10^{-6}$, which can be naturally obtained via the Froggatt-Nielsen mechanism, as explained above. Note that without the Majorana mass term the neutrinos would only have a Dirac mass, which would require a much smaller Yukawa coupling. Our explanation for the smallness of neutrino masses thus utilises a combination of the Froggatt-Nielsen and see-saw mechanisms.

The constraints derived in the previous subsections imply that our model requires a finite range for both the effective Yukawa coupling and effective Majorana mass scale: $10^{-8} \lesssim Y_n \lesssim 10^{-6}$, 30 MeV $\lesssim M_n \lesssim T_{sph}$. Note that sterile neutrinos with masses below 500 MeV are in tension with big-bang nucleosynthesis (BBN) [298]. Masses around a few GeV may be within reach of future experiments such as SHiP [298]. For $\epsilon_{FN} = 0.1$ the above range of the Yukawa couplings can be obtained for $6 \leq Q_n \leq 8$, where we have taken all $q_{n_i} = Q_n$. Given that all the couplings in Eq. 8.3.3

are real, a concrete prediction of our model is a CP-even neutrino mass matrix, which is still comfortably within the parameter space allowed by current neutrino experiments [299].

8.3.3   Site k: the backreaction potential & dark matter

A new strong sector

The kth site is responsible for generating the backreaction potential via the non-QCD model of Ref. [44], where the relaxion, ϕ, is the axion of a new strong sector. In our setup, more specifically, it is the kth angular mode, π_k, that is the true axion of the sector. Recall that $\langle \pi_k | \phi \rangle \approx 3^{-k}$ and thus the ratio $\pi_k / f \sim \phi / f_k$.

The new strong sector, with field tensor $G'_{\mu\nu}$, consists of two new vector-like leptons described by Weyl spinors $\{L, L^c\}$ and $\{N, N^c\}$. These are charged under the new strong group, with the non-conjugate L and N having the same electroweak quantum numbers as SM lepton doublets and right-handed neutrinos respectively.

The interactions in this sector are described by the Lagrangian,

$$\mathcal{L}_{\text{BR}} \supset y_1 LHN + y_2 L^c H^\dagger N^c - m_L LL^c - m_N NN^c + (\pi_k / f) G' \tilde{G}' + \text{h.c.} \quad (8.3.12)$$

with the usual definition of the dual field tensor $\tilde{G}'_{\mu\nu} = \epsilon_{\mu\nu\alpha\beta} G'^{\alpha\beta}$. As with site 0, we see that site k is coupled to the Standard Model via the Higgs.

Generating the backreaction

We follow the reasoning in Refs. [44,284] and assume that $m_N \ll 4\pi f_c \ll m_L$ so that, similarly to QCD, we obtain a chiral condensate $\langle NN^c \rangle = 4\pi f_c^3$. We now consider NN^c contributions after L has been integrated out,

$$m_N NN^c + \frac{y_1 y_2 H^\dagger H}{m_L} NN^c = (m_N + \Delta m_N) NN^c. \quad (8.3.13)$$

After chiral condensation of NN^c, non-perturbative effects induce a contribution to the potential for π_k in analogy to the QCD case in Section 7.1.1,

$$- 4\pi f_c^3 (m_N + \Delta m_N) \cos(\pi_k / f) = -4\pi f_c^3 (m_N + \Delta m_N) \cos(\phi / f_k), \quad (8.3.14)$$

By comparison with the backreaction potential in Eq. 8.2.3, we see,

$$V_{\text{br}} = -4\pi f_c^3 (m_N + \Delta m_N) \cos(\phi / f_k) \equiv -\Lambda_c^4 \cos(\phi / f_k). \quad (8.3.15)$$

The Δm_N term can give a Higgs-dependent term via the VEV $\langle H^\dagger H \rangle = v^2$ or a radiative Higgs-independent term via closure of the HL loop,

$$\frac{y_1 y_2 H^\dagger H}{m_L} \rightarrow \frac{y_1 y_2 v^2}{m_L} + \frac{y_1 y_2 m_L}{16\pi^2} \, . \tag{8.3.16}$$

Hence, combined with the Higgs-independent m_N term, we have two Higgs-independent terms and one Higgs-dependent term. As explained in Section 8.2, the relaxion mechanism relies on the backreaction only turning on once the Higgs field acquires a VEV. It is therefore paramount that the Higgs-dependent contribution dominates. This is the case if,

$$f_c \lesssim v, \qquad m_L \lesssim 4\pi v \, . \tag{8.3.17}$$

Next, we consider that $(m_N + \Delta m_N) \sim \Delta m_N$ must be smaller than $4\pi f_c$ for the condensate to have formed in the first place so that $\Lambda_c^4 \equiv 4\pi f_c^3 \Delta m_N \lesssim (16\pi^2) f_c^4$ and thus in combination with Eq. 8.3.17,

$$\Lambda_c^4 \lesssim (16\pi^2) v^4. \tag{8.3.18}$$

With these constraints in mind, we now have the backreaction potential shown in Eq. 8.2.3, with appropriate Higgs-dependent behaviour.

Obtaining the relic abundance

The explanation for dark matter requires no additional ingredient. This is due to the fact that during the second phase of rolling, the relaxion gets misaligned from its original stopping point by an angle [287],

$$\Delta\theta \; = \; \frac{\Delta\phi}{f} \; \simeq \; \frac{1}{20}\left(\frac{m_\phi}{H(T_c)}\right)^2 \tan\frac{\phi_0}{f} \, . \tag{8.3.19}$$

As shown in Ref. [287], this sets off relaxion oscillations that can give rise to the observed dark matter relic abundance,

$$\Omega h^2 \; \simeq \; 3\Delta\theta^2 \left(\frac{\Lambda_d}{1 \text{ GeV}}\right)^4 \left(\frac{100 \text{ GeV}}{T_{\text{osc}}}\right)^3 \, . \tag{8.3.20}$$

Note that the correct relic density can always be reproduced by choosing an appropriate value of $\tan\frac{\phi_0}{f}$. While there is some room for this in the relaxion mechanism, as the relaxion is spread across multiple vacua at the end of its rolling, the probability distribution of the relaxion field peaks for $\mathcal{O}(1)$ values of $\tan\frac{\phi_0}{f}$ [300]. Thus the extent to which $\tan\frac{\phi_0}{f}$ deviates from unity can be interpreted as a measure of the tuning required to get the correct relic abundance.

8.3.4 Site N: the rolling potential & strong CP

Generating the rolling potential

As shown in Ref. [224], the rolling potential in Eqs. 8.2.1 and 8.2.2 can be generated by a minimal modification of the SM up sector, namely the addition of a vector-like pair, (ψ, ψ^c), where ψ has the same quantum numbers as an up-type singlet. Furthermore, as shown in Ref. [223] and discussed in Section 7.1.2, the same modification can also give a Nelson-Barr solution [213, 285] to the strong CP problem, provided we impose an additional Z_2 symmetry.

The Lagrangian terms for the relevant interactions are,

$$\mathcal{L}_{\mathrm{NB}} = Y^u_{ij} Q \tilde{H} u^c + y^i_\psi \psi \Phi_N u^c_i + \tilde{y}^i_\psi \psi \Phi^*_N u^c_i + \mu_\psi \psi \psi^c + \mathrm{h.c.}$$

The ψ, ψ^c and Φ_N are odd under the Z_2 symmetry, which forbids the term $QH\psi^c$. Recall that an exact CP symmetry has been imposed and thus all couplings are real. The $\mathrm{U(1)}_N$ symmetry is collectively broken by y^i_ψ and $\tilde{y}^i_\psi$, leading to breaking of the relaxion shift symmetry. Any radiative Φ^2_N terms get VEV contributions,

$$\Phi^2_N + \mathrm{h.c.} \sim f^2 \cos(\phi/F). \tag{8.3.21}$$

The 1-loop $\Phi_N \to \Phi_N$ diagram gives the $r^2_{\mathrm{roll}} M^4$ in the roll potential (Eq. 8.2.1) whereas the $\Phi^2_N H^\dagger H$ box diagram gives the $\mu^2(\phi)$ term in Eq. 8.2.2. For the loop diagram generating the first term, we have taken the the cut-off for the ψu^c loop to be the mass of the clockwork radial modes, $m_\rho \sim f$. Evaluating these loop expressions and matching to the roll potential coefficients, we can identify,

$$M \sim \frac{\sqrt{y^i_\psi \tilde{y}^j_\psi (Y^{u\dagger} Y^u)_{ij}}}{4\pi} f, \qquad r_{\mathrm{roll}} \sim \frac{4\pi \sqrt{y^k_\psi \tilde{y}^k_\psi}}{y^i_\psi \tilde{y}^j_\psi (Y^{u\dagger} Y^u)_{ij}}. \tag{8.3.22}$$

Nelson-Barr solution to the strong CP problem

The Lagrangian in Eq. 8.3.21 also provides a solution to the strong CP problem, with Φ_N playing the role of a Nelson-Barr field. We know that this field gets a complex VEV,

$$\langle \Phi_N \rangle = \frac{f}{\sqrt{2}} e^{i\pi_N/f}, \tag{8.3.23}$$

such that CP is spontaneously broken. Once the relaxion stops, the phase, $\theta_N = \langle \pi_N \rangle / f \sim \phi/F$, enters the 4×4 matrix for the up sector as discussed in Section 7.1.2,

$$M_u = \begin{pmatrix} (\mu_\psi)_{1\times 1} & (B)_{1\times 3} \\ (0)_{3\times 1} & (vY^u)_{3\times 3} \end{pmatrix}, \tag{8.3.24}$$

where $B_i = f(y_\psi^i e^{i\theta_N} + \tilde{y}_\psi^i e^{-i\theta_N})/\sqrt{2}$. The phase, θ_N, is nothing but the phase of the cosine of the rolling potential at the relaxion stopping point. Note that the bottom-left element in the above mass matrix is zero due to the absence of the $QH\psi^c$ term in the Lagrangian, which in turn is a direct consequence of the Z_2 symmetry. This ensures that at tree level there is no contribution to $\bar{\theta}_{QCD}$ from the phase, θ_N, as $\text{Arg}(\det(M_u)) = 0$, where we use the fact that μ_ψ is real. On the other hand, for $\mu^2 + B_i B_i^* \gg v^2$, we can integrate out the vector-like pair to give an effective 3×3 mass-squared matrix of the SM up-quark sector with an $\mathcal{O}(1)$ phase. This gets translated into an $\mathcal{O}(1)$ phase in the CKM matrix $V_{CKM} = V_{u_L}^\dagger V_{d_L}$ (see Ref. [224]). Radiative effects can spoil the solution to the strong CP problem unless $y_\psi \lesssim 10^{-2}$ [224].

Before going to the next section we would like to point out that there appears to be no obvious difficulty in extending our model along the lines of Ref. [286] to also address the SM flavour puzzle for the charged leptons and quarks. At the cost of complicating our model, this can be achieved by identifying one of the intermediate sites of the clockwork chain with the flavon for the charged fermions and the Abelian symmetry at this site with a Froggatt-Nielsen flavour symmetry. In order not to generate a $\bar{\theta}_{QCD}$, the charge assignment of the SM fermions must be anomaly-free with respect to QCD as emphasised in [286] where an example charge assignment was also presented. We do not explore this direction further and stick to our more minimal set-up here.

With the various sectors of the model explained, we collect the constraints encountered along the way and look at the resultant parameter space.

8.4   The parameter space

A plot of the constraints and bounds on the (m_ϕ, M) parameter space is shown in Fig. 8.4. Let us summarise the constraints from the previous sections:

1. **Cosomological evolution**: The red band at the top shows the region where the value of the cut-off, M, exceeds the upper bound imposed in Eq. 8.2.7. The vertical green band shows the region that is ruled out by requiring, $m_\phi < 5H(T_c)$, the condition in Eq. 8.2.9 that the relaxion does not overshoot the barriers of the backreaction potential once they reappear after reheating. Here we have taken the maximal value $T_c = T_{sph}$ (see Section 8.3.2).

2. **Spontaneous baryogenesis**: We fix the f_k/f ratio according to Eq. 8.3.10 such that each point in the plot gives the correct baryon asymmetry.

3. **Backreaction**: The blue shaded region corresponds to the region $\Lambda_c^2 > 16\pi^2 v^2$ ruled out by the requirement (see Section 8.3.3) that the Higgs-dependent parts of the backreaction potential dominate over any Higgs-independent contribution.

4. **Dark matter**: The dashed lines show the required value of $\tan(\phi_0/f_k)$ to reproduce the correct dark matter density in Eq. 8.3.20. As explained below Eq. 8.3.20, the extent to which $\tan\frac{\phi_0}{f}$ deviates from unity can be interpreted as a measure of the required tuning. The orange region shows fifth force constraints that arise due to the fact that the relaxion mixes with the Higgs boson with a mixing angle (see Ref. [301]),

$$\sin\theta \sim \frac{\Lambda_c^4}{vf_k m_h^2}. \tag{8.4.1}$$

Finally, the region to the left of the dashed line may be probed in future atomic physics experiments if there is an overdensity of relaxion dark matter around the earth [302, 303].

5. **Nelson-Barr**: From Eq. 8.3.22 we see that for a given value of f and y_ψ one can fix the value of the Higgs mass cut-off , M, giving us the scale on the right hand side of the frame.

6. **Hierarchy problem**: The grey band at the bottom shows the region where the relaxion mechanism is unable to raise the Higgs cut-off beyond 2 TeV.

We see from Fig. 8.4 that after all the constraints are imposed, a finite allowed region remains that remarkably contains the region in which tuning to obtain the correct relic density for dark matter is minimal.

We will comment in the next section on how this allowed region can be probed further by future experiments.

8.5 Summary

We have presented a simultaneous solution to five BSM puzzles: namely the lightness of the Higgs boson in the absence of TeV-scale new physics, dark matter, matter-antimatter asymmetry, neutrino masses and the strong CP problem. While our construction is admittedly more involved than some other attempts to solve BSM puzzles in a unified way [278, 279, 282, 283], this is because we also use cosmological relaxation to achieve the challenging task of obtaining a light Higgs boson without
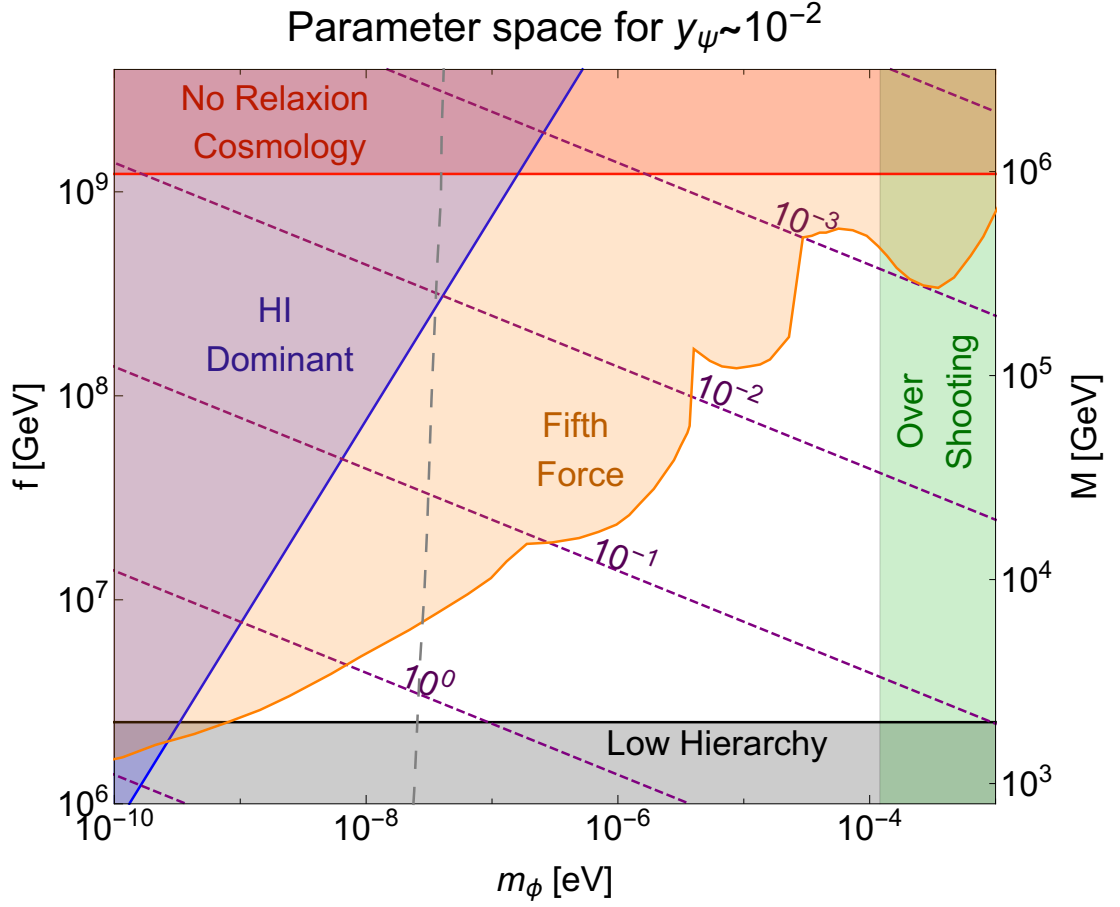
Figure 8.4: *The parameter space for an all-in-one relaxion in the (m_ϕ, f) plane. For each value of f, taking the maximal value $y_\psi = 10^{-2}$, the value of the Higgs mass cut-off, M, is fixed as shown on the right-hand side of the frame (see Eq. 8.3.22). The red band shows the region violating the bounds imposed by cosmological requirements in [44]; blue denotes the region where the Higgs-independent contributions to the backreaction are no longer subdominant [44]; the orange region shows the fifth-force exclusions due to the mixing of ϕ with the Higgs [301]; green denotes the region in which the relaxion overshoots the backreaction barriers after reheating (see Section 8.2) for the maximal value $T_c = T_{sph}$; and the purple dashed lines show the tuning needed to reproduce the correct relic density [284]. The grey band at the bottom shows the region where the relaxion mechanism is unable to raise the Higgs cut-off beyond 2 TeV. Finally, the region to the left of the dashed line may be probed in future atomic physics experiments if there is an overdensity of relaxion dark matter around the earth [302, 303].*

adding any TeV-scale states that cut off the Higgs mass divergence. Our construction has all the ingredients of a standard relaxion model – such as a chain of clockwork scalars and a TeV-scale strong sector – but beyond this we only make minimal modifications by adding three RH neutrinos and an up-type $SU(2)_L$ singlet vector-like quark pair.

Our all-in-one relaxion set-up gives a diverse set of observational predictions. Our construction predicts the absence of a CP-violating phase in the neutrino mass matrix and GeV-scale sterile neutrinos potentially close to the reach of future experiments such as SHiP [298]. The strong CP phase in our model is non-zero and may be detectable in future experiments. The finite allowed parameter space in Fig. 8.4 can also be probed by future atomic physics experiments [302,303] or future improvements in fifth force experiments. Finally, we would like to point out the interesting trade-off that exists in Fig. 8.4 between the Higgs mass cut-off scale and the tuning required to reproduce the correct abundance of dark matter. The least-tuned regions correspond to cut-off values smaller than 100 TeV, a scale where top partners in a full solution to the hierarchy problem can be seen in future high-energy colliders.

Chapter 9

Conclusions

In this thesis, we have explored three avenues of Higgs research. These differ in context and approach but all have the Higgs boson in common. We have seen how studying its interactions and properties can lead to a better understanding of both the physics that may have occurred in the past and the new physics we may see in the future. Here we present an overview of the physics and conclusions discussed in all three parts of this thesis. More detailed conclusions can be found at the end of each part.

The 125 GeV scalar boson of interest was discovered at a particle collider, namely the Large Hadron Collider (LHC). We began in Part I by looking at what we can learn about the Higgs from such colliders, present and future. As of the time of writing, the discovery of the Higgs boson in 2012 remains the most-recent direct sign of new particle physics. The lack of discoveries of any supersymmetric partners or other expected weak-scale candidates has led to the popularisation of a more general parametric approach to new physics: the Standard Model Effective Field Theory (SMEFT). In the SMEFT framework we trade speculation on possible UV completions for a tower of lower-energy effective operators encapsulating all possible UV effects (satisfying the appropriate Standard Model symmetries). We can truncate this tower of operators and look at the leading effects of the SMEFT operators on collider processes.

Through the 'BSM primary' parametrisation, we can translate the unbroken-phase SMEFT Wilson coefficients into broken-phase collider-friendly parameters. The measurement of Higgs interactions at colliders through various decay and production channels can be used to constrain these parameters and in turn quantify deviations from the Standard Model.

While many studies focus on total rate information alone, we argue that increasing integrated luminosities will allow for the use of more complex differential observables.

We show that using such differential observables can resurrect effects that would otherwise be lost in a total rate analysis. In our specific cases of Higgs associated production with an electroweak boson, analytic knowledge of the helicity amplitudes instructed a decomposition into nine angular structures. Measurement or inference of the relevant angles for collision events allows us to estimate the coefficients of each of these nine structures for a given process via a so-called 'method of moments'. The sensitivity of this method relies on the preservation of the angular structures, which can be affected by experimental cuts, showering and higher-order corrections. The results obtained suggest that these structures do remain largely intact and that access to the full angular dependence leads to improved sensitivity, particularly for the $hV^{\mu\nu}V_{\mu\nu}$ and $hV^{\mu\nu}\tilde{V}_{\mu\nu}$ interactions. This method could be applied in other Higgs processes to provide more observables for a global fit.

In estimating the sensitivity of the method of moments, we considered the projected integrated luminosities of the future high-luminosity LHC (HL-LHC). As well as increasing luminosities, there is an interest in increasing energies, with excitement surrounding the possible discoveries of the proposed future circular colliders (FCCs). While there are plenty of popular new particle candidates from the model-building community, one mustn't overlook the Higgs itself.

The Higgs boson is the first known fundamental scalar and as such could exhibit unusual behaviour at higher energies. More theoretical studies of scalar ϕ^4 theory suggest that the constructive interference and factorial growth in Feynman diagram numbers with multiplicity can lead to exponential rates at high energies. This begs the question of whether we should expect such behaviour of the Higgs, despite its embedding in a more complex non-scalar theory.

In Part II we reviewed and derived the semiclassical method for calculating scalar multiparticle rates, via the coherent state formalism. The method was then applied to an idealised semiclassical regime, in which the coupling approaches zero and the multiplicity approaches infinity such that their product is constant but large. Such a regime is inherently non-perturbative and thus requires a semiclassical treatment. In reality, the coupling would simply be small and the multiplicity large, but the idealised limit above serves as our best approximation.

We show that under the assumption of the semiclassical regime and an isolated scalar sector, we expect an exponential rate. Whether the rate is exponentially growing or decaying depends on the interplay of two terms: a kinetic term and a coupling×multiplicity term. We find that there is always a multiplicity for which the latter term wins, triggering exponential growth. This exponential growth occurs at multiplicities close to the kinematically-allowed maximum.

One therefore wonders if we should expect such behaviour of the Higgs at future higher-energy experiments, a phenomenon dubbed Higgsplosion. While the idealised calculations presented in this thesis and other recent works referenced therein form a great foundation, there is much work left to do in order to fully assess the plausibility of Higgsplosion as a real process in nature.

A potential side effect of exponentially-growing multiparticle rates could be the cutting-off of Higgs loop integrals. This would limit quadratic corrections to the Higgs mass and solve, or at least improve, the hierarchy problem. Another potential solution to the hierarchy problem was discussed in Part III, in which the Higgs vacuum expectation value was set dynamically via the cosmic evolution of a relaxion field.

We took a step back from the formal non-perturbative calculations and looked at the Higgs as a piece of a greater model, aiming to solve five big problems in fundamental physics: hierarchy, dark matter, strong CP, neutrino masses and baryon asymmetry. Minor field content additions to existing non-QCD relaxion models allow us to construct a theory that solves these problems, while simultaneously generating the rolling and backreaction potentials required for the relaxion mechanism. The success of this model is rooted in three separated scales. The scale hierarchy is generated by a clockwork, with the relevant physics to each scale taking place at the appropriate clockwork site. Experimental and cosmological considerations reveal a constrained parameter space for such a model with a finite non-excluded region, much of which can be probed by future experiments.

Over the course of this thesis, we have encountered a great variety of physics: from the analysis of computer-simulated collision data, to formal non-perturbative methods, to model building and wider cosmological considerations. We have also seen the Higgs in a number of guises. In the context of colliders, it is a mysterious new opportunity for measurement; yet in the context of model building it is often a useful tool in connecting different physics sectors. We have presented a method to increase sensitivity to new physics at future colliders, discussed possible high-energy peculiarities and proposed a combined solution to some of the leading problems in fundamental physics.

The Higgs boson is a fountain of experimental and theoretical curiosity. We are optimistic that the work presented in this thesis will be of benefit in the continued development of Higgs physics in the years to come.

Appendix A

Additional information from "A Differential Analysis of the SMEFT Vh Mode"

A.1   Two solutions for the neutrino z momentum

For processes involving the decay of a W boson to a lepton, ℓ, and a neutrino, ν, there is usually an ambiguity in the kinematics arising from the experimentally-evasive neutrino. Here we derive this two-fold ambiguity for our process of interest.

Consider the process $pp \to W(\ell\nu)h(b\bar{b})$, as studied in Chapter 3. Using lepton isolation and fatjet techniques (see Section 3.5), we can expect to know the lab-frame four momenta of the isolated lepton and the Higgs boson, p^ℓ and p^h, to a decent accuracy.

The initial partons should be moving along the beam axis, which we choose to be the z axis in the lab frame Cartesian coordinates. We therefore expect the transverse momenta of the decay products to sum to zero by conservation of momentum. Hence, we can infer that,

$$p^\nu_{x,y} = -p^\ell_{x,y} - p^h_{x,y}. \tag{A.1.1}$$

We now make the assumption that the W boson is on-shell, by requiring,

$$(p^\nu + p^\ell)^2 = m_W^2. \tag{A.1.2}$$

We also assume a massless neutrino $E^{\nu 2} = p_x^{\nu 2} + p_y^{\nu 2} + p_z^{\nu 2} = p_T^{\nu 2} + p_z^{\nu 2}$. The on-shell condition in Eq. A.1.2 can be rearranged to obtain a quadratic equation for our unknown, the z momentum of the neutrino,

$$4(p_z^{\ell\,2} - E^{\ell\,2})p_z^{\nu\,2} + 4A p_z^\ell p_z^\nu + (A^2 - 4p_T^{\nu 2}E^{\ell\,2}) = a p_z^{\nu\,2} + b p_z^\nu + c = 0, \tag{A.1.3}$$

with $A = m_W^2 + (p_x^\nu + p_x^\ell)^2 + (p_y^\nu + p_y^\ell)^2 - E^{\ell 2} - p_T^{\nu 2}$. Provided the discriminant, $b^2 - 4ac$, is positive, we obtain two solutions for p_z^ν. Given that the calculations for each angle used in the method of moments relies on these solutions, we obtain two possible values for each angle in the Wh analysis. This is discussed in Section 3.3.3.

A.2   Packages, algorithms & tools

This appendix acts as a glossary for the PACKAGES, **algorithms** and **tools** mentioned in Section 3.5.

A.2.1   Packages

FeynRules & UFOs

FEYNRULES [142] is a MATHEMATICA-based [304] package that calculates the Feynman rules for any Quantum Field Theory (QFT) model, given some minimal information needed to describe said model. It creates a Universal FeynRules Output (UFO) file, which can be fed into other tools. We use the UFO as an input to the MADGRAPH event generator [145].

NLOCT

NLOCT [143] is also a package that creates UFO outputs. It is needed in conjunction with FEYNRULES [142] when one wishes to use a model file to do next-to-leading-order (NLO) event generation with the MADGRAPH event generator [145] (or any other UFO-supporting generator). Specifically, it calculates the UV and R_2 counterterms required in one-loop calculations. UV counterterms are essential to remove ultraviolet divergences that appear at the loop level, whereas R_2 terms originate from the one-loop integrands that carry $(n-4)$-dimensional pieces in the numerators and n-dimensional terms in the denominators. As and when required, we manually insert the R_2 terms in the NLO model as the usage of publicly-available NLOCT version is restricted to renormalisable interactions only.

MadGraph (MG5_aMC@NLO)

MG5_AMC@NLO [145] is a particle physics phenomenology framework capable of many functions. We specifically use it for event generation and showering via PYTHIA8 [151, 152]. Inside this framework, real emission corrections are performed

following the **FKS subtraction** method [146], whereas virtual corrections are done using the **OPP reduction** technique [147]. The MC@NLO formalism [148] takes care of the matching between the LO matrix element and parton shower, thus avoiding double counting, using the **MLM merging** scheme. In our study, decay of heavy bosons has been carried out with the help of MADSPIN [150].

MadSpin

MADSPIN [150] is a tool interfaced within MADGRAPH [145] used to decay narrow resonances at LO while preserving spin correlation and finite width effects to a good accuracy. It is useful for decaying resonances in events produced at NLO, as MADGRAPH alone does not allow specification of daughter particles at NLO beyond core process. For example, in our study we use MADSPIN to specify and carry out the decay of the heavy bosons. That is to say, MADSPIN allows us to specify the process $pp \to V(\ell\ell)h(b\bar{b})$ over just $pp \to Vh$.

NNPDF2.3@NLO

NNPDF2.3@NLO [144] is a library of parton distribution functions (PDFs). PDFs are probability density functions (usually obtained from experimental data) describing the probability of finding a certain parton with some momentum fraction in a given hadron. A library of PDFs, such as NNPDF, is a required input for event generation within MADGRAPH [145].

Pythia8

PYTHIA8 [151, 152] is a tool for evolving a few-body hard process to a complex multihadronic final state. We use it within the MADGRAPH [145] framework to perform parton showering, hadronisation and fragmentation.

Analysis using ROOT, HEPMC and FastJet

Our analysis is written in C++ using ROOT, HEPMC and FASTJET [153]. After event generation and parton showering, the MADGRAPH [145] framework stores the showered events in a HEPMC file (High Energy Physics Monte Carlo). This CERN-supported file format can then be read into our analysis script.

Within the analysis script we perform standard sorting and selection. This includes triggering, jet algorithms and lepton isolation. All sorting, definition and manipulation of jets is done with the help of FASTJET.

It is within this script, for example, that we demand a fatjet with two b-tagged subjets (see the **BDRS algorithm** and Section 3.5 for more details). The final events surviving all requirements fill ROOT histograms and are saved in a ROOT file, ready for further analysis (such as **BDT** fitting) and presentation.

ROOT TMVA

TMVA [154] (Toolkit for Multivariate Data Analysis) is a ROOT toolkit for machine learning and multivariate classification. We specifically use it for its **boosted decision tree** (BDT) capabilities. It takes a ROOT file as input (in our case this ROOT file is generated in the C++ analysis step from a HEPMC file) and creates a new ROOT file with the new MVA information included.

We train the BDT using a variety of kinematic parameters, while of course omitting the parameters of interest we later use in implementing the method of moments (see Section 3.4). We use the BDT to choose optimal cuts on our parameters. It has been shown in Ref. [101] that a multivariate analysis is more effective for our purposes than a simple cut-and-count analysis.

MCFM

MCFM [160–162] is a parton-level Monte Carlo program that calculates cross sections for processes at hadron colliders. Depending on the process, the cross section can be calculated to NLO or even NNLO. In our study, we use it to compute a flat K-factor for some of our background processes, which were not generated at NLO.

A.2.2 Algorithms & tools

NLO: FKS Subtraction & OPP Reduction

When extending calculations to next-to-leading order (NLO), we obtain two new contributions to the cross section on top of the Born contribution: real emissions and virtual corrections. Schematically,

$$\sigma^{\mathrm{NLO}} = \int d\Phi_{\mathcal{B}}[\mathcal{B}_n(\Phi_{\mathcal{B}}) + \mathcal{V}_n(\Phi_{\mathcal{B}})] + \int d\Phi_{\mathcal{R}}\mathcal{R}_n(\Phi_{\mathcal{R}}), \qquad (\text{A.2.1})$$

where $\mathcal{B}_n$ is the regular leading order (LO) Born contribution; $\mathcal{V}_n$ is the virtual correction coming from the addition of a closed loop; and $\mathcal{R}_n$ is the real emission correction coming from the emission of an additional particle, such as a gluon. Note that $d\Phi_{\mathcal{B}}$ is an n-body final-state phase space whereas $d\Phi_{\mathcal{R}}$ is an $(n+1)$-body final-state phase space.

Calculating loop integrals for the virtual corrections can be very complicated. A number of reduction techniques exist that decompose a more complex loop integral into a sum of simpler scalar integrals. The OPP reduction method [147] is particularly powerful as the reduction occurs at the integrand level. Our study implements the OPP reduction method within the MadGraph [145] framework.

The virtual corrections, as they are, can have UV divergences as the loop momentum can be infinitely-large. Through regularisation and renormalisation, the UV divergences can be accounted for by the addition of counterterms. In our workflow, these counterterms are calculated and included in the model using NLOCT [143].

Both virtual and real corrections experience infrared divergences. These too will be regularised but no renormalisation is needed: for physical observables the two infrared divergences must cancel each other out, due to the BN and KLN theorems (see Refs. [50, 305–307]). The difficulty in this calculation is that these divergences exist in different terms, being integrated in different phase spaces, and that the cancellation generally only occurs after integration. As a further difficulty, one cannot integrate numerically in a general D dimensions.

The standard way to deal with these problems is to use a subtraction scheme. These schemes involve the addition of two new terms: the real subtraction term, $\mathcal{S}_n$, which lives in $\Phi_\mathcal{R}$ and the integrated subtraction term, $\mathcal{I}_n$, which lives in $\Phi_\mathcal{B}$. These two terms satisfy,

$$\int d\Phi_\mathcal{B}\mathcal{I}_n(\Phi_\mathcal{B}) - \int d\Phi_\mathcal{R}\mathcal{S}_n(\Phi_\mathcal{R}) = 0. \tag{A.2.2}$$

Hence, Eq. A.2.1 can be written,

$$\sigma^{\text{NLO}} = \int d\Phi_\mathcal{B}[\mathcal{B}_n(\Phi_\mathcal{B}) + \mathcal{V}_n(\Phi_\mathcal{B}) + \mathcal{I}_n(\Phi_\mathcal{B})] + \int d\Phi_\mathcal{R}[\mathcal{R}_n(\Phi_\mathcal{R}) - \mathcal{S}_n(\Phi_\mathcal{R})]. \tag{A.2.3}$$

This idea of subtraction and the construction of these subtraction terms are the basis of subtraction algorithms. The FKS subtraction scheme [146] is one such method of numerically implementing subtraction. Our study implements the FKS method within the MadGraph [145] framework.

Jet algorithms: the Cambridge-Aachen algorithm (CA)

The Cambridge-Aachen algorithm [308, 309] is a jet clustering algorithm. As discussed in Section 2.1.1, jets are a fairly-collimated spray of hadrons resulting from final-state radiation of QCD particles produced in collisions (for more details on jets see Ref. [50]). Jet algorithms provide a way to quantitatively define jets by clustering tagged objects together.

Broadly speaking, there are two common classes of jet algorithms:

- **Cone algorithms**: These algorithms are geometrically intuitive and involve clustering objects based on their separation in the detector. A central point and jet size, R_0, are chosen. Particles within radius R_0 of the central point form part of the jet.

- k_T **algorithms**: These algorithms are rather less intuitive and involve recursive procedures. The resultant jets often have irregular shapes. The type of k_T algorithm is defined by its value of p. We define two distances in (momentum space)^{2p},

$$d_i = (k_{Ti})^{2p}, \qquad d_{ij} = \min\{d_i, d_j\}\frac{R_{ij}}{R_0}, \qquad (A.2.4)$$

  for jet size R_0; R_{ij} is the separation between particle i and particle j in the (y, ϕ) plane, where y is the rapidity and ϕ is the azimuthal angle; k_{Ti} is the transverse momentum of particle i with respect to the beam axis. As such, d_{ij} is a new measure of distance between particles i and j.

  The algorithm now iterates, with each step finding the lowest value in the full set $\{d_i, d_{ij}\}$ (i.e. for all combinations of i and j). If the minimum value is a d_i, particle i is labelled a final jet and removed. If it is a d_{ij}, particles i and j are clustered into one particle by four-vector summation. The process generally repeats until all d-values are above some critical d_c or there are no particles left. These k_T algorithms provide a weighting by some multiple of the transverse momentum. For more discussion on jet algorithms, readers are referred to Refs. [50, 310].

In our study, we focus on the Cambridge-Aachen algorithm (specifically as part of a BDRS treatment [52]), which is a k_T algorithm with $p = 0$. This makes it rather strange as a "k_T algorithm" as there is in fact no weighting by transverse momentum: $d_i = 1 \forall i$. In other words, the closest pairs of particles/objects are iteratively combined until all objects have separation $R_{ij} > R_0$.

Our jet algorithms are implemented within FASTJET [153].

Fat jets & the BDRS Algorithm

When a fast-moving Higgs undergoes $h \to b\bar{b}$ decay, a 'fatjet' is constructed containing the two b quarks. We consider one fatjet of $R = 1.2$, rather than two separate narrower ($R \sim 0.4$) b-tagged jets. This is motivated by the fact that a hard gluon may be emitted at a large angle. This hard gluon would be missed in the two-narrower-jets approach.

We utilise a slightly-modified version of the popular BDRS algorithm [52] for classifying these fat jets as $h(b\bar{b})$ jets. This procedure helps us in maximising the signal by

retaining extra radiations and in discriminating electroweak-scale resonant signals from strong QCD backgrounds, see also [156, 157].

The jets are recombined upon using the **Cambridge-Aachen algorithm** [308, 309], with a considerably large cone radius in order to contain the maximum number of decay products ensuing from a resonance. The jet clustering process is then reversed step by step until the mass of a subjet, $m_{j_1} < \mu m_j$ with $\mu = 0.66$, where m_j is the mass of the fatjet. This step is called the *mass drop* and is required to occur without a significant asymmetric splitting,

$$\frac{\min(p_{T,j_1}^2, p_{T,j_2}^2)}{m_j^2} \Delta R_{j_1,j_2}^2 > y_{\text{cut}}, \tag{A.2.5}$$

where $y_{\text{cut}} = 0.09$. When this condition is not satisfied, the softer subjet, j_2, is removed from the list and the subjets of j_1 are subjected to the aforementioned criteria. This procedure is repeated iteratively until the aforementioned condition is met. This algorithm terminates when one obtains two subjets, $j_{1,2}$ which abide by the mass drop condition.

The aim of the mass drop procedure is to identify the Higgs fatjet as the sum of two hard b-tagged subjets with separation and radius $R_{b\bar{b}} = \Delta R_{j_1,j_2}$. However, the mass drop step does not improve the resonance reconstruction significantly and more fine-tuning is necessary to segregate the signal from the background.

A further step is performed: *filtering*. In this step, the constituents of the subjets j_1 and j_2 are further recombined using the CA algorithm but with a smaller cone radius $R_{\text{filt}} = \min(0.3, R_{b\bar{b}}/2)$. This algorithm chooses only the hardest-three-filtered subjets in order to reconstruct the resonance, thus filtering away much of the underlying event contamination. As shown in Ref. [52], the filtering step significantly reduces the active area of the initial fatjet. The resonance in question is the SM-like Higgs boson and thus the hardest-two-filtered subjets are required to be *b*-tagged.

In the original paper [52], the Higgs boson is considered to have a mass of 115 GeV. In our study, we find that the filtered cone radius $R_{\text{filt}} = \max(0.2, R_{b\bar{b}}/2)$ performs better in reducing the backgrounds, see also [156, 157]. Finally, we require the hardest-two-filtered subjets to be *b*-tagged with tagging efficiencies of 70%. Moreover, the misidentification rate of light subjets faking as *b*-subjets is taken as 2%.

MLM Merging

Merging is a procedure that helps to avoid double counting between matrix element and parton showering, and construct more reliable inclusive distributions. Consider $pp \to W^+$, which in the parton showering stage will involve initial state radiation in

the form of a gluon from the initial quarks. However, the process $pp \to W^+ j$ has the same diagram at the matrix-element level. Similarly, the $pp \to W^+$ process with two gluon emissions in the parton showering stage will have a counting overlap with the process $pp \to W^+ j$ (+ 1 gluon emission from showering) and the matrix-element level $pp \to W^+ jj$ process. We need to produce reliable inclusive samples and avoid overcounting.

MLM merging [149] is a leading-order jet matching technique, which can be used within MADGRAPH [145]. The basic idea is that we make a phase space cut between the matrix-element level (ME) and parton-shower level (PS); this is the matching scale. Parton showering reliably predicts the soft collinear behaviour while the matrix-element calculation is a far better description of the harder interactions. We thus divide the phase space into a softer region and a harder region and match the two distributions at the matchings scale dividing these regions. We check that all jets after PS are matched to ME partons at this matching scale. This procedure helps regularise the soft collinear ME divergence and correct the large-momentum PS behaviour, resulting in more accurate and smooth jet distributions.

Boosted Decision Trees (BDT) & the Kolmogorov-Smirnov statistic

Decision trees are used in classification problems with binary structure [155]. An input event is determined to be signal or background based on sequential decisions made by cuts on different discrimination variables. This results in a highly-non-linear partitioning of the phase space of events into regions identified as signal or background.

Decision trees are often made more robust by 'boosting'. We use adaptive boosting, where each new tree learns from the errors made by the trees before it. Decision trees with such boosting implemented are referred to as boosted decision trees (BDTs).

It is possible for classifiers like BDTs to overtrain on a sample: this refers to when a classifier is trained to the point that it can classify the training data with excellent results but as a result fails to classify other similar samples. The classifier becomes too strict and is completely optimised for a very specific dataset. Overtraining can be avoided by ensuring the Kolmogorov-Smirnov statistic is at least $\mathcal{O}(0.1)$ [155]. The Kolmogorov-Smirnov statistic is simply a measure of the similarity between two distributions.

In our study, we implement a BDT treatment using TMVA [154], the ROOT Toolkit for Multivariate Data Analysis. TMVA also provides built in support for the Kolmogorov-Smirnov statistic.

Appendix B

Additional information from "The Coherent State Formalism"

B.1 Projection of scalar field state onto coherent state

The aim of this appendix is to derive the expression for the overlap $\langle\phi|\{a\}\rangle$ between the eigenstate of the field operator ϕ and the coherent state in a scalar QFT. We begin by inserting the coherent state definition,

$$\langle\phi|\{a\}\rangle \;=\; \langle\phi|\exp\left[\int d\mathbf{k}\, a_{\mathbf{k}}\hat{a}_{\mathbf{k}}^{\dagger}\right]|0\rangle\,, \tag{B.1.1}$$

and then representing the creation operator $\hat{a}_{\mathbf{k}}^{\dagger}$ in terms of the original field $\hat{\phi}$ and conjugate momentum $\hat{\pi} = \partial_t\hat{\phi}$ field operators in Fourier space,

$$\tilde{\hat{\phi}}(t,\mathbf{k}) := \int d^3x\, e^{-i\mathbf{k}\cdot\mathbf{x}}\,\hat{\phi}(t,\mathbf{x})\,, \qquad \tilde{\hat{\pi}}(t,\mathbf{k}) := \int d^3x\, e^{-i\mathbf{k}\cdot\mathbf{x}}\,\partial_t\hat{\phi}(t,\mathbf{x})\,. \tag{B.1.2}$$

The states in the overlap formula in Eq. B.1.1 are the eigenstates of the corresponding operators at $t = 0$,

$$\tilde{\hat{\phi}}(t=0,\mathbf{k})\,|\phi\rangle \;=\; \tilde{\phi}(0,\mathbf{k})\,|\phi\rangle\,, \quad \hat{a}_{\mathbf{k}}(t=0)\,|\{a\}\rangle \;=\; a_{\mathbf{k}}\,|\{a\}\rangle\,. \tag{B.1.3}$$

Hence we should compute the creation operators $\hat{a}_{\mathbf{k}}^{\dagger}$ in the definition of the coherent state in Eq. B.1.1 at $t = 0$. For the annihilation and creation operators we have the

standard expressions,

$$\hat{a}_{\mathbf{k}} = \sqrt{\frac{\omega_{\mathbf{k}}}{2}} \left(\hat{\tilde{\phi}}(0, \mathbf{k}) + \frac{i\hat{\tilde{\pi}}(0, \mathbf{k})}{\omega_{\mathbf{k}}} \right) ,$$

$$\hat{a}_{\mathbf{k}}^{\dagger} = (\hat{a}_{\mathbf{k}})^{\dagger} = \sqrt{\frac{\omega_{\mathbf{k}}}{2}} \left(\hat{\tilde{\phi}}(0, -\mathbf{k}) - \frac{i\hat{\tilde{\pi}}(0, -\mathbf{k})}{\omega_{\mathbf{k}}} \right) .$$

(B.1.4)

To simplify the expression for the creation operator in Eq. B.1.4 we introduce a short-hand notation,

$$\hat{\phi}_{\mathbf{k}} := \hat{\tilde{\phi}}(0, -\mathbf{k}) = \int d\mathbf{x} \, e^{i\mathbf{k}\cdot\mathbf{x}} \, \hat{\phi}(0, \mathbf{x}) , \quad \text{and} \quad \hat{\pi}_{\mathbf{k}} := \hat{\tilde{\pi}}(0, -\mathbf{k}) .$$

(B.1.5)

For the overlap in Eq. B.1.1 we have,

$$\langle \phi | \{a\} \rangle = \langle \phi | \exp \left[\int d\mathbf{k} \, a_{\mathbf{k}} \hat{a}_{\mathbf{k}}^{\dagger} \right] |0\rangle$$

$$= \langle \phi | \exp \left[\int d\mathbf{k} \, a_{\mathbf{k}} \sqrt{\omega_{\mathbf{k}}/2} \left(\hat{\phi}_{\mathbf{k}} - i\omega_{\mathbf{k}}^{-1} \hat{\pi}_{\mathbf{k}} \right) \right] |0\rangle .$$

(B.1.6)

In analogy with QM, $\phi_{\mathbf{k}}$ represents the generalised coordinate, and

$$\hat{\pi}_{\mathbf{k}} = -i \frac{\partial}{\partial \phi_{\mathbf{k}}} ,$$

(B.1.7)

is the conjugate momentum operator. Note that since $\phi(x) \in \mathbb{R}$, $\phi_{\mathbf{k}}^* = \phi_{-\mathbf{k}}$ so $|\phi_{\mathbf{k}}|^2 = \phi_{\mathbf{k}} \phi_{\mathbf{k}}^* = \phi_{\mathbf{k}} \phi_{-\mathbf{k}}$. Hence,

$$\langle \phi | \{a\} \rangle = \exp \left[\int d\mathbf{k} \, a_{\mathbf{k}} \sqrt{\omega_{\mathbf{k}}/2} \left(\phi_{\mathbf{k}} - \omega_{\mathbf{k}}^{-1} \frac{\partial}{\partial \phi_{\mathbf{k}}} \right) \right] \langle \phi | 0 \rangle$$

$$= N \exp \left[\int d\mathbf{k} \, a_{\mathbf{k}} \sqrt{\omega_{\mathbf{k}}/2} \left(\phi_{\mathbf{k}} - \omega_{\mathbf{k}}^{-1} \frac{\partial}{\partial \phi_{\mathbf{k}}} \right) \right] e^{-\int d\mathbf{p} \, \omega_{\mathbf{p}} \phi_{\mathbf{p}} \phi_{-\mathbf{p}}/2},$$

(B.1.8)

where N is some normalisation and $\langle \phi | 0 \rangle$ is analogous to $\langle q | 0 \rangle$ in QM. We now make use of the following relation,

$$e^{\hat{A}+\hat{B}} = e^{-[\hat{A},\hat{B}]/2} e^{\hat{A}} e^{\hat{B}} \quad \text{if} \quad [\hat{A}, \hat{B}] \in \mathbb{C},$$

(B.1.9)

with $\hat{A}$ and $\hat{B}$ choices,

$$\hat{A} = \int d\mathbf{k} \sqrt{\omega_{\mathbf{k}}/2} \, \hat{a}_{\mathbf{k}} \phi_{\mathbf{k}}$$

$$\hat{B} = -\int d\mathbf{p} \, \omega_{\mathbf{p}}^{-1} \sqrt{\omega_{\mathbf{p}}/2} \, \hat{a}_{\mathbf{p}} \frac{\partial}{\partial \phi_{\mathbf{p}}}.$$

(B.1.10)

Recalling that $[\phi_{\mathbf{k}}, \partial_{\phi_{\mathbf{p}}}] = -\delta^3(\mathbf{k} - \mathbf{p})$ and $\omega_{\mathbf{k}} = \omega_{-\mathbf{k}}$, we find that,

$$
\begin{aligned}
[\hat{A}, \hat{B}] &= -\frac{1}{2} \int d\mathbf{k} \, d\mathbf{p} \, a_{\mathbf{k}} a_{\mathbf{p}} \sqrt{\omega_{\mathbf{k}}/\omega_{\mathbf{p}}} [\phi_{\mathbf{k}}, \partial_{\phi_{\mathbf{p}}}] \\
&= \frac{1}{2} \int d\mathbf{k} \, d\mathbf{p} \, a_{\mathbf{k}} a_{\mathbf{p}} \sqrt{\omega_{\mathbf{k}}/\omega_{\mathbf{p}}} \delta(\mathbf{k} - \mathbf{p}) \quad\quad\quad \text{(B.1.11)} \\
&= \frac{1}{2} \int d\mathbf{k} \, a_{\mathbf{k}} a_{-\mathbf{k}}.
\end{aligned}
$$

Therefore, application of the relation in Eq. B.1.9 yields,

$$
\begin{aligned}
e^{\hat{A}+\hat{B}} &= \exp\left[\int d\mathbf{k} \, a_{\mathbf{k}} \sqrt{\omega_{\mathbf{k}}/2} \left(\phi_{\mathbf{k}} - \omega_{\mathbf{k}}^{-1} \frac{\partial}{\partial \phi_{\mathbf{k}}} \right) \right] \\
&= e^{-\frac{1}{4} \int d\mathbf{k} \, a_{\mathbf{k}} a_{-\mathbf{k}}} \exp\left(\int d\mathbf{k} \, a_{\mathbf{k}} \sqrt{\omega_{\mathbf{k}}/2} \phi_{\mathbf{k}} \right) \exp\left(-\int d\mathbf{k} \, a_{\mathbf{k}} (2\omega_{\mathbf{k}})^{-1/2} \frac{\partial}{\partial \phi_{\mathbf{k}}} \right).
\end{aligned}
$$
$$\text{(B.1.12)}$$

We note that though slightly abstract, the last term is in fact the operator for a translation in $\phi_{\mathbf{k}}$-space by $a_{\mathbf{k}}(2\omega_{\mathbf{k}})^{-1/2}$. Therefore, $\langle \phi | 0 \rangle$, has its argument shifted: $\phi_{\mathbf{k}} \to \phi_{\mathbf{k}} - a_{\mathbf{k}}(2\omega_{\mathbf{k}})^{-1/2}$, giving,

$$
\begin{aligned}
\langle \phi | \{a\} \rangle &\propto e^{-\frac{1}{4} \int d\mathbf{k} \, a_{\mathbf{k}} a_{-\mathbf{k}}} \exp\left(\int d\mathbf{k} \, a_{\mathbf{k}} \sqrt{\omega_{\mathbf{k}}/2} \phi_{\mathbf{k}} \right) \times \\
&\quad \exp\left(-\frac{1}{2} \int d\mathbf{k} \, \omega_{\mathbf{k}} (\phi_{\mathbf{k}} - a_{\mathbf{k}}(2\omega_{\mathbf{k}})^{-1/2})(\phi_{-\mathbf{k}} - a_{-\mathbf{k}}(2\omega_{\mathbf{k}})^{-1/2}) \right) \\
&\propto e^{-\frac{1}{4} \int d\mathbf{k} \, a_{\mathbf{k}} a_{-\mathbf{k}}} \exp\left(\int d\mathbf{k} \, a_{\mathbf{k}} \sqrt{\omega_{\mathbf{k}}/2} \phi_{\mathbf{k}} \right) \times \\
&\quad \exp\left(-\frac{1}{2} \int d\mathbf{k} \, \omega_{\mathbf{k}} \phi_{\mathbf{k}} \phi_{-\mathbf{k}} - \frac{1}{4} \int d\mathbf{k} \, a_{\mathbf{k}} a_{-\mathbf{k}} + \int d\mathbf{k} \sqrt{\frac{\omega_{\mathbf{k}}}{8}} [\phi_{\mathbf{k}} a_{-\mathbf{k}} + \phi_{-\mathbf{k}} a_{\mathbf{k}}] \right) \\
&\propto \exp\left(-\frac{1}{2} \int d\mathbf{k} \, a_{\mathbf{k}} a_{-\mathbf{k}} - \frac{1}{2} \int d\mathbf{k} \, \omega_{\mathbf{k}} \phi_{\mathbf{k}} \phi_{-\mathbf{k}} + \int d\mathbf{k} \sqrt{2\omega_{\mathbf{k}}} a_{\mathbf{k}} \phi_{-\mathbf{k}} \right).
\end{aligned}
$$
$$\text{(B.1.13)}$$

Recall that $\phi_{\mathbf{k}}$ is the shorthand for $\tilde{\phi}(-\mathbf{k})$, and equivalently, $\phi_{-\mathbf{k}} = \tilde{\phi}(\mathbf{k})$; with this in mind we recover the expression in Eq. 5.2.14 for the overlap $\langle \phi | \{a\} \rangle$ used in the rest of the paper.

Appendix C

Additional information from "The Semiclassical Method"

C.1 Contributions of $S[\phi]$ to saddle-point equations of $\tilde{\phi}_{i,f}$

Recall the action, $S[\phi(x)]$, in $d+1$ dimensions,

$$
\begin{aligned}
S[\phi(x)] &= \int d^{d+1}x \frac{1}{2} \left[(\partial_t \phi)^2 - |\nabla \phi|^2 - 2V(\phi) \right] \\
&= \frac{1}{2} \int_{t_i}^{t_f} dt \int d^d x [\partial_t(\phi \partial_t \phi) - \phi \partial_t^2 \phi - |\nabla \phi|^2 - 2V(\phi)].
\end{aligned}
\tag{C.1.1}
$$

Only the total derivative part of this integral,

$$
S_{\text{Boundary}}[\phi_i, \phi_f] = \frac{1}{2} \int_{t_i}^{t_f} dt \int d^d x \, \partial_t(\phi \, \partial_t \phi) = \frac{1}{2} \int d^d x \, (\phi_f \partial_t \phi_f - \phi_i \partial_t \phi_i), \quad \text{(C.1.2)}
$$

will contribute to the saddle-point equations for $\tilde{\phi}_i$ and $\tilde{\phi}_f$. Other terms on the right hand side of Eq. C.1.1 contribute instead to the ϕ equation. Focusing on the total derivative, we have,

$$
\int d\mathbf{x} \, \phi_f \partial_t \phi_f = \int d\mathbf{p} \, \tilde{\phi}_f(\mathbf{p}) \partial_t \tilde{\phi}_f(-\mathbf{p}). \tag{C.1.3}
$$

where $\partial_t \phi_f$ is $\partial_t \phi$ evaluated at time t_f (and similarly for $\partial_t \phi_i$).

Hence, the complete saddle-point equation for say $\tilde{\phi}_f$ is,

$$
i \frac{\delta S_{\text{Boundary}}[\phi_i, \phi_f]}{\delta \tilde{\phi}_f(\mathbf{k})} + \frac{\delta [B(\phi_f; b^*)]^*}{\delta \tilde{\phi}_f(\mathbf{k})} = 0. \tag{C.1.4}
$$

Using the last equation in Eq. 6.1.26 for $[B(\phi_f; b^*)]^*$, we find,

$$i\partial_t \tilde{\phi}_f(\mathbf{k}) - \omega_\mathbf{k} \tilde{\phi}_f(\mathbf{k}) + \sqrt{2\omega_\mathbf{k}} b^*_{-\mathbf{k}} e^{i\omega_\mathbf{k} t_f} = 0, \qquad (\text{C.1.5})$$

which is equivalent to the saddle-point equation (Eq. 6.1.39). The same logic can be used to recover Eq. 6.1.38.

C.2   Comments on more general saddle-points

How can one be certain that only a single semi-classical solution dominates the multi-particle rate? To address this question let us recall the defining properties of the saddle-point solution we are after.

Our specific solution to the boundary value problem in Minkowski space is character-ised by a single point-like singularity located at the origin, as shown in Fig. C.1 (a). The energy E of the solution is vanishing at all t in the interval $-\infty < t < 0$, and is non-vanishing and equal to $\sqrt{s}$ for $0 < t < +\infty$. The solution in Fig. C.1 (a) is singular at the origin, $x^\mu = 0$. This is precisely the point where the operator $\mathcal{O}^\dagger$ is located in the corresponding 'Feynman diagram' contribution to the matrix element,

$$\mathcal{M}^\dagger_{X \to n} = {}^{\text{in}}\langle X|n\rangle^{\text{out}}_{\text{1PI}} = \langle 0|\mathcal{O}^\dagger(0)\,\mathcal{S}^\dagger|n\rangle_{\text{1PI}}, \qquad (\text{C.2.1})$$

as shown schematically in Fig. C.1 (b). The presence of this point-like singularity at the origin explains the jump in the energy of the classical solution from $E = 0$ to $E = \sqrt{s}$ when time passes from $t < 0$ to $t > 0$, and in Fig. C.1 (b) it corresponds to an injection of energy $E = \sqrt{s}$ by the local operator.

One can also consider multi-centred solutions, i.e. semi-classical saddle-points ob-tained by iterating the solutions with a single singularity into more complicated saddle-points with multiple singularities. These would result in multiple jumps in energy for each time the singularity is encountered. As such, these multi-centred saddle-points would contribute to matrix elements with multiple insertions of local operators rather than the matrix element with a single $\mathcal{O}^\dagger$ in Eq. C.2.1.

Furthermore, by comparing contributions to the cross-section (i.e. to the matrix element squared) arising from the simple single-singularity solution in Fig. C.2 (a) to that of the multi-centred solution in Fig. C.2 (b), one can see that the latter contribute to one-particle reducible, rather than 1PI matrix elements.

In this work we will concentrate on the contributions to Eq. C.2.1 and will assume that the saddle-point solutions we will construct are the only saddle-points with
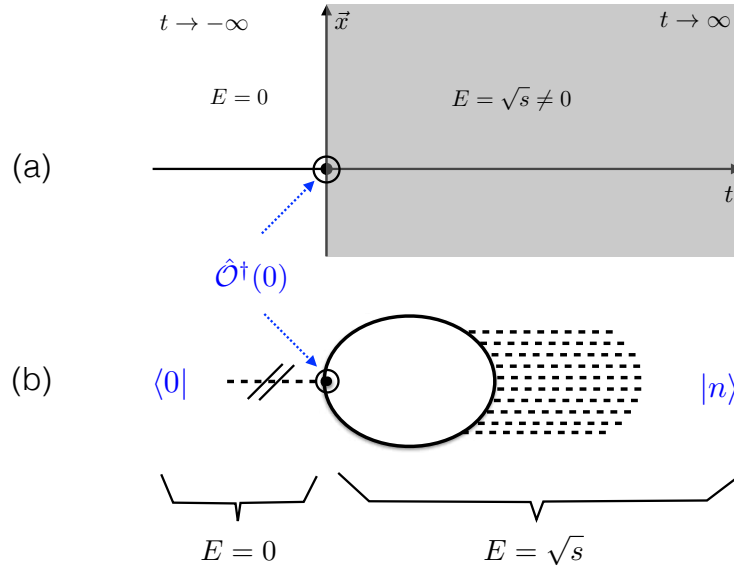
Figure C.1: *Plot (a) shows a classical field configuration with a single jump in energy at the singular point at the origin $t = 0 = \vec{x}$ in Minkowski space. Plot (b) depicts the contribution of such saddle-point configuration to the amplitude in Eq. C.2.1 using a Feynman-diagram-type representation. Saddle-point configurations with a single jump in energy contribute to the 1PI matrix elements, but not to the one-particle-reducible ones (cf. Fig. C.2 (b)).*

a single point-like singularity in Minkowski space that contribute to these matrix elements. If additional saddles of this type do exist, their contributions would have to be added to the ones we will be computing here.

C.3   Variation of the real part of the Euclidean action $\delta \mathrm{Re} S_E[\phi]$

In this appendix we derive the formula in Eq. 6.1.76. In varying the surface A, we expect the solutions to change, as well as the position of the surface,

$$
\begin{aligned}
\delta S &= S[\phi_1'(x) \, \mathrm{on} \, A'] - S[\phi_1(x) \, \mathrm{on} \, A] \\
&= \Big(S[\phi_1'(x) \, \mathrm{on} \, A'] - S[\phi_1(x) \, \mathrm{on} \, A'] \Big) + \Big(S[\phi_1(x) \, \mathrm{on} \, A'] - S[\phi_1(x) \, \mathrm{on} \, A] \Big).
\end{aligned}
$$
$$(C.3.1)$$

Hence, there will be two contributions to $\delta S_E^{(1)}[\phi_1]$:

1. First contribution to $\delta S_E^{(1)}[\phi_1]$ comes from the change $\phi_1 \to \phi_1' = \phi_1 + \delta \phi_1$ in

$$\langle 0|\hat{\mathcal{O}}^\dagger \hat{S}^\dagger \hat{P}_E |n\rangle\langle n|\hat{P}_E \hat{S}\hat{\mathcal{O}}|0\rangle$$

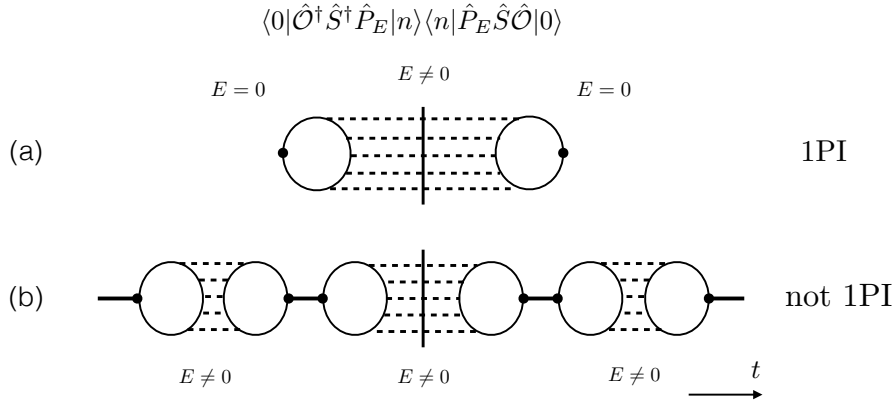**Figure C.2:** *Contributions to the n-particle rate (see Eq. 6.1.10). Plot (a) shows the one-particle-irreducible contribution to $\langle 0|\hat{\mathcal{O}}^\dagger \hat{S}^\dagger \hat{P}_E \hat{P}_n \hat{S}\hat{\mathcal{O}}|0\rangle_{1PI}$ from a saddle-point configuration with a single energy jump. Plot (b) shows one-particle-reducible contributions to the rate. They necessarily require multiple jumps from vanishing to non-vanishing energies and arise from saddle-point configurations with multiple singular points in Minkowski space.*

field solution,

$$-\int d^d x \int_\infty^{\tau_0(\mathbf{x})} d\tau\, \delta\left(\frac{1}{2}(\partial_\mu \phi_1)^2 + V(\phi_1)\right) = -\int_A ds(n^\mu \partial_\mu \phi_1)\delta\phi_1, \qquad \text{(C.3.2)}$$

which is obtained by using Gauss' theorem and the fact that $\phi_1(x)$ satisfies the Euler-Lagrange equation. We are left in Eq. C.3.2 with the boundary term, on the surface of A. Note that ds is shorthand for the appropriate d-dimensional integration measure on the d-dimensional singularity surface, for surface coordinates s_i.

2. Second contribution to $\delta S_E^{(1)}[\phi_1]$ comes from the change in the position of the surface, $x^\mu(s_i) \to x^\mu(s_i) + n^\mu \delta x(s_i)$. It is given by,

$$-\int_A ds\left[\left(\frac{1}{2}(\partial_\mu \phi_1)^2 + V(\phi_1)\right)\delta x(s)\right], \qquad \text{(C.3.3)}$$

with details in Appendix C.4.

Adding the contributions in Eqs. C.3.2 and C.3.3, we have a total variation of $S_E^{(1)}$ of,

$$\delta S_E^{(1)}[\phi_1] = -\int_A ds\left[(n^\mu \partial_\mu \phi_1)\delta\phi_1 + \left(\frac{1}{2}(\partial_\mu \phi_1)^2 + V(\phi_1)\right)\delta x(s)\right]. \qquad \text{(C.3.4)}$$

We now use the regularisation imposed in Section 6.1.3, noting that $\phi_1|_A = \phi_1'|_{A'} =$

ϕ_0,

$$\delta\phi_1(x^\mu) = \phi_1'(x^\mu) - \phi_1(x^\mu) = \phi_1'(x^\mu) - \phi_1'(x^\mu + n^\mu \delta x) = -(n^\mu \partial_\mu \phi_1)\delta x(s), \quad \text{(C.3.5)}$$

so that Eq. C.3.4 can be rewritten as,

$$\delta S_E^{(1)}[\phi_1] = \int_A ds \left[\left((n^\mu \partial_\mu \phi_1)^2 - \frac{1}{2}(\partial_\mu \phi_1)^2 - V(\phi_1)\right)\delta x(s)\right]. \quad \text{(C.3.6)}$$

Finally, recall that ϕ_1 is constant on A and thus the tangential derivative vanishes: we need only consider normal derivatives, $n^\mu \partial_\mu \phi_1 = \partial_n \phi_1$. Therefore, we find,

$$\delta S_E^{(1)}[\phi_1] = \int_A ds \left[\left(\frac{1}{2}(\partial_n \phi_1)^2 - V(\phi_1)\right)\delta x(s)\right]. \quad \text{(C.3.7)}$$

Similarly, for $S_E^{(2)}[\phi_2]$ in Eq. 6.1.71, we find,

$$\delta S_E^{(2)}[\phi_2] = -\int_A ds \left[\left(\frac{1}{2}(\partial_n \phi_2)^2 - V(\phi_2)\right)\delta x(s)\right]. \quad \text{(C.3.8)}$$

Adding these two contributions together and noting that $\phi_1 = \phi_2$ on A (but not their normal derivatives), we find,

$$\delta S_E^{(1)}[\phi_1] + \delta S_E^{(2)}[\phi_2] = \frac{1}{2}\int_A ds \left((\partial_n \phi_1)^2 - (\partial_n \phi_2)^2\right)\delta x(s). \quad \text{(C.3.9)}$$

The case for $S^{(3)}[\phi_2]$ is a little different. This third part of the integration contour does not encounter the singularity surface and thus we only expect a contribution from the change in field solution, $\phi_2 \to \phi_2 + \delta\phi_2$,

$$-i\delta S^{(3)}[\phi_2] = -i\left[\int d^d x (\hat{t}^\mu \partial_\mu \phi_2)\delta\phi_2\right]_{t=0}^{t\to\infty} = -i\int d^d x\, \partial_t \phi_2 \delta\phi_2 \bigg|_{t\to\infty}, \quad \text{(C.3.10)}$$

in a similar vein to Eq. C.3.2. The contribution from $t \to 0$ vanishes due to the equivalent relation for $\delta\phi_2$ as for $\delta\phi_1$ in Eq. C.3.5, recalling that $\delta x|_{t=0} = 0$. It will turn out that we do not need to consider this Minkowski boundary term as it is purely imaginary and thus does not appear in the $\mathrm{Im}S[\phi] \sim \mathrm{Re}S_E[\phi]$ term in Eq. 6.1.60.

Consider the above term rewritten in terms of momentum-space fields,

$$-i\int d\mathbf{x}\, \partial_t \phi_2(x)\delta\phi_2(x)\bigg|_{t\to\infty} = -i\int d\mathbf{k}\, \partial_t \tilde{\phi}_2(\mathbf{k})\delta\tilde{\phi}_2(-\mathbf{k})\bigg|_{t\to\infty}. \quad \text{(C.3.11)}$$

Inserting the late-time asymptotics (see Eq. 6.1.69) of $\tilde{\phi}_2(\mathbf{k})$ and further noticing

that, since $\tilde{\phi}_2(\mathbf{k})$ and $\tilde{\phi}_2'(\mathbf{k})$ obey the same asymptotics, so does $\delta\tilde{\phi}_2(\mathbf{k})$,

$$\delta\tilde{\phi}_2(\mathbf{k}) = \frac{1}{\sqrt{2\omega_\mathbf{k}}}(\delta b_\mathbf{k} e^{\omega_\mathbf{k}T - \theta - i\omega_\mathbf{k}t} + \delta b_{-\mathbf{k}}^* e^{i\omega_\mathbf{k}t}), \qquad t \to +\infty, \tag{C.3.12}$$

we rewrite the expression in Eq. C.3.11 as follows,

$$-i\delta S^{(3)}[\phi_2] = -i\int d\mathbf{k}\, \partial_t\tilde{\phi}_2(\mathbf{k})\delta\tilde{\phi}_2(-\mathbf{k})\Big|_{t\to\infty} = -\int d\mathbf{k}\,(b_\mathbf{k}\delta b_\mathbf{k}^* - b_\mathbf{k}^*\delta b_\mathbf{k})e^{\omega_\mathbf{k}T - \theta}, \tag{C.3.13}$$

which is purely imaginary.

Hence, Eq. C.3.13 does not contribute to the variation of the real part of the Euclidean action, which thus is given by the expression on the right-hand side of Eq. C.3.9, confirming the formula for $\delta\,\mathrm{Re}S_E[\phi]$ in Eq. 6.1.76.

C.4   Contribution to $S_E^{(1)}$ from changes to integration range

Before variation, we have,

$$S_E^{(1)} = -\int d^dx \int_\infty^{\tau_0(\mathbf{x})} d\tau\, \mathcal{L}_E(\phi_1) = -\int d^dx \int_\infty^{\tau_0(\mathbf{x})} d\tau\, \left(\frac{1}{2}(\partial_\mu\phi_1)^2 + V(\phi_1)\right). \tag{C.4.1}$$

We now consider the difference between this and the case where the singularity surface A is distorted to A', so that the spacetime coordinates describing it, $x^\mu(s_i) \to x^\mu(s_i) + n^\mu\delta x(s_i)$, where s_i are coordinates on the surface.

It is easily shown for the 1-dimensional integral, that the variation under a small shift in integration range, Δ, gives a boundary term,

$$\int_a^b [f(x + \Delta) - f(x)]dx = [f(x)\Delta]_a^b, \tag{C.4.2}$$

in the limit of small Δ. Applied to Eq. C.4.1, with $\tau_0(\mathbf{x}) \to \tau_0(\mathbf{x}) + \delta\tau_0(\mathbf{x})$, we find,

$$-\left[\int d^dx \mathcal{L}_E(\phi_1)\delta\tau_0(\mathbf{x})\right]_\infty^{\tau_0(\mathbf{x})}. \tag{C.4.3}$$

Of course, $\delta\tau_0(\mathbf{x})$ is only non-zero on surface A and so the above term can be written as an integral over the singularity surface A,

$$-\int_A ds\mathcal{L}_E(\phi_1)\delta x(s) = -\int_A ds\left[\left(\frac{1}{2}(\partial_\mu\phi_1)^2 + V(\phi_1)\right)\delta x(s)\right], \tag{C.4.4}$$

as stated in Eq. 6.1.76 in Section 6.1.3. Note that ds is shorthand for the appropriate d-dimensional integration measure on the d-dimensional singularity surface, for surface coordinates s_i.

Bibliography

[1] S. Banerjee, R. S. Gupta, J. Y. Reiness and M. Spannowsky, *Resolving the tensor structure of the Higgs coupling to Z-bosons via Higgs-strahlung*, *Phys. Rev.* **D100** (2019) 115004, [1905.02728].

[2] S. Banerjee, R. S. Gupta, J. Y. Reiness, S. Seth and M. Spannowsky, *Towards the ultimate differential SMEFT analysis*, 1912.07628.

[3] V. V. Khoze and J. Reiness, *Review of the semiclassical formalism for multiparticle production at high energies*, *Phys. Rept.* **822** (2019) 1–52, [1810.01722].

[4] V. V. Khoze, J. Reiness, M. Spannowsky and P. Waite, *Precision measurements for the Higgsploding Standard Model*, *J. Phys.* **G46** (2019) 065004, [1709.08655].

[5] R. S. Gupta, J. Y. Reiness and M. Spannowsky, *All-in-one relaxion: A unified solution to five particle-physics puzzles*, *Phys. Rev.* **D100** (2019) 055003, [1902.08633].

[6] P. A. M. Dirac and R. H. Fowler, *The quantum theory of the electron*, *Proceedings of the Royal Society of London. Series A, Containing Papers of a Mathematical and Physical Character* **117** (1928) 610–624, [https://royalsocietypublishing.org/doi/pdf/10.1098/rspa.1928.0023].

[7] S. Tomonaga, *On a Relativistically Invariant Formulation of the Quantum Theory of Wave Fields**, *Progress of Theoretical Physics* **1** (08, 1946) 27–42, [https://academic.oup.com/ptp/article-pdf/1/2/27/24027031/1-2-27.pdf].

[8] J. Schwinger, *On quantum-electrodynamics and the magnetic moment of the electron*, *Phys. Rev.* **73** (Feb, 1948) 416–417.

[9] J. Schwinger, *Quantum electrodynamics. i. a covariant formulation*, *Phys. Rev.* **74** (Nov, 1948) 1439–1461.

[10] R. P. Feynman, *Space-time approach to quantum electrodynamics*, *Phys. Rev.* **76** (Sep, 1949) 769–789.

[11] R. P. Feynman, *The theory of positrons*, *Phys. Rev.* **76** (Sep, 1949) 749–759.

[12] R. P. Feynman, *Mathematical formulation of the quantum theory of electromagnetic interaction*, *Phys. Rev.* **80** (Nov, 1950) 440–457.

[13] F. Englert and R. Brout, *Broken symmetry and the mass of gauge vector mesons*, Phys. Rev. Lett. **13** (Aug, 1964) 321–323.

[14] P. W. Higgs, *Broken symmetries and the masses of gauge bosons*, Phys. Rev. Lett. **13** (Oct, 1964) 508–509.

[15] G. S. Guralnik, C. R. Hagen and T. W. B. Kibble, *Global conservation laws and massless particles*, Phys. Rev. Lett. **13** (Nov, 1964) 585–587.

[16] S. Glashow, *Partial symmetries of weak interactions*, Nucl.Phys. **22** (1961) 579–588.

[17] S. Weinberg, *A model of leptons*, Phys. Rev. Lett. **19** (Nov, 1967) 1264–1266.

[18] H. Fritzsch, M. Gell-Mann and H. Leutwyler, *Advantages of the color octet gluon picture*, Phys.Lett.B **47** (1973) 365–368.

[19] D. J. Gross and F. Wilczek, *Ultraviolet behavior of non-abelian gauge theories*, Phys. Rev. Lett. **30** (Jun, 1973) 1343–1346.

[20] H. D. Politzer, *Reliable perturbative results for strong interactions?*, Phys. Rev. Lett. **30** (Jun, 1973) 1346–1349.

[21] M. E. Peskin and D. V. Schroeder, *An Introduction to quantum field theory.* Addison-Wesley, Reading, USA, 1995.

[22] M. D. Schwartz, *Quantum Field Theory and the Standard Model.* Cambridge University Press, 2014.

[23] M. Srednicki, *Quantum field theory.* Cambridge University Press, 2007.

[24] S. Weinberg, *The quantum theory of fields. Vol. 3: Supersymmetry.* Cambridge University Press, 2013.

[25] H. E. Logan, *TASI 2013 lectures on Higgs physics within and beyond the Standard Model*, `1406.1786`.

[26] G. S. Guralnik, C. R. Hagen and T. W. B. Kibble, *Global Conservation Laws and Massless Particles*, Phys. Rev. Lett. **13** (1964) 585–587.

[27] P. W. Higgs, *Spontaneous symmetry breakdown without massless bosons*, Phys. Rev. **145** (May, 1966) 1156–1163.

[28] T. W. B. Kibble, *Symmetry breaking in non-abelian gauge theories*, Phys. Rev. **155** (Mar, 1967) 1554–1561.

[29] A. Akeroyd and S. Moretti, *Enhancement of H to gamma gamma from doubly charged scalars in the Higgs Triplet Model*, Phys. Rev. D **86** (2012) 035015, [`1206.0535`].

[30] P. J. E. Peebles and B. Ratra, *The cosmological constant and dark energy*, Reviews of Modern Physics **75** (Apr, 2003) 559–606.

[31] K. S. Babu, *TASI Lectures on Flavor Physics*, in *Proceedings of Theoretical Advanced Study Institute in Elementary Particle Physics on The dawn of the LHC era (TASI 2008): Boulder, USA, June 2-27, 2008*, pp. 49–123, 2010, `0910.2948`, DOI.

[32] J. M. Cornwall, D. N. Levin and G. Tiktopoulos, *Derivation of gauge invariance from high-energy unitarity bounds on the s matrix*, *Phys. Rev. D* **10** (Aug, 1974) 1145–1167.

[33] C. E. Vayonakis, *Born Helicity Amplitudes and Cross-Sections in Nonabelian Gauge Theories*, *Lett. Nuovo Cim.* **17** (1976) 383.

[34] I. Brivio, T. Corbett, O. Éboli, M. Gavela, J. Gonzalez-Fraile, M. Gonzalez-Garcia et al., *Disentangling a dynamical higgs*, *JHEP* **03** (2014) 024, [`1311.1823`].

[35] T. Cohen, *As scales become separated: Lectures on effective field theory*, 2019.

[36] C. Csáki and P. Tanedo, *Beyond the Standard Model*, in *Proceedings, 2013 European School of High-Energy Physics (ESHEP 2013): Paradfurdo, Hungary, June 5-18, 2013*, pp. 169–268, 2015, `1602.04228`, DOI.

[37] S. P. Martin, *A Supersymmetry primer*, `hep-ph/9709356`.

[38] L. Randall and R. Sundrum, *Large mass hierarchy from a small extra dimension*, *Physical Review Letters* **83** (Oct, 1999) 3370–3373.

[39] C. Autermann, *Experimental status of supersymmetry after the LHC Run-I*, *Prog. Part. Nucl. Phys.* **90** (2016) 125–155, [`1609.01686`].

[40] G. F. Giudice, *Naturally speaking: The naturalness criterion and physics at the lhc*, *Perspectives on LHC Physics* (Jun, 2008) 155–178.

[41] S. Mukhi, *String theory: a perspective over the last 25 years*, *Class. Quant. Grav.* **28** (2011) 153001, [`1110.2569`].

[42] V. V. Khoze and M. Spannowsky, *Higgsploding universe*, *Phys. Rev.* **D96** (2017) 075042, [`1707.01531`].

[43] V. V. Khoze and M. Spannowsky, *Higgsplosion: Solving the Hierarchy Problem via rapid decays of heavy states into multiple Higgs bosons*, *Nucl. Phys.* **B926** (2018) 95–111, [`1704.03447`].

[44] P. W. Graham, D. E. Kaplan and S. Rajendran, *Cosmological Relaxation of the Electroweak Scale*, *Phys. Rev. Lett.* **115** (2015) 221801, [`1504.07551`].

[45] CMS collaboration, S. Chatrchyan et al., *Observation of a new boson at a mass of 125 GeV with the CMS experiment at the LHC*, *Phys. Lett.* **B716** (2012) 30–61, [`1207.7235`].

[46] ATLAS collaboration, G. Aad et al., *Observation of a new particle in the search for the Standard Model Higgs boson with the ATLAS detector at the LHC*, *Phys. Lett.* **B716** (2012) 1–29, [`1207.7214`].

[47] CDF, D0 collaboration, G. J. Davies, *Higgs boson searches at the tevatron,*
Front.Phys.(Beijing) **8** (2013) 270–284.

[48] CDF, D0 collaboration, T. Aaltonen et al., *Evidence for a particle produced*
in association with weak bosons and decaying to a bottom-antibottom quark
pair in higgs boson searches at the tevatron, Phys.Rev.Lett. **109** (2012)
071804, [`1207.6436`].

[49] M. Cepeda et al., *Report from Working Group 2, CERN Yellow Rep. Monogr.*
7 (2019) 221–584, [`1902.00134`].

[50] J. Campbell, J. Huston and F. Krauss, *The black book of quantum*
chromodynamics: a primer for the LHC era. Oxford University Press, Oxford,
2018, 10.1093/oso/9780199652747.001.0001.

[51] T. Han, *Collider phenomenology: Basic knowledge and techniques*, in *Physics*
in D >= 4. Proceedings, Theoretical Advanced Study Institute in elementary
particle physics, TASI 2004, Boulder, USA, June 6-July 2, 2004, pp. 407–454,
2005, `hep-ph/0508097`, DOI.

[52] J. M. Butterworth, A. R. Davison, M. Rubin and G. P. Salam, *Jet*
substructure as a new Higgs search channel at the LHC, Phys. Rev. Lett. **100**
(2008) 242001, [`0802.2470`].

[53] ATLAS collaboration, M. Aaboud et al., *Measurement of the Higgs boson*
mass in the $H \to ZZ^* \to 4\ell$ and $H \to \gamma\gamma$ channels with $\sqrt{s} = 13$ TeV pp
collisions using the ATLAS detector, Phys. Lett. **B784** (2018) 345–366,
[`1806.00242`].

[54] LHC HIGGS CROSS SECTION WORKING GROUP collaboration, J. R.
Andersen et al., *Handbook of LHC Higgs Cross Sections: 3. Higgs Properties*,
`1307.1347`.

[55] ATLAS collaboration, G. Aad et al., *Combined measurements of Higgs boson*
production and decay using up to 80 fb^{-1} of proton-proton collision data at
$\sqrt{s} = 13$ TeV collected with the ATLAS experiment, Phys. Rev. **D101** (2020)
012002, [`1909.02845`].

[56] FCC collaboration, A. Abada et al., *FCC Physics Opportunities, Eur. Phys.*
J. **C79** (2019) 474.

[57] FCC collaboration, A. Abada et al., *HE-LHC: The High-Energy Large*
Hadron Collider, Eur. Phys. J. ST **228** (2019) 1109–1382.

[58] FCC collaboration, A. Abada et al., *FCC-ee: The Lepton Collider, Eur.*
Phys. J. ST **228** (2019) 261–623.

[59] ATLAS COLLABORATION collaboration, *Combined measurements of Higgs*
boson production and decay using up to 80 fb^{-1} of proton–proton collision
data at $\sqrt{s} = 13$ TeV collected with the ATLAS experiment, Tech. Rep.
ATLAS-CONF-2018-031, CERN, Geneva, Jul, 2018.

[60] CMS collaboration, A. M. Sirunyan et al., *Combined measurements of Higgs boson couplings in proton-proton collisions at $\sqrt{s}$ = 13 TeV, Submitted to: Eur. Phys. J.* (2018) , [`1809.10733`].

[61] G. Panico, F. Riva and A. Wulzer, *Diboson Interference Resurrection, Phys. Lett.* **B776** (2018) 473–480, [`1708.07823`].

[62] T. Appelquist and J. Carazzone, *Infrared singularities and massive fields, Phys. Rev. D* **11** (May, 1975) 2856–2861.

[63] H. Georgi, *Effective field theory, Ann. Rev. Nucl. Part. Sci.* **43** (1993) 209–252.

[64] C. P. Burgess, *Introduction to Effective Field Theory, Ann. Rev. Nucl. Part. Sci.* **57** (2007) 329–362, [`hep-th/0701053`].

[65] W. Skiba, *Effective Field Theory and Precision Electroweak Measurements*, in *Physics of the large and the small, TASI 09, proceedings of the Theoretical Advanced Study Institute in Elementary Particle Physics, Boulder, Colorado, USA, 1-26 June 2009*, pp. 5–70, 2011, `1006.2142`, DOI.

[66] A. Lenz, *Lifetimes and heavy quark expansion, Int. J. Mod. Phys.* **A30** (2015) 1543005, [`1405.3601`].

[67] B. Grzadkowski, M. Iskrzynski, M. Misiak and J. Rosiek, *Dimension-Six Terms in the Standard Model Lagrangian, JHEP* **10** (2010) 085, [`1008.4884`].

[68] W. Buchmüller and D. Wyler, *Effective lagrangian analysis of new interactions and flavour conservation, Nuclear Physics B* **268** (1986) 621 – 653.

[69] R. Alonso, E. E. Jenkins, A. V. Manohar and M. Trott, *Renormalization Group Evolution of the Standard Model Dimension Six Operators III: Gauge Coupling Dependence and Phenomenology, JHEP* **04** (2014) 159, [`1312.2014`].

[70] G. F. Giudice, C. Grojean, A. Pomarol and R. Rattazzi, *The Strongly-Interacting Light Higgs, JHEP* **06** (2007) 045, [`hep-ph/0703164`].

[71] K. Hagiwara, S. Ishihara, R. Szalapski and D. Zeppenfeld, *Low energy effects of new interactions in the electroweak boson sector, Phys. Rev. D* **48** (Sep, 1993) 2182–2203.

[72] A. Dedes, W. Materkowska, M. Paraskevas, J. Rosiek and K. Suxho, *Feynman rules for the Standard Model Effective Field Theory in Rxi-gauges, JHEP* **06** (2017) 143, [`1704.03888`].

[73] R. S. Gupta, A. Pomarol and F. Riva, *BSM Primary Effects, Phys. Rev.* **D91** (2015) 035001, [`1405.0181`].

[74] R. Gauld, B. D. Pecjak and D. J. Scott, *One-loop corrections to $h \to b\bar{b}$ and $h \to \tau\bar{\tau}$ decays in the Standard Model Dimension-6 EFT: four-fermion operators and the large-m_t limit, JHEP* **05** (2016) 080, [`1512.02508`].

[75] J. M. Cullen, B. D. Pecjak and D. J. Scott, *NLO corrections to $h \to b\bar{b}$ decay in SMEFT*, *JHEP* **08** (2019) 173, [1904.06358].

[76] J. Elias-Miró, C. Grojean, R. S. Gupta and D. Marzocca, *Scaling and tuning of EW and Higgs observables*, *JHEP* **05** (2014) 019, [1312.2928].

[77] E. E. Jenkins, A. V. Manohar and M. Trott, *Renormalization Group Evolution of the Standard Model Dimension Six Operators I: Formalism and lambda Dependence*, *JHEP* **10** (2013) 087, [1308.2627].

[78] W. Buchmuller and D. Wyler, *Effective Lagrangian Analysis of New Interactions and Flavor Conservation*, *Nucl. Phys.* **B268** (1986) 621–653.

[79] S. Banerjee, S. Mukhopadhyay and B. Mukhopadhyaya, *New Higgs interactions and recent data from the LHC and the Tevatron*, *JHEP* **10** (2012) 062, [1207.3588].

[80] S. Banerjee, S. Mukhopadhyay and B. Mukhopadhyaya, *Higher dimensional operators and the LHC Higgs data: The role of modified kinematics*, *Phys. Rev.* **D89** (2014) 053010, [1308.4860].

[81] R. Contino, M. Ghezzi, C. Grojean, M. Muhlleitner and M. Spira, *Effective Lagrangian for a light Higgs-like scalar*, *JHEP* **07** (2013) 035, [1303.3876].

[82] C. Englert and M. Spannowsky, *Effective Theories and Measurements at Colliders*, *Phys. Lett.* **B740** (2015) 8–15, [1408.5147].

[83] G. Amar, S. Banerjee, S. von Buddenbrock, A. S. Cornell, T. Mandal, B. Mellado et al., *Exploration of the tensor structure of the Higgs boson coupling to weak bosons in $e^+ e^-$ collisions*, *JHEP* **02** (2015) 128, [1405.3957].

[84] M. Buschmann, D. Goncalves, S. Kuttimalai, M. Schonherr, F. Krauss and T. Plehn, *Mass Effects in the Higgs-Gluon Coupling: Boosted vs Off-Shell Production*, *JHEP* **02** (2015) 038, [1410.5806].

[85] N. Craig, M. Farina, M. McCullough and M. Perelstein, *Precision Higgsstrahlung as a Probe of New Physics*, *JHEP* **03** (2015) 146, [1411.0676].

[86] J. Ellis, V. Sanz and T. You, *Complete Higgs Sector Constraints on Dimension-6 Operators*, *JHEP* **07** (2014) 036, [1404.3667].

[87] J. Ellis, V. Sanz and T. You, *The Effective Standard Model after LHC Run I*, *JHEP* **03** (2015) 157, [1410.7703].

[88] S. Banerjee, T. Mandal, B. Mellado and B. Mukhopadhyaya, *Cornering dimension-6 HVV interactions at high luminosity LHC: the role of event ratios*, *JHEP* **09** (2015) 057, [1505.00226].

[89] C. Englert, R. Kogler, H. Schulz and M. Spannowsky, *Higgs coupling measurements at the LHC*, *Eur. Phys. J.* **C76** (2016) 393, [1511.05170].

[90] J. Cohen, S. Bar-Shalom and G. Eilam, *Contact Interactions in Higgs-Vector Boson Associated Production at the ILC*, *Phys. Rev.* **D94** (2016) 035030, [1602.01698].

[91] S.-F. Ge, H.-J. He and R.-Q. Xiao, *Probing new physics scales from Higgs and electroweak observables at e^+ e^- Higgs factory*, *JHEP* **10** (2016) 007, [1603.03385].

[92] R. Contino, A. Falkowski, F. Goertz, C. Grojean and F. Riva, *On the Validity of the Effective Field Theory Approach to SM Precision Tests*, *JHEP* **07** (2016) 144, [1604.06444].

[93] A. Biekötter, J. Brehmer and T. Plehn, *Extending the limits of Higgs effective theory*, *Phys. Rev.* **D94** (2016) 055032, [1602.05202].

[94] J. de Blas, M. Ciuchini, E. Franco, S. Mishima, M. Pierini, L. Reina et al., *Electroweak precision observables and Higgs-boson signal strengths in the Standard Model and beyond: present and future*, *JHEP* **12** (2016) 135, [1608.01509].

[95] H. Denizli and A. Senol, *Constraints on Higgs effective couplings in $H\nu\bar{\nu}$ production of CLIC at 380 GeV*, *Adv. High Energy Phys.* **2018** (2018) 1627051, [1707.03890].

[96] T. Barklow, K. Fujii, S. Jung, R. Karl, J. List, T. Ogawa et al., *Improved Formalism for Precision Higgs Coupling Fits*, *Phys. Rev.* **D97** (2018) 053003, [1708.08912].

[97] I. Brivio and M. Trott, *The Standard Model as an Effective Field Theory*, *Phys. Rept.* **793** (2019) 1–98, [1706.08945].

[98] T. Barklow, K. Fujii, S. Jung, M. E. Peskin and J. Tian, *Model-Independent Determination of the Triple Higgs Coupling at e+e- Colliders*, *Phys. Rev.* **D97** (2018) 053004, [1708.09079].

[99] H. Khanpour and M. Mohammadi Najafabadi, *Constraining Higgs boson effective couplings at electron-positron colliders*, *Phys. Rev.* **D95** (2017) 055026, [1702.00951].

[100] C. Englert, R. Kogler, H. Schulz and M. Spannowsky, *Higgs characterisation in the presence of theoretical uncertainties and invisible decays*, *Eur. Phys. J.* **C77** (2017) 789, [1708.06355].

[101] S. Banerjee, C. Englert, R. S. Gupta and M. Spannowsky, *Probing Electroweak Precision Physics via boosted Higgs-strahlung at the LHC*, *Phys. Rev.* **D98** (2018) 095012, [1807.01796].

[102] A. Biekötter, T. Corbett and T. Plehn, *The Gauge-Higgs Legacy of the LHC Run II*, 1812.07587.

[103] D. Goncalves and J. Nakamura, *Boosting the $H \to$ invisibles searches with Z boson polarization*, *Phys. Rev.* **D99** (2019) 055021, [1809.07327].

[104] F. F. Freitas, C. K. Khosa and V. Sanz, *Exploring SMEFT in VH with Machine Learning*, `1902.05803`.

[105] A. Azatov, R. Contino, C. S. Machado and F. Riva, *Helicity selection rules and noninterference for BSM amplitudes*, *Phys. Rev.* **D95** (2017) 065014, [`1607.05236`].

[106] K. Hagiwara, R. D. Peccei, D. Zeppenfeld and K. Hikasa, *Probing the Weak Boson Sector in e+ e- —> W+ W-*, *Nucl. Phys.* **B282** (1987) 253–307.

[107] A. Azatov, R. Contino, C. S. Machado and F. Riva, *Helicity selection rules and noninterference for BSM amplitudes*, *Phys. Rev.* **D95** (2017) 065014, [`1607.05236`].

[108] G. Panico, F. Riva and A. Wulzer, *Diboson Interference Resurrection*, *Phys. Lett.* **B776** (2018) 473–480, [`1708.07823`].

[109] A. Azatov, J. Elias-Miro, Y. Reyimuaji and E. Venturini, *Novel measurements of anomalous triple gauge couplings for the LHC*, *JHEP* **10** (2017) 027, [`1707.08060`].

[110] B. Bellazzini and F. Riva, *New phenomenological and theoretical perspective on anomalous ZZ and Z? processes*, *Phys. Rev.* **D98** (2018) 095021, [`1806.09640`].

[111] B. Henning and T. Melia, *Constructing effective field theories via their harmonics*, *Phys. Rev.* **D100** (2019) 016015, [`1902.06754`].

[112] I. Dunietz, H. R. Quinn, A. Snyder, W. Toki and H. J. Lipkin, *How to extract CP violating asymmetries from angular correlations*, *Phys. Rev.* **D43** (1991) 2193–2208.

[113] A. S. Dighe, I. Dunietz and R. Fleischer, *Extracting CKM phases and $B_s - \bar{B}_s$ mixing parameters from angular distributions of nonleptonic B decays*, *Eur. Phys. J.* **C6** (1999) 647–662, [`hep-ph/9804253`].

[114] F. James, *Statistical methods in experimental physics*. World Scientific Singapore, 2006.

[115] F. Beaujean, M. Chrzaszcz, N. Serra and D. van Dyk, *Extracting Angular Observables without a Likelihood and Applications to Rare Decays*, *Phys. Rev.* **D91** (2015) 114012, [`1503.04100`].

[116] B. Grzadkowski, Z. Hioki, K. Ohkuma and J. Wudka, *Optimal-observable analysis of possible new physics using the b quark in gamma gamma —> t anti-t —> bX*, *Phys. Lett.* **B593** (2004) 189–197, [`hep-ph/0403174`].

[117] R. M. Godbole, D. J. Miller and M. M. Muhlleitner, *Aspects of CP violation in the H ZZ coupling at the LHC*, *JHEP* **12** (2007) 031, [`0708.0458`].

[118] R. Godbole, D. J. Miller, K. Mohan and C. D. White, *Boosting Higgs CP properties via VH Production at the Large Hadron Collider*, *Phys. Lett.* **B730** (2014) 275–279, [`1306.2573`].

[119] R. M. Godbole, D. J. Miller, K. A. Mohan and C. D. White, *Jet substructure and probes of CP violation in Vh production*, *JHEP* **04** (2015) 103, [1409.5449].

[120] J. Gratrex, M. Hopfer and R. Zwicky, *Generalised helicity formalism, higher moments and the $B \to K_{J_K}(\to K\pi)\bar{\ell}_1 \ell_2$ angular distributions*, *Phys. Rev.* **D93** (2016) 054008, [1506.03970].

[121] K. Kondo, *Dynamical Likelihood Method for Reconstruction of Events With Missing Momentum. 1: Method and Toy Models*, *J. Phys. Soc. Jap.* **57** (1988) 4126–4140.

[122] J. S. Gainer, J. Lykken, K. T. Matchev, S. Mrenna and M. Park, *The Matrix Element Method: Past, Present, and Future*, in *Proceedings, 2013 Community Summer Study on the Future of U.S. Particle Physics: Snowmass on the Mississippi (CSS2013): Minneapolis, MN, USA, July 29-August 6, 2013*, 2013, 1307.3546, http://www.slac.stanford.edu/econf/C1307292/docs/submittedArxivFiles/1307.3546.pdf.

[123] D. E. Soper and M. Spannowsky, *Finding physics signals with event deconstruction*, *Phys. Rev.* **D89** (2014) 094005, [1402.1189].

[124] S. Prestel and M. Spannowsky, *HYTREES: Combining Matrix Elements and Parton Shower for Hypothesis Testing*, *Eur. Phys. J.* **C79** (2019) 546, [1901.11035].

[125] J. Brehmer, K. Cranmer, F. Kling and T. Plehn, *Better Higgs boson measurements through information geometry*, *Phys. Rev.* **D95** (2017) 073002, [1612.05261].

[126] J. Brehmer, K. Cranmer, G. Louppe and J. Pavez, *Constraining Effective Field Theories with Machine Learning*, *Phys. Rev. Lett.* **121** (2018) 111801, [1805.00013].

[127] C. Englert, P. Galler, P. Harris and M. Spannowsky, *Machine Learning Uncertainties with Adversarial Neural Networks*, *Eur. Phys. J.* **C79** (2019) 4, [1807.08763].

[128] R. T. D'Agnolo and A. Wulzer, *Learning New Physics from a Machine*, *Phys. Rev.* **D99** (2019) 015014, [1806.02350].

[129] CMS collaboration, S. Chatrchyan et al., *Observation of a new boson at a mass of 125 GeV with the CMS experiment at the LHC*, *Phys. Lett.* **B716** (2012) 30–61, [1207.7235].

[130] A. Pomarol, *Higgs Physics*, in *Proceedings, 2014 European School of High-Energy Physics (ESHEP 2014): Garderen, The Netherlands, June 18 - July 01 2014*, pp. 59–77, 2016, 1412.4410, http://inspirehep.net/record/1334375/files/arXiv:1412.4410.pdf.

[131] A. Pomarol and F. Riva, *Towards the Ultimate SM Fit to Close in on Higgs Physics*, *JHEP* **01** (2014) 151, [1308.2803].

[132] A. Falkowski and F. Riva, *Model-independent precision constraints on dimension-6 operators*, *JHEP* **02** (2015) 039, [`1411.0669`].

[133] G. D'Ambrosio, G. F. Giudice, G. Isidori and A. Strumia, *Minimal flavor violation: An Effective field theory approach*, *Nucl. Phys.* **B645** (2002) 155–187, [`hep-ph/0207036`].

[134] G. Isidori and M. Trott, *Higgs form factors in Associated Production*, *JHEP* **02** (2014) 082, [`1307.4051`].

[135] G. Gounaris, J. L. Kneur, D. Zeppenfeld, Z. Ajaltouni, A. Arhrib, G. Bella et al., *Triple gauge boson couplings*, 1996.

[136] R. Franceschini, G. Panico, A. Pomarol, F. Riva and A. Wulzer, *Electroweak Precision Tests in High-Energy Diboson Processes*, *JHEP* **02** (2018) 111, [`1712.01310`].

[137] J. Nakamura, *Polarisations of the Z and W bosons in the processes $pp \to ZH$ and $pp \to W^{\pm}H$*, *JHEP* **08** (2017) 008, [`1706.01816`].

[138] J. C. Collins and D. E. Soper, *Angular Distribution of Dileptons in High-Energy Hadron Collisions*, *Phys. Rev.* **D16** (1977) 2219.

[139] K. Hagiwara, K.-i. Hikasa and N. Kai, *Parity Odd Asymmetries in W Jet Events at Hadron Colliders*, *Phys. Rev. Lett.* **52** (1984) 1076.

[140] V. D. Barger, K.-m. Cheung, A. Djouadi, B. A. Kniehl and P. M. Zerwas, *Higgs bosons: Intermediate mass range at e+ e- colliders*, *Phys. Rev.* **D49** (1994) 79–90, [`hep-ph/9306270`].

[141] C. Delaunay, G. Perez, H. de Sandes and W. Skiba, *Higgs Up-Down CP Asymmetry at the LHC*, *Phys. Rev.* **D89** (2014) 035004, [`1308.4930`].

[142] A. Alloul, N. D. Christensen, C. Degrande, C. Duhr and B. Fuks, *FeynRules 2.0 - A complete toolbox for tree-level phenomenology*, *Comput. Phys. Commun.* **185** (2014) 2250–2300, [`1310.1921`].

[143] C. Degrande, *Automatic evaluation of UV and R2 terms for beyond the Standard Model Lagrangians: a proof-of-principle*, *Comput. Phys. Commun.* **197** (2015) 239–262, [`1406.3030`].

[144] R. D. Ball et al., *Parton distributions with LHC data*, *Nucl. Phys.* **B867** (2013) 244–289, [`1207.1303`].

[145] J. Alwall, R. Frederix, S. Frixione, V. Hirschi, F. Maltoni, O. Mattelaer et al., *The automated computation of tree-level and next-to-leading order differential cross sections, and their matching to parton shower simulations*, *JHEP* **07** (2014) 079, [`1405.0301`].

[146] S. Frixione, Z. Kunszt and A. Signer, *Three jet cross-sections to next-to-leading order*, *Nucl. Phys.* **B467** (1996) 399–442, [`hep-ph/9512328`].

[147] G. Ossola, C. G. Papadopoulos and R. Pittau, *Reducing full one-loop amplitudes to scalar integrals at the integrand level*, *Nucl. Phys.* **B763** (2007) 147–169, [`hep-ph/0609007`].

[148] S. Frixione and B. R. Webber, *Matching NLO QCD computations and parton shower simulations*, *JHEP* **06** (2002) 029, [`hep-ph/0204244`].

[149] M. L. Mangano, M. Moretti, F. Piccinini and M. Treccani, *Matching matrix elements and shower evolution for top-quark production in hadronic collisions*, *JHEP* **01** (2007) 013, [`hep-ph/0611129`].

[150] P. Artoisenet, R. Frederix, O. Mattelaer and R. Rietkerk, *Automatic spin-entangled decays of heavy resonances in Monte Carlo simulations*, *JHEP* **03** (2013) 015, [`1212.3460`].

[151] T. Sjostrand, L. Lonnblad and S. Mrenna, *PYTHIA 6.2: Physics and manual*, `hep-ph/0108264`.

[152] T. Sjöstrand, S. Ask, J. R. Christiansen, R. Corke, N. Desai, P. Ilten et al., *An Introduction to PYTHIA 8.2*, *Comput. Phys. Commun.* **191** (2015) 159–177, [`1410.3012`].

[153] M. Cacciari, G. P. Salam and G. Soyez, *FastJet User Manual*, *Eur. Phys. J.* **C72** (2012) 1896, [`1111.6097`].

[154] A. Hoecker, P. Speckmayer, J. Stelzer, J. Therhaag, E. von Toerne, H. Voss et al., *TMVA - Toolkit for Multivariate Data Analysis*, *ArXiv Physics e-prints* (Mar., 2007) , [`physics/0703039`].

[155] D. Ciupke, *Study of BDT Training Configurations with an Application to the $Z/H \to \tau\tau \to ee$ Analysis*, .

[156] D. E. Soper and M. Spannowsky, *Combining subjet algorithms to enhance ZH detection at the LHC*, *JHEP* **08** (2010) 029, [`1005.0417`].

[157] D. E. Soper and M. Spannowsky, *Finding physics signals with shower deconstruction*, *Phys. Rev.* **D84** (2011) 074002, [`1102.3480`].

[158] S. Alioli, F. Caola, G. Luisoni and R. Röntsch, *ZZ production in gluon fusion at NLO matched to parton-shower*, *Phys. Rev.* **D95** (2017) 034042, [`1609.09719`].

[159] L. Altenkamp, S. Dittmaier, R. V. Harlander, H. Rzehak and T. J. E. Zirke, *Gluon-induced Higgs-strahlung at next-to-leading order QCD*, *JHEP* **02** (2013) 078, [`1211.5015`].

[160] J. M. Campbell and R. K. Ellis, *An Update on vector boson pair production at hadron colliders*, *Phys. Rev.* **D60** (1999) 113006, [`hep-ph/9905386`].

[161] J. M. Campbell, R. K. Ellis and C. Williams, *Vector boson pair production at the LHC*, *JHEP* **07** (2011) 018, [`1105.0020`].

[162] J. M. Campbell, R. K. Ellis and W. T. Giele, *A Multi-Threaded Version of MCFM*, *Eur. Phys. J.* **C75** (2015) 246, [1503.06182].

[163] I. Anderson et al., *Constraining Anomalous HVV Interactions at Proton and Lepton Colliders*, *Phys. Rev.* **D89** (2014) 035007, [1309.4819].

[164] C. Grojean, M. Montull and M. Riembau, *Diboson at the lhc vs lep*, *JHEP* **03** (2019) 020, [1810.05149].

[165] N. Berger et al., *Simplified Template Cross Sections - Stage 1.1*, 1906.02754.

[166] A. Monin, *Inconsistencies of higgsplosion*, 1808.05810.

[167] V. V. Khoze and M. Spannowsky, *Consistency of Higgsplosion in Localizable QFT*, 1809.11141.

[168] D. T. Son, *Semiclassical approach for multiparticle production in scalar theories*, *Nucl. Phys.* **B477** (1996) 378–406, [hep-ph/9505338].

[169] V. V. Khoze, *Semiclassical computation of quantum effects in multiparticle production at large lambda n*, 1806.05648.

[170] V. V. Khoze, *Multiparticle production in the large λn limit: realising Higgsplosion in a scalar QFT*, *JHEP* **06** (2017) 148, [1705.04365].

[171] J. M. Cornwall, *On the High-energy Behavior of Weakly Coupled Gauge Theories*, *Phys. Lett.* **B243** (1990) 271–278.

[172] H. Goldberg, *Breakdown of perturbation theory at tree level in theories with scalars*, *Phys. Lett.* **B246** (1990) 445–450.

[173] L. S. Brown, *Summing tree graphs at threshold*, *Phys. Rev.* **D46** (1992) R4125–R4127, [hep-ph/9209203].

[174] E. N. Argyres, R. H. P. Kleiss and C. G. Papadopoulos, *Amplitude estimates for multi - Higgs production at high-energies*, *Nucl. Phys.* **B391** (1993) 42–56.

[175] M. B. Voloshin, *Estimate of the onset of nonperturbative particle production at high-energy in a scalar theory*, *Phys. Lett.* **B293** (1992) 389–394.

[176] M. B. Voloshin, *Summing one loop graphs at multiparticle threshold*, *Phys. Rev.* **D47** (1993) R357–R361, [hep-ph/9209240].

[177] B. H. Smith, *Summing one loop graphs in a theory with broken symmetry*, *Phys. Rev.* **D47** (1993) 3518–3520, [hep-ph/9209287].

[178] E. N. Argyres, R. H. P. Kleiss and C. G. Papadopoulos, *Multiscalar amplitudes to all orders in perturbation theory*, *Phys. Lett.* **B308** (1993) 292–296, [hep-ph/9303321].

[179] M. V. Libanov, V. A. Rubakov, D. T. Son and S. V. Troitsky, *Exponentiation of multiparticle amplitudes in scalar theories*, *Phys. Rev.* **D50** (1994) 7553–7569, [hep-ph/9407381].

[180] M. V. Libanov, D. T. Son and S. V. Troitsky, *Exponentiation of multiparticle amplitudes in scalar theories. 2. Universality of the exponent*, *Phys. Rev.* **D52** (1995) 3679–3687, [`hep-ph/9503412`].

[181] M. B. Voloshin, *Nonperturbative methods*, in *27th International Conference on High-energy Physics (ICHEP 94) Glasgow, Scotland, July 20-27, 1994*, pp. 0121–134, 1994, `hep-ph/9409344`.

[182] V. V. Khoze, *Multiparticle Higgs and Vector Boson Amplitudes at Threshold*, *JHEP* **07** (2014) 008, [`1404.4876`].

[183] V. V. Khoze, *Perturbative growth of high-multiplicity W, Z and Higgs production processes at high energies*, *JHEP* **03** (2015) 038, [`1411.2925`].

[184] C. Degrande, V. V. Khoze and O. Mattelaer, *Multi-Higgs production in gluon fusion at 100 TeV*, *Phys. Rev.* **D94** (2016) 085031, [`1605.06372`].

[185] A. S. Gorsky and M. B. Voloshin, *Nonperturbative production of multiboson states and quantum bubbles*, *Phys. Rev.* **D48** (1993) 3843–3851, [`hep-ph/9305219`].

[186] M. V. Libanov, V. A. Rubakov and S. V. Troitsky, *Multiparticle processes and semiclassical analysis in bosonic field theories*, *Phys. Part. Nucl.* **28** (1997) 217–240.

[187] J. Jaeckel and V. V. Khoze, *Upper limit on the scale of new physics phenomena from rising cross sections in high multiplicity Higgs and vector boson events*, *Phys. Rev.* **D91** (2015) 093007, [`1411.5633`].

[188] J. S. Gainer, *Measuring the Higgsplosion Yield: Counting Large Higgs Multiplicities at Colliders*, `1705.00737`.

[189] V. V. Khoze, J. Reiness, J. Scholtz and M. Spannowsky, *A Higgsploding Theory of Dark Matter*, `1803.05441`.

[190] L. D. Faddeev and A. A. Slavnov, *Gauge fields: Introduction to quantum theory*, *Front. Phys.* **50** (1980) 1–232.

[191] P. G. Tinyakov, *Instanton like transitions in high-energy collisions*, *Int. J. Mod. Phys.* **A8** (1993) 1823–1886.

[192] S. Yu. Khlebnikov, V. A. Rubakov and P. G. Tinyakov, *Instanton induced cross-sections below the sphaleron*, *Nucl. Phys.* **B350** (1991) 441.

[193] L. D. Landau, *On the theory of transfer of energy at collisions I*, *Phys. Zs. Sowiet.* **1** (1932) 88.

[194] R. J. Glauber, *The Quantum theory of optical coherence*, *Phys. Rev.* **130** (1963) 2529–2539.

[195] R. J. Glauber, *Coherent and incoherent states of the radiation field*, *Phys. Rev.* **131** (1963) 2766–2788.

[196] W.-M. Zhang, D. H. Feng and R. Gilmore, *Coherent states: Theory and some Applications*, *Rev. Mod. Phys.* **62** (1990) 867–927.

[197] V. A. Rubakov and P. G. Tinyakov, *Towards the semiclassical calculability of high-energy instanton cross-sections*, *Phys. Lett.* **B279** (1992) 165–168.

[198] V. A. Rubakov, D. T. Son and P. G. Tinyakov, *An Example of semiclassical instanton like scattering: (1+1)-dimensional sigma model*, *Nucl. Phys.* **B404** (1993) 65–90, [hep-ph/9212309].

[199] A. M. Jaffe, *High-energy Behavior In Quantum Field Theory. I. Strictly Localizable Fields*, *Phys. Rev.* **158** (1967) 1454–1461.

[200] R. Rajaraman, *Solitons and instantons. An introduction to solitons and instantons in quantum field theory*, *Amsterdam, Netherlands: North-Holland.* (1982) 409.

[201] N. Dorey, T. J. Hollowood, V. V. Khoze and M. P. Mattis, *The Calculus of many instantons*, *Phys. Rept.* **371** (2002) 231–459, [hep-th/0206063].

[202] V. A. Rubakov and D. T. Son, *Renormalization group for multiparticle production in (2+1)-dimensions around the threshold*, in *8th International Seminar on High-energy Physics (Quarks 94) Vladimir, Russia, May 11-18, 1994*, pp. 233–240, 1994, hep-ph/9406362.

[203] L. Landau and E. Lifshitz, *Quantum Mechanics: Non-Relativistic Theory.* Course of Theoretical Physics. Elsevier Science, 1981.

[204] S. R. Coleman, *The fate of false vacuum. 1. Semiclassical theory*, *Phys. Rev.* **D15** (1977) 2929–2936.

[205] M. Shifman, *Advanced topics in quantum field theory*, *Cambridge University press* (2012) 622.

[206] S. V. Iordanskii and L. P. Pitaevskii, *Multiphoton boundary of the excitation spectrum in He II*, *Sov. Phys. JETP* **49** (1979) 386.

[207] M. B. Voloshin, *On strong high-energy scattering in theories with weak coupling*, *Phys. Rev.* **D43** (1991) 1726–1734.

[208] S. Yu. Khlebnikov, *Semiclassical approach to multiparticle production*, *Phys. Lett.* **B282** (1992) 459–465.

[209] D. Diakonov and V. Petrov, *Nonperturbative isotropic multiparticle production in Yang-Mills theory*, *Phys. Rev.* **D50** (1994) 266–282, [hep-ph/9307356].

[210] C. Bachas, *A Proof of exponential suppression of high-energy transitions in the anharmonic oscillator*, *Nucl. Phys.* **B377** (1992) 622–648.

[211] J. Jaeckel and S. Schenk, *Exploring High Multiplicity Amplitudes in Quantum Mechanics*, 1806.01857.

[212] R. Peccei, *Qcd, strong cp and axions*, in *KOSEF-JSPS Winter School on Recent Developments in Particle and Nuclear Theory*, vol. 29, pp. S199–S208, 1996, `hep-ph/9606475`.

[213] A. E. Nelson, *Naturally Weak CP Violation*, *Phys. Lett.* **136B** (1984) 387–391.

[214] S. M. Barr, *Solving the strong* CP *problem without the peccei-quinn symmetry*, *Phys. Rev. Lett.* **53** (Jul, 1984) 329–332.

[215] S. M. Barr, *A Natural Class of Nonpeccei-quinn Models*, *Phys. Rev.* **D30** (1984) 1805.

[216] C. A. Baker et al., *An Improved experimental limit on the electric dipole moment of the neutron*, *Phys. Rev. Lett.* **97** (2006) 131801, [`hep-ex/0602020`].

[217] R. J. Crewther, P. Di Vecchia, G. Veneziano and E. Witten, *Chiral Estimate of the Electric Dipole Moment of the Neutron in Quantum Chromodynamics*, *Phys. Lett.* **88B** (1979) 123.

[218] V. Baluni, CP-*nonconserving effects in quantum chromodynamics*, *Phys. Rev. D* **19** (Apr, 1979) 2227–2230.

[219] R. D. Peccei and H. R. Quinn, *CP Conservation in the Presence of Instantons*, *Phys. Rev. Lett.* **38** (1977) 1440–1443.

[220] R. D. Peccei and H. R. Quinn, *Constraints Imposed by CP Conservation in the Presence of Instantons*, *Phys. Rev.* **D16** (1977) 1791–1797.

[221] M. Dine, *TASI lectures on the strong CP problem*, in *Flavor physics for the millennium. Proceedings, Theoretical Advanced Study Institute in elementary particle physics, TASI 2000, Boulder, USA, June 4-30, 2000*, pp. 349–369, 2000, `hep-ph/0011376`.

[222] Particle Data Group collaboration, M. Tanabashi, K. Hagiwara, K. Hikasa, K. Nakamura, Y. Sumino, F. Takahashi et al., *Review of particle physics*, *Phys. Rev. D* **98** (Aug, 2018) 030001.

[223] L. Bento, G. C. Branco and P. A. Parada, *A Minimal model with natural suppression of strong CP violation*, *Phys. Lett.* **B267** (1991) 95–99.

[224] O. Davidi, R. S. Gupta, G. Perez, D. Redigolo and A. Shalit, *The Nelson-Barr Relaxion*, *Phys. Rev.* **D99** (2019) 035014, [`1711.00858`].

[225] M. C. Gonzalez-Garcia and Y. Nir, *Neutrino masses and mixing: evidence and implications*, *Rev. Mod. Phys.* **75** (Mar, 2003) 345–402.

[226] S. Bilenky, C. Giunti and W. Grimus, *Phenomenology of neutrino oscillations*, *Progress in Particle and Nuclear Physics* **43** (Jan, 1999) 1–86.

[227] C. Giunti and C. W. Kim, *Fundamentals of Neutrino Physics and Astrophysics.* 2007.

[228] Super-Kamiokande Collaboration collaboration, Y. Fukuda, T. Hayakawa, E. Ichihara, K. Inoue, K. Ishihara, H. Ishino et al., *Evidence for oscillation of atmospheric neutrinos*, *Phys. Rev. Lett.* **81** (Aug, 1998) 1562–1567.

[229] SNO Collaboration collaboration, Q. R. Ahmad, R. C. Allen, T. C. Andersen, J. D. Anglin, G. Bühler, J. C. Barton et al., *Measurement of the rate of $\nu_e + d \rightarrow p + p + e^-$ interactions produced by ^8b solar neutrinos at the sudbury neutrino observatory*, *Phys. Rev. Lett.* **87** (Jul, 2001) 071301.

[230] SNO Collaboration collaboration, Q. R. Ahmad, R. C. Allen, T. C. Andersen, J. D.Anglin, J. C. Barton, E. W. Beier et al., *Direct evidence for neutrino flavor transformation from neutral-current interactions in the sudbury neutrino observatory*, *Phys. Rev. Lett.* **89** (Jun, 2002) 011301.

[231] P. Minkowski, *$\mu \rightarrow e\gamma$ at a rate of one out of 109 muon decays?*, *Physics Letters B* **67** (1977) 421 − 428.

[232] S. F. King, *Neutrino mass models*, *Rept. Prog. Phys.* **67** (2004) 107–158, [hep-ph/0310204].

[233] A. Ibarra, E. Molinaro and S. T. Petcov, *Tev scale see-saw mechanisms of neutrino mass generation, the majorana nature of the heavy singlet neutrinos and $(\beta\beta)0\nu$-decay*, *Journal of High Energy Physics* **2010** (Sep, 2010) .

[234] J. Barry, W. Rodejohann and H. Zhang, *Light sterile neutrinos: models and phenomenology*, *Journal of High Energy Physics* **2011** (Jul, 2011) .

[235] C. D. Froggatt and H. B. Nielsen, *Hierarchy of Quark Masses, Cabibbo Angles and CP Violation*, *Nucl. Phys.* **B147** (1979) 277–298.

[236] I. Baldes, T. Konstandin and G. Servant, *Flavor cosmology: Dynamical yukawas in the froggatt-nielsen mechanism*, *JHEP* **12** (2016) 073, [1608.03254].

[237] J. M. Cline, *Baryogenesis*, in *Les Houches Summer School - Session 86: Particle Physics and Cosmology: The Fabric of Spacetime Les Houches, France, July 31-August 25, 2006*, 2006, hep-ph/0609145.

[238] R. H. Cyburt, *Primordial nucleosynthesis for the new cosmology: Determining uncertainties and examining concordance*, *Phys.Rev.D* **70** (2004) 023505, [astro-ph/0401091].

[239] W. Hu and S. Dodelson, *Cosmic microwave background anisotropies*, *Ann.Rev.Astron.Astrophys.* **40** (2002) 171–216, [astro-ph/0110414].

[240] E. W. Kolb and M. S. Turner, *The Early Universe, Front. Phys.* **69** (1990) 1–547.

[241] A. Sakharov, *Violation of cp invariance, c asymmetry, and baryon asymmetry of the universe*, *Sov.Phys.Usp.* **34** (1991) 392–393.

[242] G. 't Hooft, *Symmetry breaking through bell-jackiw anomalies*, *Phys. Rev. Lett.* **37** (Jul, 1976) 8–11.

[243] V. Kuzmin, V. Rubakov and M. Shaposhnikov, *On the anomalous electroweak baryon number nonconservation in the early universe*, *Phys.Lett.B* **155** (1985) 36.

[244] S. Davidson, E. Nardi and Y. Nir, *Leptogenesis*, *Phys.Rept.* **466** (2008) 105–177, [`0802.2962`].

[245] C. Jarlskog, *Commutator of the quark mass matrices in the standard electroweak model and a measure of maximal* CP *nonconservation*, *Phys. Rev. Lett.* **55** (Sep, 1985) 1039–1042.

[246] A. G. Cohen and D. B. Kaplan, *Thermodynamic Generation of the Baryon Asymmetry*, *Phys. Lett.* **B199** (1987) 251–258.

[247] A. G. Cohen and D. B. Kaplan, *Spontaneous Baryogenesis*, *Nucl. Phys.* **B308** (1988) 913–928.

[248] A. G. Cohen, D. B. Kaplan and A. E. Nelson, *Spontaneous baryogenesis at the weak phase transition*, *Phys. Lett.* **B263** (1991) 86–92.

[249] A. De Simone and T. Kobayashi, *Cosmological Aspects of Spontaneous Baryogenesis*, *JCAP* **1608** (2016) 052, [`1605.00670`].

[250] D. E. Morrissey and M. J. Ramsey-Musolf, *Electroweak baryogenesis*, *New Journal of Physics* **14** (Dec, 2012) 125003.

[251] J. H. Oort, *The force exerted by the stellar system in the direction perpendicular to the galactic plane and some related problems*, *Bull. Astron. Inst. Netherlands* **6** (1932) 249–287.

[252] F. Zwicky, *Die Rotverschiebung von extragalaktischen Nebeln*, *Helvetica Physica Acta* **6** (Jan, 1933) 110–127.

[253] V. C. Rubin, W. K. Ford, Jr. and N. Thonnard, *Extended rotation curves of high-luminosity spiral galaxies. IV. Systematic dynamical properties, Sa through Sc*, *Astrophys. J.* **225** (1978) L107–L111.

[254] R. Massey, T. Kitching and J. Richard, *The dark matter of gravitational lensing*, *Rept. Prog. Phys.* **73** (2010) 086901, [`1001.1739`].

[255] W. J. Percival, C. M. Baugh, J. Bland-Hawthorn, T. Bridges, R. Cannon, S. Cole et al., *The 2df galaxy redshift survey: the power spectrum and the matter content of the universe*, *Monthly Notices of the Royal Astronomical Society* **327** (Nov, 2001) 1297–1306.

[256] SDSS collaboration, D. J. Eisenstein et al., *Detection of the Baryon Acoustic Peak in the Large-Scale Correlation Function of SDSS Luminous Red Galaxies*, *Astrophys. J.* **633** (2005) 560–574, [`astro-ph/0501171`].

[257] D. Clowe, M. Bradač, A. H. Gonzalez, M. Markevitch, S. W. Randall, C. Jones et al., *A direct empirical proof of the existence of dark matter*, *The Astrophysical Journal* **648** (Aug, 2006) L109–L113.

[258] Planck collaboration, P. A. R. Ade et al., *Planck 2015 results. XX. Constraints on inflation*, *Astron. Astrophys.* **594** (2016) A20, [1502.02114].

[259] Planck collaboration, P. A. R. Ade et al., *Planck 2015 results. XIII. Cosmological parameters*, *Astron. Astrophys.* **594** (2016) A13, [1502.01589].

[260] Planck collaboration, N. Aghanim et al., *Planck 2018 results. VI. Cosmological parameters*, 1807.06209.

[261] B. D. Fields, *The primordial lithium problem*, *Ann. Rev. Nucl. Part. Sci.* **61** (2011) 47–68, [1203.3551].

[262] LIGO Scientific Collaboration and Virgo Collaboration collaboration, B. P. Abbott, R. Abbott, T. D. Abbott, M. R. Abernathy, F. Acernese, K. Ackley et al., *Observation of gravitational waves from a binary black hole merger*, *Phys. Rev. Lett.* **116** (Feb, 2016) 061102.

[263] LIGO Scientific Collaboration and Virgo Collaboration collaboration, B. P. Abbott, R. Abbott, T. D. Abbott, F. Acernese, K. Ackley, C. Adams et al., *Gw170817: Observation of gravitational waves from a binary neutron star inspiral*, *Phys. Rev. Lett.* **119** (Oct, 2017) 161101.

[264] B. Carr, *Primordial black holes as dark matter and generators of cosmic structure*, *Illuminating Dark Matter* (2019) 29–39.

[265] C. Alcock, R. A. Allsman, D. R. Alves, T. S. Axelrod, A. C. Becker, D. P. Bennett et al., *MACHO project limits on black hole dark matter in the 1–30 $m_\odot$ range*, *The Astrophysical Journal* **550** (apr, 2001) L169–L172.

[266] Y. Ali-Haïmoud, E. D. Kovetz and M. Kamionkowski, *Merger rate of primordial black-hole binaries*, *Phys. Rev. D* **96** (Dec, 2017) 123523.

[267] P. Tisserand, L. Le Guillou, C. Afonso, J. N. Albert, J. Andersen, R. Ansari et al., *Limits on the macho content of the galactic halo from the eros-2 survey of the magellanic clouds*, *Astronomy & Astrophysics* **469** (Apr, 2007) 387–404.

[268] T. D. Brandt, *Constraints on macho dark matter from compact stellar systems in ultra-faint dwarf galaxies*, *The Astrophysical Journal* **824** (Jun, 2016) L31.

[269] G. Bertone and D. Hooper, *History of dark matter*, *Rev. Mod. Phys.* **90** (2018) 045002, [1605.04909].

[270] H. P. Nilles, *Supersymmetry, Supergravity and Particle Physics*, *Phys. Rept.* **110** (1984) 1–162.

[271] A. B. Lahanas, *LSP as a Candidate for Dark Matter*, *Lect. Notes Phys.* **720** (2007) 35–68, [hep-ph/0607301].

[272] M. E. Peskin, *Supersymmetric dark matter in the harsh light of the Large Hadron Collider*, Proc. Nat. Acad. Sci. **112** (2014) 12256–12263.

[273] M. Schumann, *Direct detection of wimp dark matter: concepts and status*, Journal of Physics G: Nuclear and Particle Physics **46** (Aug, 2019) 103003.

[274] E. Charles, *Indirect dark matter searches: Status and prospects*, in *Proceedings, 2nd World Summit on Exploring the Dark Side of the Universe (EDSU2018): Point a Pitre, Guadeloupe, France, June 25-29, 2018*, vol. EDSU2018, p. 012, SISSA, 2018, DOI.

[275] P. Fox, A. Pierce and S. D. Thomas, *Probing a QCD string axion with precision cosmological measurements*, `hep-th/0409059`.

[276] A. E. Nelson and J. Scholtz, *Dark Light, Dark Matter and the Misalignment Mechanism*, Phys. Rev. **D84** (2011) 103501, [`1105.2812`].

[277] S. D. M. White, C. S. Frenk and M. Davis, *Clustering in a Neutrino Dominated Universe*, Astrophys. J. **274** (1983) L1–L5.

[278] G. Ballesteros, J. Redondo, A. Ringwald and C. Tamarit, *Unifying inflation with the axion, dark matter, baryogenesis and the seesaw mechanism*, Phys. Rev. Lett. **118** (2017) 071802, [`1608.05414`].

[279] G. Ballesteros, J. Redondo, A. Ringwald and C. Tamarit, *Standard Model?axion?seesaw?Higgs portal inflation. Five problems of particle physics and cosmology solved in one stroke*, JCAP **1708** (2017) 001, [`1610.01639`].

[280] A. Salvio, *A Simple Motivated Completion of the Standard Model below the Planck Scale: Axions and Right-Handed Neutrinos*, Phys. Lett. **B743** (2015) 428–434, [`1501.03781`].

[281] A. Salvio, *Critical Higgs inflation in a Viable Motivated Model*, Phys. Rev. **D99** (2019) 015037, [`1810.00792`].

[282] Y. Ema, K. Hamaguchi, T. Moroi and K. Nakayama, *Flaxion: a minimal extension to solve puzzles in the standard model*, JHEP **01** (2017) 096, [`1612.05492`].

[283] L. Calibbi, F. Goertz, D. Redigolo, R. Ziegler and J. Zupan, *Minimal axion model from flavor*, Phys. Rev. **D95** (2017) 095009, [`1612.08040`].

[284] S. A. Abel, R. S. Gupta and J. Scholtz, *Out-of-the-box baryogenesis during relaxation*, Phys. Rev. D **100** (Jul, 2019) 015034.

[285] S. M. Barr, *Solving the Strong CP Problem Without the Peccei-Quinn Symmetry*, Phys. Rev. Lett. **53** (1984) 329.

[286] O. Davidi, R. S. Gupta, G. Perez, D. Redigolo and A. Shalit, *The hierarchion, a relaxion addressing the Standard Model's hierarchies*, JHEP **08** (2018) 153, [`1806.08791`].

[287] A. Banerjee, H. Kim and G. Perez, *Coherent relaxion dark matter*, 1810.01889.

[288] B. Batell, G. F. Giudice and M. McCullough, *Natural heavy supersymmetry*, *JHEP* **12** (2015) 162, [1509.00834].

[289] B. Batell, M. A. Fedderke and L.-T. Wang, *Relaxation of the composite higgs little hierarchy*, *JHEP* **12** (2017) 139, [1705.09666].

[290] M. Kawasaki, T. Kobayashi and F. Takahashi, *Non-Gaussianity from Curvatons Revisited*, *Phys. Rev.* **D84** (2011) 123506, [1107.6011].

[291] K. Choi, H. Kim and T. Sekiguchi, *Dynamics of the cosmological relaxation after reheating*, *Phys. Rev.* **D95** (2017) 075008, [1611.08569].

[292] R. S. Gupta, Z. Komargodski, G. Perez and L. Ubaldi, *Is the Relaxion an Axion?*, *JHEP* **02** (2016) 166, [1509.00047].

[293] K. Choi, H. Kim and S. Yun, *Natural inflation with multiple sub-Planckian axions*, *Phys. Rev.* **D90** (2014) 023545, [1404.6209].

[294] K. Choi and S. H. Im, *Realizing the relaxion from multiple axions and its UV completion with high scale supersymmetry*, *JHEP* **01** (2016) 149, [1511.00132].

[295] D. E. Kaplan and R. Rattazzi, *Large field excursions and approximate discrete symmetries from a clockwork axion*, *Phys. Rev.* **D93** (2016) 085007, [1511.01827].

[296] M. D'Onofrio, K. Rummukainen and A. Tranberg, *Sphaleron Rate in the Minimal Standard Model*, *Phys. Rev. Lett.* **113** (2014) 141602, [1404.3565].

[297] K. Dick, M. Lindner, M. Ratz and D. Wright, *Leptogenesis with Dirac neutrinos*, *Phys. Rev. Lett.* **84** (2000) 4039–4042, [hep-ph/9907562].

[298] S. Alekhin et al., *A facility to Search for Hidden Particles at the CERN SPS: the SHiP physics case*, *Rept. Prog. Phys.* **79** (2016) 124201, [1504.04855].

[299] F. Capozzi, E. Lisi, A. Marrone and A. Palazzo, *Current unknowns in the three neutrino framework*, *Prog. Part. Nucl. Phys.* **102** (2018) 48–72, [1804.09678].

[300] R. S. Gupta, *Relaxion measure problem*, *Phys. Rev.* **D98** (2018) 055023, [1805.09316].

[301] T. Flacke, C. Frugiuele, E. Fuchs, R. S. Gupta and G. Perez, *Phenomenology of relaxion-Higgs mixing*, *JHEP* **06** (2017) 050, [1610.02025].

[302] S. Aharony, N. Akerman, R. Ozeri, G. Perez, I. Savoray and R. Shaniv, *Constraining Rapidly Oscillating Scalar Dark Matter Using Dynamic Decoupling*, 1902.02788.

[303] A. Banerjee, D. Budker, J. Eby, H. Kim and G. Perez, *Relaxion Stars and their detection via Atomic Physics*, 1902.08212.

[304] W. R. Inc., "Mathematica, Version 12.0."
`https://www.wolfram.com/mathematica`.

[305] T. Kinoshita, *Mass singularities of Feynman amplitudes*, *J. Math. Phys.* **3** (1962) 650–677.

[306] T. D. Lee and M. Nauenberg, *Degenerate Systems and Mass Singularities*, *Phys. Rev.* **133** (1964) B1549–B1562.

[307] F. Bloch and A. Nordsieck, *Note on the radiation field of the electron*, *Phys. Rev.* **52** (Jul, 1937) 54–59.

[308] Y. L. Dokshitzer, G. D. Leder, S. Moretti and B. R. Webber, *Better jet clustering algorithms*, *JHEP* **08** (1997) 001, [`hep-ph/9707323`].

[309] M. Wobisch and T. Wengler, *Hadronization corrections to jet cross-sections in deep inelastic scattering*, in *Monte Carlo generators for HERA physics. Proceedings, Workshop, Hamburg, Germany, 1998-1999*, pp. 270–279, 1998, `hep-ph/9907280`, `https://inspirehep.net/record/484872/files/arXiv:hep-ph_9907280.pdf`.

[310] R. Atkin, *Review of jet reconstruction algorithms*, *Journal of Physics: Conference Series* **645** (oct, 2015) 012008.